STAT3-induced metabolic reprogramming in post-ischemic astrocytes and the further impact on neuronal respiration and synaptogenesis

Inaugural-Dissertation

For
the doctoral degree of

Dr. rer. nat.

From the Faculty of Biology
University of Duisburg-Essen

Germany

Submitted by

Mina Borbor

Born in Tehran, Iran

September 2022

The experiments underlying the present work were conducted at the Department of Neurology at the University of Duisburg-Essen.

1. Examiner: Prof. Dr. Med. Dirk M. Hermann

2. Examiner: PD Dr. Phil. Josephine Herz

3. Examiner: Prof. Dr. rer. nat. Alessandro Prigione

Chair of the Board of Examiners: Prof. Dr. med. Joachim Fandrey

Date of the oral examination: ___________27.03.2023____________________

DOI: 10.17185/duepublico/78138
URN: urn:nbn:de:hbz:465-20230425-081520-1

Table of Contents

List of abbreviations

Abbreviation	Description
1`Ab	Primary antibodies
2-DG	2-Deoxy-d-glucose
AGCs	Aspartate-glutamate carriers
ALDH1L1	Aldehyde dehydrogenase 1 L1
ANOVA	Analysis of variance
APS	Ammonium persulfate
AraC	Cytosine β-D-arabinofuranoside
ATP	Adenosine triphosphate
BBB	Blood-brain barrier
BCA	Bicinchoninic acid assay
BSA	Bovine serum albumin
CBF	Cerebral blood flow
CBV	Cerebral blood volume
CCCP	Carbonyl cyanide m-chlorophenylhydrazone
CKO	Conditional knock-out
CM	Conditioned medium
CMRO2	Cerebral metabolic rate for oxygen
CNS	Central nervous system
CSF	Cerebral spinal fluid
DAMP	Damage-associated molecular pattern
DIV	Days in vitro
DMSO	Dimethyl sulfoxide
DNA	Deoxyribonucleic acid
DS	Donkey serum
E 15	Embryonic stage 15
EAAT1	Excitatory amino acid transporter 1
EAAT2	Excitatory amino acid transporter 2
ECAR	Extracellular acidification rate
ECM	Extracellular matrix
ETC	Electron transport chain
FADH2	Flavin adenine dinucleotide hydrogen

FAs	Fatty acids
FCCP	Carbonyl cyanide-4-(trifluoromethoxy) phenylhydrazone
FDA	Food and drug administration
GABA	Gamma-aminobutyric acid
GAD	Glutamate decarboxylase
GAPDH	Glyceraldehyde 3-phosphate dehydrogenase
GAT3	GABA transporter
GCs	Glutamate carriers
GDH	Glutamine dehydrogenase
GEF	Glucose extraction fraction
GFAP	Glial fibrillary acidic protein
GLAST1	Glutamate aspartate transporter 1
GlnD,	Glutamine deprived
GLT	Glutamate transporter 1
GlucD	Glucose deprived
Glut 1	Glucose transporter 1
GP	Glycogen phosphorylase
GP130	Glycoprotein 130
GPCRs	G-protein coupled receptors
GRA	Glycolytic rate assay
GS	Glycogen synthetase
GSH	Glutathione (reduced form)
H	Hour
HCl	Hydrochloric acid
HEPES	4-(2-hydroxyethyl)-1-piperazineethanesulfonic acid
HIF	Hypoxia-inducible factor
HRE	hypoxic response element
HRP	Horseradish peroxidase
HyD	Hybrid detector
I/R	Ischemia/reperfusion
ICC	Immunocytochemistry
IL6	Interleukin 6
IMM	Inner mitochondrial membrane

Inc/dec	Increase/decrease
JAK 2	Janus kinase 2
kDa	Kilodalton
LDH	Lactate dehydrogenase
MAP2	Microtubule-associated protein 2
MCAO	Middle cerebral artery occlusion
MCT	Monocarboxylate transporter
Mito Sox	Mitochondrial superoxide
MM	Mitochondrial matrix
MMP	Mitochondrial membrane potential
MPTP	Mitochondrial permeability transition pore
MRI	Magnetic resonance imaging
MSA	Mito stress assay
MSCs	Mesenchymal stromal cells
MW	Molecular weight
NaCl	Sodium chloride
NADH	Nicotinamide adenine dinucleotide hydrogen
NADPH	Nicotinamide adenine dinucleotide phosphate
Neu+Ast	Neuron+Astrocyte co-cultures
NOX	NADPH oxidase
OAA	Oxaloacetate
OCR	Oxygen consumption rate
OEF	Oxygen extraction fraction
OGlnD	Oxygen/ glutamine deprived
OGlucD	Oxygen/glucose-deprived
OPCs	Oligodendrocyte progenitor cells
OXPHOS	Oxidative phosphorylation
PBS	Phosphate buffered saline
PC	Pyruvate carboxylase
PDH	Pyruvate dehydrogenase
Pdk1	Pyruvate dehydrogenase lipoamide kinase isozyme
PDL	Poly-D-lysine hydrobromide
PEP	phosphoenolpyruvate

PET	Positron emission tomography
PFA	Paraformaldehyde
PGM	Phosphoglucomutase
PIAs	Protein inhibitor of activated STATs
PKM	Pyruvate kinase M
PLO	Poly-L-ornithine hydrobromide
pM	Pico Molar
Ppi	Pyrophosphate
PPP	Pentose phosphate pathway
PRP	Platelet rich plasma
PSD95	postsynaptic density protein 95
PTMs	post-transcriptional modifications
r.u.	Relative unit
rCBF	Regional cerebral blood flow
RGB	Red-green-blue
RLU	Relative light unit
ROS	Reactive oxygen species
Rot/AA	Rotenone/Antimycin
RT	Room temperature
RTK	Receptor tyrosine kinase
SDS	Sodium dodecyl sulphate
SH2	Src homology 2
SIE	Sis-inducible element
SOCS	Suppressors of cytokine signaling
SODs	Superoxide dismutase
SRE	STAT3 response element
SSA	Succinic semialdehyde
STAT3	Signal transducer and activator of transcription 3
TAD	Transactivation domain
TBST	Tris-buffered saline Tween 20
TEMED	Tetramethyl ethylenediamine
TF	Transcription factor
TGFβ	Transforming growth factor-beta

TMRM	Tetramethyl rhodamine methyl ester perchlorate
TPA	Tissue plasminogen activator
UDP-Glucose	Uridine diphosphate Glucose
UTP	Uridine triphosphate
VEGF	Vascular endothelial growth factors
VGLUT1	Vesicular glutamate transporter 1
WT	Wild type
XF	Extracellular flux
α-KG	α-ketoglutarate

List of figures

List of tables

Summary

Activation of the signal transducer and activator of transcription (STAT) 3 is characteristic for a subpopulation of perilesional reactive astrocytes after stroke. Reactive astrocytes are crucial for sealing the injury in the post-ischemic brain. However, reactive astrogliosis diminishes the astrocytic neuroprotective properties in many neurodegenerative diseases. Based on previous knowledge indicating that STAT3 regulates the metabolic response in various disease models, this study explores the role of STAT3 signaling in metabolic reprogramming of an ischemia/reperfusion (I/R) model comprised of cultured astrocytes and their co-cultured neurons.

This study addresses the crosstalk between STAT3, hypoxic inducible factor (HIF) and pyruvate kinase M (PKM) 2 in I/R astrocytes, which were activated or inhibited for STAT3 canonical signaling by Interleukin 6 (IL6) or Stattic. Next, the metabolic properties and glycogen deposits in STAT3-activated or inhibited I/R astrocytes were analyzed. In addition, the impact of glycogen mobilization on astrocytic mitochondrial respiration and reducing capacity were addressed. Finally, the response from neurons co-cultured with STAT3 activated or inhibited I/R astrocytes was studied in terms of mitochondrial respiration and synaptic/neurite density. Further, STAT3 signaling and metabolic properties of glucose/glutamine-deprived astrocytes and their impact on co-cultured neurons were analyzed.

Our data reveal that a network of STAT3, PKM2, and HIF signaling drives a glycolytic profile in I/R astrocytes, circumventing mitochondrial respiration. Consumption of glycogen boosts mitochondrial turnover in STAT3-inhibited I/R astrocytes supporting mitochondrial respiration and synapses of co-cultured neurons. In contrast, STAT3-activated I/R astrocytes with compromised mitochondria induce mitochondrial impairment and synapse degradation in co-cultured neurons, indicating that STAT3 signaling in I/R astrocytes abolishes astrocytic mitochondrial-relevant support for neurons. On the contrary, consecutive STAT3 signaling in glucose-deprived astrocytes boosts mitochondrial respiration and protects synapses in co-cultured neurons. However, glutamine depletion does not activate STAT3 transcriptional properties, induces mitochondrial ROS, and fails to support the co-cultured neurons' mitochondrial respiration and synapses.

Zusammenfassung

Die Aktivierung des Signal Transducer and Activator of Transcription 3 (STAT3) ist charakteristisch für eine Subpopulation perilesionaler reaktiver Astrozyten nach einem Schlaganfall. Reaktive Astrozyten sind für die Versiegelung der Verletzung im post-ischämischen Gehirn von entscheidender Bedeutung. Die reaktive Astrogliose beeinträchtigt jedoch die neuroprotektiven Eigenschaften der Astrozyten bei vielen neurodegenerativen Erkrankungen. Ausgehend von früheren Erkenntnissen, die darauf hindeuten, dass STAT3 Stoffwechselreaktionen in verschiedenen Krankheitsmodellen reguliert, wird in dieser Studie die Rolle der STAT3-Signalübertragung bei der metabolischen Reprogrammierung eines Ischämie/Reperfusionschadens (I/R) untersucht, anhand eines Modells, das aus kultivierten Astrozyten und deren co-kultiviereten Neuronen besteht.

Diese Studie befasste sich mit der Wechselwirkung von STAT3, dem hypoxischen induzierbaren Faktor (HIF) und der Pyruvatkinase M (PKM) 2 in I/R-Astrozyten, die für die kanonische STAT3-Signalgebung durch Interleukin 6 (IL6) oder Stattic aktiviert bzw. gehemmt wurden. Anschließend wurden die Stoffwechseleigenschaften und Glykogenablagerungen in STAT3-aktivierten oder gehemmten I/R-Astrozyten sowie die Auswirkungen der Glykogenmobilisierung auf die mitochondriale Atmung der Astrozyten analysiert. Schließlich wurden Neuronen, die mit STAT3-aktivierten oder gehemmten I/R-Astrozyten co-kultiviert sind, im Hinblick auf die mitochondriale Atmung und die Synapsen-/Neuritendichte untersucht. Darüber hinaus wurden die STAT3-Signalübertragung und die metabolischen Eigenschaften von Astrozyten unter Glukose-/Glutamin-Entzug untersucht und ihre Auswirkungen auf co-kultivierte Neuronen analysiert.

Unsere Daten zeigen, dass STAT3-, PKM2- und HIF-Signalwege ein glykolytisches Profil in I/R-Astrozyten fördern, wodurch die mitochondriale Atmung umgangen wird. Der Verbrauch von Glykogen steigert den mitochondrialen Umsatz in STAT3-inhibierten I/R-Astrozyten und unterstützt so die mitochondriale Atmung und die Synapsen der co-kultivierte Neuronen. STAT3-aktivierte I/R-Astrozyten führen zu mitochondrialer Beeinträchtigung und Synapsenabbau in co-kultivierte Neuronen, was darauf hindeutet, dass STAT3-Signale in I/R-Astrozyten die astrozytäre mitochondriale Unterstützung für Neuronen verringern. Im Gegensatz dazu steigert

eine konsekutive STAT3-Aktivierung in Astrozyten unter Glukoseentzug die mitochondriale Atmung und schützt Synapsen in co-kultivierte Neuronen. Der Mangel an Glutamin aktiviert jedoch nicht die Transkriptionseigenschaften von STAT3, induziert mitochondriales ROS und unterstützt nicht die mitochondriale Atmung der co-kultivierte Neuronen und die Synapsen.

1. Introduction

1.1 Prevalence of stroke

On average, every 3 minutes, someone dies of a stroke (Virani et al. 2021) and stroke survivors commonly experience permanent disabilities (Lallukka et al. 2018; Yamashita and Abe 2012). Stroke risk is dependent on modifiable risk factors such as high blood pressure, obesity, hyperlipidemia, smoking, a sedentary lifestyle, and an unhealthy diet (Virani et al. 2021). According to the affected brain region and severity of the injury, the recovery rate varies between patients (Rathore et al. 2002).

There are two types of strokes: hemorrhagic stroke and ischemic stroke. Over 28% of stroke cases are hemorrhagic (WSO 2022). Hemorrhagic stroke occurs when a vessel in the circle of Willis bursts due to aneurysms or arteriovenous malformations, causing abnormal bleeding in the brain. Intracranial pressure caused by bleeding and subsequent acute blood coagulation results in immense brain tissue damage or even death (Musuka et al. 2015). In fact, hemorrhagic stroke has a high mortality rate of annually 3 million people in 3.4 million new intracerebral hemorrhages (WSO 2022). In this case, immediate surgical intervention is required to remove the intracranial hematoma and reduce the intracranial pressure. Furthermore, endovascular therapy could be employed to treat a further aneurysm (Unnithan and Mehta 2022; Musuka et al. 2015).

On the other hand, over 62% of stroke cases are ischemic (WSO 2022). Ischemic stroke occurs when a brain vessel, commonly the middle cerebral artery (MCA), is occluded (Hui, Tadi, and Patti 2022). Artery occlusion can result from atherosclerosis, thrombus, and embolus. Ischemic stroke has a lower mortality rate compared with hemorrhagic stroke (3.3 million people from 7.6 new ischemic strokes annually) (WSO 2022), and rapid restoration of blood flow after symptom onset improves stroke outcome significantly (Hacke et al. 2008). Commonly, thrombolytic agents such as recombinant tissue plasminogen activator (rtPA) are intravenously administrated to dissolve the blood clots and restore the blood flow (Hacke et al. 2008). However, evidence has shown that rtPA treatment remains beneficial up to 4.5 h after symptom onset (Hacke et al. 2008; Clark et al. 2000). This short time window severely limits the application of rtPA in the clinic. Endovascular thrombectomy with stent retriever devices has been proven to improve stroke outcomes in stroke patients with large vessel occlusions up to 24 hours after symptom onset (Nogueira et al. 2018). Limited therapeutic options for ischemic stroke have prompted research on the pathophysiology of ischemic stroke to identify novel stroke therapeutics.

1.2 Pathophysiology of ischemic stroke

As a result of vascular occlusion and ischemia-reperfusion injury, the brain tissue undergoes sequential cerebral pathological events known as ischemic cascade (Figure 1). At first, the brain exerts several strategies such as vasodilation to evade ischemia. However, vasculature blockage gradually hampers the supply of oxygen and nutrients. Lack of oxygen and glucose initially reduces neuronal oxidative metabolism and adenosine triphosphate (ATP) synthesis (Hata et al. 2000). Besides, hypoxia promotes anaerobic metabolism in neurons and glia with lactic acid as a byproduct (Rehncrona, Rosen, and Siesjo 1981; Welsh et al. 1980). Hypoxia-induced anaerobic metabolism is less energy-productive and lactate acidosis disturbs the acid-base balance in neural cells (Goldman et al. 1989; Kraig, Pulsinelli, and Plum 1985; Welsh et al. 1980). Lack of ATP in neurons disturbs the functionality of ATP-dependent ion exchange pumps such as Na^+/K^+ ATPases and Na^+/Ca^{2+} ATPases, causing intracellular accumulation of Na^+ and $Ca2^+$. Thus, ATP shortage causes an anoxic depolarization in the neuronal membrane (Anderson et al. 2005; Candelario-Jalil 2009; Dirnagl, Iadecola, and Moskowitz 1999).

Furthermore, the reverse stoichiometry of the ions results in an osmotic gradient increasing the intracellular water molecules and cytotoxic edema (Liebeskind et al. 2019). ATP deficiency in neurons and downregulation of the astrocytic glutamate transporters cause extracellular glutamate accumulation (Dirnagl, Iadecola, and Moskowitz 1999; Yi and Hazell 2006; Wu and Tymianski 2018). Consequently, α-amino-3-hydroxy-5-methyl-4-isoxazole propionic acid (AMPA) receptors and N-methyl-D-aspartate (NMDA) receptors are activated. Activation of voltage-dependent channels contributes to further glutamate release and excitotoxicity (Yi and Hazell 2006; Wu and Tymianski 2018). Furthermore, active NMDArs and defected Na^+/Ca^{2+} ATPases facilitate intracellular Ca^{2+} increase (Tanaka et al. 1997; Kristian and Siesjo 1998; Dirnagl, Iadecola, and Moskowitz 1999).

High intracellular Ca^{2+} initiates intracellular protein degradation and lipid peroxidation by activating enzymes such as proteases and lipases (Kristian and Siesjo 1998; Candelario-Jalil 2009). Furthermore, Ca^{2+} induces the formation of free radicals and reactive oxygen species (ROS) (Brennan et al. 2009; Kristian and Siesjo 1998). In addition, increasing mitochondrial Ca^{2+} caused by oxidative stress opens the mitochondrial permeability transition pore (MPTP). Persistent MPTPs result in mitochondrial swelling, cytochrome C release and activation of the apoptosis cascade (Kristian and Siesjo 1998; Li, Sun, et al. 2020).

On the other hand, damaged brain cells release damage-associated molecular patterns (DAMPs). DAMPs subsequently initiate the expression of adhesion molecules on the endothelial cell surface, which results in BBB disintegration and immune cell infiltration into the brain parenchyma (Ge et al. 2000; Liesz et al. 2015). The compromised BBB also allows fluid to enter the brain parenchyma causing vasogenic edema (Krueger et al. 2019). In addition, reactive astrogliosis occurs in response to the expanding inflammation, where the astrocytes form a scar around the injury to restrain the inflammation to the lesion core (Sofroniew 2009; Liddelow and Barres 2017).

Eventually, the ischemic cascade causes massive cell death and tissue degeneration leaving an irreversible necrotic tissue known as the ischemic lesion core. The core of an ischemic lesion is the tissue adjacent to the obstructed artery that essentially contains dead cells and fibrotic tissue. However, this area is surrounded by a salvageable peri-infarcted area (Lo 2008; Hakim 1998), which is “functionally impaired but morphologically intact” (Heiss et al. 2001; Hakim 1998). This tissue has a low regional cerebral blood flow (rCBF) of below 20 ml/100 g/min (Heiss et al. 2001; Hakim 1998). Insufficient perfusion restricts the access to oxygen and glucose that instantly affects oxidative phosphorylation (OXPHOS) in neurons. The probability of saving the peri-infarct tissue increases upon an immediate reestablishment of blood flow, allowing the formation of collateral circulation and renourishment of the area (Musuka et al. 2015; Lo 2008). The possibility of salvaging the peri-infarct tissue appoints this area as one of the main targets for therapeutic interventions (Li, Sun, et al. 2020; Warner et al. 1996; L, X, and Z 2016; Ranjan et al. 1993; Liu, Levine, and Winn 2010; Puisieux et al. 1994). Nevertheless, it should be emphasized that the existence of peri-infarct tissue is profoundly reliant on scar-forming reactive astrocytes, and in absence of glial scar, peri-infarct tissue is recruited to lesion core in the mouse MCA occlusion (MCAO) model (Li et al. 2008). Reactive astrocyte's crucial role in ischemic stroke has prompted researchers to dissect the characteristics of these cells in vivo and in vitro.

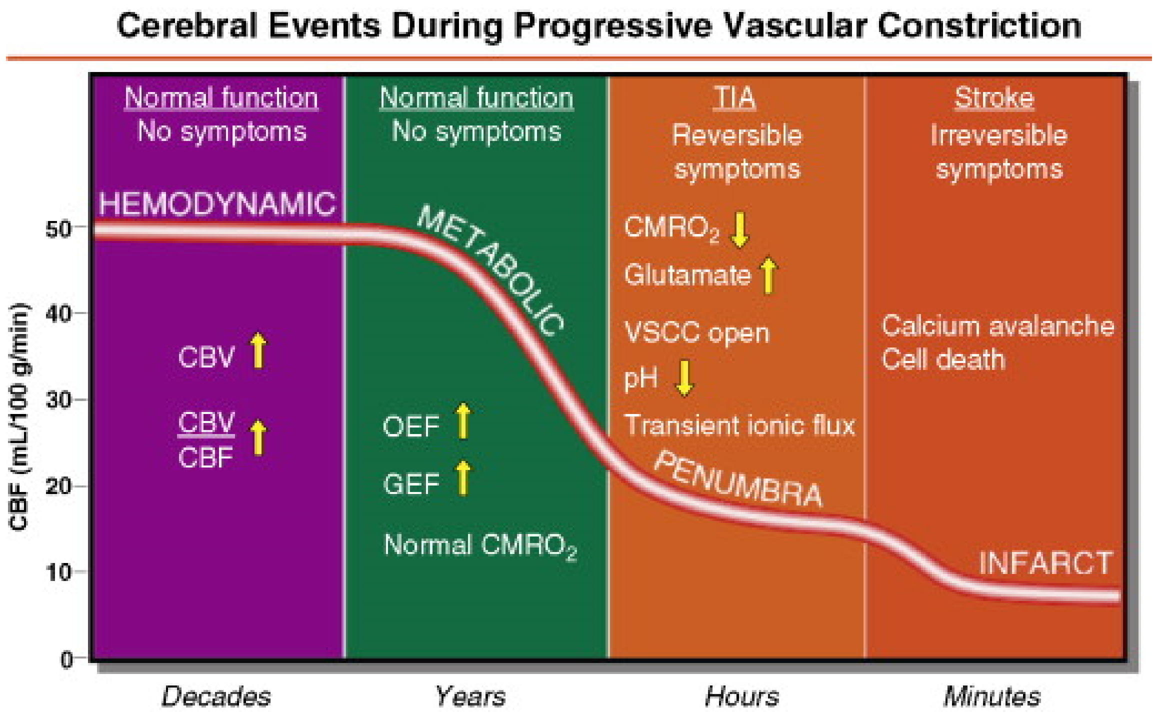

Figure 1: Cerebral events during the progressive vascular constriction

(Purple) Hemodynamic phase: Cerebral blood flow (CBF) declines slightly (<50 ml/100 g/min); vasodilation occurs to increase cerebral blood volume (CBV) and retain the CBF within the threshold. **(Green) Metabolic phase:** Blood flow is continuously reduced, and oxygen extraction fraction (OEF) and glucose extraction fraction (GEF) increase to conserve cerebral metabolic rate for oxygen (CMRO2). **(Light orange) Penumbra phase:** Normal CMRO2 cannot be further achieved due to the exhaustion of OEF and GEF accompanied by fragile perfusion (<20 ml/100 g/min). Oxidative ATP synthesis is replaced by anaerobic metabolism, causing acidosis. Ion exchange pumps lose functionality, leading to transient ion flux and opening the voltage-sensitive calcium channels (VSCCs), causing an extracellular accumulation of glutamate. This phase is succeeded with reversible symptoms. **(Dark orange) Infarct phase:** Perfusion drops below 12 ml/100 g/min. ATP synthesis is fully dismantled, and overall depolarization takes over the affected tissue. The so-called "calcium avalanche" stands for the massive intracellular translocation of calcium which is accompanied by massive cell death. This phase has an irreversible impact on the tissue (Hakim 1998), permission is obtained (supplementary,7.1.1)

1.3 Stroke and reactive astrogliosis

Astrocytes are among the most abundant cells in the brain tissue. The relative ratio of astrocytes and neurons in different species indicated that astrocytes are more abundant in animals with more complex brains. This suggests that more astrocytes are required to support synapses and regulate neurogenesis as well as synaptogenesis (Nedergaard, Ransom, and Goldman 2003).

Following an ischemic insult, some astrocytic characteristics are ablated, reduced, or enhanced depending on injury severity (Sofroniew 2000). Upon reactive astrogliosis (Figure 2), astrocytes leave their resting state, undergo hypertrophy, and upregulate their intermediate filaments, such as glial fibrillary acidic protein (GFAP), nestin, and vimentin (Kindy, Bhat, and Bhat 1992). Reactive astrogliosis begins as early as 4 h after the onset of ischemia in response to signals from apoptotic/necrotic cells, hypoxia, acidosis and infiltrating immune cells (Kindy, Bhat, and Bhat 1992; Kim et al. 2016; Pekny and Nilsson 2005; Zamanian et al. 2012). Initially, reactive astrocytes proliferate and migrate towards the lesion core to build the so-called glial scar around the infarct zone (Kindy, Bhat, and Bhat 1992) (Figure 2). This process is necessary to reconstruct BBB, restrain infiltration of immune cells and reduce neuronal cell death (Sofroniew 2009).

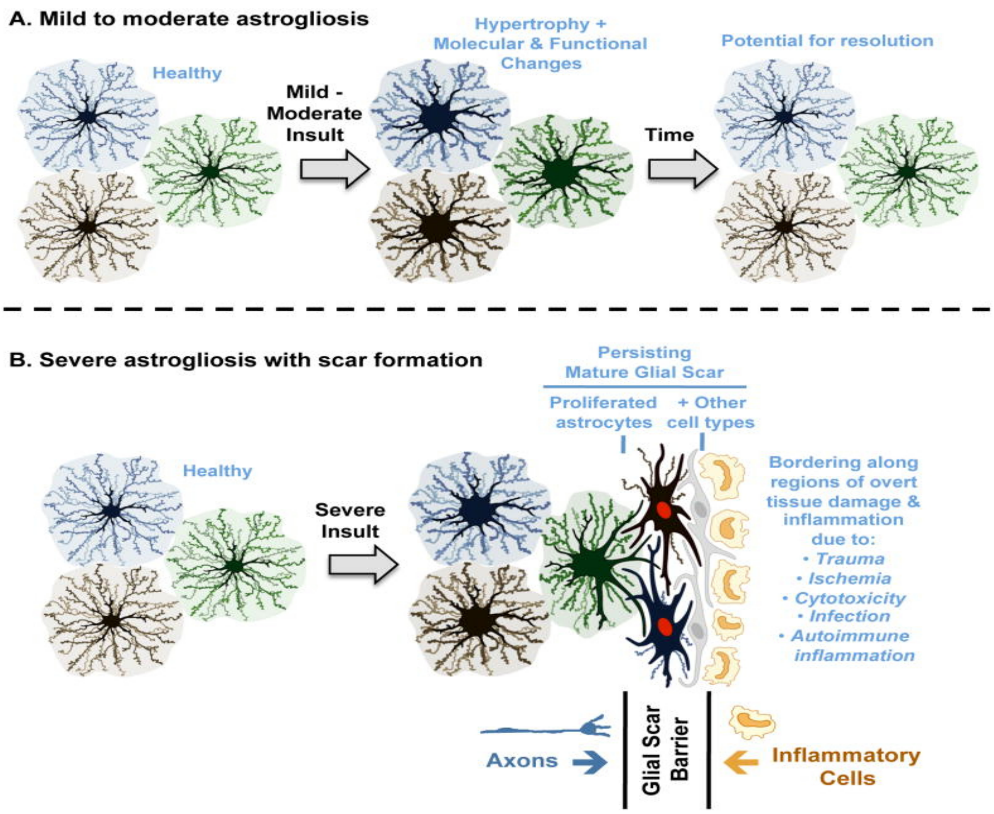

Figure 2: Reactive astrogliosis

Depending on duration, severity and spatial distance to injury, astrocytes undergo a mild **(A)** or severe **(B)** reactive astrogliosis. In mild injuries **(A)**, astrocytes undergo moderate astrogliosis **(A)**, in which a transient molecular and functional alteration leads to a short-term hypertrophy. However, in response to a severe insult **(A)**, astrocytes modify the entire molecular and functional profile to build a persisting and mature glia scar **(B)**. This process is accompanied by the proliferation and upregulation of intermediate filaments. Together with other cell types, astrocytes wall off the injury. The glia scar restrains the immune cells from entering the infarct zone, reducing the secondary inflammation caused by infiltrated immune cells. As a result of scar formation, axonal outgrowth towards the lesion core is hampered. (Sofroniew 2009) under the license 5238711500154, Elsevier

Despite their protective roles, scar-forming reactive astrocytes have also been shown to prevent axonal regeneration and neurite outgrowth (Smith, Miller, and Silver 1986; McKeon et al. 1991; Bush et al. 1999; Costa et al. 2002; Smith-Thomas et al. 1994). The heterogeneous nature of astrocytes substantially impacts the extent of their reactivity. Radial, protoplasmic, and fibrous astrocytes respond differently to injury (Chen and Swanson 2003). In addition, the severity of the injury, the spatial distance of astrocytes to lesion core, and duration after injury onset determine tasks that reactive astrocytes must fulfill (Liddelow and Barres 2017; Zamanian et al. 2012; Liddelow et al. 2017). Accordingly, reactive astrocytes are polarized into neurotoxic (A1) and neuroprotective (A2) subtypes (Liddelow and Barres 2017; Zamanian et al. 2012; Liddelow et al. 2017). Transcriptomics studies done by Zamanian et al. 2012 classify MCAO-derived reactive astrocytes as neuroprotective A2 subtypes. Nevertheless, Zamanian et al. categorize MCAO reactive astrocytes into pro-inflammatory phenotypes in the early stages and anti-inflammatory profiles in later stages post-ischemia. The ambiguity in astrocytic response was associated to different tasks that reactive astrocytes accomplish at different post-ischemic stages. While the immediate pro-inflammatory response is required to restrain the injury, the late anti-inflammatory response promotes tissue remodeling and reconstruction (Zamanian et al. 2012; Chen and Swanson 2003).

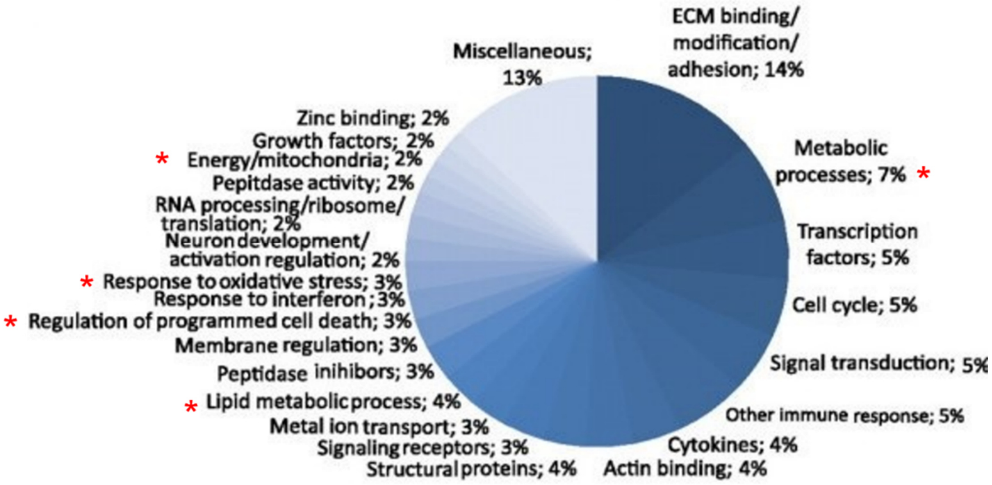

Figure 3: Transcriptomics of reactive astrocytes isolated from MCAO brains

Hierarchical clustering of the astrocytic gene expression in MCAO-derived reactive astrocytes. Red asterisks mark the changes of the genes that are involved in regulating astrocytic metabolism mitochondrial-specific genes, apoptosis and antioxidant defense (Zamanian et al. 2012)) (CC BY 4.0).

1.4 Astrocytic metabolism

1.4.1 Metabolism in resting astrocytes

Astrocytic metabolism in the resting state is divided into energy-producing and biosynthesis pathways. Astrocytic double-sided metabolism is required to fulfill energy demand and maintain homeostasis in the brain. Glycolysis, tricarboxylic acid cycle (TCA), and OXPHOS are energy-producing pathways, which can also serve biosynthetic purposes. Astrocytic biosynthesis is crucial for replenishing vital molecules such as antioxidants, gliotransmitters, glycogen, and ketone bodies (Rose et al. 2020).

Glucose is the preferential metabolic substrate in astrocytes, which is taken up through glucose transport 1 (Glut1), enwrapping the astrocytic end-feet around intraparenchymal capillaries (Prebil et al. 2011). Consuming glucose, astrocytes produce energy and provide the carbon backbone for biosynthesis (Castro et al. 2009; Rose et al. 2020). Glucose is initially phosphorylated to glucose 6-phosphate by hexokinase, allowing it to further participate in glycolysis, the pentose phosphate pathway, or glycogenesis (Prebil et al. 2011).

Although astrocytes undergo oxidative metabolism, the principal source of ATP is glycolysis with lactate as the primary metabolic product (Prebil et al. 2011; Supplie et al. 2017). Glycolytic lactate is released through the astrocytic monocarboxylate transporter (MCT) 1 and 4 (Rose et al. 2020). Astrocytes modulate neuronal metabolism by supplying glucose (Gandhi et al. 2009) or promoting lactate uptake in neurons (Rice 2000; Castro et al. 2007). Synaptic glutamate stimulates astrocytic ascorbate release (Castro et al. 2007; Lane and Lawen 2013), which is taken up by neurons through sodium vitamin C transporters (Castro et al. 2008). Intracellular accumulation of the ascorbate in neurons reduces glucose consumption and increases lactate uptake through MCT2 (Castro et al. 2007; Castro et al. 2008). Using lactate dehydrogenase (LDH), neurons convert lactate to pyruvate for further oxidative metabolism, circumventing glycolysis (Rose et al. 2020; Turner and Adamson 2011).

Glycolysis in astrocytes also generates pyruvate, which enters mitochondria through mitochondrial pyruvate carriers (MPCs) (Figure 4, 4 Black). One of the crucial steps in glycolysis is the conversion of the phosphoenolpyruvate (PEP) to pyruvate catalyzed by pyruvate kinase M (PKMs) (Figure 4, 2 Black). PKMs appear in cytoplasmic tetrameric or nuclear dimeric forms. Cytosolic tetrameric PKM dephosphorylates the PEP to pyruvate and facilitates ATP generation at the end of the glycolysis. On the contrary, PKM dimers translocate into the nuclei and regulate genes responsible for lactate-generating glycolysis (Gao et al. 2012; Zhang, Deng, et al. 2019). Within mitochondria, pyruvate dehydrogenase (PDH) oxidizes pyruvate to the acetyl-CoA (Judge and Dodd 2020).

Apart from glucose, astrocytes consume fatty acids (FA)/ketone bodies (Le Foll and Levin 2016; Valdebenito et al. 2016) that enter astrocytes through MCTs. Within the cytoplasm, FAs are activated and enter astrocytic mitochondria, where they undergo β-oxidation to generate acetyl-CoA (Rose et al. 2020).

Acetyl-CoA further enters the tricarboxylic acid cycle (TCA), which eventually generates nicotinamide adenine dinucleotide hydrogen (NADH) and flavin adenine dinucleotide hydrogen (FADH2). NADH and FADH2 are the main inputs in OXPHOS that take place in the inner mitochondrial membrane (IMM), particularly in the electron transport chain (ETC). ETC is constituted of protein transporters or enzymes, which are reduced by NADH and FADH2. ETC protein complexes utilize the energy from donated electrons to pump protons into inner mitochondrial space (IMS) and eventually reduce O_2 to H_2O at complex IV (Figure 4, 5 Black). Consequently, a proton gradient known as proton motif force is formed between the mitochondrial matrix (MM) and the IMS, facilitating proton flux through ATP-synthetase (complex V) leading to ATP generation. Each NADH provides 2.5 ATP and each FADH2 produces 1.5 ATP. As a result, OXPHOS generates substantially more ATP than lactate-generating glycolysis (Figure 4, Black 4 and 5). However, less advanced ETC in astrocytes initiates more OXPHOS-mediated ROS compared to neurons due to electron leakage from ETC (Lopez-Fabuel et al. 2016)

Besides ATP synthesis, 30-50 % of pyruvate transported in astrocytic mitochondria is consumed for synthetic purposes rather than OXPHOS (Weber and Barros 2015). Due to pyruvate carboxylase (PC), 4.3-fold of the glycolytic pyruvate in astrocytic mitochondria is decarboxylated to oxaloacetate (OAA) instead of being dehydrogenized to acetyl-CoA. Astrocytic TCA constantly replenishes the TCA intermediates such as oxaloacetate (OAA), citrate and α-ketoglutarate (α-KG) in a process known as anaplerosis. Furthermore, astrocytes integrate a proportion of absorbed neurotransmitters in their TCA cycle, which can fuel both OXPHOS and anaplerotic reactions (Figure 4, Black 6 and 8). Glutamate, for instance, is transported into astrocytic mitochondria and transaminated into α-KG (Rose et al. 2020). Interestingly, glutamate entry in the TCA cycle is dependent on extracellular glutamate (McKenna et al. 1996). Similarly, excess gamma-aminobutyric acid (GABA) is transported to MM to be metabolized to succinate (Schousboe, Bak, and Waagepetersen 2013). Accumulation of these metabolites in the mitochondrial matrix enables astrocytes to undergo gluconeogenesis and de novo synthesis of FA, amino acids, and antioxidants (Rose et al. 2020).

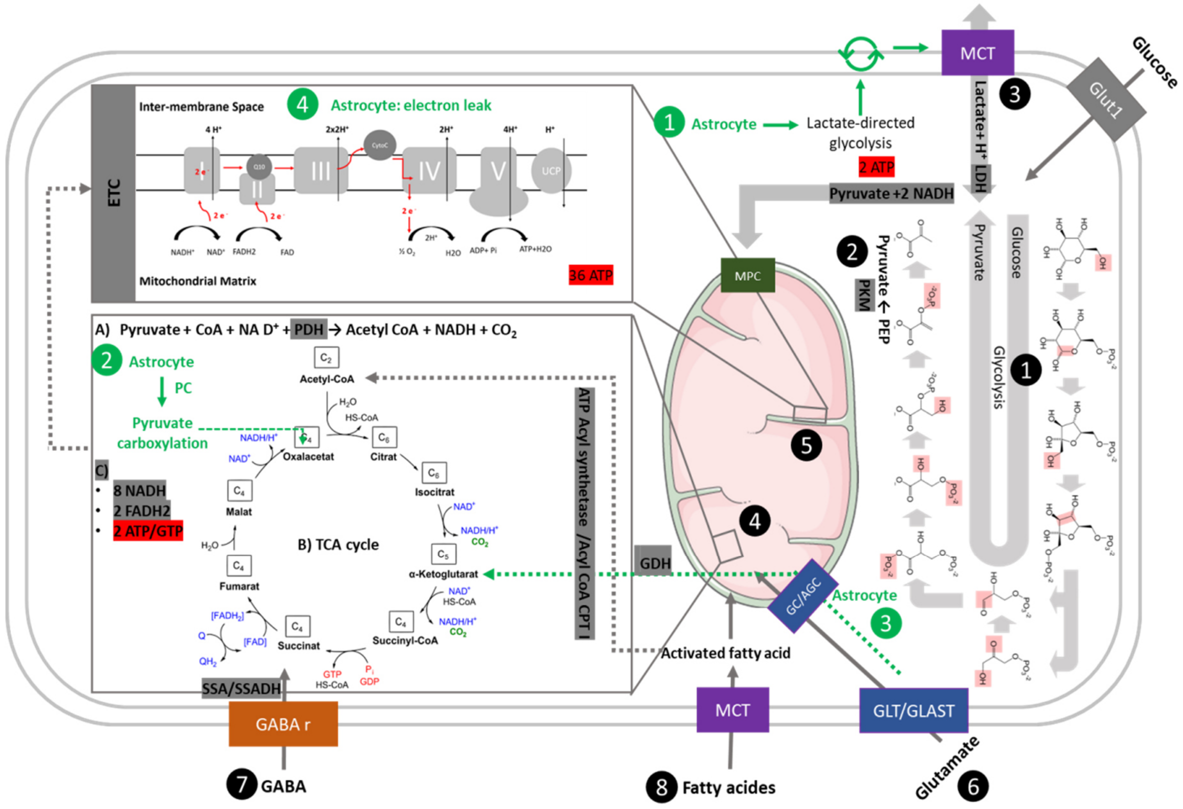

Figure 4: Astrocytic metabolism

Glucose metabolism:(1 Black) through glycolysis glucose is metabolized to pyruvate. **(2 Black)** pyruvate kinase M (PKM) catalyzes phosphoenolpyruvate (PEP) oxidation to pyruvate, generating 2 ATP and NADH for each glucose, subsequent pyruvate mitochondrial transport through mitochondrial pyruvate carriers (MPCs). **(3 Black)** lactate dehydrogenase (LDH) catalyzes the conversion of pyruvate to lactate and subsequent lactate release through MCTs. **(1 Green)** prevalent lactate-directed glycolysis in astrocytes. **(4 Black) (A)** In mitochondrial matrix (MM), pyruvate dehydrogenase (PDH) catalyzes pyruvate oxidation to acetyl-CoA. **(2 Green)** prevalent pyruvate carboxylation (PC) to oxaloacetate (OAA) in astrocytes. **(B)** Acetyl-CoA enters the tricarboxylic acid cycle (TCA) and **(C)** generates NADH, FADH2 and ATP/GTP. **(5 Black)** NADH and FADH2 reduce the protein complex I and II of the electron transport chain (ETC), causing the electron transport across ETC and O_2 reduction to H_2O in complex IV. Protons enter ATP-synthase, causing phosphorylation of ADP to ATP (30-32 ATP). **Neurotransmitter metabolism (6 Black)** glutamate enters through GLT/GLAST, GABA enters through GABA receptors (GABA r). Both are transported to MM through mitochondrial glutamate carriers (GCs) and aspartate-GCs (AGCs); glutamate gets deaminated to α-ketoglutaraldehyde (α-KG) by glutamine dehydrogenase (GDH), **(7 Black)** GABA gets converted to succinate by semialdehyde (SSA) and succinic semialdehyde dehydrogenase (SSADH) **(8 Black) fatty acid (FA) s metabolism:** FAs enter through MCTs, get activated in the cytoplasm, and undergo β-oxidation to the Acetyl-CoA, NADH and FADH2 in MM. **(4 Green)** electron leakage is enhanced in astrocytic ETC. Background information is adopted from (Judge and Dodd 2020) Glycolysis: Thomas Shafee, CC BY 4.0, TCA cycle Yikrazuul, CC BY 3.0

The pentose phosphate pathway (PPP) (Figure 5) is another biosynthetic pathway, which is 5 to 7 times more in resting astrocytes compared to neurons (Takahashi 2021). PPP is neither ATP dependent nor generating ATP. It is an anabolic process in which glucose is oxidized to 5-carbon sugars (pentoses). In essence, PPP is constituted of oxidative and non-oxidative phases. In the oxidative phase (Figure 5, 2), a proportion of glucose-6-P is oxidized into pentose (ribulose 5-phosphate). The energy derived from this reaction reduces 2 NADP+ into NADPH. NADPH serves as a primary electron donor in cellular reactions, mainly during the antioxidant defense. It also contributes to the biosynthesis of fatty acids. In the non-oxidative phase, pentoses resulting from the oxidative phase are transformed into other substantial pentoses, namely ribose-5-phosphate, to replenish nucleotide synthesis. The oxidative phase is irreversible. However, the pentoses can be subjected to a variety of enzymatic reactions upon cellular metabolic request giving rise to several intermediate metabolites. These intermediate metabolites can be consumed in glycolysis and other cellular pathways (Judge and Dodd 2020).

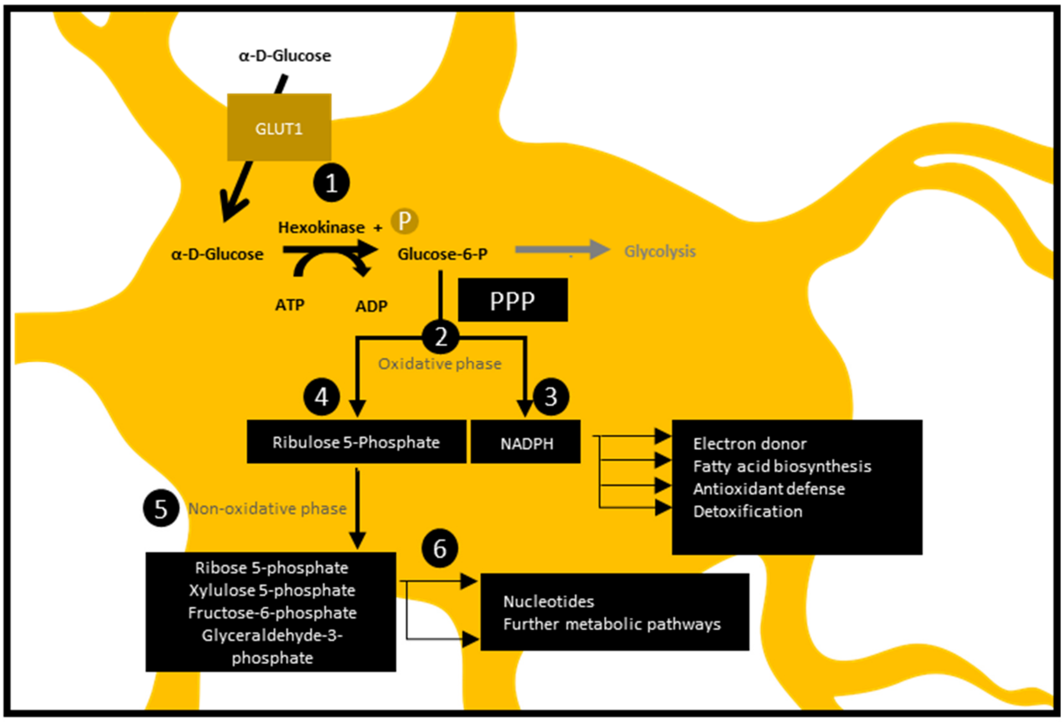

Figure 5: Pentose phosphate pathway

(1) Hexokinases catalyze α-D-glucose phosphorylation to glucose 6-phosphate. **(2)** glucose-6-P enters the pentose phosphate pathway (PPP), **(4)** oxidized in a pentose (ribulose 5-phosphate) and reduces NADP+ into the NADPH. **(3)** NADPH serves as an electron donor and can participate in fatty acids biosynthesis. **(5)** In the non-oxidative phase, ribulose 5-phosphate is transformed into other pentoses like ribose-5-phosphate (6) to replenish the nucleotide synthesis and other metabolic pathways **(5)**. General information is extracted from (Judge and Dodd 2020).

Another biosynthetic property of astrocytes is stockpiling excess glucose in glycogen form through glycogenesis (Gruetter 2003). Glycogenesis is energy-independent, involving several metabolic intermediates and enzymes (Figure 6, Black 2-5). Upon glucose scarcity, the glycogen reservoir is degraded into glucose 6-phosphate in an ATP-independent process called glycogenolysis (Figure 6, 1 and 2 red). Glycogen phosphorylase (GP) is activated during glycogenolysis, while glycogen synthase (GS), which is required for glycogenesis, is inhibited. Activated GP binds to glycogen bodies and releases the glucose 1-phosphate, which is further phosphor-mutated to glucose 6-phosphate (Benarroch 2010)(Figure 6, 1 and 2 red). Glucose 6-phosphate can be further metabolized to generate energy.

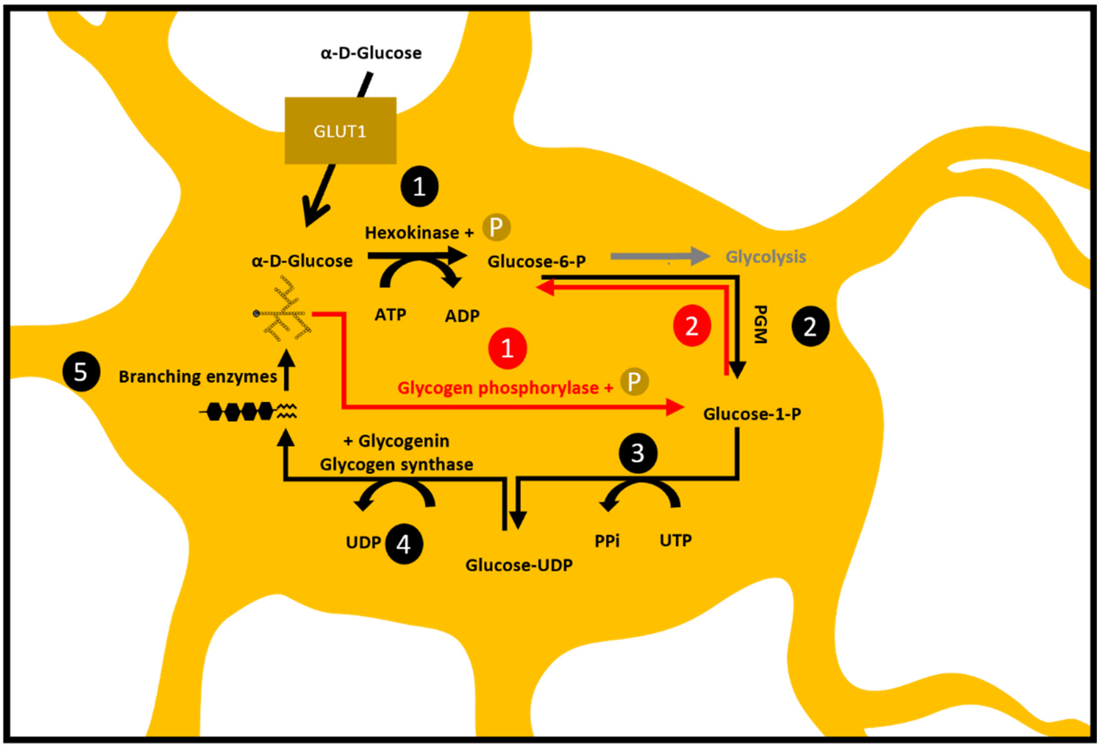

Figure 6: Glycogenesis and glycogenolysis

Glycogenesis:(1 Black) Hexokinases catalyze α-D-glucose phosphorylation to glucose 6-phosphate. **(2 Black)** Excess glucose-6-P is converted to glucose-1-P in a bidirectional reaction facilitated by Phosphoglucomutase (PGM). **(3 Black)** UTP—glucose-1-phosphate uridylyltransferase adopts a uridine triphosphate (UTP) to attach a uridine diphosphate UDP to glucose-1-P, converting it to active nucleotide uridine diphosphate Glucose (UDP-glucose) generating 1 inorganic phosphate (pi). glucose-1-phosphate + UTP ↔UDP-glucose + pyrophosphate (ppi). **(4 Black)** At first, glycogen synthetase (GS) catalyzes the attachment of the glucose from the UDP-glucose to a self-glycosylating enzyme known as glycogenin. Glucose attachment is via α1→4 glycosidic bond-forming a glycogen primer. **(5 Black)** More UDP-glucose targets the initial glycogen primer to polymerize the main glycogen branches. Side branches are formed via α1→6 glycosidic bonds using branching enzyme**. Glycogenolysis**: lack of glucose stimulates glycogen degradation **(1 Red).** Glycogen phosphorylase (GP) incorporates main glycogen branches and cleaves the α1→4 glycosidic bonds. Transferring a phosphate group to each glucose, GP forms glucose-1-P. Step **(2 Red)** Glucose-1-P is converted to glucose 6-P through PGM catalytic activity and can enter the glycolysis process. General information was extracted from (Whelan 2007; BiochenDen 2020).

Astrocytic biosynthesis support neurons constantly through gliotransmitters like ATP (Coco et al. 2003; Harada, Kamiya, and Tsuboi 2015), D-serine (Oliet and Mothet 2006; Henneberger et al. 2010) and glutamate (Rose et al. 2020). Besides, astrocytes also support neuronal metabolism by releasing viable mitochondria (Falchi et al. 2013).

1.4.2 Metabolism in ischemic reactive astrocytes

Metabolism in stroke-derived reactive astrocytes has been less discussed in the literature. Transient impairment of mitochondrial respiration is characteristic of cerebral ischemia (Hillered, Siesjo, and Arfors 1984; Sims and Pulsinelli 1987). Although post-ischemic mitochondrial dysfunction is reportedly attributed to neurons, Reichert et al. demonstrated that mitochondria of hypoxic astrocytes are also depolarized and form mitochondrial permeability transition pores (MPTP) (Reichert, Kim-Han, and Dugan 2001). MPTPs provide a nonspecific channel from MM to the outer mitochondrial membrane (OMM), enabling the entry of larger molecules and protons into mitochondria. As a result of proton intrusion to MM, IMM is further depolarized, electron transfer in ETC becomes leaky, free radicals are formed and ATP synthesis is impaired. Furthermore, because of increased mitochondrial permeability, mitochondria swell and OMM ruptures, which leads to the release of cytochrome C and activation of canonical apoptosis cascade (Li, Sun, et al. 2020).

To minimize mitochondrial damage, perilesional reactive astrocytes that maintain access to glucose (Nedergaard 1988) undergo anaerobic glycolysis to provide ATP (Becerra-Calixto and Cardona-Gomez 2017; Hillered, Siesjo, and Arfors 1984). This process is accompanied by massive lactate release (Nedergaard 1988; Hillered, Siesjo, and Arfors 1984) and increasing astrocytic intra and extracellular acidosis. Although the glycolytic ATP is sufficient for maintaining ionic gradient, acidity lower than pH=6.6 is not tolerated and eventually causes apoptosis in reactive astrocytes (Nedergaard 1988).

Ischemia also affects astrocytic biosynthetic pathways such as PPP and glycogenolysis. The literature approach towards PPP flux in reactive astrocytes is puzzling. While Takashi et al. demonstrated that hypoxia and glucose deprivation increase the PPP flux (Takahashi 2011), Kathagen et al. showed that astrocytes prioritize energy-producing pathways over PPP after ischemia (Kathagen et al. 2013). Furthermore, PPP fails to synthesize sufficient NADPH in MCAO-driven A1 reactive astrocytes (Guo et al. 2021).

Further studies on ischemic brains suggested that glycogen mobilization is restricted in reactive astrocytes, mainly in the infarct surrounding tissue (Kajihara et al. 2001; Cai et al. 2020). The inability to mobilize glycogen in reactive astrocytes has a detrimental effect on both energy-producing and biosynthetic pathways (Guo et al. 2021).

1.5 Multifaceted roles of STAT3

Signal transducer and activator of transcription (STAT) 3 is a pleiotropic protein that plays multiple roles in glia reactivity in many acute and chronic neurodegenerative diseases. Besides transcription activity, STAT3 plays a critical role in regulating cellular metabolism, mitochondrial respiration, cytoskeletal rearrangements, and senescence (Ceyzeriat et al. 2016).

Canonical STAT3 signaling is activated through Janus kinases (JAKs). JAKs are multimeric receptors associated with kinases and with an extracellular binding domain, which are activated by cytokines, hormones and growth factors. Upon activation, JAKs' extracellular binding domains are phosphorylated and undergo conformational changes to phosphorylate their intracellular kinases at tyrosine (Y) residues (Ceyzeriat et al. 2016). Prior to activation, suppressors of cytokine signaling (SOCS) inhibit cytoplasmic STAT3 monomers in their Src Homology 2 (SH2) domains (Heinrich et al. 2003). Upon activation, JAKs recruit STAT3 monomers to the cell membrane, where SOCS is detached from STAT3 and STAT3 is phosphorylated at Y705. Liberation from SOCS initiates dimerization of STAT3 monomers followed by nuclear translocation of dimerized STAT3. Activated nuclear STAT3 binds to the STAT3 response element (SRE) within the nuclei and regulates downstream gene expression (Ceyzeriat et al. 2016). Nevertheless, STAT3 can still be deactivated in nuclei through protein inhibitors of activated STATs (PIAs) (Heinrich et al. 2003). Furthermore, phosphorylation is not always essential for STAT3 transcription activities (Yang and Stark 2008).

Alternative STAT3 signaling cascades involve STAT3 Y705 phosphorylation via other receptors such as G-protein coupled receptors (GPCRs) or non-receptor tyrosine kinases (Ceyzeriat et al. 2016).

STAT3 non-canonical activation is associated with non-transcriptional activities and is mainly accompanied by post-transcriptional modifications (PTMs) other than phosphorylation at Y705. In non-canonical activation mode, STAT3 serves as a crucial structural and functional regulator. One of the STAT3 essential roles is to regulate the mitochondrial electron transport chain (ETC), in which phosphorylation occurs at serine (S) 727 (Yang and Rincon 2016). Acetylated STAT3 can also improve mitochondrial ATP synthesis by binding to pyruvate dehydrogenase (PDH) and converting more pyruvate to acetyl-coenzyme A (CoA) (Xu et al. 2016). STAT3 p (S

727) can regulate p (Y705) negatively (Chung, Uchida, et al. 1997) or positively (Wen, Zhong, and Darnell 1995); however, STAT3 transcriptional activity is dependent on Y705 phosphorylation (Wen, Zhong, and Darnell 1995).

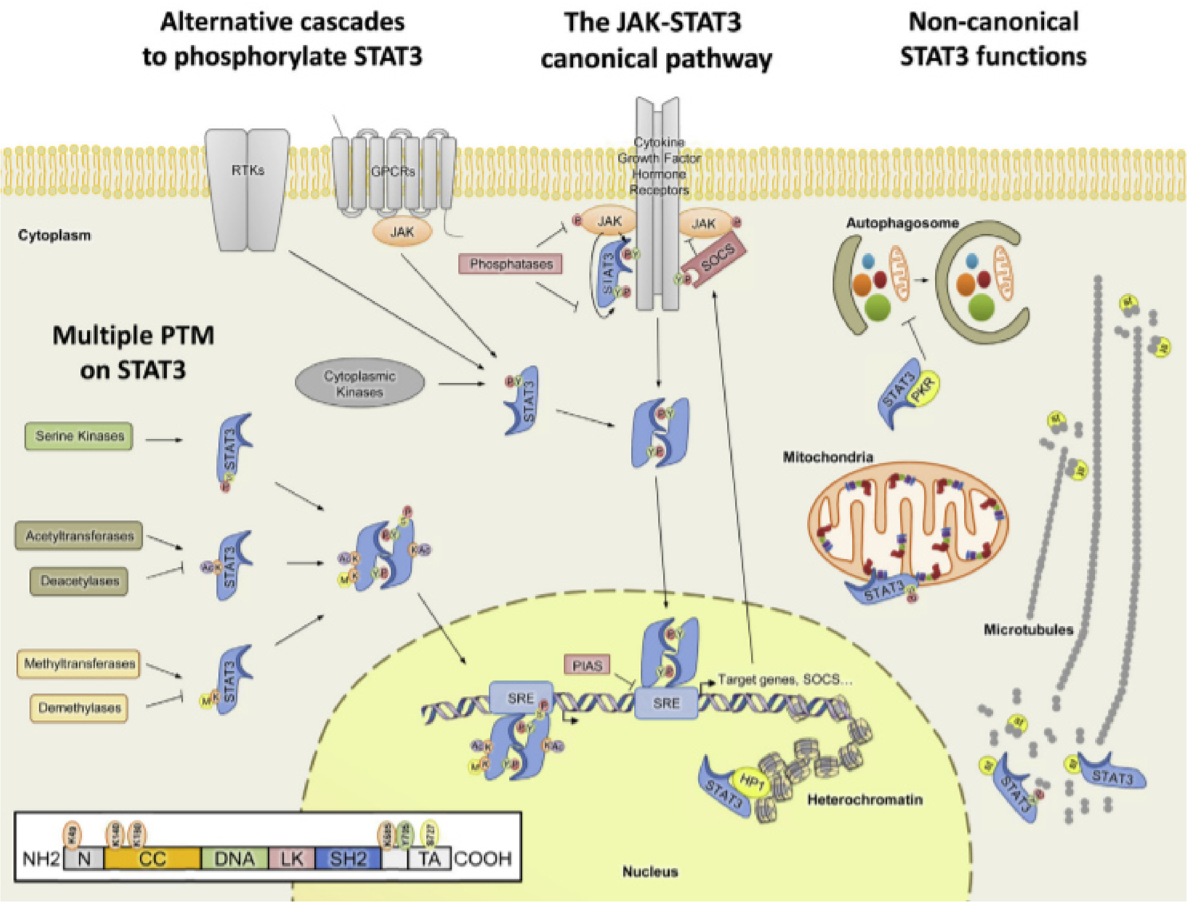

Figure 7: STAT3 multitasking abilities

(Middle) STAT3 canonical activation through Janus kinase (JAK) receptors. Ligands bind to the JAK receptor causing conformational changes accompanied by the transphosphorylation in JAKs tyrosine residues. Next, monomeric STAT3 is recruited to the membrane, where it is liberated from the cytoplasmic inhibitors suppressors of cytokine signaling (SOCS) and phosphorylated in the tyrosine residues of its Src Homology (SH2) domains. The phosphorylated monomers form a homodimer and then translocate in the nuclei. The STAT3 homodimers can still be deactivated through protein inhibitors of activated STAT3 (PIAS) in the nuclei. Otherwise, they target certain genomic regions known as STAT3 response element (SRE) and regulate the expression of the downstream genes. **(Top left) Alternative STAT3 activation:** STAT3 transcription activity is accomplished by activating other receptors such as receptor tyrosine kinase (RTK) or GPCRs and cytoplasmic kinases. **(Middle left) STAT3 post-translational modifications (PTM):** STAT3 can undergo several (PTM), such as serine phosphorylation, acetylation, and methylation. When the STAT3 undergoes PMT, it can serve specific transcriptional tasks. However, PMT mainly enables the STAT3 to serve its non-canonical tasks. **(Right) STAT3 non-canonical activities** are referred to as the non-transcriptional tasks that the STAT3 performs in the non-nuclear compartments as regulating the cytoskeleton, mitochondrial function and formation of the autophagosomes. (Ceyzeriat et al. 2016) license ID: 5244770499666

1.6 STAT3 signaling in peri-infarct reactive astrocytes

Ischemic stroke activates STAT3 signaling in astrocytes, neurons, microglia, and endothelial cells as well as in infiltrated macrophages (Justicia, Gabriel, and Planas 2000; Choi et al. 2003; Suzuki et al. 2001; Satriotomo, Bowen, and Vemuganti 2006). In addition, cell type, recovery duration, insult severity and distance to lesion core determine the STAT3 downstream properties. For instance, STAT3 is activated in apoptotic neurons, microglia, and macrophages (Suzuki et al. 2001).

In astrocytes, STAT3 is activated shortly after an ischemic insult in the ipsilateral striatum and cortex and remains for up to 3 to 7 days (Justicia, Gabriel, and Planas 2000) and in some cases, up to 14 days after ischemia onset (Choi et al. 2003; Cheng et al. 2018). However, the current understanding of STAT3 signaling in post-ischemic reactive astrocytes is limited to observatory studies, while the STAT3 functional role has remained unclear.

1.7 Role of STAT3 in reactive astrocytes

STAT3 activation post-stroke evokes contradicting responses. In some studies, inducing STAT3 signaling alleviates the stroke aftermath (Liu et al. 2014; Jung, Kim, and Chan 2011; Jung et al. 2009), while STAT3 ablation or downregulation is beneficial in others (Huang et al. 2020; Cheng et al. 2018; Rakers et al. 2019). This discrepancy can be partially due to common study models, which neglect the contrasting roles STAT3 serves in its canonical and non-canonical modes. Current knowledge about STAT3 role in reactive astrocytes is limited to acute loss of function studies, in which STAT3 expression is severely manipulated in several disease models such as ischemic stroke (Rakers et al. 2019; Huang et al. 2020), brain metastasis (Sarmiento Soto et al. 2020) and spinal cord injury (Herrmann et al. 2008; Okada et al. 2006). According to current studies, STAT3 signaling is involved in astrocytic proliferation and scar-forming (LeComte et al. 2015; Wanner et al. 2013; Okada et al. 2006; Sarafian et al. 2010; Herrmann et al. 2008). In fact, after MCAO, reactive glia co-express STAT3 and radial glial antigen receptor to regain their stem and progenitor properties (Sirko et al. 2013) and undergo proliferation (LeComte et al. 2015). The cell cycle regulatory role of STAT3 in reactive astrocytes (Sarafian et al. 2010) enables them to fulfill their self-renewal and tissue homeostasis tasks.

In addition, intermediate filaments such as nestin, vimentin and GFAP are among prominent downstream genes regulated by STAT3 (Herrmann et al. 2008; Yeo et al. 2013; Bonni et al. 1997). Transcriptome comparison of STAT3 conditional knock-out (CKO-STAT3) and wild-type (WT) astrocytes confirms a decrease in intermediate filaments, especially in GFAP expression (Sarafian et al. 2010). STAT3-mediated cytoskeletal rearrangement promotes wound healing properties in reactive astrocytes (Wanner et al. 2013; Okada et al. 2006) and support scar formation (Herrmann et al. 2008), which is essential for immediate restriction of injury.

Sarafian et al. 2010 evaluated the crucial role of STAT3 in astrocytic mitochondrial functioning. Mitochondrial regulatory genes, particularly those responsible for OXPHOS in ETC and antioxidant defense, are affected negatively in CKO-STAT3 astrocytes. Nevertheless, the authors acknowledged that the astrocytic CKO-STAT3 model failed to differentiate the contrasting roles served by STAT3 canonical and non-canonical modes (Sarafian et al. 2010).

1.8 Contrasting roles of canonical and non-canonical STAT3s

Present understanding of STAT3 canonical signaling in reactive astrocytes relies on studies done in cancer cells, particularly, glioblastoma and astrocytoma. Astrocytoma shares similar features with stroke-derived reactive astrocytes. For instance, both undergo proliferation and migration, are exposed to hypoxia and activate STAT3 signaling (Rahaman et al. 2002; Priego et al. 2018; Liang et al. 2013). Intensified glycolytic properties enable astrocytoma to survive the hypoxic tumor microenvironment (Turner and Adamson 2011). Similarly, stroke-derived reactive astrocytes were exposed to oxygen and nutrient deficiency and mitochondrial damage. Therefore, an enhanced glycolytic profile minimizes mitochondrial turnover, oxidative stress and apoptosis. Anaerobic glycolysis in tumor cells is achieved by activating STAT3 canonical signaling (Poli and Camporeale 2015). Constitutive activation of canonical STAT3 promotes hif-1α expression and further stabilizes the HIF protein complex. HIF complex promotes lactate-generating glycolysis by regulating glycolysis-associated genes, namely, pyruvate kinase M2 (PKM2). Nuclear dimers of PKM2 regulate genes required for lactate-generating glycolysis (Demaria and Poli 2012; Zhang, Deng, et al. 2019). In a feedforward loop (Figure 8), nuclear PKM2 increases HIFs transcription activity on the one hand and activates the nuclear STAT3s on the other hand (Demaria and Poli 2012). STAT3 and PKM2 co-expression has also been observed in reactive astrocytes of several other neurodegenerative diseases (Wei et al. 2020).

Interestingly, accumulating studies show that canonical and non-canonical STAT3 serve contrasting roles. While the canonical STAT3 signaling is a key metabolic regulator in inducing glycolytic profile in cancer cells, non-canonical counterparts such as acetylated (Xu et al. 2016) and p (S 727) STAT3 empower mitochondrial respiration, antioxidant defense and anti-apoptotic features (Yang and Rincon 2016; Poli and Camporeale 2015)

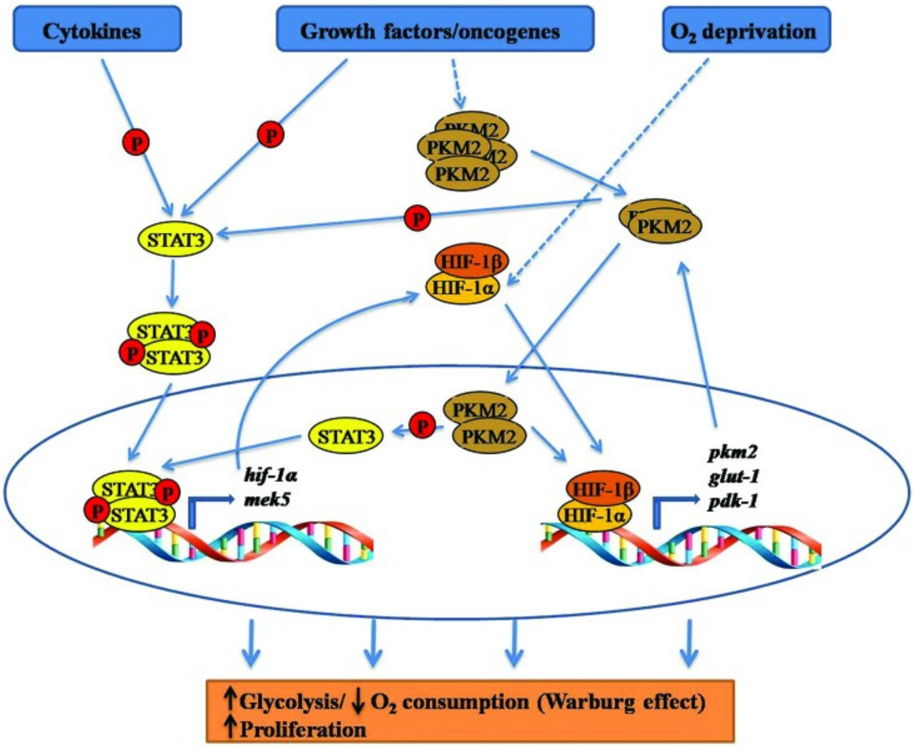

Figure 8: STAT3, PKM2 and HIF feedforward loop

(Left) In response to stimuli such as cytokines and growth factors, STAT3 is phosphorylated, dimerized and translocated in nuclei; there, it performs transcription activity by regulating the hif-1α expression. In response, the HIF-1α and β protein complex is stabilized and translocated in nuclei to regulate the expression of pkm2, glut1 and pyruvate dehydrogenase lipoamide kinase isozyme (pdk1). These genes are responsible for increasing lactate-generating glycolysis. **(Middle)** In response to the cytokine and growth factor, the dimer isoform of the PKM2 is translocated in nuclei. Within nuclei, it activates the STAT3 as well as the HIF-1α and β protein complex stabilization and their further transcription activity, which leads to an increase in glycolysis. Cytoplasmic PKM2 dimers can also activate the cytoplasmic STAT3. **(Right)** as a result of oxygen deprivation, HIF-1α and β protein complex are stabilized and translocated in nuclei, where it regulates downstream glycolysis responsible genes, namely PKM2. Transcription of the PKM2 replenishes the feedforward loop (Demaria and Poli 2012). Graphic is adopted from (Demaria and Poli 2012) with permission (Supplementary 7.1.3).

2 Aim of the study

Ischemic stroke is a primary cause of death and disability that commonly threatens elderly people with a declined metabolism. Nuclear translocation of STAT3 was detected in reactive astrocytes post-stroke already two decades ago. Since then, several studies have shown that STAT3 signaling is associated with astrocytic reactivity, proliferation, glial scar formation, and revealed contradictory roles of canonical and non-canonical modes of STAT3 activation. As a crucial metabolic regulator, STAT3 may be essential for regulating astrocytic metabolism and their impact on the neighboring neurons in stroke. Deciphering the role of STAT3 in astrocyte-neuronal metabolic interaction was the main goal of this study.

To achieve this goal, an indirect co-culture containing separatable astrocytic and neuronal compartments was established. Astrocytes were exposed to ischemia/reoxygenation (I/R) to mimic stroke while STAT3 signaling was manipulated by IL6 or Stattic, which activate and inhibit canonical STAT3 signaling correspondingly. Treated astrocytes were then co-cultured with untreated neurons to study the impact of the astrocytic STAT3 on neuronal function. By correlating STAT3 expression and activity in ischemic astrocytes with neuronal morphology, synaptogenesis and metabolism, we aimed to understand the mechanisms of astrocyte-mediated secondary neurodegeneration in ischemia.

Recent studies revealed that STAT3 triggers HIF and PKM2 as a part of feed-forward loop that promotes glycolysis in cancer and immune cells. Whether similar mechanism is activated in I/R astrocytes was unknown. Here, we evaluated STAT3-PKM2-HIF activation in our in vitro model using immunocytochemistry and functional luciferase reporter gene assay.

The mechanisms of metabolic switching in post-ischemic astrocytes has remained speculative. Our objective was therefore to explore STAT3 mediated regulation of astrocytic metabolism using mutually complementing methods. Using Seahorse XF-analysis of real-time glycolysis and mitochondrial OXPHOS, we determined how modulation of STAT3 activity regulates astrocytic metabolism. The analysis of live-cell metabolism was further supported by extracellular L-lactate and mitochondrial membrane potential (MMP) measurements. In addition, ETC electron leakage was analyzed by measuring mitochondrial superoxide formation (Mito SOX) in STAT3 activated/inhibited I/R astrocytes.

The role astrocytic glycogen gains growing attention in context of restorative therapies in ischemic stroke. Although some studies demonstrated glycogen aggregation in peri-infarct astrocytes, the underlying mechanisms and the role of glycogen utilization has been poorly investigated. In this study, we studied glycogen mobilization in STAT3 activated/inhibited I/R astrocytes. We further explored how inhibition of astrocytic glycogen phosphorylase (GP) affected astrocyte-neuronal interactions in ischemia.

To our best knowledge, astrocytic fuel-switching ability and its impact on neurons have not been investigated. Therefore, an additional objective of this study was to elucidate the impaction of different substates (glutamine and glucose) depletion on STAT3 activation and downstream metabolic responses in astrocytes, and their impact on the co-cultured neurons.

3 Materials and Methods

3.1 Experimental design

This experimental research on the impact of astrocytic STAT3 signaling on astrocyte-neuron interaction and cellular metabolism was performed predominantly in vitro using a previously established indirect astrocytes-neurons co-culture model (Gottschling et al. 2016). The experimental design of this study is depicted in Figure 9.

At first, STAT3 signaling was activated or inhibited in astrocytes of indirect astrocyte-neuron co-cultures using IL6 (canonical upstream of STAT3 signaling) or Stattic (STAT3 dimerization inhibitor). Then astrocyte cultures were further exposed to ischemia/reoxygenation (I/R) to simulate the ischemic stroke. In addition, glycogen mobilization was inhibited in STAT3 activated/inhibited I/R astrocytes using glycogen phosphorylase inhibitor (GPinh). Furthermore, to elucidate the role of STAT3 signaling in substrate-specific metabolic plasticity, astrocytes of the indirect astrocyte-neuron co-cultures were incubated with a glucose/glutamine-deprived medium. Finally, to evaluate the impact of treated astrocytes on neuronal respiration and synaptogenesis, they were co-cultured with non-treated mature neurons for 24 h.

Confocal/widefield microscopy was coupled with image analysis approaches to address astrocytic STAT3 and PKM2 nuclear/cytoplasmic dynamics and glycogen deposits, astrocytic and neuronal morphological alteration, and neuronal synapses.

In addition, a dual-luciferase reporter gene assay was utilized to evidence STAT3 and HIF transcription activity in astrocytes, while astrocytic reactivity was determined by immunoblotting astrocytic lysate with GFAP antibodies.

Astrocytic metabolism was addressed by coupling real-time glycolysis (Seahorse XF glycolytic rate assay-GRA) with actual enzyme-linked immunoassay (ELISA) measurement of L-lactate in the astrocytic conditioned medium (CM). In addition, astrocytic mitochondrial OXPHOS was assessed using Seahorse XF mitochondrial stress assay (MSA). As a complementary approach to OXPHOS, astrocytic mitochondrial membrane potential (MMP) was evaluated from live-cell microscopy images of the tetramethylrhodamine, tethyl Ester (TMRM) accumulation in astrocytic mitochondria.

Electron leakage and mitochondrial superoxide (Mito SOX) were measured using live-cell images of astrocytes incubated with Mito SOX indicator, while astrocytic cellular reducing capacity was determined by MTT assay.

Eventually, using MSA, mitochondrial OXPHOS was compared in co-cultured neurons, while neurite/synaptic density was evaluated from neuronal immunocytochemistry (ICC) images.

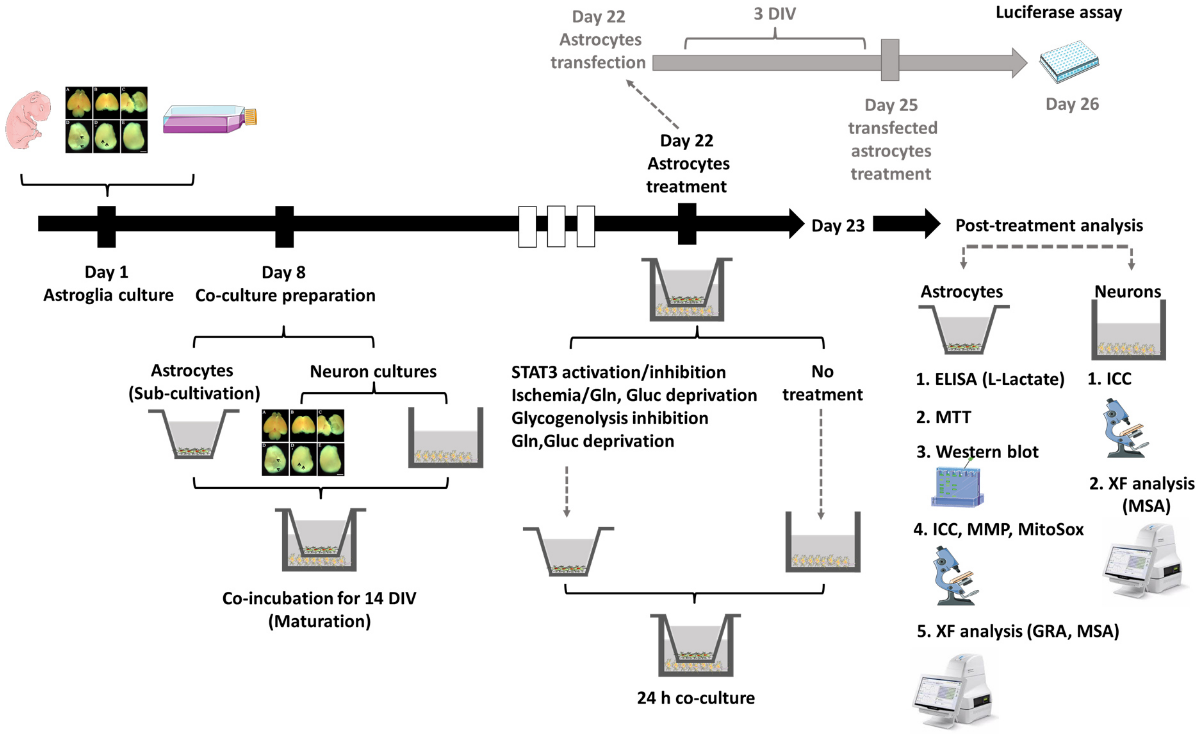

Figure 9: Experimental design

(Day1) Preparation of mixed glial cultures from postnatal (P1-2 days) mice cortices followed by subsequent 7 days in vitro (DIV) cultivation. **(Day 8)** Astrocytes sub-cultivation and neuron cultures preparation from E 15 mice hippocampal tissue. Co-incubation of astrocytes and neurons in indirect co-cultures for 14 DIV for further maturation. **(Day 22)** STAT3 activation/inhibition via pre-post incubation of mature astrocytes (21 DIV) with IL6/Stattic, additional ischemia-glutamine/glucose (Gln/Gluc) deprivation and glycogenolysis inhibition. Besides, incubation of astrocytes with Gln/Gluc deprived media. Further incubation of the treated astrocytes with untreated neurons for 24 h. **(Day 23) post-treatment analysis:** Astrocytes: **(1)** measuring L-lactate in astrocytic conditioned medium (ELISA). **(2)** MTT, **(3)** protein isolation and immunoblotting, **(4)** immunocytochemistry (ICC) and live-cell confocal microscopy of astrocytic TMRM (MMP) and Mito SOX. **(5)** Seahorse XF analysis, particularly glycolytic rate assay (GRA) and mito stress assay (MSA). Neurons: **(1)** Immunocytochemistry and **(2)** Seahorse XF analysis (MSA). **(Day22 gray)** Astrocyte transfection and incubation with corresponding plasmids for 3 DIV. **(Day 25)** Treatment of transfected astrocytes. **(Day 26)** Dual-luciferase reporter gene assay. Dissection procedure images were adopted from (Schildge et al. 2013) Creative Commons Public Domain Mark 1.0 and the image of the seahorse XF analyzer was adopted from Agilent open sources. Permission was acquired (supplementary 7.1.4).

3.2 Materials and equipment

Table 1: Equipment

Item	Brand and reference number	Country of origin
Centrifuge	Sigma-Aldrich (2-16PK)	Hamburg, Germany
Centrifuge	Eppendorf (5810R)	Hamburg, Germany
Centrifuge	Beckmann Coulter (Avanti J-26 XP)	Brea, CA, U.S.A.
Centrifuge	Eppendorf (MiniSpin)	Hamburg, Germany
Centrifuge	Beckmann Coulter (Optima L7-65)	Brea, CA, U.S.A.
Centrifuge	ThermoFisher (vacuum centrifuge SPC111V)	Waltham, MA, U.S.A.
Dissection set	Dumont (157.235)	Heidelberg, Germany
Freezer	Liebherr - 20 °C freezer	Biberach, Germany
Freezer	ThermoFisher - 80 °C freezer	Waltham, MA, U.S.A.
Gel electrophoresis system	Biorad	Hercules, California, U.S.A.
Heating block	Eppendorf	Hamburg, Germany
Hypoxia chamber	Toepffer Lab Systems	Göppingen, Germany
Incubator (non-CO_2)	Binder	Tuttlingen, Germany
Incubator cell culture	Eppendorf (Galaxy 170S)	Hamburg, Germany
laminar flow hood (Class II)	ThermoFisher (HERASAFE KS)	Waltham, MA, U.S.A.
Magnetic stirrer	IKA (IKAMAG)	Staufen, Germany
Microplate luminescence reader	BioTek (ELx800)	Winooski, Vermont, U.S.A.
Microplate absorbance reader	Biorad (iMark™)	Hercules, CA, U.S.A.
Microscope	ThermoFisher (AMG EVOS FL)	Waltham, MA, U.S.A.
Microscope	Zeiss ELYRAPS.1SIM/PALM/STORM/TIRF and LSM710	Wetzlar, Germany
Microscope	Zeiss AxioObserver.Z1 and Apotome	Oberkochen, Germany
Microscope	Zeiss Leica TCS SP8	Wetzlar, Germany
Microscope	Olympus BX51	Tokia, Japan
Mini-spin centrifuge	Eppendorf MiniSpin®/ MiniSpin® plus	Wesseling-Berzdorf. Germany
Molecular imager	General Electric Amersham™ Imager 680	Boston, MA, U.S.A.
Multi-dispenser pipette	Eppendorf	Wesseling-Berzdorf, Germany

Neubauer counting chamber	LO Laboroptik	Friedrichsdorf, Germany
pH-Meter	Hanna Instruments (HI 2215)	Vöhringen, Germany
Power supply	PowerPac/Biorad	Hercules, California, U.S.A.
Refrigerator	Liebherr 4 °C refrigerator	Biberach, Germany
Roller mixer	PHOENIX instrument (RS-TR05)	Garbsen, Germany
Rotator	Biometra (WT17)	Bremen, Germany
Scale	Kern (ABS 80-4)	Balingen-Frommern, Germany
Scale	Kern (EMB scale 200-2)	Balingen-Frommern, Germany
Scale	Kern (EW scale 4200-2NM)	Balingen-Frommern, Germany
Seahorse XFe24 analyzer	Agilent	Santa Clara, CA, U.S.A.
Shaker	Heidolph (DSG 304/M4)	Schwabach, Germany
TransBlot®Turbo™transferSystem	Biorad (1704150)	Hercules, California, U.S.A.
Ultrasonic homogenisator	SONOPLUS Bandelin,	Berlin, Germany
Vortex	Scientific industries Vortex Genie-2	New York, U.S.A.
Vortexing machine	IKA	Staufen, Germany
Water bath	Jolabo EM	Seelbach, Germany
Western blot gel releaser	Biorad (Cat.No 1653320)	Hercules, California, U.S.A.
Western blot set	Biorad	Hercules, California, U.S.A.
Western blot short plates	Biorad (Cat.No 1653308)	Hercules, California, U.S.A.
Western blot spacer plates	Biorad (Cat.No 1653311)	Hercules, California, U.S.A.

Table 2: Consumables

Item	Brand and reference number	Country of origin
Cell culture 24-well plates	SARSTEDT 83.3922	Nümbrecht, Germany
Cell culture 96-well plates	SARSTEDT 83.3924	Nümbrecht, Germany
Cell scrapper	SARSTEDT (REF44780))	Nümbrecht, Germany

Coverslips (10 mm)	Paul Marienfeld (0117500)	Baden-Württemberg, Germany
Coverslips (13 mm)	Paul Marienfeld (0117530)	Baden-Württemberg, Germany
Filter paper	GE Whatman	Dassel, Germany
Flacon tubes (15 ml)	SARSTEDT (REF62.547.254)	Nümbrecht, Germany
Flacon tubes (50 ml)	SARSTEDT (REF62.544.502)	Nümbrecht, Germany
Imaging dishes (µ-Dish 35 mm)	Ibidi (81156)	Gräfelfing, Germany
Microscope slides	Engelbrecht	Edermünde, Germany
Molecular biology filter	Biosphere (REF 70.1130.210)	Marburg, Germany
Multi-dispenser pipette tips	Eppendorf (REF12526)	Wesseling-Berzdorf, Germany
Needle (gauge 27)	BD (302200)	New Jersey, U.S.A.
Needle (gauge 27)	BD (300400)	New Jersey, U.S.A.
Nitrocellulose membranes (0.2 µm)	Bio-Rad (1620112)	Hercules, California, U.S.A.
PARAFILM® M	Sigma-Aldrich (P7793)	Darmstadt, Germany
Pasteur pipettes 230 mm	VWR (Cat.No 612-1702)	Pennsylvania, U.S.A.
Petri-dish (Four Internal Wells)	Greiner Bio-One CELLSTAR (627170)	Kremsmünster, Austria
Petri-dishes (6 mm)	SARSTEDT (REF83.39101)	Nümbrecht, Germany
Pipette tips 10 µl (colorless)	SARSTEDT (REF70.1130)	Nümbrecht, Germany
Pipette tips 1000µl (Blue)	SARSTEDT (REF70.762.10)	Nümbrecht, Germany
Pipette tips 200µl (yellow)	SARSTEDT (REF70.780.012)	Nümbrecht, Germany
Pipette tips 5000µl (colorless)	Eppendorf (I1053.0000)	Wesseling-Berzdorf, Germany
Plates (6 wells)	SARSTEDT (REF83.3920.005)	Nümbrecht, Germany
Plates (96 well)	SARSTEDT (REF83.3924)	Nümbrecht, Germany
Reaction micro-tubes 0.5ml	SARSTEDT (REF72.704.400)	Nümbrecht, Germany

Reaction micro-tubes 1.5 ml	SARSTEDT (REF72.706.400)	Nümbrecht, Germany
Reaction micro-tubes 1.5 ml	Eppendorf (107.004)	Wesseling-Berzdorf, Germany
Reaction micro-tubes 2 ml	Eppendorf (120.94)	Wesseling-Berzdorf, Germany
Seahorse cell culture 24-well plate	Agilent (100777-004)	Santa Clara, CA, U.S.A.
Seahorse sensor cartridges	Agilent (102342-100)	Santa Clara, CA, U.S.A.
Serologic pipettes 10ml	SARSTEDT (REF86.1254.001)	Nümbrecht, Germany
Serologic pipettes 25ml	SARSTEDT (REF88.1658.001)	Nümbrecht, Germany
Serologic pipettes 2ml	SARSTEDT (REF86.1252.001)	Nümbrecht, Germany
Serologic pipettes 5ml	SARSTEDT (REF88.1253.001)	Nümbrecht, Germany
Sterile filter	SARSTEDT (REF83.1826.001)	Nümbrecht, Germany
Syringe (1 ml)	BD (11612491)	New Jersey, U.S.A.
T25/T75 cell culture flasks	SARSTEDT (REF83.3911.002)	Nümbrecht, Germany
Trans-well Inserts (0.4 µm)	SARSTEDT (83.3932.041)	Nümbrecht, Germany

Table 3: Animals

Item	Brand and reference number	Country of origin
Black 6 mice	Envigo (C57BL/6JCrl)	Indianapolis, IN, U.S.A.

Table 4: General chemicals

Item	Brand and reference number	Country of origin
3-(4,5-Dimethyl-2-thiazolyl)-2,5-diphenyl-2H-tetrazolium-bromide (MTT)	Serva (203.95.03)	Heidelberg, Germany
Acetic acid	Merk (64-19-7)	Darmstadt, Germany
Acryl amid	ROTH Gel30 (3029.1)	Karlsruhe, Germany
Ammonium persulfate (APS)	ROTH (9592.3)	Karlsruhe, Germany
Bis-benzimid H 33258 (Hoechst)	ThermoFisher (H3570)	Waltham, MA, U.S.A.
Bovine serum albumin (BSA)	Serva (11926.03)	Heidelberg, Germany

Bovine serum albumin Fraction	PAA Laboratories (K41-001)	Amsterdam, Netherlands
Bromophenol blue	Merk (L580411422 945)	Darmstadt, Germany
Carbonylcyanidemchlorophenyl-hydrazone (CCCP)	Abcam (141229)	MA, U.S.A.
D- (+)-Glucose	Sigma-Aldrisch (G8270-100G)	Darmstadt, Germany
Dimethylsulfoxide (DMSO)	ThermoFisher (20688)	Waltham, MA, U.S.A.
Dithiothreitol (DTT)	ThermoFisher (R0861)	Waltham, MA, U.S.A.
Donkey serum (DS)	Sigma-Aldrich (D9663)	Hamburg, Germany
Ethanol 100%	VWR chemicals (UN1170)	Pennsylvania, U.S.A.
Fluoromount-G	Southern Biotech (0100-01)	Birmingham, AL, U.S.A.
Glo lysis buffer	Promega (E266A)	Madison, Wisconsin, U.S.A.
Glycin	ROTH (3908.3)	Karlsruhe, Germany
HEPES	Sigma-Aldrich (H3375)	Darmstadt, Germany
Hoechst 33342	ThermoFisher (H3570)	Waltham, MA, U.S.A.
Laemmli sample buffer 4x	Bio-Rad (1610747)	Hercules, California, U.S.A.
L-cystein	Sigma-Aldrich (168149)	Darmstadt, Germany
Lipofectamine 2000	Thermo Fisher Scientific (11668027)	Waltham, MA, U.S.A.
L-Lysin	Sigma-Aldrich (L5501)	Darmstadt, Germany
Red mitochondrial superoxide indicator (Mito Sox)	Invitrogen (M36008)	Paisley, UK
NP-40	Fluka BioChemika	Morristown, NJ, U.S.A.
Paraformaldehyde (PFA)	Sigma-Aldrich (30525-89-4)	Darmstadt, Germany
PBS	Biochrom (L 1825)	Berlin, Germany
PBS tablets	Medicago (09-9420-10)	Uppsala, Sweden
Phosphatase inhibitor	Roche (Pefabloc® SC 11429868001)	Basel, Switzerland
Poly-L-ornithine hydrobromide	Sigma-Aldrich (P3655)	Darmstadt, Germany
Ponceau S	Sigma-Aldrich (P7170)	Darmstadt, Germany
Protease inhibitor	Sigma-Aldrich (11836170001)	Darmstadt, Germany
Protein marker VI (10 - 245) prestained	PanReacAppichem (A8889)	Darmstadt, Germany
Seahorse XF calibrant	Agilent (100840-000)	Santa Clara, CA, U.S.A.
Skim milk powder	Millipore (70166)	Darmstadt, Germany
Sodium chloride (NaCl)	Sigma-Aldrich (433209)	Darmstadt, Germany
Sodium dodecyl sulfate (SDS)	Sigma-Aldrich (151-21-3)	Darmstadt, Germany
Sodium L-lactate	Sigma-Aldrich (L7022)	Darmstadt, Germany
Sterile and endotoxin-free water	Ampuwa Plastipur (13LfP235)	Bad Homburg, Germany

Tetramethylethylenediamine (TEMED)	ROTH (110-18-9)	Karlsruhe, Germany
Tetramethylrhodaminemethylester perchlorate (TMRM)	Invitrogen (T668)	Schwerte, Germany
Tris/Glycine/SDS electrophoresis buffer	Bio-Rad (1610772EDU)	Hercules, California, U.S.A.
Tris-Base	ROTH (4855.5)	Karlsruhe, Germany
Trishydrochloride	Applichem (1185-53-1)	Darmstadt, Germany
Triton X-100	Sigma-Aldrich (T8787)	Darmstadt, Germany
Triton™ X-100	Sigma-Aldrich (X100)	Darmstadt, Germany
Tween 20	Sigma-Aldrich (P9416)	Darmstadt, Germany

Table 5: Materials for cell culture

Item	Brand and reference number	Country of origin
B-27	ThermoFisher (A3582801)	Waltham, MA, U.S.A.
Cytosineβ-D-arabinofuranoside (AraC)	Sigma-Aldrich (C1768)	Darmstadt, Germany
D-(+)-glucose	Agilent (103577-100)	Santa Clara, CA, U.S.A.
Deoxyribonuclease II	Sigma Aldrich (D8764-30KU)	Darmstadt, Germany
Dimethyl sulfoxide cell culture	Applichem (A3672,0250)	Darmstadt, Germany
Distilled water	ThermoFisher (15230001)	Waltham, MA, U.S.A.
Dulbecco's modified eagle medium (DMEM)	ThermoFisher (11965084)	Waltham, MA, U.S.A.
Dulbecco's modified eagle medium (DMEM)	Agilent (103680-100)	Santa Clara, CA, U.S.A.
Fetal bovin serum (FBS)	Gibco (10082147)	Carlsbad, CA, U.S.A.
Glycogen phosphorylase inhibitor	Sigma-Aldrich (361515)	Darmstadt, Germany
Hanks' balanced salt solution (HBSS)	ThermoFisher (14025092)	Waltham, MA, U.S.A.
L-glutamine	ThermoFisher (25030081)	Waltham, MA, U.S.A.
L-glutamine	Agilent (103579-100)	Santa Clara, CA, U.S.A.
Murine IL6	Peprotech (216-16)	Hamburg, Germany
Neurobasal-A medium (GlucD)	ThermoFisher (A2477501)	Waltham, MA, U.S.A.
Neurobasal Medium (GlnD)	ThermoFisher (21103049)	Waltham, MA, U.S.A.
Papain	Worthington (LS003126)	Lakewood, NJ, U.S.A.
Penicillin/Streptomycin (P/S)	ThermoFisher (15140122)	Waltham, MA, U.S.A.
Phosphate buffered saline	ThermoFisher (14190144)	Waltham, MA, U.S.A.
Stattic	Tocris (2798)	Bristol, United Kingdom

Trypan blue solution	Sigma (T8154)	Steinheim, Germany
Trypsin/EDTA solution	ThermoFisher (25200056)	Waltham, MA, U.S.A.

Table 6: Coating reagents

Item	Brand and reference number	Country of origin
Poly-D-lysine hydrobromide (PDL)	Merck (P6407)	Darmstadt, Germany
Poly-L-ornithine hydrobromide	Sigma-Aldrich (P3655)	Darmstadt, Germany
Laminin/Entactin	Corning (354259)	Bedford, MA, U.S.A.

Table 7: Kits

Item	Brand and reference number	Country of origin
Dual-glo® luciferase assay kit	Promega (E2920)	Madison, WI, U.S.A.
Clarity western ECL substrate	Bio-Rad (1705061)	Hercules, California, U.S.A.
Colorimetric/fluorometric assay	Biovision (K607-100)	Milpitas, CA, U.S.A.
Pierce BCA protein assay kit	ThermoFisher	Waltham, MA, U.S.A.
Seahorse XF Cell Mito Stress assay	Agilent (103015-100)	Santa Clara, CA, U.S.A.
Seahorse XF glycolytic rate assay	Agilent (103344-100)	Santa Clara, CA, U.S.A.
Turbo RTA mini transfer Kit	Bio-Rad (1704272)	Hercules, California, U.S.A.

Table 8: Antibodies

Primary Ab

Item	Brand and reference number	Country of origin
GAPDH monoclonal rabbit	Cell signaling (2118S)	Danvers, MA, U.S.A.
GFAP monoclonal (2.2B10) rat	Invitrogen, ThermoFisher (13-0300)	Waltham, MA, U.S.A.
Glycogen mouse monoclonal	A generous gift from Prof. Hitoshi Ashida (ESG1A9)	Kobe University, Rokkoudai, Japan
MAP2 donkey polyclonal rabbit	Synaptic Systems (188 004)	Goettingen, Germany
PKM mouse monoclonal (C-11)	Santa Cruz Biotechnology (sc-365684)	Dallas, Texas, U.S.A.
PSD95 sdAb -FluoTag-X2 monoclonal mouse	Synaptic Systems(N3702-At488-L)	Goettingen, Germany
PSD 95 monoclonal mouse	Millipore (MAB1598)	Darmstadt, Germany

STAT3 (D3Z2G) monoclonal rabbit	Cell Signaling (12640S)	Danvers, MA, U.S.A.
VGLUT1 polyclonal guinea pig	Synaptic Systems (135 304)	Goettingen, Germany

Secondary Ab

Item	**Brand and reference number**	**Country of origin**
Alexa 594 donkey anti-rabbit	ThermoFisher (A212091661238)	Waltham, MA, U.S.A.
Alexa Fluor 488 donkey anti-mouse	ThermoFisher (A21202)	Waltham, MA, U.S.A.
Alexa Fluor 594 donkey anti Rat	ThermoFisher (A212091661238)	Waltham, MA, U.S.A.
Alexa Fluor 647 donkey anti-guinea pig	Jackson (2340476)	Ely, UK
Alexa Fluor 647 donkey anti-rabbit	Jackson (711-605-152)	Ely, UK
Cy3 affinipure donkey anti-rabbit IgG	Jackson (2307443)	Ely, UK
Goat anti-rabbit IgG-HRP	Santa Cruz Biotechnology (sc-2004)	Dallas, Texas, U.S.A.
Normal rat IgG-HRP	Santa Cruz Biotechnology (sc-2750)	Dallas, Texas, U.S.A.

Table 9: Software

Item	**Brand and reference number**	**Country of origin**
ImageJ-FIJI-win64	National Institutes of Health (NIH)	Bethesda, MD, U.S.A.
OriginPro2020	OriginLab	Northampton, MA, U.S.A.
GraphPad Prism 8.3.0	Prism	San Diego, CA, U.S.A.
Wave desktop 2.4 software	Agilent	Santa Clara, CA, U.S.A.

Table 10: Plasmids

Item	**Brand and reference number**	**Country of origin**
pGL4.47[luc2P/SIE/Hygro]	Promega (E404A)	Madison, Wisconsin, U.S.A.
pGL4.42[luc2P/HRE/Hygro]	Promega (E4001)	Madison, Wisconsin, U.S.A.
pGL4.75	Promega (E693A)	Madison, Wisconsin, U.S.A.

3.3 Methods

3.3.1 Legal issues and animal housing

The experimental procedure was performed in accordance with guidelines enforced by the local government (Bezirksregierung Düsseldorf) and conducted in compliance with the European Union animal handling act to care and use of laboratory animals (Directive 2010/63/EU). C57BL/6JCrl (Envigo, Indianapolis, IN, USA) were kept in a group of 5 animals/cage in a regular inverse 12 h light/dark cycle in the Vivarium of the University Hospital Essen with access to the food and water ad libitum.

3.3.2 Primary cultures

Table 11: Media composition

Medium	Composition
Dissection medium	HBSS supplemented with 0.6% D- (+)-glucose.
Digestion medium	HBSS supplemented with 30 U/ml papain and 60 U/ml deoxyribonuclease II and 0.24 mg/ml L-cysteine
Astrocyte’s cultivation medium	DMEM high glucose, 10% FBS and 1% P/S
Sub-cultivation medium	Neurobasal medium supplemented with 2% B-27, 1 mM L-glutamine, 1% P/S.

3.3.2.1 Astroglia

Astroglia mixed cultures were prepared according to (McCarthy and de Vellis 1980; Gottschling et al. 2016) protocol. Cortices from postnatal mice days 1-2 (P1-2) were dissected in a dissection medium (Table 11). After meninges removal, tissue was incubated in the digestion medium (Table 11) for 30 min at 37°C. After that, the digestion medium was removed, and the tissue was dissociated and washed with the astrocyte cultivation medium (Table 11). Dissociated cells were resuspended in the cultivation medium and cultivated in flasks coated previously with 10 µg/ml Poly-D-lysine hydrobromide (PDL) at 37°C and 5% CO_2. After 3 days in vitro (DIV), medium was refreshed. After 7 DIV, when cells formed a monolayer, microglia and OPCs were detached from astrocytes cultures by shaking the glia cultures for 3 h at 250 RPM and 37°C and 5% CO_2. Subsequently, the cultures were incubated with 4.7 µg/ml Cytosine β-D-arabinofuranoside (AraC) for 3 DIV to inhibit microglia, neurons and OPCs propagation in astrocyte cultures.

3.3.2.2 Sub-cultivation of astrocytes

After a minimum of 3 DIV incubation with AraC, astrocytes were washed once with prewarmed magnesium/calcium deprived phosphate buffered saline (PBS), detached using 1 ml trypsin/EDTA, neutralized and triturated in the astrocyte cultivation medium. Next, they were washed once in the cultivation medium, centrifuged at 1000 RPM for 5 min and resuspended in the sub-cultivation medium (Table 11).

At first, all consumables required for astrocyte sub-cultivation were coated with 10 µg/ml PDL and an appropriate quantity of astrocytes were seeded as described in Table 12.

Table 12: Astrocyte's quantity/experiment

Experiment	Cell number	Consumable
Indirect co-cultures	80,000	Inserts (0.4 µm pore size)
Luciferase reporter gene assay	70,000	24-well plates
Seahorse XF glycolytic rate assay	30,000	Seahorse 24- well plates
Seahorse mito stress assay	30,000	Seahorse 24- well plates
Live-cells imaging (MMP)	100,000	35 mm imaging dishes
Live-cells imaging (Mito Sox)	100,000	100,000
MTT assay	30,000	96-well plates
Glycogen inhibition (ICC)	50,000	4-ring petri-dishes
Western Blot	1,000,000	6-well plates

All astrocyte sub-cultures were grown for a further 14 DIV to maturate, therefore they were 21 DIV before treatments.

3.3.2.3 Astrocyte-neuron indirect co-cultures

Astrocyte sub-cultivation and neuron cultures preparation was carried out on the same day. Before dissection, 13 mm coverslips and Seahorse 24- well Plates were coated with 15 µg/ml poly-L-ornithine hydrobromide (PLO) for 24 h. Then, PLO-coated consumables were washed three times with 1x PBS and coated with 5 µg/ml laminin/entactin for 24 h.

Neuronal cultures were prepared from hippocampal tissue of embryonic stage 15 (E 15) mice. The dissection and digestion procedure were similar to astroglia cultures (section 3.3.2.1). After removal of the digestion medium, the digested tissue was washed three times in Neurobasal Plus Medium and 2% FBS and triturated in sub-cultivation medium (Table 11). Then, 50,000 neurons were plated as 50 µl droplets on each coverslip and 30,000 neurons/100 µl sub-cultivation medium was seeded in Seahorse plates. When neurons were attached to coverslips, the sub-cultivation medium was added until the volume reached 500 µl. Lastly, astrocyte inserts, and neuron cultures were co-incubated for 14 DIV 37°C and 5% CO_2.

3.3.3 Transfection

Mature astrocytes (21 DIV) in 24-well plates (Table 13) were co-transfected with 2 µg of pGL4.47 [luc2P/SIE/Hygro] (Table 13) and 0.5 µg pGL4.75 (Table 13) to measure the sis inducible element (SIE), a STAT3 response element (SRE) luciferase activity. To measure hypoxic response element (HRE) luciferase activity, 21 DIV astrocytes were transfected with 2 µg pGL4.42 [luc2P/HRE/Hygro] and 0.5 µg pGL4.75 (Table 13). Transfections were carried out using Lipofectamine 2000 for 72 h following the manufacturer's instructions (Table 7).

Table 13: Plasmids concentration

Plasmid	Experiment	Concentration
pGL4.47[luc2P/SIE/Hygro]	SIE/SRE (Firefly-luciferase)	2 µg/ml
pGL4.42[luc2P/HRE/Hygro]	HRE (Firefly-luciferase)	2 µg/ml
pGL4.75	Renilla-luciferase	0.5 µg/ml

3.3.4 Treatments

3.3.4.1 Ischemia/reperfusion (I/R) in astrocytes

To mimic I/R, 21 DIV astrocytes were transiently exposed to ischemia and Gln/Gluc deprivation followed by 24 h reoxygenation and re-supplementation of full media. Therefore, 24 h prior to treatment, glucose/pyruvate deprived (GlucD, A2477501, ThermoFischer) and glutamine deprived (GlnD, 21103049, ThermoFischer) media were degassed in a hypoxia chamber with 1 % oxygen pressure. The sub-cultivation medium was removed during the experiment and astrocytes were washed with warm PBS to remove residual glucose and glutamine. Then, astrocytes were transferred to the hypoxia chamber with 1 % oxygen pressure and incubated with the oxygen/ glutamine deprived (OGlnD) or oxygen/glucose-pyruvate deprived (OGlucD) medium for 1 h. Afterward, astrocytes were transferred back to normoxia and hypoxic media was replaced with sub-cultivation medium (Table 11) for 24 h. For the astrocyte

Gln/Gluc-deprived experiment, 21 DIV astrocytes were incubated with either GlucD or GlnD medium for 24 h (Table 14).

Table 14: Ischemia/reperfusion (I/R) in astrocytes

Ischemia/reperfusion model	Vehicle normoxia: 24 h incubation with sub-cultivation medium Oxygen/glutamine deprivation (OGlnD): 1 h/4 h reoxygenation in sub-cultivation medium Oxygen glucose/pyruvate deprivation (OGlucD): 1 h/24 h reoxygenation in sub-cultivation medium
Glutamine/glucose deprivation model	Glutamine deprivation (GlnD): 24 h incubation with GlnD medium Glucose/Pyruvate Deprivation (GlucD): 24 h incubation with GlucD medium

3.3.4.2 STAT3 activation/inhibition in I/R astrocytes

In this experiment, canonical STAT3 signaling is activated/inhibited in normoxic and I/R (OGlnD and OGlucD) conditions, as described in Table 15. To activate STAT3 canonical signaling, astrocyte cultures were incubated with 50 ng/ml recombinant Murine IL6 as the central STAT3 canonical upstream signaling cytokine. To inhibit canonical STAT3 signaling, astrocyte cultures were incubated with 200 pM Stattic, a small peptide that binds to STAT3 SH2 domains and hampers STAT3 dimerization and nuclear translocation (Schust et al. 2006). Both IL6 and Stattic treatments were carried out 1 h prior to the ischemia and throughout 24 h reoxygenation period (Table 15).

Table 15: STAT3 activation/inhibition in I/R astrocytes

Vehicle	24 h normoxia in sub-cultivation medium 1 h OGlnD 24 h reoxygenation in sub-cultivation medium 1 h OGlucD 24 h reoxygenation in sub-cultivation medium
STAT3 activation	24 h 50 ng/ml IL6 (normoxia) in sub-cultivation medium 1 h 50 ng/ml IL6 /1 h OGlnD /24 h reoxygenation in sub-cultivation medium+50 ng/ml IL6 1 h 50 ng/ml IL6 /1 h OGlucD /24 h reoxygenation in sub-cultivation medium+50 ng/ml IL6
STAT3 inhibition	24 h 200 pM Stattic (normoxia) in sub-cultivation medium 1 h 200 pM /1 h OGlnD /24 h reoxygenation in sub-cultivation medium+200 pM 200 pM 1 h/ OGlucD 1 h/24 h reoxygenation in sub-cultivation medium+200 pM

3.3.4.3 Glycogen mobilization in STAT3 activated/inhibited I/R astrocytes

Glycogen mobilization was studied in STAT3 activated/inhibited I/R astrocytes by inhibiting glycogen phosphorylase (GP), a crucial enzyme in glycogenolysis. Astrocytes were treated with 10 µM GP inhibitor (GPinh) in addition to STAT3 activation/inhibition. GP inhibitor was added to the cultures together with IL6/Stattic 1 h prior to ischemia and during 24 h reoxygenation (Table 16).

Table 16: GP inhibition in STAT3 activated/inhibited I/R astrocytes

Vehicle	24 h normoxia in sub-cultivation medium 1 h OGlucD /24 h reoxygenation in sub-cultivation medium
Vehicle (GP-inhibition)	24 h normoxia in sub-cultivation medium+10 µM GPinh 1 h 10 µM GPinh /1 h OGlucD /24 h reoxygenation in sub-cultivation medium+10 µM GPinh
STAT3 activation	24 h normoxia 50 ng/ml IL6 in sub-cultivation medium 1 h 50 ng/ml IL6 /1 h OGlucD /24 h reoxygenation in sub-cultivation medium+50 ng/ml IL6
STAT3 activation (GP-inhibition)	24 h normoxia 50 ng/ml IL6+10 µM GPinh in sub-cultivation medium 1 h 50 ng/ml IL6+10 µM GPinh /1 h OGlucD /24 h reoxygenation in sub-cultivation medium+50 ng/ml IL6+10 µM GPinh
STAT3 inhibition	24 h normoxia 200 pM Stattic in sub-cultivation medium 1 h 200 pM /1 h OGlucD /24 h reoxygenation in sub-cultivation medium+200 pM
STAT3 inhibition (GP-inhibition)	24 h normoxia 200 pM Stattic+10 µM GPinh in sub-cultivation medium 1 h 200 pM+10 µM GPinh /1 h OGlucD /24 h reoxygenation in sub-cultivation medium +200 pM+10 µM GPinh

3.3.4.4 Lactate supplementation to neuronal cultures

To study the role of astrocytic lactate on neuronal synapses and neurite density, 50 µM sodium L-lactate was supplemented to the 14 DIV neuron cultures. The lactate concentration was adopted from the highest concentration of the astrocytic released lactate measured in section 3.3.6. After 24 h incubation, neurons were fixed for further ICC and confocal microscopy (section3.3.5.2).

3.3.5 Immunocytochemistry

3.3.5.1 Astrocytes

Table 17: Solutions for astrocytes immunocytochemistry

Solutions	components
Permeabilization/blocking buffer (PBT2)	0.2 % Triton X-100 in PBS (PBT2) + 5% DS
Diluent for primary antibodies (1`Ab)	0.1 % Triton X-100 in PBS (PBT1)
Diluent for secondary antibodies (2`Ab)	0.1 % Triton X-100 in PBS (PBT1) + 2 % DS

Initially, astrocytes were permeabilized and blocked with PBT2 (Table 17) for 1 h and subsequently incubated with primary antibodies (1`Ab); STAT3 rabbit monoclonal 1:200, GFAP rat monoclonal antibody 1:500, glycogen (ESG1A9) mouse monoclonal 1:100 (Nakamura-Tsuruta et al. 2012), PKM2 mouse monoclonal 1:200 in PBT1 (Table 17), at 4°C overnight. The next day, primary antibodies were washed three times with 1x PBS and astrocytes were incubated with secondary antibodies (2`Ab): Alexa Fluor 647 donkey anti rabbit, Alexa Fluor 594 donkey anti-rat, Alexa Fluor 488 donkey anti-mouse and Hoechst 33342 all diluted 1:1000 in their corresponding diluent (Table 17) at room temperature (RT) for 1 h. Then, astrocytes in inserts were washed three times with 1x PBS; inserts membranes were disassociated and mounted in Fluoromount-G on microscope slides.

Image acquisition was performed using LSM710 (Zeiss, Wetzlar, Germany) with a 20x objective Plan-Apochromat (numerical aperture, 0.8), air immersion. Three random areas in each sample were selected and scanned as 5 Z-Stacks, with a frame of 0.5 x 0.5 µm and a thickness of 1 µm. The nuclear/cytoplasmic ratio of STAT3 and PKM2 fluorescent intensity was evaluated using ImageJ-FIJI-win64 (processing and analysis macro supplementary 7.2.1).

The size and quantity of glycogen bodies were determined using ImageJ-FIJI-win64 (processing and analysis macro-supplementary 7.2.2) and normalized to the number of nuclei (analysis macro, supplementary 7.2.3).

3.3.5.2 Neurons

Table 18: Solutions for neurons immunocytochemistry

Solutions	Components
Permeabilization/blocking buffer (Tris-Abdil)	150 mM NaCl, 50 mM Tris-Base, 100 mM L-lysin, 0.1 % Triton X-100, 1 % BSA, PH:7.4 + 5% DS
Diluent for primary antibodies (1`Ab)	Tris-Abdil
Diluent for secondary antibodies (2`Ab)	Tris-Abdil + 2 % DS

Fixed neurons were permeabilized and blocked with permeabilization/blocking solution (Table 18) for 1 h. Then they were incubated with 1`Ab: vesicular glutamate transporter (VGLUT) 1 polyclonal guinea pig 1:200, postsynaptic density protein (PSD) 95 monoclonal mouse 1:500, microtubule-associated protein (MAP) 2 donkey polyclonal rabbit 1:500 in corresponding diluent (Table 18) at 4°C overnight. The next day, 1`Ab were washed three times with 1x PBS and neurons were incubated with 2`Ab: Alexa Fluor 647 donkey anti-guinea pig, Alexa Fluor 594 donkey anti-rabbit, Alexa Fluor 488 donkey anti-mouse, Hoechst 33342 1:1000 in the corresponding diluent (Table 18) for 1 h at RT then coverslips were washed three times with PBS and mounted in Fluoromount G on microscope slides.

Map2 stained cultures were scanned using LSM710 (Zeiss, Germany) with a 20x objective Plan-Apochromat (numerical aperture, 0.8), air immersion. Three random areas were selected and scanned as 3 Z-Stacks, with a frame of 0.5 x 0.5 µm and a thickness of 1 µm. All the microscopy settings remained the same throughout the experiments. Then, the density of the neuronal processes was determined using ImageJ-FIJI-win64 (processing and analysis macro, supplementary 7.2.4). The processes were normalized to the number of the MAP2 stained neuronal cell bodies in each field of view (manually counted).

Neuronal synapses were scanned using LSM710 (Zeiss, Germany) with a 63x objective Plan-Apochromat (numerical aperture, 1.4), oil immersion. Three random areas in each sample were selected and scanned as 5 Z-Stacks, with a frame of 0.05x 0.05 µm and a thickness of 0.5 µm. All the microscopy settings remained the same throughout the experiments.

Image preprocessing analysis was performed to obtain the same-sized red-green-blue (RGB) images (preprocessing macro, Supplementary 7.2.5) and using synapse counter v. 1.1 Image J plug-in (Dzyubenko et al. 2016), the colocalization of the pre and post-synaptic puncta were quantified.

3.3.6 Extracellular lactate

After 24 h treatment/reoxygenation, astrocytic conditioned media (CM) was collected. CM of biological replicas (astrocytic inserts) was combined and centrifuged at 700 g for 5 min to remove the cell debris. Then the supernatant was immediately frozen at -80°C to minimize the lactate dehydrogenase (LDH) activity. Additionally, corresponding astrocytic nuclei were stained with 1:1000 Hoechst 33342 and the whole insert was scanned using tiling-Stitching method (Zeiss AxioObserver.Z1 and Apotome, Zeiss, Oberkochen, Germany).

The frozen CM was thawed, vortexed and diluted 1:200 in lactate assay buffer to keep the lactate concentration within the optimal detection range. L-lactate concentration was measured using ELISA-based colorimetric/fluorometric assay kit (Table 7). In this way, all standards and samples were loaded in a 96 well plate in triplicates. A triplicate was designated for the background and another for the sub-cultivation medium as a negative control. After 30 min incubation of the reaction mix and samples at RT and dark, the absorbance was measured at 570 nm using iMark™ microplate absorbance reader and the concentration of L-lactate was measured according to the instructions provided by the manufacturer. Eventually, the measured L-lactate concentration was normalized to the sum of the Hoechst-stained nuclei in each condition.

3.3.7 Dual-luciferase reporter gene assay

A reporter gene assay is a suitable tool to measure the transcription activity of transcription factors like STAT3 and HIF. Here, the dual-luciferase reporter system contains firefly and renilla luciferases, which catalyze reactions with different bioluminescent products: firefly luciferase converts D-luciferin into oxyluciferin while renilla facilitates the conversion of coelenterazine to coelenteramide. In this study, astrocytes were transiently co-transfected with two expression vectors (section 3.3.3). One plasmid contains the firefly luciferase gene downstream of the response elements for STAT3 or HIF (SRE/SIE or HRE) under the control of a minimal promoter. The second vector carries the renilla luciferase gene downstream of a constitutively active promoter providing a continuous expression of renilla in order to normalize for transfection efficiency. Upon induction of STAT3 or HIF expression, they bind to their response element and provide STAT3/HIF-dependent firefly expression. Thus, incubating cell lysate with substrate cocktail, which includes D-luciferin and coelenterazine, generates light (Ohmiya 2014). Firefly relative light unit (RLU) was normalized to renilla RLU, which represents cellular expression potential (Figure 10).

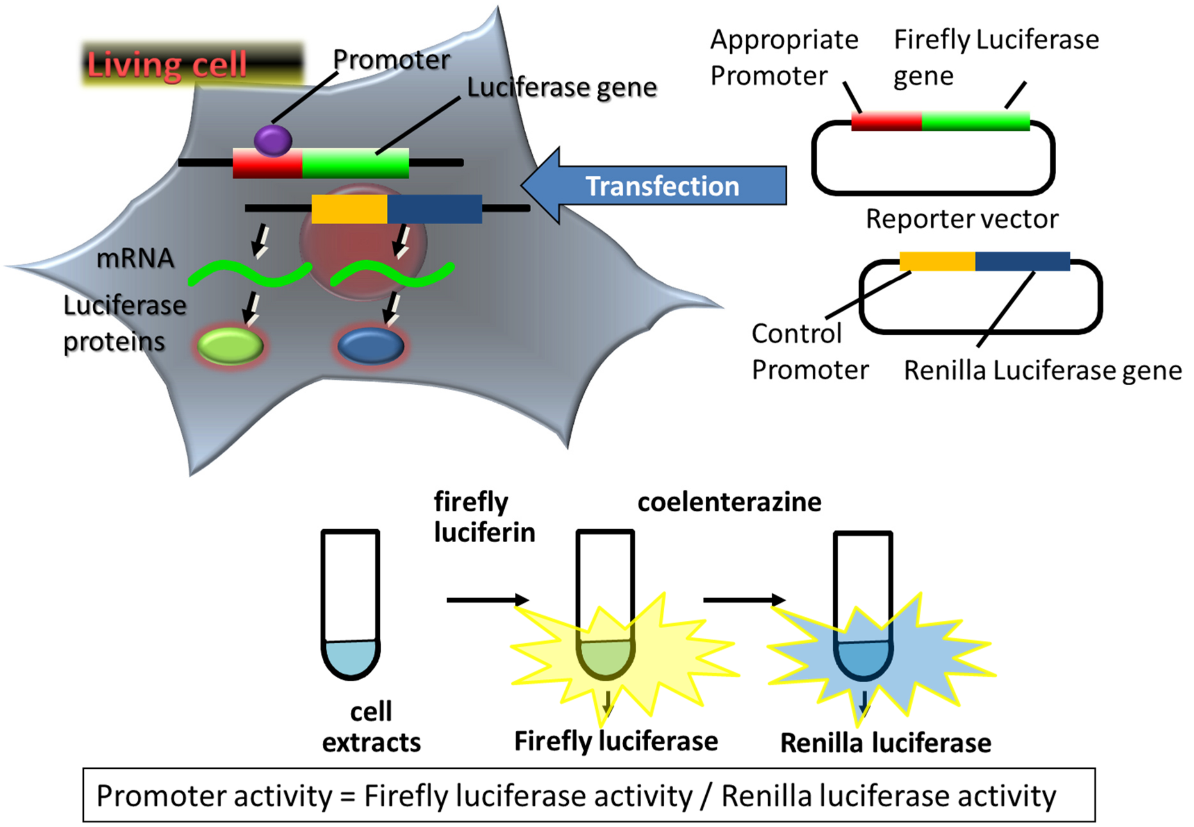

Figure 10: Dual-luciferase reporter gene assay

(Top right) Firefly luciferase is cloned downstream to an appropriate promoter, while renilla luciferase is cloned downstream to a control promoter. The cells are transiently co-transfected with both vectors till both firefly and renilla luciferase are expressed by host cells **(top left)**. Then cells are lysed, and the lysate is incubated initially with a cocktail containing D-luciferin. Synthesized luciferase catalyzes the conversion of D-luciferin to the bioluminescence oxyluciferin. Then, the lysate is incubated with a substrate cocktail containing coelenterazine, which quenches the firefly signal and initiates a secondary bioluminescent signal, representing cellular synthetic potential. Light can be calculated by a luminometer **(bottom)**. This way, promoter activity is measured by normalizing the firefly signal to the renilla luminescence **(bottom).** The figure was reproduced from online material published by (Ohmiya 2014) with permission (Supplementary 7.1.5)

This study measured SIE-luciferase activity after 24 h reoxygenation/treatment, while HRE-luciferase activity was measured right after hypoxia. First, cells were lysed using Glo lysis buffer (E266A, Promega). Next, according to the manufacturer's instruction, luminescent signals were generated using dual-glo Luciferase assay Kit (Table 7). Eventually, the relative light unit (RLU) was measured with ELx800 microplate reader (BioTek).

3.3.8 Seahorse extracellular flux analysis

Seahorse extracellular flux analysis (Seahorse XF) is based on two fundamental metabolic pathways, glycolysis and mitochondrial OXPHOS. Each seahorse assay contains a cell culture plate in which cells of interest are cultivated and a sensor cartridge. The sensor cartridge is composed of 24 central empty cavities (Figure 11, A), which are coated with 2 oxygen and pH-sensitive fluorophore probes (Figure 11, B and C). Sensor cartridges are coupled with Seahorse cell culture plates before measurement. During measurement, the sensor cartridge's central cavities create a 200 µm transient micro chamber above the cells (Figure 11, D). Once coupled, sensor cartridge and cell culture plate are placed in the XF analyzer, optic bundle units are inserted in the central cavities of cartridges (Figure 11, D). Optic bundle units facilitate excitation of oxygen and pH-sensitive fluorophores and detect emission each time oxygen or proton quenches these fluorophores. This way, real-time oxygen and proton concentrations are measured over time. In addition, sensor cartridges contain 4 injection ports (A-D), which are used to inject inhibitors, stimulators, or substrates. Thereby, intracellular oxygen consumption rate (OCR) and extracellular acidification rate (ECAR) can be measured before and after injection of reagents (Figure 11).

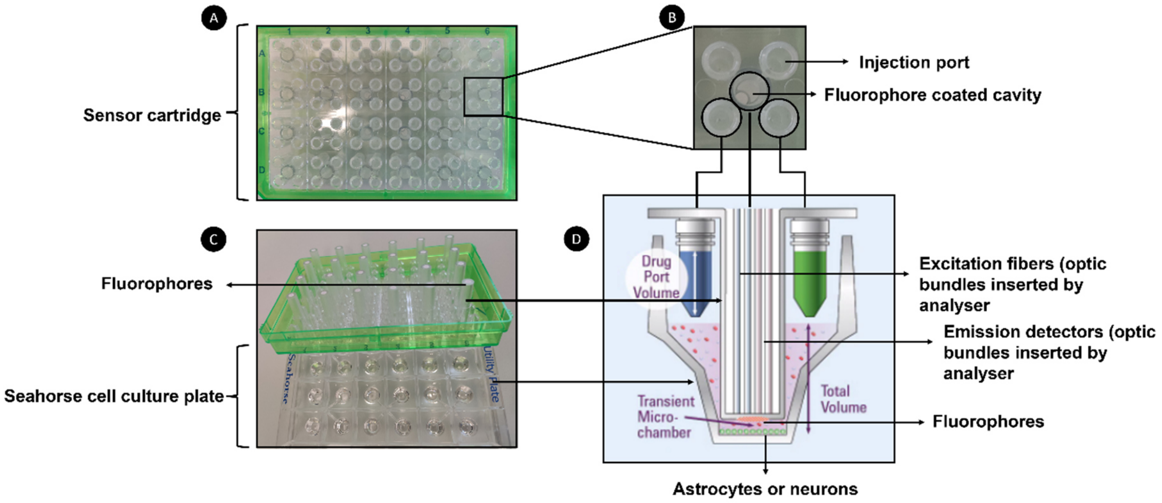

Figure 11: Overview of the Seahorse XF analysis

(A) Seahorse XF sensor cartridge consists of 24 units (black box), each designated for a well in the XF seahorse cell culture plate. **(B)** Zoomed-in image of a sensor cartridges unit with 4 injection ports and a central column-like cavity coated with 2 fluorophore probes at the bottom. **(C)** A sensor cartridge (above) and seahorse cell culture plate (bottom). **(D)** After coupling the sensor cartridge and cell culture plate, the central cavity creates a transient microchamber above the cells. Placing coupled cartridge and plate, the XF analyzer inserts fiber optic bundles in the sensor cartridge's central cavities, allowing fluorophores excitation and collecting the emitted light when oxygen or proton quenches the probe. Optical fiber units are connected to the XF analyzer and transfer obtained data to the XF analyzer. Reagents are injected using injection ports, while real-time extracellular oxygen or proton are measured. The cartoon of the optical bundle unit was reproduced from Agilent online sources with permission (supplementary 7.1.4)

Agilent provides Seahorse XF analyzer, consumables, substrates and inhibitors. All Seahorse XF protocols and technical information in this study is according to Agilent published guidelines for glycolytic rate assay and mitochondria stress assay. Further supporting information can be found in (Ludikhuize et al. 2021).

3.3.8.1 Glycolytic rate assay

In this study, Seahorse XF glycolytic rate assay (GRA) (Table 7) was utilized to analyze astrocytic glycolysis after 24 reoxygenation/treatments. One day before the experiment, Seahorse XF sensor cartridges were hydrated using the XF calibrant and placed in a non-CO_2 incubator at 37°C overnight. To balance the pH, 1 h before the experiment, the treatment medium was removed. The cells were washed once and incubated for 45-60 min with 500 µl Seahorse XF assay medium containing seahorse-specific phenol red-free DMEM supplemented with the 1 mM L-glutamine and 5 mM D- (+)-glucose in a non-CO_2 incubator at 37°C. The concentration of additives was adjusted according to the astrocytic sub-cultivation medium (Table 11).

Meanwhile, 50 µM Rotenone/Antimycin (Rot/AA) and 500 mM 2-deoxy-D-glucose (2-DG) were prepared in the Seahorse assay medium. Rot/AA was further diluted 1:10 (0.5 µM) and compounds were loaded in their respective injection ports (Port A and B). Eventually, GRA was measured using XF seahorse GRA template provided in Wave desktop 2.4 software. After initial calibration, the assay plate was loaded and the real-time OCR and ECAR were measured. Based on measured OCR and ECAR, proton efflux rate (PER) is calculated (Figure 12). Basal PER drops right after Rot/AA injection, suggesting inhibition of mitochondrial acidification after blocking complex I and III of ETC. Blocking mitochondrial acidification provides exclusive cytoplasmic acidification, which is attributed to lactate-directed glycolysis. Prolonged incubation of cells with Rot/AA blocks mitochondria-associated glycolysis, causing an increase in PER. Measuring maximum PER after Rot/AA injection provides an indirect insight into mitochondria-directed glycolysis prior to Rot/AA injection. GRA is completed with the 2-DG injection that causes a decrease in PER due to 2-DG competitive binding to glucose hexokinase. Post-2-DG acidification is attributed to non-glycolytic acidification

(Figure 12, A). Simultaneous measured OCR provides an insight into the real-time mitochondrial respiration (Figure 12, B). At the end of GRA, both culture plate and cartridge are ejected; cells were fixed with 4 % PFA and stained with 1:1000 the Hoechst 33342. Hoechst-stained nuclei were scanned using AMG EVOS FL MICROSCOPY and counted using Fiji ImageJ-win64. Parameters were normalized to the quantified nuclei using Wave desktop 2.4 software. Excel reports were generated from the wave software. In this study, lactate-directed glycolysis is referred to as the glyoPER (automatically calculated by wave). The mitochondria-directed glycolysis[1] was manually calculated after subtracting the glycoPER from the compensatory glycolysis (automatically calculated by wave). Other criteria such as non-glycolytic (Post 2-DG) acidification and mitoOCR/glycoPER were extracted from the automatically calculated values in the wave.

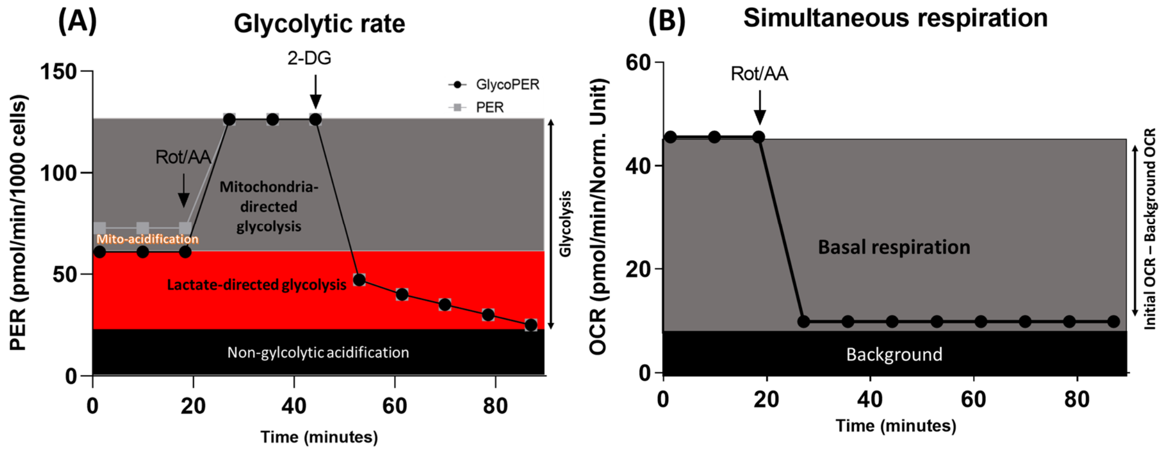

Figure 12: Glycoltic rate assay (GRA)

A) Representative glycolytic rate assay (GRA). Using GRA, real-time proton efflux rate (PER) is measured before and after sequential injection of the Rot/AA and 2-DG. Rot/AA blocks mitochondrial respiration, inhibiting mitochondrial acidification and determining lactate-directed glycolysis (red). Subtraction of lactate-directed glycolysis from Rot/AA-induced maximum PER equals mitochondria-directed glycolysis (grey). 2-DG decreases glycolysis through competitive binding to glucose hexokinase, revealing non-glycolytic acidification (black). **B)** Representative simultaneous mitoOCR. Initial OCR drops to the baseline after blocking the complex I and III of ETC by Rot/AA. Subtracting background OCR (black) from the total OCR indicates basal respiration (grey).

---

[1] Mitochondria-directed glycolysis is a compensatory glycolytic pathway that is analyzed by wave and excludes basal glycolysis. It involves a higher uptake of glucose to meet astrocytes' energy demands, increased pyruvate conversion to lactate, and elevated glycogenolysis within the astrocytes. This proportion of glycolysis directly impacts astrocytic mitochondrial respiration section 4.4.1; therefore, we named it mitochondria-directed glycolysis.

3.3.8.2 Mito stress assay

Astrocytic and neuronal mitochondrial OXPHOS was addressed using an XF mito stress assay (MSA) kit (Table 7) after 24 h reoxygenation/treatment. OXPHOS takes place in the mitochondrial inner membrane (IMM), where the mitochondrial electron transport chain (ETC) and ATP-synthetase facilitate ATP synthesis (section1.4.1). Through MSA, basal OCR and ECAR are initially measured prior to the sequential injection of ETC inhibitors. Then ATP-synthetase is blocked using Oligomycin, which drops OCR dramatically. The difference between basal OCR and the OCR after Oligomycin injection is attributed to ATP-linked respiration. Next, carbonyl cyanide-4-(trifluoromethoxy) phenylhydrazone (FCCP) is injected, which as an uncoupler, causes IMM depolarization. FCCP injection increases the OCR to its maximal level and introduces a criterion known as spare respiratory capacity. Finally, rotenone and antimycin (Rot/AA) is injected, which block ETC's complex I and III, minimizing the OCR to its baseline (Figure 13).

In this study, the sensor cartridge and culture plate were prepared as described in section 3.3.8.1. Then, injection ports were loaded with 5, 1.25 and 5 µM oligomycin, FCCP and Rot/AA, respectively, according to the instruction manual. Next, real-time OCR and ECAR were measured using Seahorse XF analyzer and the MSA template provided in Wave desktop 2.4 software. After assay completion, cells were fixed, and nuclei were stained with Hoechst 33342 and scanned as described in section 3.3.8.1. Nuclei were counted using Fiji ImageJ-win64 and all parameters were normalized to nuclei number using Wave desktop 2.4 software. Excel reports were generated from the normalized parameters. Parameters such as basal respiration, ATP-linked respiration and spare capacity were extracted from automatically calculated reports in wave software (Figure 13).

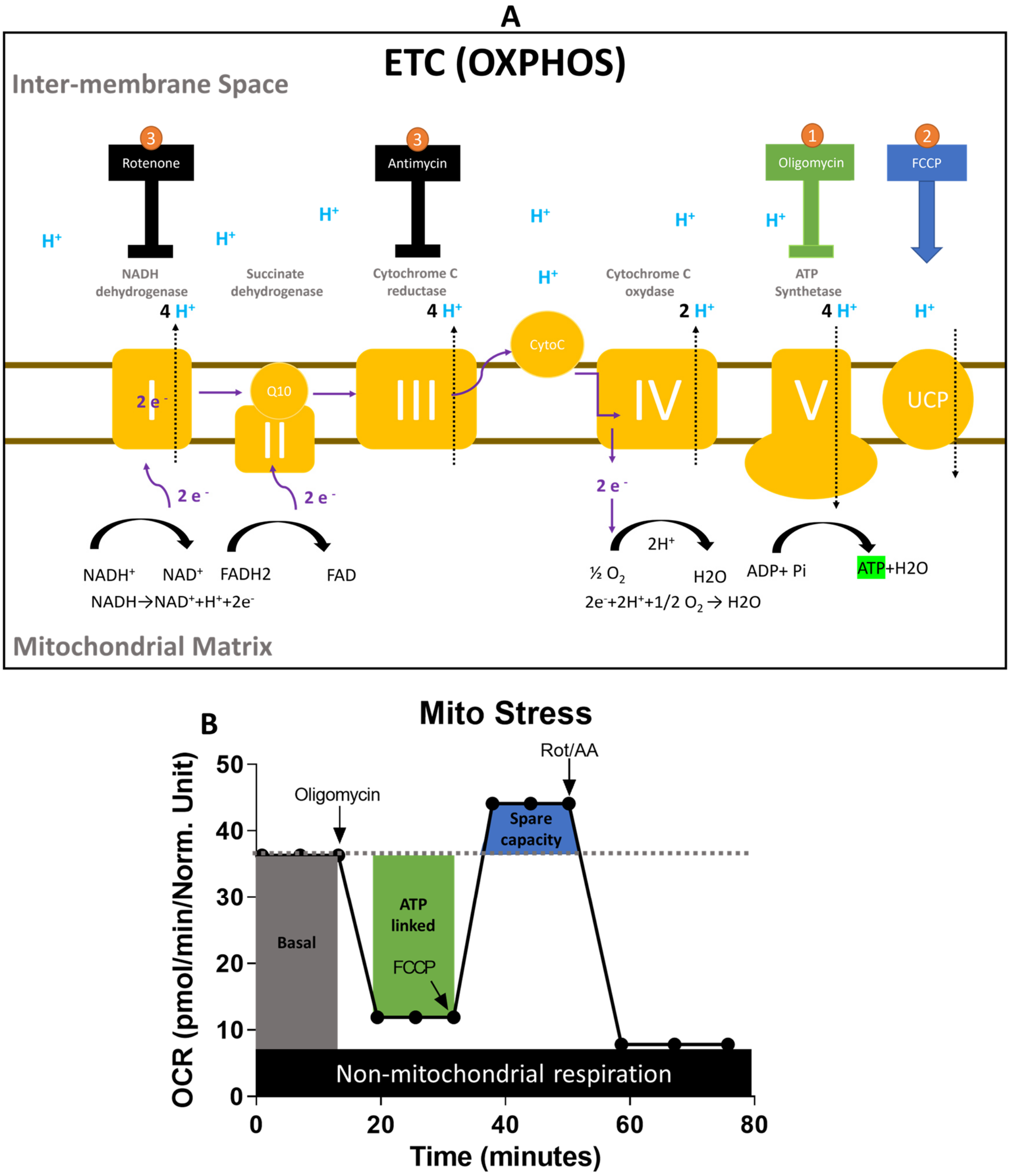

Figure 13: Mito stress assay (MSA)

A) Schematic view of mito stress assay (MSA) targeting OXPHOS. OXPHOS contains ETC and ATPase which are protein complexes spanned across the IMM to perform the oxidation on TCA-derived NADH and FADH2 (ETC) and phosphorylation of ADP to ATP (ATPase). Uncoupling proteins (UCPs) in IMM provide a fine-tuned proton entrance to the MM. MSA initially blocks the ATP-synthetase via Oligomycin (1- green), then initiate proton intrusion to MM via uncoupler FCCP and eventually blocks the complex I and III with Rot/AA to baseline. **B)** Explanatory astrocytic MSA graph. Real-time OCR is measured before and after a sequential injection of the Oligomycin, FCCP and Rot/AA. Basal respiration (grey) is initial OCR after subtraction of non-mitochondrial respiration (horizontal black). ATP-linked respiration (green column) is OCR after Oligomycin injection. Spare respiratory capacity (blue column) is basal respiration subtracted from FCCP-induced maximum respiration.

3.3.9 Mitochondrial membrane potential

To confirm mitochondrial respiration measurements, a complementary approach was used to further evaluate astrocytic MMP (Ϫψ) after 24 h reoxygenation/treatment. In this respect, 5 nM tetramethylrhodamine methyl ester perchlorate (TMRM) was added to astrocytes reoxygenation/treatment medium for 24 h. TMRM is a mitochondrial membrane potential indicator that is accumulated in mitochondria with a polarized IMM (Figure 14, A). After 24 h incubation, TMRM fluorescent intensity was recorded before and after 5 µM carbonyl cyanide m-chlorophenylhydrazone (CCCP) injection. CCCP is used to uncouple proton gradients between IMM and MM and reduce MMP to baseline. Images were obtained using live-cell confocal imaging Leica TCS SP8 fully automated epifluorescence confocal microscope (Zeiss, Wetzlar, Germany). Image acquisition was carried out using 63x (glycerin) HC PL APO motCORR CS2 (numerical aperture of 1.3), 142 x 142 µm single plane confocal images for 8 minutes with an interval of 1 second for each image. TMRM was excited at 552 nm and emission was collected at 572 nm using a gated HyD detection. Semi-quantitative analysis was carried out using ImageJ-FIJI-win64. The mean fluorescent intensity of each image per second was measured within 8 minutes of recording before and after CCCP injection and plotted in a time scaled XY graph (GraphPad Prism 8.3.0). Minimum TMRM fluorescent intensity (Fmin) after CCCP injection (as background fluorescent) was subtracted from the maximum intensity (Fmax) prior to the CCCP injection (Ϫψ= Fmax-Fmin) (Figure 14, B). Meanwhile, nuclei were counted in each field of view and Ϫψ was normalized to cell number.

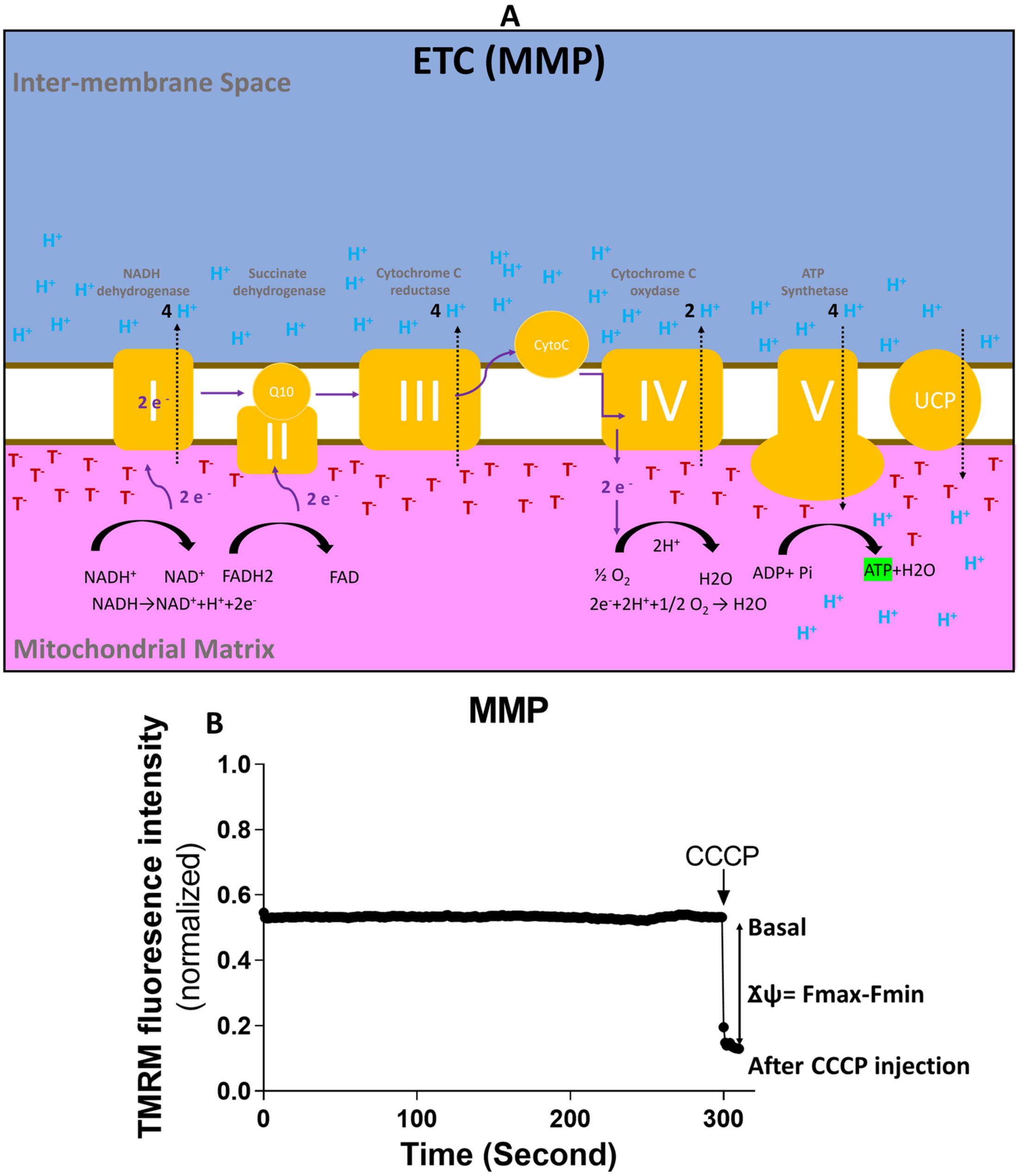

Figure 14: Mitochondrial membrane potential (MMP)

A) Schematic view of ETC's role in maintaining mitochondrial membrane potential (MMP). ETC expels protons from MM (Pink) to IMM (Blue), creating a proton gradient between IMS and MM known as MMP. MMP facilitates passive proton transfer from IMS to MM through ATPases, resulting in ATP synthesis. As a result, positively charged TMRM accumulates in polarized mitochondria.
B) Representative MMP analysis model. Ꭓψ is the subtraction of TMRM fluorescence intensity after CCCP injection (Fmin) from maximum TMRM fluorescence intensity before CCCP injection (Fmax).

3.3.10 Mitochondrial superoxide formation (Mito SOX)

Mitochondrial superoxide (Mito SOX) is generated physiologically after mitochondrial respiration in ETC (Figure 15). In this study Mito SOX was measured after 24 h reoxygenation/treatment by incubating astrocytes with 2.5 µM of Mito Sox Red indicator and 1:1000 Hoechst 33342 for 30 minutes. Subsequently, live-cell time-lapse confocal imaging was performed using Leica TCS SP8 fully automated epifluorescence confocal microscope (Zeiss, Germany). Image acquisition was carried out using 63x (glycerin) HC PL APO motCORR CS2 (numerical aperture of 1.3) in 3 random areas with an absorption/emission 510/580 nm detected by gated HyD detector. Images were acquired for Mito Sox (red channel) and the cell nuclei (Hoechst channel). Semi-quantitative analysis was carried out using ImageJ-FIJI-win64 and the mean fluorescent intensity of Mito SOX was normalized to nuclei number.

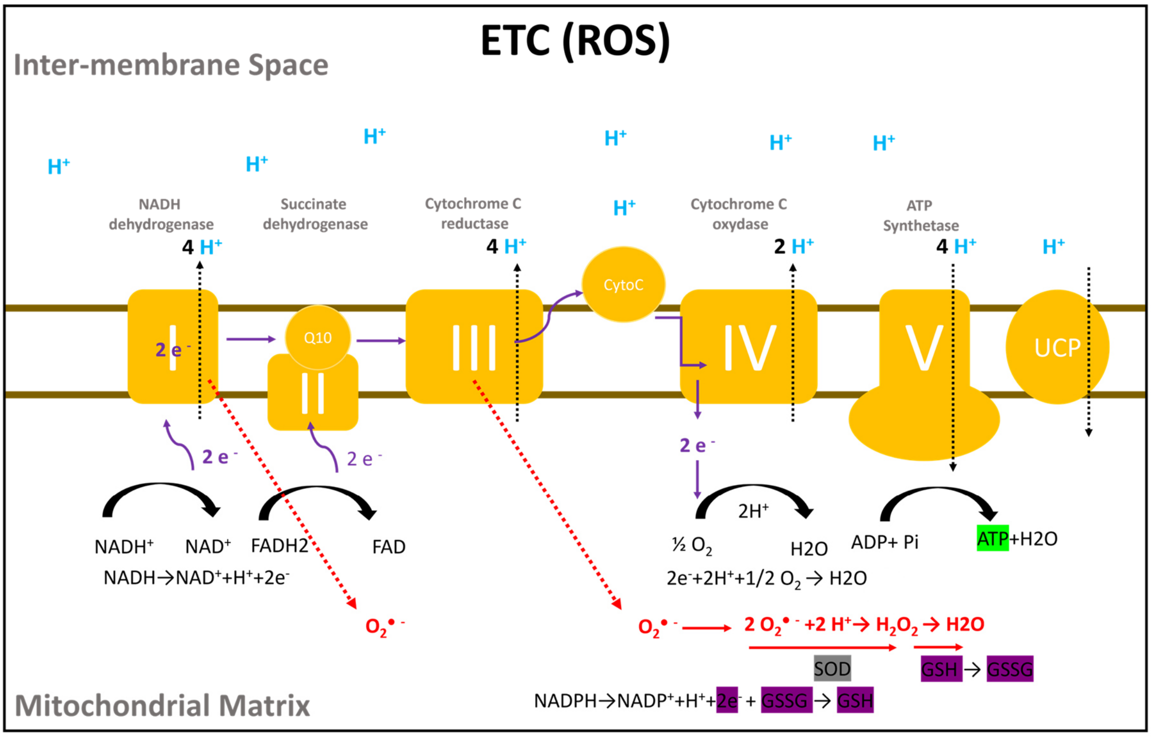

Figure 15: Mitochondrial superoxide (Mito SOX)

schematic view of the ETC-derived (superoxide). Mitochondrial Superoxide (Mito SOX) is formed due to electron leakage (red-pointed arrows), mainly in complexes I and III of the ETC (Payen et al. 2019). Mito SOX is eventually scavenged by enzymatic (SOD) and non-enzymatic (NADPH-GSH) antioxidant defense systems. Impairment in either electron transfer or antioxidant defense results in mitochondrial superoxide increase.

3.3.11 MTT

MTT assay was performed 24 h after reoxygenation/treatment to study astrocyte's ability to reduce tetrazolium to formazan in response to treatments. In this respect, astrocytes were incubated with 1 mg/ml 3-(4,5-Dimethyl-2-thiazolyl)-2,5- diphenyl-2H-tetrazolium-bromide for 1h at 37 °C and 5 % CO_2 till purple formazan crystals were observable. Then the treatment media was removed, and the cells were lysed in dimethylsulfoxide (DMSO), 10 % sodium dodecyl sulfate (SDS) and 0.6 % acetic acid. After a short mixing, absorbance was measured at 570 nm.

3.3.12 Protein analysis

3.3.12.1 Protein isolation

After 24 h reoxygenation/treatment, the astrocytic medium was removed, and astrocytes were washed twice with cold PBS. Then, 500 µl of 1x NP-40 Surfact-Amps supplemented with protease and phosphatase inhibitors was added to astrocytes. Then, astrocytes were scrapped, collected in microtubes and incubated on ice for 20 min with constant mixing. Subsequently, lysates were sonicated three times with a continuous power of 3 for 10 seconds on ice and centrifuged at 10,000 g. After centrifugation, the supernatant containing soluble cytoplasmic proteins was collected.

3.3.12.2 BCA assay

The bicinchoninic acid (BCA) assay was utilized to determine the protein concentration using the Pierce BCA protein assay kit (Table 7). All procedures were performed according to the manufacturer’s instruction and the absorbance was measured at 570 nm. The concentration of the proteins was estimated according to the concentration of the standards provided in the BCA kit.

According to the total protein concentration, 25 µg of the proteins in each condition was diluted in a mixture of the NP-40, loading buffer and dithiothreitol (DTT). The prepared samples were boiled for 5 min at 95°C.

3.3.12.3 Western blot

Table 19: Polyacrylamide gel

10 % Separation gel (2 gels)		Stacking gel (4 gels)	
Acrylamide 30 %	5 ml	Acrylamide 30 %	2.60 ml
Tris-HCl 1.5 M (pH: 8.8)	3.75 ml	Tris-HCl 0.5 M (pH 6.8)	5 ml
Milli-Q water	6.25 ml	Milli-Q water	12.20 ml
APS 10 %	70 µl	APS 10 %	140 µl
TEMED	20 µl	TEMED	40 µl

10% polyacrylamide gel with a thickness of 1 mm were used (Table 19). Next, 25 µg of each sample was prepared in laemmli buffer and loaded in respective pockets of the polyacrylamide gels. Gel electrophoresis was carried out using 1x tris/glycine/SDS buffer at 80 mv for 20 min followed by 1 h at 120 mv. Then, proteins were transferred to 0.2 µm nitrocellulose membranes using turbo RTA mini-transfer kit (Table 7) and semi-Turbo blot transfer "mixed molecular weight" program for 2 mini gels for 15 min. Afterwards, total transferred protein was stained with Ponceau S for 5 min. Images of Ponceau S-stained blots were acquired using a colorimetric imager. Subsequently, Ponceau staining was removed using 1x Tris-buffered saline supplemented with 1 % Tween 20 (TBST) and blots were blocked in 5 % skim milk in TBST for 2 h. Next, membranes were incubated 1' Abs: GFAP rat monoclonal antibody (MW: 50 kD) 1:1000 and housekeeping protein glyceraldehyde 3-phosphate dehydrogenase (GAPDH) monoclonal rabbit (MW: 37 kD) 1:5000, both diluted in 3 % Bovine Serum Albumin (BSA) prepared in TBST at 4°C overnight.

The next day, all membranes were washed thrice with 1x TBST, each for 5 min. Then, the membranes were incubated with the corresponding 2'Abs; normal rat IgG-HRP, goat anti-rabbit IgG-HRP diluted in 3 % BSA prepared in TBST at RT for 1 h. All membranes were washed thrice with 1x TBST, each for 5 min. Conjugated HRP was enhanced with clarity western ECL substrate, and the chemiluminescent signal was acquired using Amersham Imager 680. Using Image J FIJI, the mean intensity of GFAP bands and total protein input (ponceau S staining) was assessed after Luke Miller instructions (lukemiller.org 2010), and GFAP was normalized to the total protein input.

3.4 Statistical analysis

All graphs were prepared with GraphPad Prism 8 and OriginPro 2019b. Data are presented as box and whisker plots, scatter interval plots, and bar graphs. Box plots comprise median (horizontal line), mean (middle square), interquartile range (IQR), and whiskers extending from minimum to maximum data points. Horizontal lines in scatter interval plots and bar graphs represent the mean and the whiskers in bar graph represent standard error of mean (s.e.m).

Single data points show increase/decrease compared to the means of their respective controls, that is, the normoxic vehicle group.

Statistical analysis was performed using GraphPad Prism 8 and OriginPro 2019b. A normality test was performed for all experimental groups. Single comparisons were done using two-tailed t-tests for parametric data with welch correction and Mann

Whitney for non-parametric. For multiple comparisons, depending on the nature of variables one way, two way, or three-way analysis of variance (ANOVA) followed by Tukey tests as post-hoc test. The significant level was set as $\alpha = 0.05$, and $p \leq 0.05$ values indicated significant intergroup differences. Individual statistical analysis for each experiment, sample size and biological/technical replicates were noted in figure captions. Critical changes mentioned throughout the text in result section are mean±s.e.m.

4 Results

4.1 Astrocytes support neuronal respiration and synaptogenesis

Astrocytes support neuronal mitochondrial metabolism through the lactate shuttle. To verify the astrocytic lactate release in this study, the actual L-lactate was compared in CM collected from mature astrocytes (21 DIV) versus the astrocytic culture medium (section 3.3.6). Data suggested that astrocytes released lactate extensively (133±9%)[2] while the medium contained no lactate (Figure 16, B).

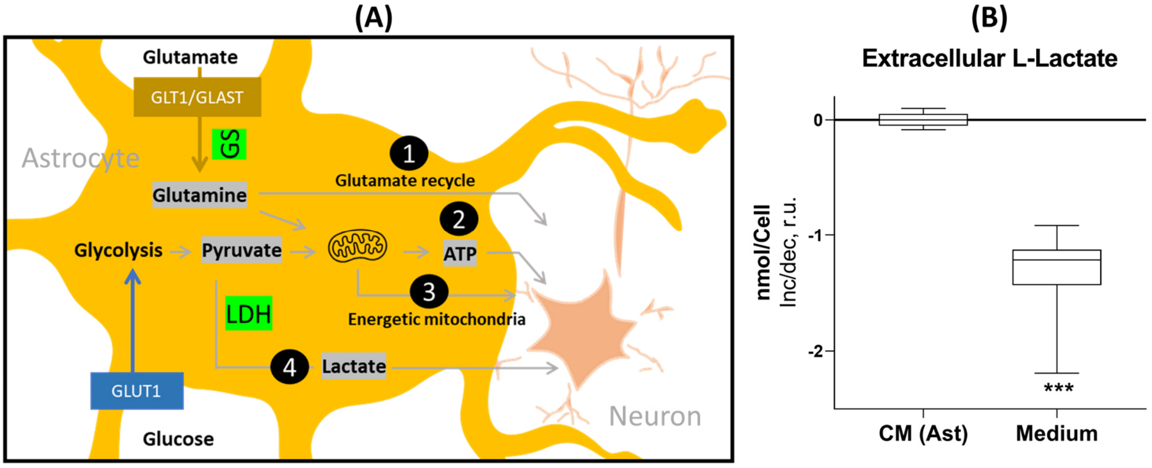

Figure 16: Astrocytes support neurons metabolically

(A) Schematic view of astrocytic metabolic-supportive roles **(1)** glutamine support through glutamate re-uptake and recycling via glutamine synthetase (GS, green) **(2)** ATP release **(3)** shuttling energetic (viable) mitochondria **(4)** converting pyruvate to lactate using lactate dehydrogenase (LDH) and lactate release. **B)** Extracellular L-lactate. Normalized difference (r.u.) with the conditioned medium of astrocytes (CM-Ast) mean is shown as box plots (IQR, min-max). Significant changes with the control are noted as * $p \leq 0.05$/** $p \leq 0.005$/*** $p \leq 0.0005$, as indicated by two-tailed student t-tests, n=4.

In this study, mitochondrial OXPHOS and neuronal synaptogenesis were compared in neuron cultures grown with astrocyte co-cultures for 14 DIV (Neu+Ast) versus 14 DIV neurons, which were grown without astrocyte co-cultures (Neu-Ast).

Mitochondrial OXPHOS was measured using Seahorse mito stress assay (MSA), which suggests that Neu+Ast had significantly higher basal and ATP-linked respiration (23±9% and 38±13%, respectively) as well as spare respiratory capacity (57±14%) compared to Neu-Ast (Figure 17).

---

[2] All presented data throughout the text in result section are mean±s.e.m.

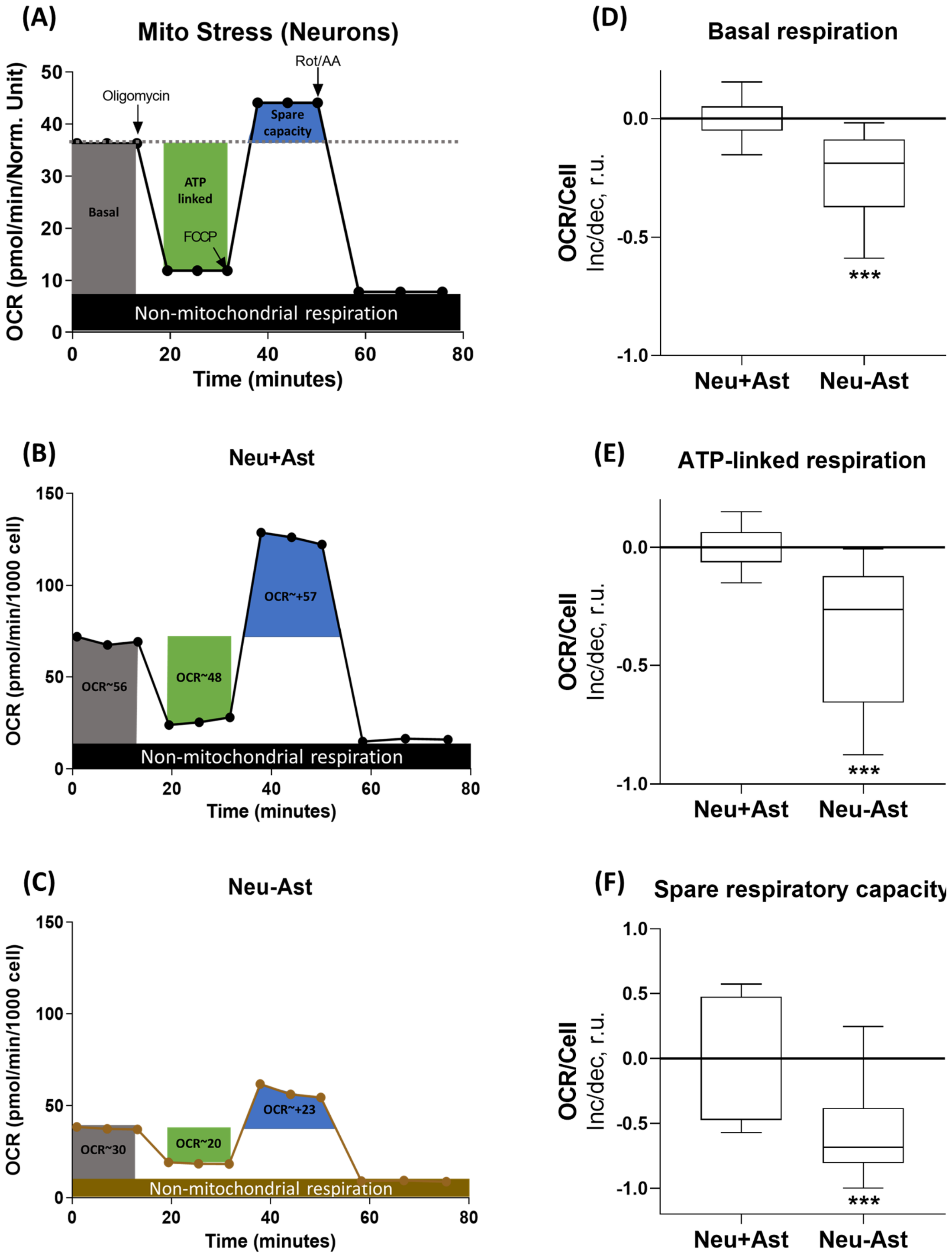

Figure 17: Astrocytes support neuronal respiration

(A) Explanatory seahorse mito stress assay (MSA) graph depicting real-time oxygen consumption rate (OCR) over time before and after the sequential injection of the Oligomycin, FCCP and Rot/AA. Non-mitochondrial respiration (black horizontal box), basal respiration (grey column), ATP-linked OCR (green column), and spare respiratory capacity (blue column). OCR values (Y-axis) is normalized to cell number (Hoechst) in each well multiplied by factor of 1000 and accordingly presented with the corresponding unit. (**B**) Representative MSA of neurons co-cultured with astrocytes (Neu+Ast) vs (**C**) neurons without astrocyte co-cultures (Neu-Ast). **(D)** Basal respiration, **(E)** ATP-linked, and **(F)** spare capacity in Neu+Ast vs Neu-Ast. Normalized difference (r.u.) with the mean of Neu+Ast is shown as box plots (IQR, min-max). Significant changes with the control are noted as * p≤0.05/** p≤0.005/*** p≤0.0005, as indicated by two-tailed student t-test, n=3.

Quantification of colocalized presynaptic marker VGLUT1 and postsynaptic PSD 95 showed significantly more functional synapses (35±5%) in Neu+Ast compared to Neu-Ast (Figure 18, A and B).

Furthermore, the absence of astrocytes did not affect the density of neurons significantly. (Figure 18, C and D).

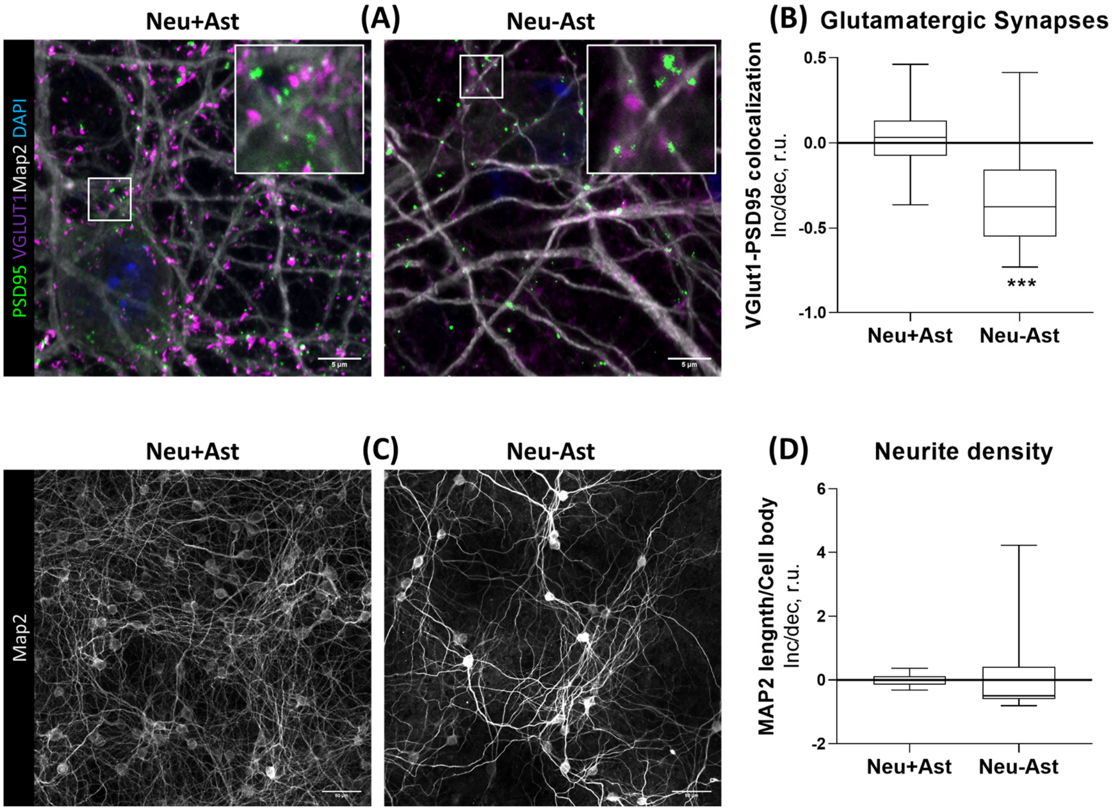

Figure 18: Astrocytes support the neuronal synaptogenesis

(A) Representative neuron immunostainings with presynaptic marker VGLUT1 (purple), postsynaptic marker PSD95 (green) and neuronal marker MAP2 (grey) in Neu+Ast vs Neu-Ast. (**B)** Colocalization of pre-post synaptic markers (VGLU1-PSD95). (**C**) Representative neuron immunostainings with MAP2. (**D**) Neurite density. Normalized difference (r.u.) with the mean of Neu+Ast is shown as box plots (IQR, min-max). Significant changes with the control are noted as * p≤0.05/** p≤0.005/*** p≤0.0005, as indicated by two-tailed student t-test, n=3.

4.2 STAT3 induces reactive astrogliosis in I/R astrocytes

This study addressed the role of canonical and alternative STAT3 signaling in inducing reactivity in ischemic astrocytes.

Mature astrocytes (21 DIV) from indirect co-cultures (section 3.3.2.3) were exposed to oxygen-glucose deprivation (OGlucD, 1% oxygen) for 1 h followed by immediate reperfusion with high glucose (4.5 mg/ml) medium for 24 h to mimic ischemia/reperfusion (I/R) injury. In addition, oxygen-glutamine deprivation (OGlnD) was utilized as a comparison for nutrient-oxygen deficiency model. To address the specific role of STAT3, astrocytes subjected to OGlucD and OGlnD were additionally incubated with either 50 ng/ml IL6 or 200 pM Stattic before and throughout the hypoxia and reperfusion period (pre-post treatment, Table 15).

Astrocytic STAT3 immunostainings were utilized to measure the STAT3's nuclear/cytoplasmic fluorescence ratio, and the higher fluorescent intensity in nuclei was referred to as STAT3 nuclear translocation.

STAT3 nuclear translocation was increased in OGlucD and IL6-OGlucD astrocytes by 4±1% and 7±1%, respectively. In contrast, Stattic decreased STAT3 nuclear translocation in both normoxic and OGlucD astrocytes by 4±1% and 2±2% respectively, compared to their corresponding vehicle. Neither IL6 nor Stattic treatment affected STAT3 nuclear translocation in OGlnD astrocytes significantly (Figure 19).

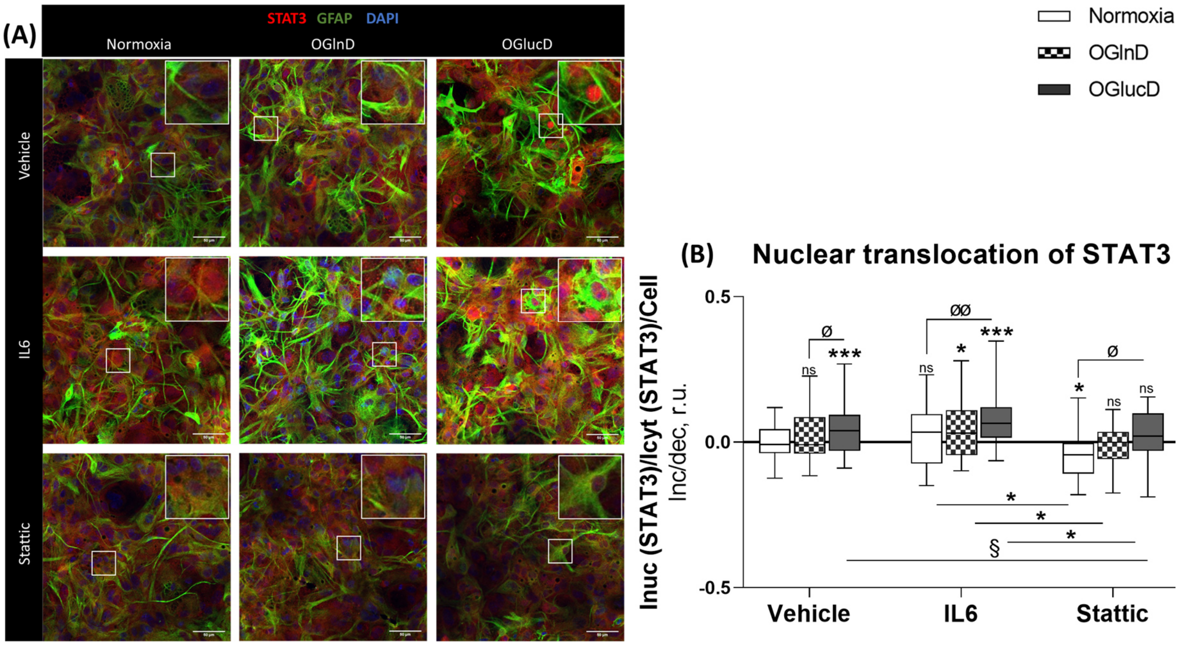

Figure 19: Nuclear STAT3 in OGlucD astrocytes

(A) Representative immunostaining of astrocytes with STAT3 (red), GFAP (green) and Hoechst (blue) in the vehicle (top row), IL6-treated (middle row) and Stattic-treated (bottom-row) astrocytes after normoxia (left column), oxygen glutamine deprivation (OGlnD, middle column), and oxygen-glucose deprivation (OGlucD). Cropped white boxes are random zoomed areas. Scale bar 50 µm. **(B)** STAT3 nuclear translocation. Normalized difference (r.u.) with the normoxic vehicle (control) mean is shown as box plots (IQR, min-max). Significant changes with the control are noted as *, effects of hypoxia and treatments are shown with § and ø, correspondingly. *, §, ø p≤0.05/**, §§, øø p≤0.005/***,§§§, øøø p≤0.0005, as indicated by 2-way ANOVA and Tukey tests, n=5. ns, no significant difference with the control.

To investigate whether nuclear STAT3 regulates gene transcription, a luciferase-based reporter gene assay was performed using the sis-inducible element (SIE) upstream of a minimal promoter followed by a firefly luciferase gene. SIE is a STAT3 response element (SRE), which is targeted by canonically activated STAT3. Binding of STAT3 to SIE/SRE activates transcription of the firefly luciferase and its activity corresponds to STAT3 activation (Figure 20, A).

SRE-luciferase activity (Figure 20, B) was increased by 9±7% in the vehicle and 25±7% in the IL6-OGlucD astrocytes. Besides, Stattic reduces SRE activity by 23±4% in normoxic astrocytes while it returned the activity to baseline in OGlucD astrocytes. In addition, SRE activity was reduced in the vehicle, IL6 and Stattic-treated OGlnD astrocytes, suggesting that STAT3 signaling was not activated in OGlnD astrocytes. On the other hand, neither STAT3 nuclear translocation nor transcription activity was observed in normoxic IL6 after 24 h, presumably due to IL6's short half-life (Toft, Falahati, and Steensberg 2011; Lyngso, Simonsen, and Bulow 2002). Therefore, incubation of the astrocytes with the same concentration of IL6 for 3 h showed an increased SRE activity (supplementary 7.3.1).

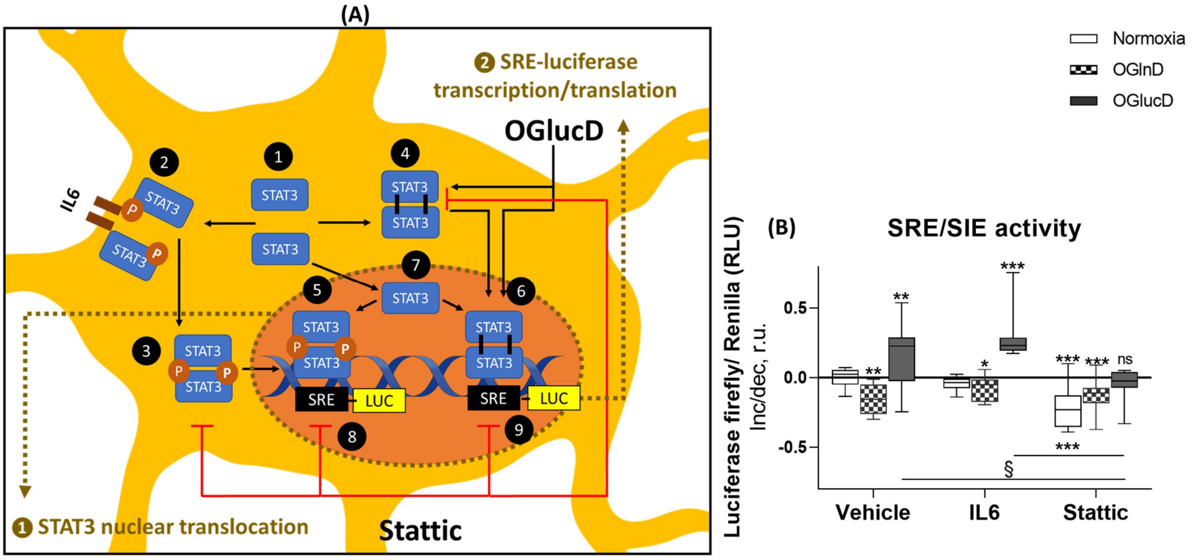

Figure 20: STAT3 transcription activity in OGlucD astrocytes

(A) Schematic view of astrocytic SRE/SIE-luciferase reporter gene assay. **(1 brown)** Nuclear STAT3 regulates SRE-luciferase expression **(2 brown)**. OGlucD and IL6 activate STAT3 signaling, causing STAT3 monomers phosphorylation **(2)**, dimerization **(3),** or dimerization without phosphorylation **(4)**. Dimerized **(5 and 6)** or monomer STAT3 **(7)** enter nuclei and regulate downstream SRE-luciferase transcription **(8 and 9).** Dimerization is blocked by Stattic (red lines). **B)** SRE-luciferase activity. Relative light unit (RLU) of firefly/renilla luciferase. Normalized difference (r.u.) with the normoxic vehicle (control) mean is shown as box plots (IQR, min-max). Significant changes with the control are noted as *, effect of treatments is shown with §. * §, p≤0.05/**, §§ p≤0.005/***, §§§ p≤0.0005, as indicated by 2-way ANOVA and Tukey tests, n=5. ns, no significant difference with the control.

The protein expression of GFAP, as one of the crucial genes regulated by STAT3 (Herrmann et al. 2008; Yeo et al. 2013; Bonni et al. 1997; Sarafian et al. 2010) was studied in STAT3-induced/inhibited I/R astrocytes. (Figure 21). Immunoblots indicated that GFAP expression was increased in OGlucD astrocytes by 31±23%. In addition, IL6 increased GFAP expression in normoxic and OGlucD astrocytes (IL6-OGlucD:135±65%), while Stattic reduced it in normoxic astrocytes by 36±12% and OGlucD astrocytes by 33±7% compared to normoxic vehicle. Stattic also alleviated astrocytic reactivity in OGlucD astrocytes by 65±24% compared to vehicle-OGlucD.

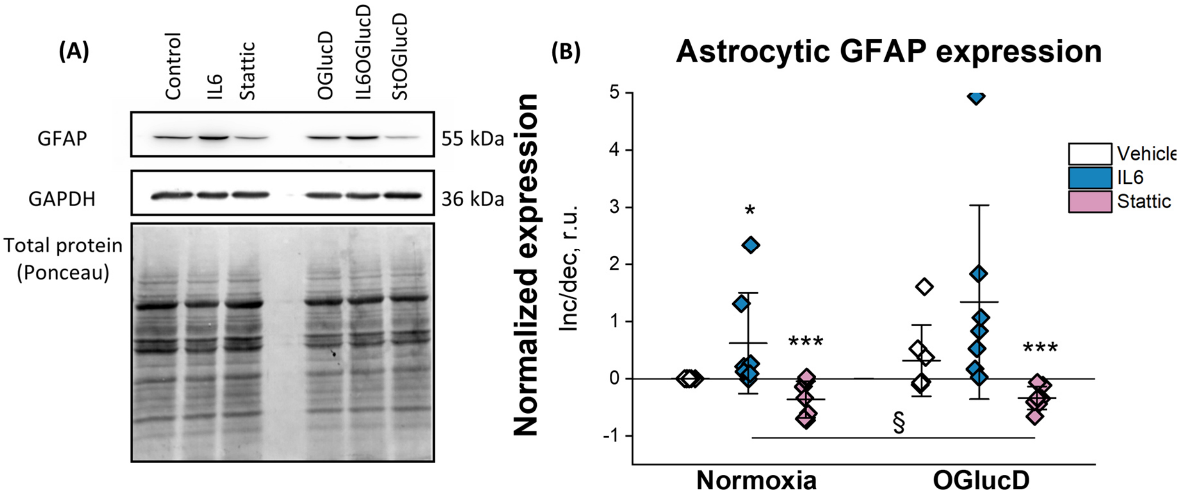

Figure 21: STAT3-induced reactive astrogliosis in OGlucD astrocytes

(A) Representative GFAP immunoblots (above), GAPDH (middle) and total protein input (Ponceau, bottom). **B)** Astrocytic reactivity. The relative GFAP/total protein input intensity. Normalized difference (r.u.) with the normoxic vehicle (control) mean is shown as scatter-interval plot (IQR-min-max). Significant changes with the control are noted as *, effect of treatments is shown with §. *, § $p \leq 0.05$/**, §§, $p \leq 0.005$/***, §§§ $p \leq 0.0005$, as indicated by 2-way ANOVA and Tukey tests, n=5.

4.3 STAT3 signaling induces lactate-directed glycolysis

Glycolytic properties of STAT3-induced/inhibited I/R astrocytes were studied using Seahorse glycolytic rate assay (GRA) (section 3.3.8.1). GRA provides insight into lactate-directed glycolysis (GlycoPER), mitochondria-directed glycolysis, non-glycolytic (post-2-DG) acidification, and the ratio of mitochondrial respiration to lactate-directed glycolysis (mitoOCR/glycoPER).

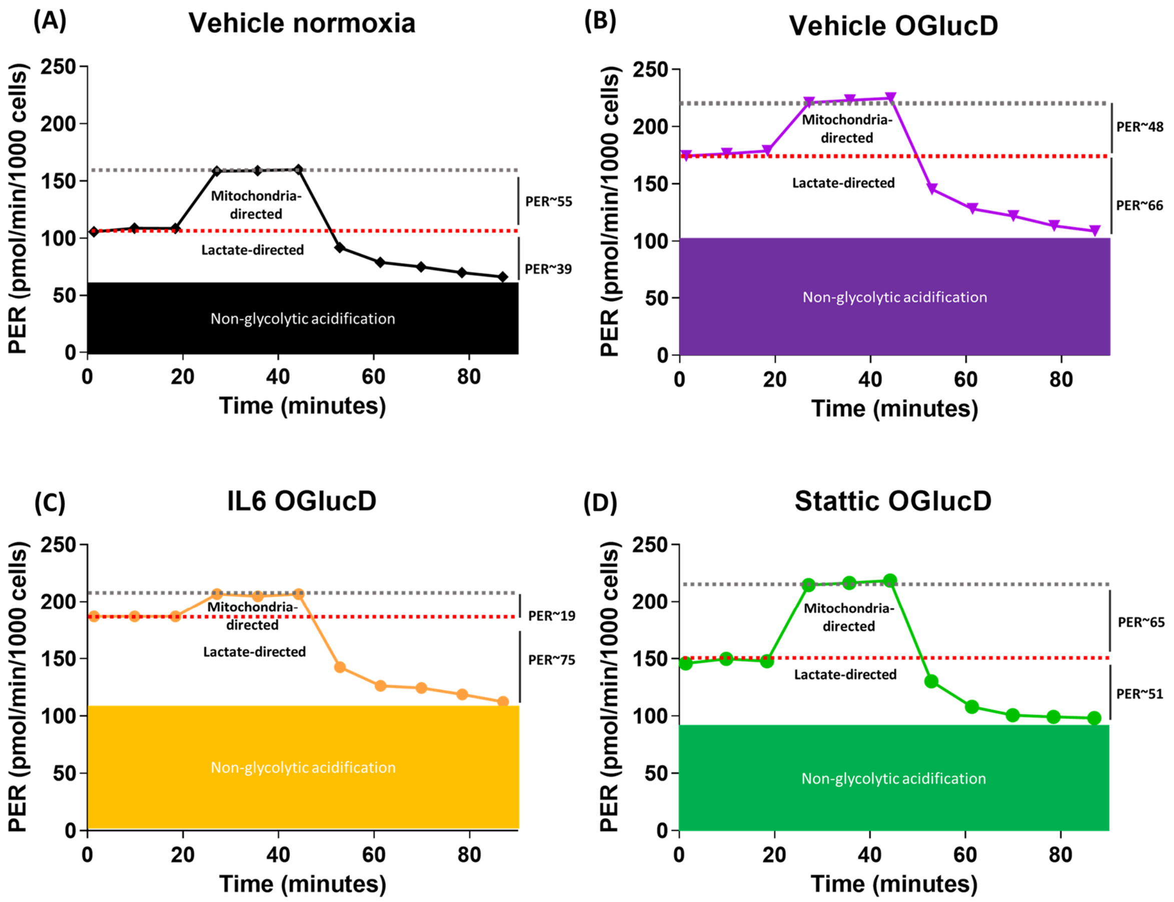

Figure 22: Astrocytic Seahorse glycolytic rate assay

Representative Seahorse XF glycolytic rate assay (GRA) in the **(black, A)** vehicle normoxia**,** (**purple, B)** vehicle-OGlucD, **(yellow, C)** IL6-OGlucD, and **(green, D)** Stattic-OGlucD. Red-pointed lines indicate proton efflux rate (PER) associated with lactate-directed glycolysis, and gray vertical pointed lines indicate maximum PER after Rot/AA injection. The difference between initial PER and maximum PER is associated with mitochondria-directed glycolysis. Non-mitochondrial glycolysis is attributed to the PER after 2-DG injection (horizontal-colored boxes). Lactate or mitochondria-directed PER is noted on the right side of each graph.

Lactate-directed glycolysis (Figure 23, A) was increased significantly in all I/R astrocytes (OGlnD:41±14%, OGlucD: 39±10%, IL6-OGlnD: 23±6%, IL6-OGlucD: 44±8%, Stattic-OGlnD: 31±12%). Conversely, the effect was less pronounced in Stattic-OGlucD astrocytes (14±6%) and insignificantly decreased compared to vehicle-OGlucD astrocytes 24±12% (Figure 23, A). Besides ischemic astrocytes, lactate-directed glycolysis was increased in the normoxic IL6-treated astrocytes by 10±4% but reduced in normoxic Stattic-treated astrocytes by 11±4%.

As a complementary approach, actual L-lactate was measured in astrocytic CM via ELISA (Figure 23, B). Extracellular L-lactate was also increased in the vehicle-OGlucD (41±19%) as well as the IL6-treated astrocytes significantly (IL6-OGlnD: 45±8%, IL6-

OGlucD: 40±5%). However, lactate concentration was significantly decreased in Stattic-OGlucD astrocytes compared to vehicle-OGlucD condition (47±21%, mean±s.e.m.) (Figure 23, B). Inhibition of STAT3 signaling did not affect OGlnD astrocytes significantly denoting that these cells did not follow a STAT3-regulated glycolytic pattern.

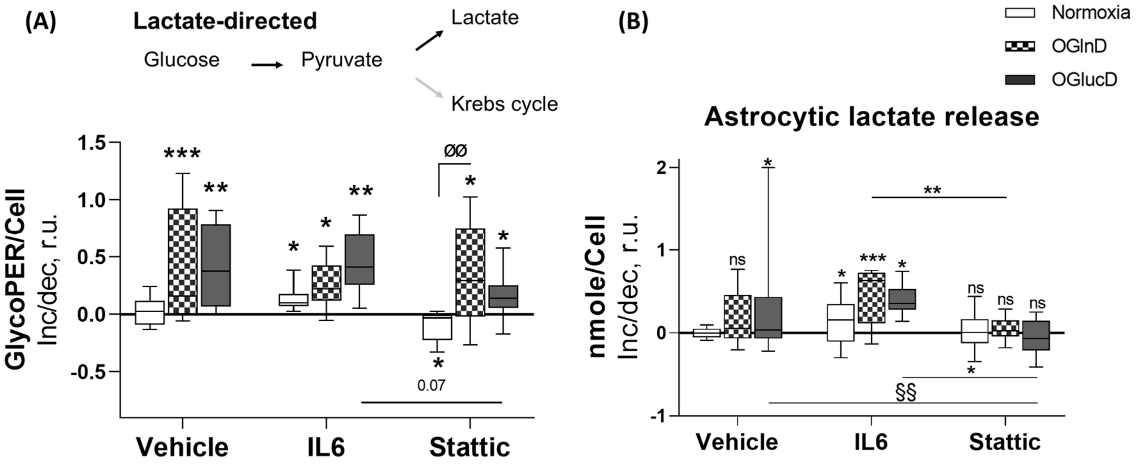

Figure 23: STAT3 signaling induces lactate-directed glycolysis in astrocytes

(A) Seahorse-derived lactate-directed glycolysis. **(B)** L-Lactate in astrocytic conditioned medium (CM). All obtained values are normalized to the cell number (Hoechst staining) and normalized difference (r.u.) with the normoxic vehicle (control) mean is shown as box plots (IQR, min-max). Significant changes with the control are noted as *, effects of hypoxia and treatments are shown with § and ø, correspondingly. *, §, ø $p \leq 0.05$/**, §§, øø $p \leq 0.005$/***, §§§, øøø $p \leq 0.0005$, as indicated by 2-way ANOVA and Tukey tests, GRA-n=8, lactate (ELISA)-n=6. ns, no significant difference with the control.

Mitochondria-directed glycolysis is attributed to the fraction of the glycolysis with pyruvate as the end product (Figure 24, A). This type of glycolysis supports the Krebs cycle and mitochondrial respiration. Data from mitochondria-directed glycolysis mirrored lactate-directed glycolysis data (Figure 23, A). Hypoxia downregulated mitochondria-directed glycolysis (e.g., OGlucD: 21±6%) while the Stattic-OGlucD astrocytes increased mitochondria-directed glycolysis by 24±8% compared to vehicle-OGlucD and by 14±6% compared to the normoxic vehicle. In addition, non-glycolytic acidification, which provides insight into other sources of cytoplasmic acidification, was increased in all I/R astrocytes (Figure 24, B).

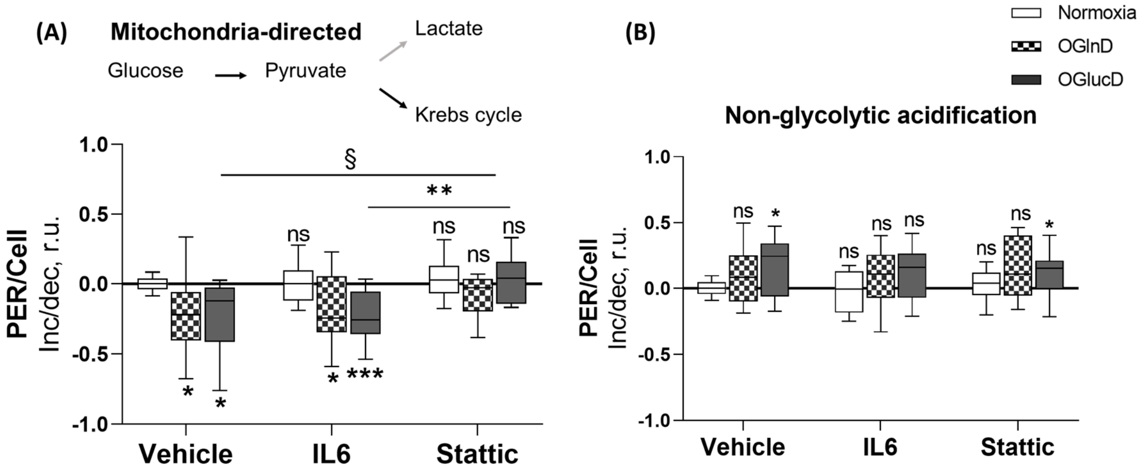

Figure 24:STAT3 signaling reduces mitochondria-directed glycolysis in astrocytes

(A) Seahorse-derived mitochondria-directed glycolysis. **B)** Non-glycolytic (Post 2-DG) acidification. All obtained values are normalized to the cell number (Hoechst staining) and normalized difference (r.u.) with the normoxic vehicle (control) mean is shown as box plots (IQR, min-max). Significant changes with the control are noted as *, effect of treatments is shown with §, correspondingly. *, § p≤0.05/**, §§ p≤0.005/***, §§§ p≤0.0005, as indicated by 2-way ANOVA and Tukey tests, n=8. ns, no significant difference with the control.

Simultaneous mitochondrial oxygen consumption rate (OCR) provides an overview about astrocytic metabolic energy map. The ratio of basal mitoOCR/glycoPER (Figure 25, C) suggested a predominant lactate-directed glycolytic profile for all I/R astrocytes except in Stattic-OGlucD. Conversely, Stattic-OGlucD astrocytes exhibited an oxidative energy map with prevalent mitochondria-directed glycolysis (Figure 24, B) and higher mitoOCR/glycoPER (Figure 25, C).

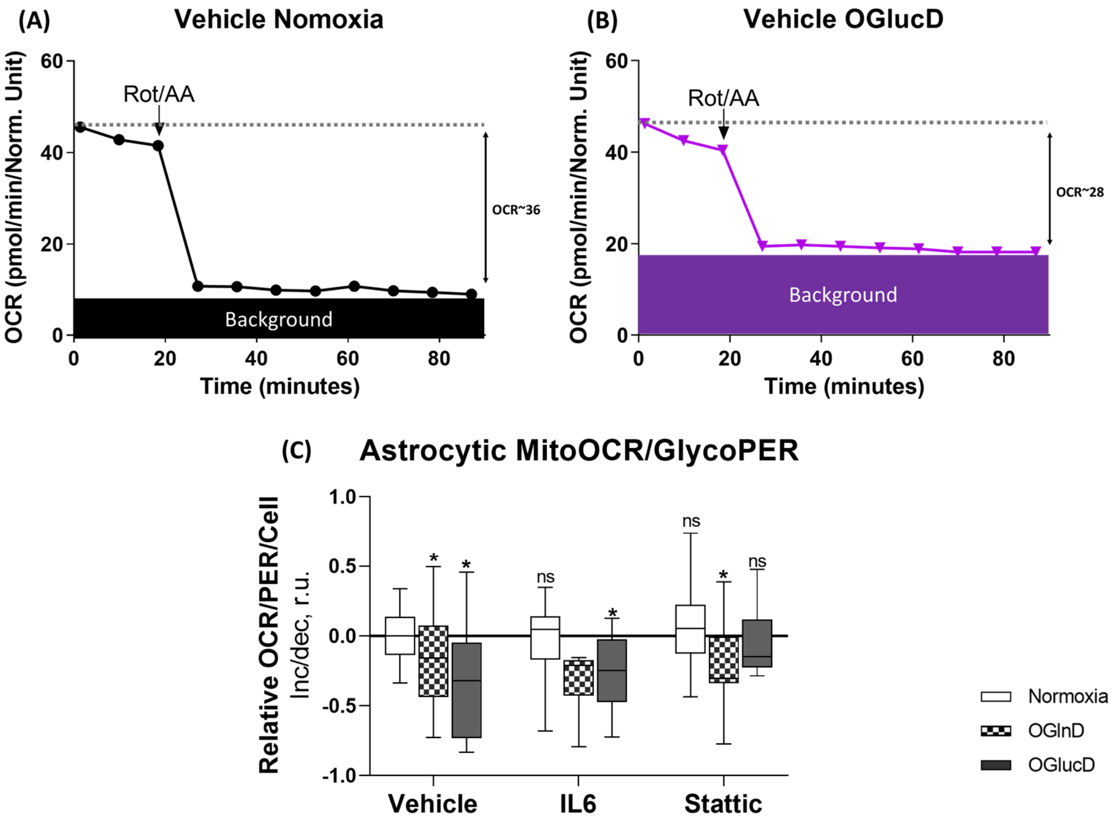

Figure 25: STAT3 signaling reduces mitoOCR/glycoPER in astrocytes

(A, black) Representative simultaneous OCR in Vehicle normoxia and **(B, purple)** vehicle-OGlucD **(C)** Ratio of the mitochondria OCR (MitoOCR) to lactate-directed glycolysis (GlycoPER). All obtained values are normalized to the cell number (Hoechst staining) and normalized difference (r.u.) with the normoxic vehicle (control) mean is shown as box plots (IQR, min-max). Significant changes with the control are noted as *. * p≤0.05/** p≤0.005/*** p≤0.0005, as indicated by 2-way ANOVA and Tukey tests, n=8, ns, no significant difference with the control.

4.4 The impact of astrocytic signaling on mitochondrial function

STAT3-induced mitochondrial properties of I/R astrocytes were analyzed by I) Seahorse mito stress assay (MSA) to study mitochondrial OXPHOS, II) accumulation of TMRM in astrocytic mitochondria to study mitochondrial membrane potential (MMP), and III) changes in astrocytic Mito SOX to study mitochondrial ROS.

4.4.1 STAT3 signaling decreases astrocytic mitochondrial OXPHOS

Seahorse MSA data has been categorized into basal and ATP-linked respiration as well as spare respiratory capacity.

Basal respiration, which is associated with initial mitochondrial-specific OCR (Figure 26, A and B, grey columns) was decreased in OGlucD astrocytes insignificantly (14±6%), while Stattic treatment compensated that by 31±8% (Figure 26, E).

ATP-linked respiration was measured after Oligomycin injection and attributed to respiration required for ATP synthesis (Figure 26, green columns). ATP-linked OCR (Figure 26, F) was decreased significantly in I/R astrocytes (OGlnD:27±5%, OGlucD: 27±8%). IL6 treatment maintained the effect at the I/R level. Nevertheless, Stattic improved ATP-linked respiration in OGlucD astrocytes by 25±8% compared to vehicle normoxia and by 53±11% compared to vehicle-OGlucD astrocytes. In addition, Stattic also improves astrocytic spare capacity by 243±83% in the Stattic-OGlucD astrocytes compared to vehicle-OGlucD (Figure 26, G). Mitochondrial respiration in OGlnD astrocytes with inactive STAT3 signaling was independent of the IL6 and Stattic treatment. Interestingly, Seahorse MSA data supported the mitoOCR/glycoPER from Seahorse GRA experiments (Figure 25, C).

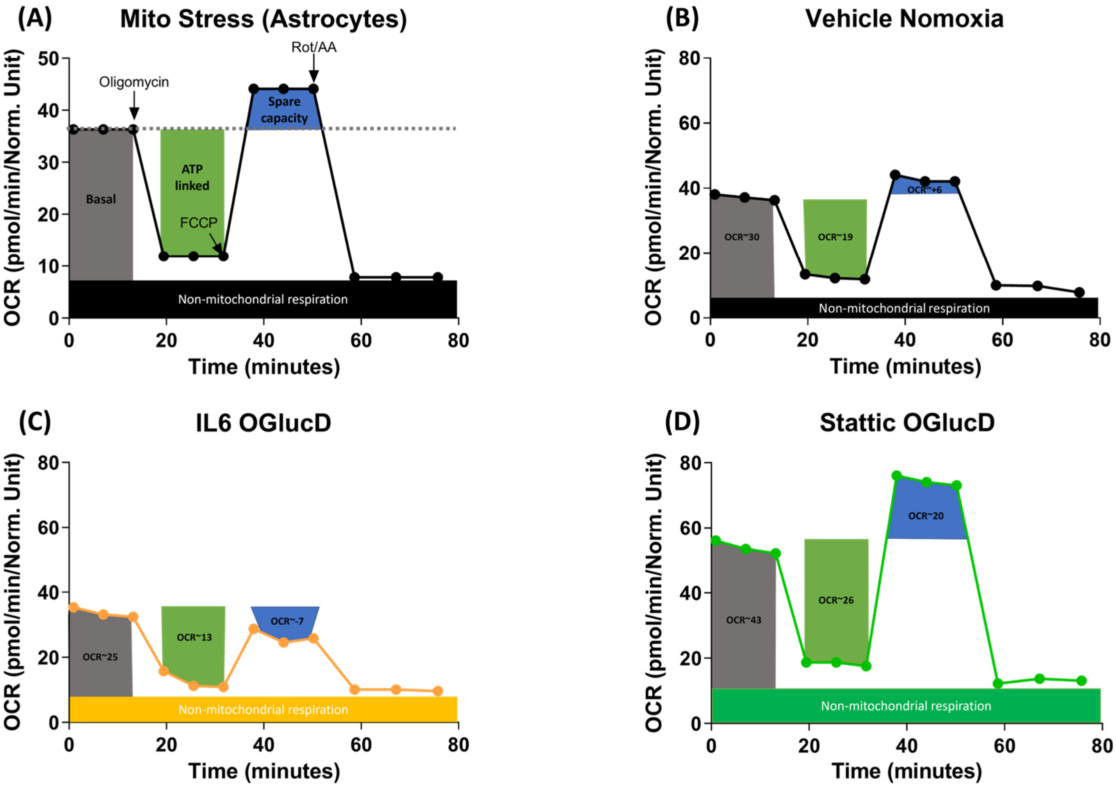

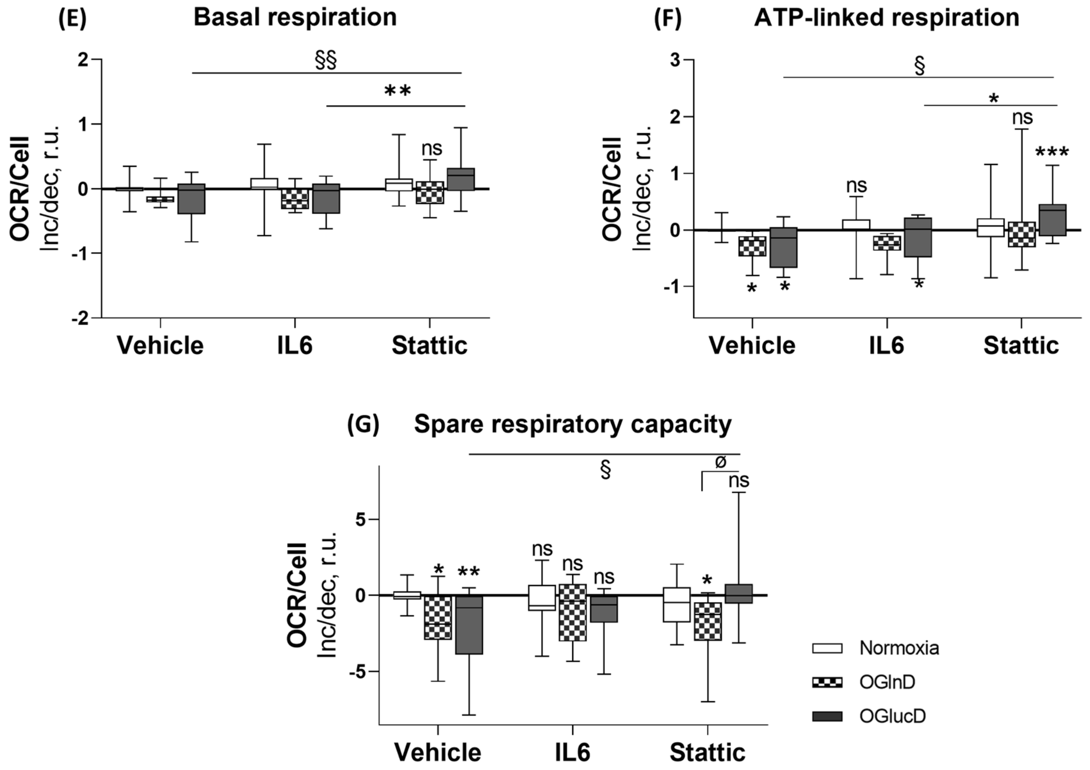

Figure 26: STAT3 signaling decreases mitochondrial OXPHOS

(A) Explanatory Seahorse mito stress assay (MSA) indicating basal OCR (grey column), ATP-linked OCR is (green columns), spare respiratory (blue columns) and non-mitochondrial respiration (black boxes) in **(B, black)** vehicle normoxia, **(C, yellow)** IL6-OGlucD and **(D, green)** Stattic-OGlucD. **(E)** Basal, **(F)** ATP-linked respiration, and **(G)** spare respiratory capacity. All obtained values are normalized to the cell number (Hoechst staining). Normalized difference (r.u.) with the normoxic vehicle (control) mean is shown as box plots (IQR, min-max). Significant changes with the control are noted as *, effects of hypoxia and treatments are shown with § and ø, correspondingly. *, §, ø $p \leq 0.05$/**, §§, øø $p \leq 0.005$/***, §§§, øøø $p \leq 0.0005$, as indicated by 2-way ANOVA and Tukey tests, n=8. ns, no significant difference with the control.

4.4.2 STAT3 signaling induces mitochondrial depolarization

Mitochondrial membrane potential (MMP) is referred to as a proton gradient between MM and IMS. ETC has a critical role in initiating and maintaining MMP. In turn, highly polarized mitochondria are required for ATP synthesis. In this study, MMP was measured in STAT3-induced/inhibited I/R astrocytes by incubating them with 5 nM TMRM during the 24 h reperfusion period. Later, the fluorescent intensity of astrocytic mitochondrial accumulated TMRM was recorded before and after injection of 5 µM uncoupler CCCP (Figure 27, A) and the Ɣψ was calculated as described in (section3.3.9). MMP (Ɣψ) was slightly decreased in vehicle-OGlucD astrocytes, while downregulation of MMP was significant in IL6-treated OGlucD astrocytes (32±3%). In contrast, Ɣψ was increased in Stattic-OGlucD astrocytes by 114±44%. On the other hand, in OGlnD conditions, astrocytic MMP did not alter after IL6 and Stattic treatment, indicating a STAT3-independent response from these cells. These findings support the data from ATP-linked respiration (Figure 26, D).

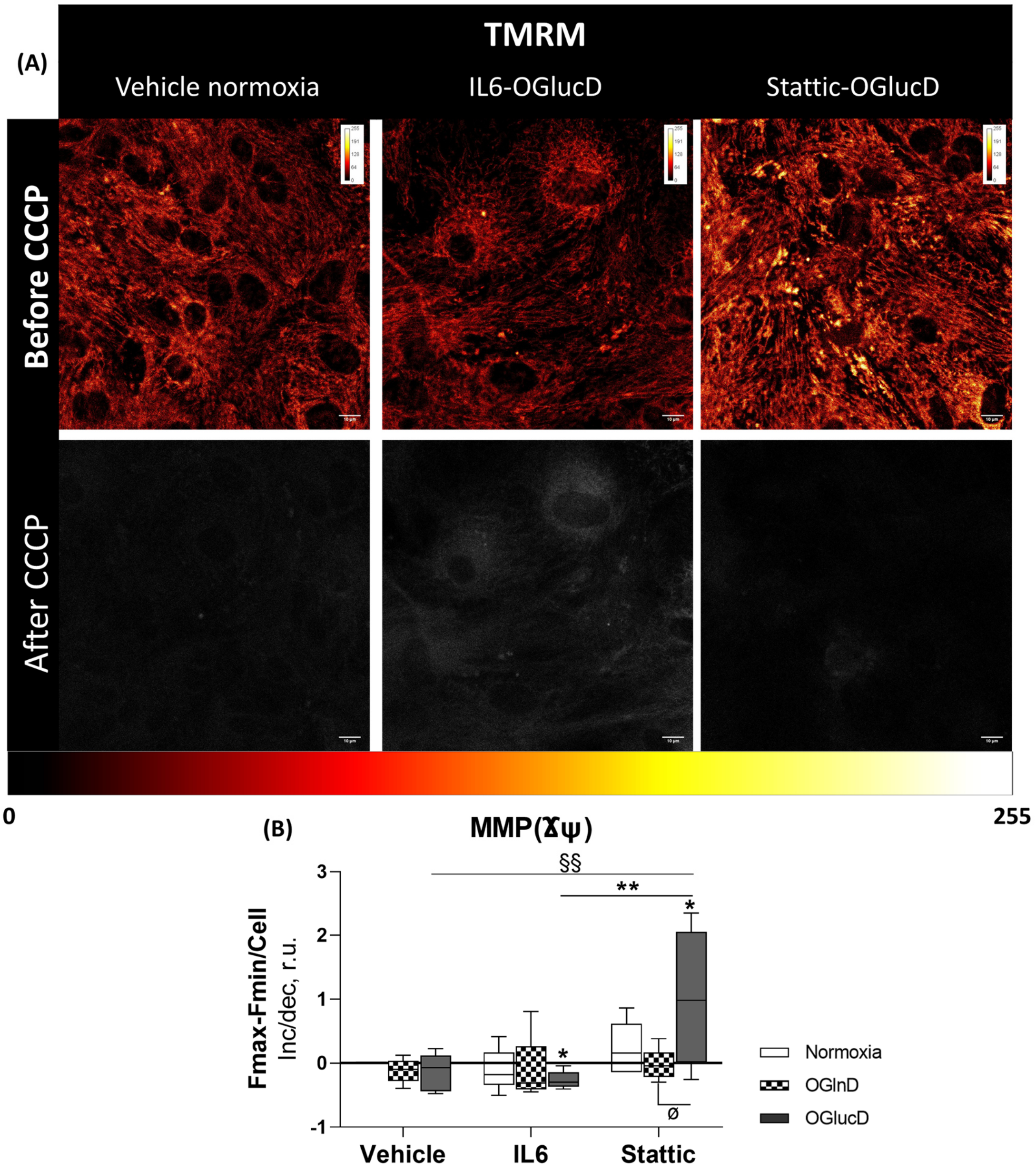

Figure 27: STAT3 signaling induces mitochondrial depolarization

(A) Representative TMRM (red) in astrocytic mitochondria in vehicle normoxia (left), IL6-OGlucD (middle) and Stattic-OGlucD (right), before CCCP (top), after injection of 5 μM CCCP (bottom). **(B)** MMP (Ɣψ) is calculated by subtracting the minimum fluorescent intensity (Fmin) after CCCP injection from the maximum fluorescent intensity (Fmax) before CCCP injection. The color scale spanned from black to white (0-255) indicates the fluorescent intensity of TMRM, with black as the lowest and yellow/grey as the highest intensity. Normalized difference (r.u.) with the normoxic vehicle (control) mean is shown as box plots (IQR, min-max). Significant changes with the control are noted as *, effects of hypoxia and treatments are shown with § and ø, correspondingly. *, §, ø $p \leq 0.05$/**, §§, øø $p \leq 0.005$/***, §§§, øøø $p \leq 0.0005$, as indicated by 2-way ANOVA and Tukey tests, n=6. ns, no significant difference with the control.

4.4.3 STAT3-independent mitochondrial ROS in I/R astrocytes

Mitochondrial superoxide generation is another ETC-induced criterion that was addressed in this study. OXPHOS generates mitochondrial superoxide (Mito SOX) physiologically during electron transport. However, Mito SOX is eventually reduced to the H_2O_2 by the mitochondrial SODs and subsequently reduced further to the H_2O by GSH (Aoyama, Watabe, and Nakaki 2008). Hypoxia essentially reduces the chances of oxygen reduction at complex IV and increases the superoxide formation (Chen et al. 2018). However, the impact of the STAT3 signaling on either superoxide formation or antioxidant response was unclear. In this study, STAT3 induced/inhibited I/R astrocytes were incubated with the fluorescent indicator of mitochondrial superoxide (Mito SOX). Then, the normalized fluorescence signal of Mito SOX was compared in all experimental groups (Figure 28). Alteration in Mito SOX signals (Figure 28, B) revealed that the Mito SOX was increased in both OGlnD and OGlucD astrocytes by 174±37% and 139±29% respectively. IL6 increase Mito SOX in OGlucD astrocytes insignificantly (97±47%, p-value: 0.056), while the Stattic treatment did not have a critical impact on it.

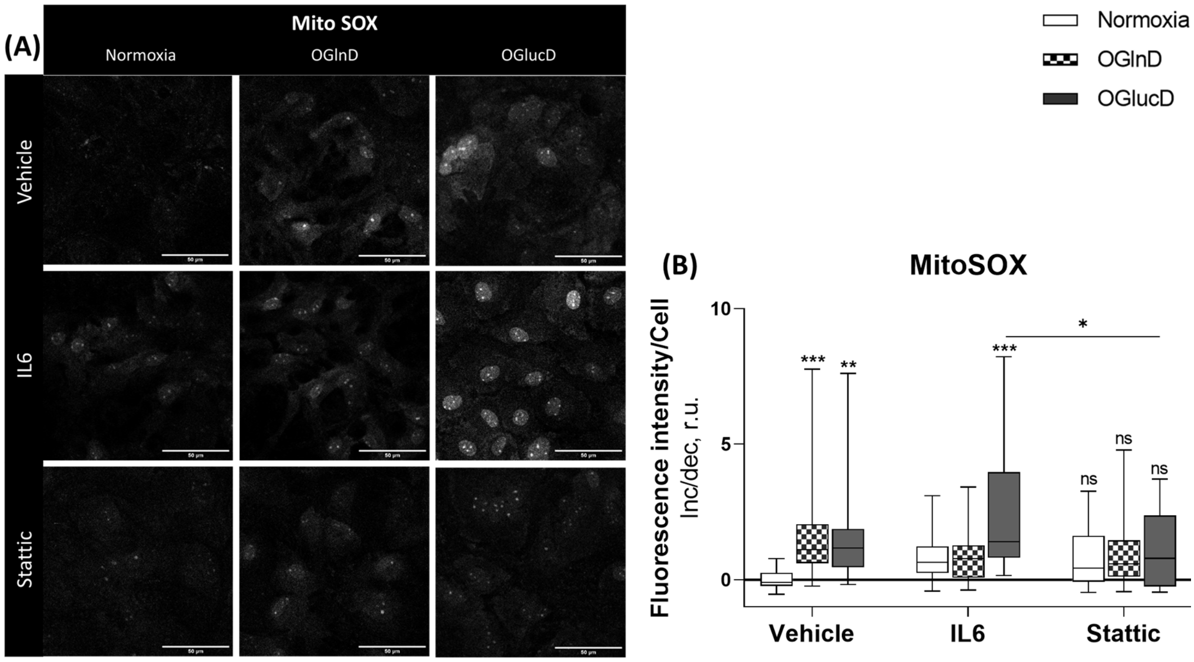

Figure 28: I/R increases astrocytic Mito SOX independent of STAT3 signaling

(A) Representative astrocytic Mito SOX (grey) in normoxia (left), OGlnD (middle) and OGlucD (right) in the vehicle group (top), treated with IL6 (middle) or Stattic (bottom). Scale bars: 50 µm. **B)** Mito SOX fluorescence intensity is normalized to cell number (Hoechst 33342). Normalized difference (r.u.) with the normoxic vehicle (control) mean is shown as box plots (IQR, min-max). Significant changes with are noted as *. *p≤0.05/** p≤0.005/*** p≤0.0005, as indicated by 2-way ANOVA and Tukey tests, n=5. ns, no significant difference with the control.

4.5 The impact of astrocytic STAT3 signaling on co-cultured neurons

This study further focuses on the impact of STAT3 activated astrocytes on mitochondrial, synaptic and dendritic properties of co-cultured neurons.

4.5.1 STAT3-inhibited I/R astrocytes boost OXPHOS in neurons

Co-cultured neurons were grown with astrocytic support for 14 DIV. Then, astrocyte cultures were separated, induced/inhibited for STAT3 signaling and exposed to I/R (Table 15). Next, treated astrocytes were co-cultured with untreated neurons for 24 h. Afterward, astrocyte co-cultures were removed, and the neuronal mitochondrial response was studied using Seahorse MSA.

Seahorse MSA data reveal that OGlnD astrocytes reduced basal and ATP-linked respiration by 24±9% and 24±10%, respectively in their co-cultured neurons. However, this downregulation was less significant in OGlucD astrocytes' co-cultured neurons (basal: 18±9%, ATP-linked: 21±9%). Basal respiration was improved in the neurons co-cultured with Stattic-OGlnD astrocytes (60±12%). However, the effect was not apparent in the ATP-linked respiration of these cells (Figure 29, F). Interestingly, basal and ATP-linked respiration (Figure 29, E, and F) were significantly improved in the neurons co-cultured with Stattic- treated OGlucD astrocytes (basal: 31±13%, ATP-linked: 71±23%). IL6-treated astrocytes did not modify the ischemic effect on neuronal mitochondria. Neuronal spare respiratory capacity was not influenced by treatments in astrocyte co-cultures (Figure 29, G). In conclusion, astrocytes Stattic treatment improved neuronal mitochondrial respiration in basal and ATP-linked levels.

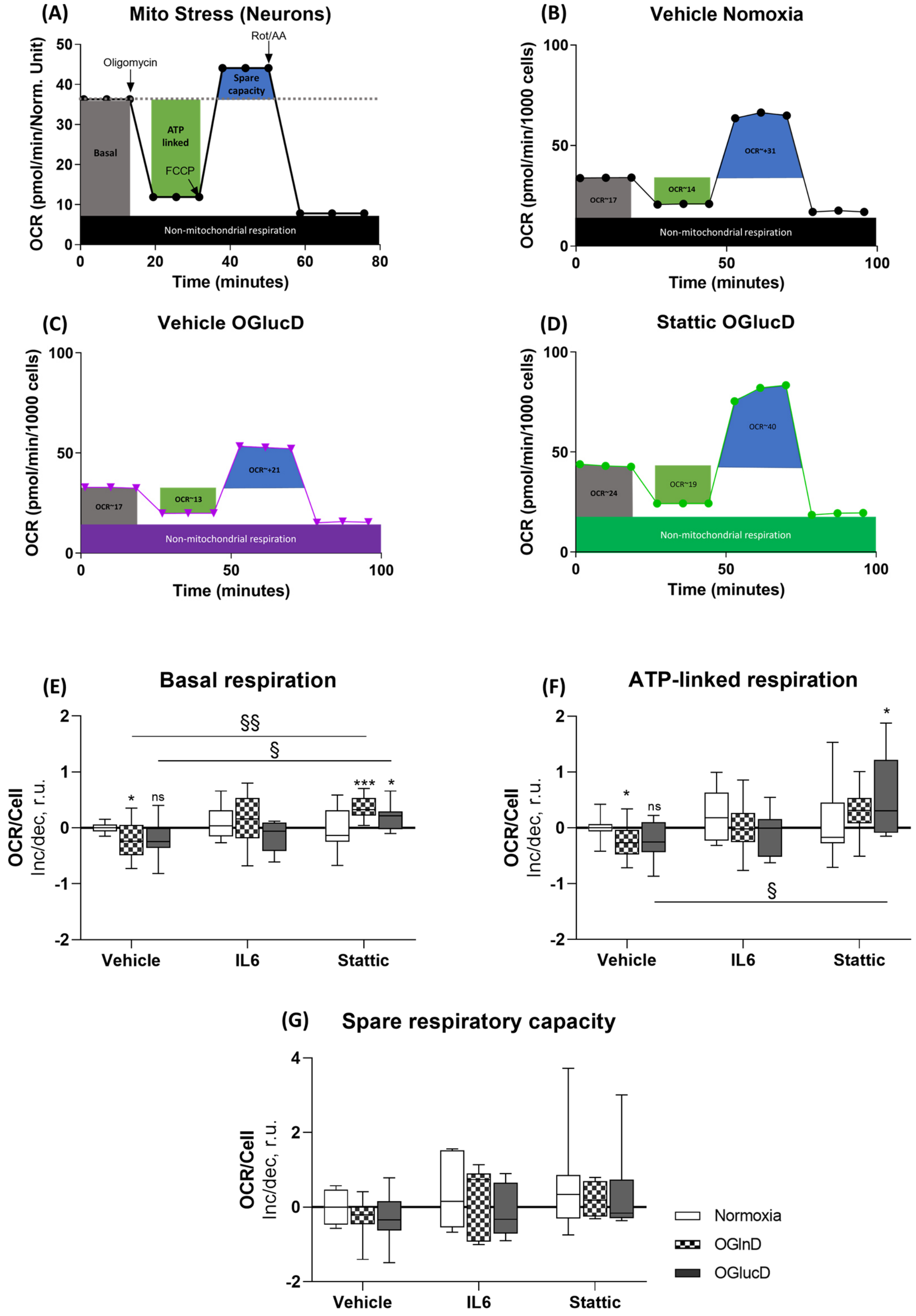

Figure 29: STAT3-inhibited OGlucD astrocytes boosts OXPHOS in neurons

(A) Explanatory Seahorse mito stress assay (MSA), basal OCR (grey column), ATP-linked OCR (green columns), spare respiratory (blue columns) and non-mitochondrial respiration (black boxes) in the neurons co-cultured with **(B, black)** vehicle normoxic, **(C, purple)** OGlucD and **(D, green)** Stattic-OGlucD. **(E)** Neuronal basal respiration, **(F)** ATP-linked respiration **(G)** spare respiratory capacity. All obtained values are normalized to the cell number (Hoechst staining) and normalized difference (r.u.) with the normoxic vehicle (control) mean is shown as box plots (IQR, min-max). Significant changes with the control are noted as *, effects of hypoxia and treatments are shown with §. *, § $p \leq 0.05$/**, §§ $p \leq 0.005$/***, §§§ $p \leq 0.0005$, as indicated by 2-way ANOVA and Tukey tests, n=5, ns, no significant difference with the control.

4.5.2 STAT3-inhibited I/R astrocytes boost neuronal synaptogenesis

Immunostainings of co-cultured neurons with pre-post glutamatergic synaptic markers (Figure 30, A) provide insight into functional synapses (Dzyubenko et al. 2016). In this study colocalization pre-post synapses were quantified. Based on synaptic density data (Figure 30, B), neurons co-cultured with OGlucD astrocytes had significantly fewer functional synapses (30±5%). Astrocytic IL6 treatment did not alter the impact of ischemic astrocytes on co-cultured neurons. In contrast, neurons co-cultured with Stattic-OGlucD astrocytes had significantly more functional synapses compared to neurons co-cultured with vehicle-OGlucD (56±5%) and IL6-OGlucD (48±9%) astrocytes.

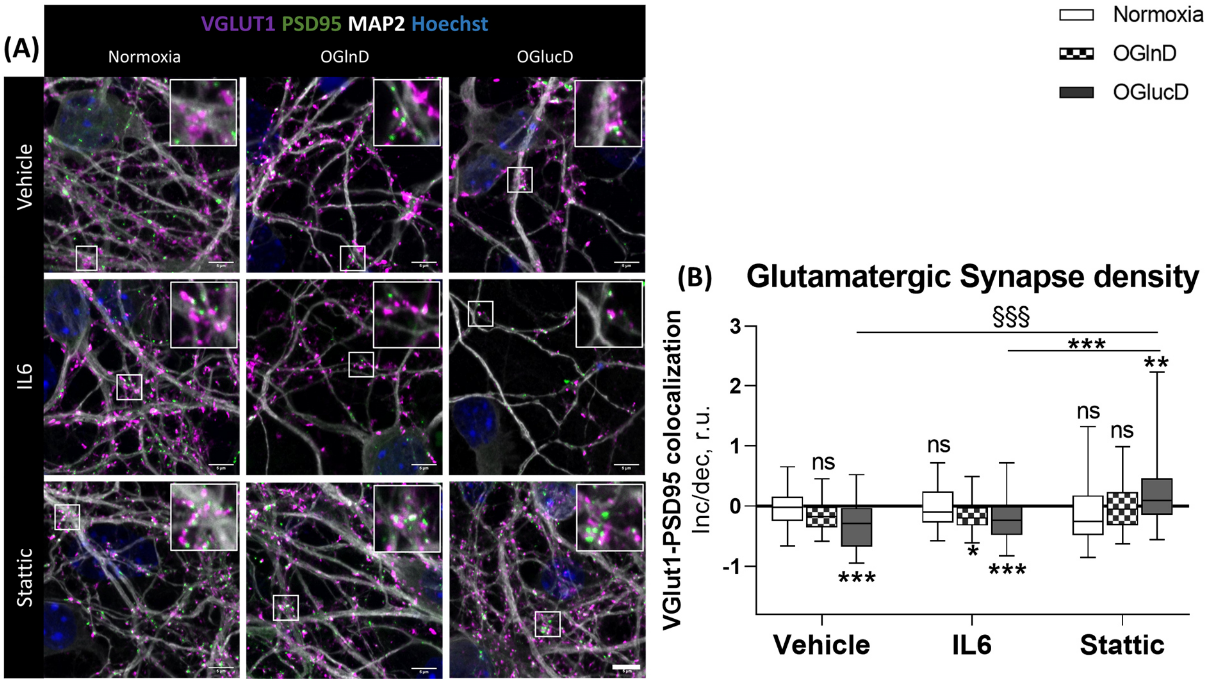

Figure 30: STAT3-inhibited OGlucD astrocytes boosts neuronal synaptogenesis

(A) Representative immunostainings of neurons for presynaptic marker VGLUT1 (Purple), postsynaptic marker (PSD95), and neuronal marker MAP2 (grey) for neurons co-cultured with normoxic (left), OGlnD (middle) and OGlucD (right) astrocytes in the vehicle group (top), IL6 (middle), or Stattic (bottom) treatment. Scale bars: 5 µm. Cropped white boxes represent random zoomed areas. **(B)** Colocalization of pre-post synaptic markers (VGLU1-PSD95). Normalized difference (r.u.) with the normoxic vehicle (control) mean is shown as box plots (IQR, min-max). Significant changes with the control are noted as *, effects of hypoxia and treatments are shown with §. *, § p≤0.05/**, §§ p≤0.005/***, §§§ p≤0.0005, as indicated by 2-way ANOVA and Tukey tests, n=6. ns, no significant difference with the control.

4.5.3 Astrocytic STAT3 signaling does not affect neurite density

Neuronal processes were labeled by MAP2 staining (Figure 31, A). Neurite density was increased in IL6-OGlucD and the Stattic-OGlnD and Stattic-OGlucD, denoting that neurite outgrowth was independent of STAT3 signaling in co-cultured astrocytes (Figure 31, B).

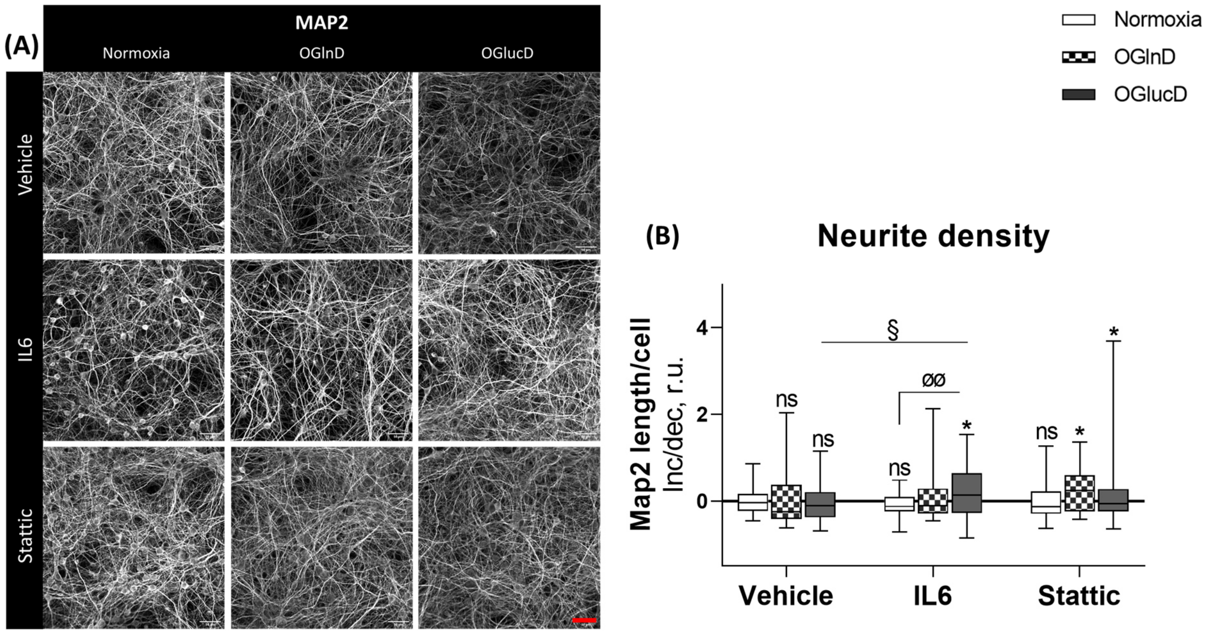

Figure 31: Astrocytic STAT3 signaling does not affect neurite density

(A) Representative neuronal MAP2 immunostaining (grey) in neurons co-cultured with in normoxic (left) oxygen, glutamine-deprived (OGlnD-middle) and oxygen glucose-deprived (OGlucD-right), vehicle (top), IL6 (middle) or Stattic (bottom) treated astrocytes. Scale bars: 50 µm. **B)** Neurite density. Normalized difference (r.u.) with the normoxic vehicle (control) mean is shown as box plots (IQR, min-max). Significant changes with the control are noted as *, effects of hypoxia and treatments are shown with § and ø, correspondingly. *, §, ø p≤0.05/**, §§, øø p≤0.005/***, §§§, øøø p≤0.0005, as indicated by 2-way ANOVA and Tukey tests, n=10. ns, no significant difference with the control.

4.5.4 Sodium lactate does not substitute the astrocytic support

Seahorse GRA data (section 4.3) revealed that STAT3 signaling increased astrocytic lactate generation. Therefore, synaptic and neurite density was compared in mature neuronal cultures grown with astrocyte co-cultures (Neu+Ast), without astrocyte co-culture (Neu-Ast) and Neu-Ast supplemented with 50 µM[3] Sodium lactate for 24 h. Neurite density was not affected in the absence of astrocytes (Neu-Ast) and after the addition of the lactate (Figure 32, D). In contrast, synapse density was severely decreased by 43±5% in the absence of the astrocytes (Figure 32, B, Neu-Ast) and lactate supplementation did not affect it (Figure 32, B, Neu-Ast+ Lactate).

---

[3] 50 µM is the mean of the highest lactate concentration in astrocytic CM. Mean of Vehicle normoxia: 28 µM ±3%, mean of highest concentration in each experiment: 57 µM ±6.5% (mean±s.e.m.)

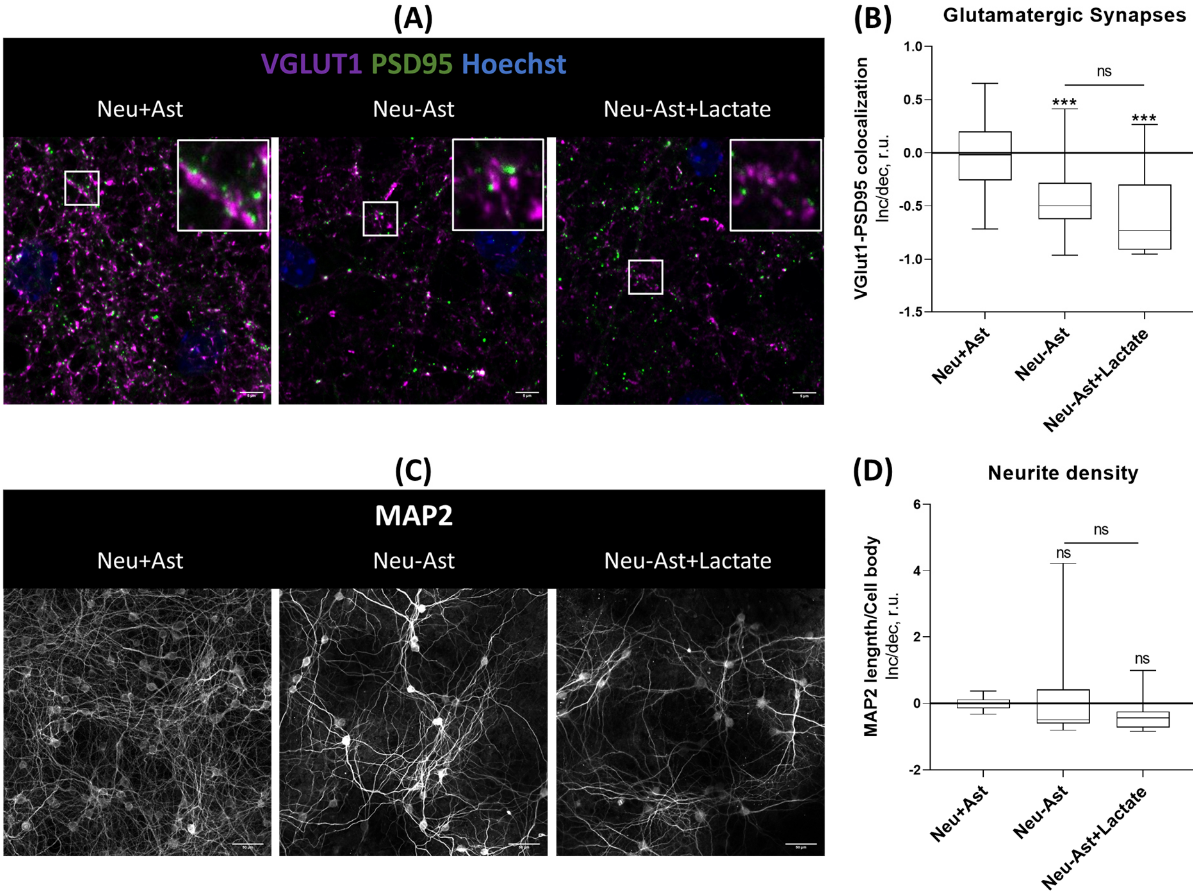

Figure 32: Lactate supplementation has no significant effect on synaptic/neurite density

(A) Representative immunostainings of neurons co-cultured with astrocytes (Neu+Ast, left), Without astrocytes (Neu-Ast, middle) and without astrocytes but supplemented with 50 µM Sodium lactate for 24 h (Neu-Ast+Lactate, right) stained for presynaptic marker VGLUT1 (purple) and postsynaptic marker (PSD95). Scale bar: 5 µm. Cropped white boxes represent random zoomed areas. **(B)** Synaptic density. **(C)** Representative MAP2 immunostaining (grey) in Neu+Ast (left), Neu-Ast (middle) and Neu-Ast+Lactate (right). Scale bars: 50 µm. **(D)** Neurite density. Normalized difference (r.u.) with the mean of Neu+Ast is shown as box plots (IQR, min-max). Significant changes with the control are noted as *. * $p \leq 0.05$/** $p \leq 0.005$/*** $p \leq 0.0005$, as indicated by one-way ANOVA and Tukey tests, n=3. ns, no significant difference with the control.

Since OGlnD condition did not induce STAT3 signaling, and STAT3 induction/inhibition did not affect metabolic response in OGlnD astrocytes, this condition was excluded from further experiments.

4.6 STAT3-PKM2 and HIF feedforward loop in I/R astrocytes

Studies on metastatic cancer cells indicate that STAT3 induces resistance in highly metastatic cancer cells (Sarmiento Soto et al. 2020; Liang et al. 2013; Priego et al. 2018). Further studies on cancer cells and reactive astrocytes (Demaria and Poli 2012;

Wei et al. 2020) revealed that STAT3 signaling promotes PKM2 nuclear translocation. In turn, nuclear PKM2 activates STAT3 within nuclei to regulate the transcription of hif1α. On the other hand, HIFs are activated in response to ischemia, form protein complexes and translocate in nuclei to regulate the expression of glycolysis-regulating genes. Based on our previous metabolic observations in this study, the following experiments address the possibility of activating the STAT3-PKM2-HIF feedforward loop to promote metabolic resistance in I/R astrocytes.

4.6.1 Reciprocal STAT3 and PKM2 activation in I/R astrocytes

In this study, PKM2 intracellular localization was addressed using immunostaining of treated astrocytes (Table 15). STAT3 and PKM2 double staining in normoxic vehicle astrocytes suggested an even distribution of both markers across cytoplasm and nuclei. PKM2 appeared as distinct cytoplasmic puncta (Figure 33, A, top), which presumably can be attributed to PKM's tetrameric isoforms. Nevertheless, I/R induced nuclear colocalization of STAT3 and PKM2 (Figure 33, b2II and III) and STAT3 membrane recruitment (Figure 33, B2, white arrows).

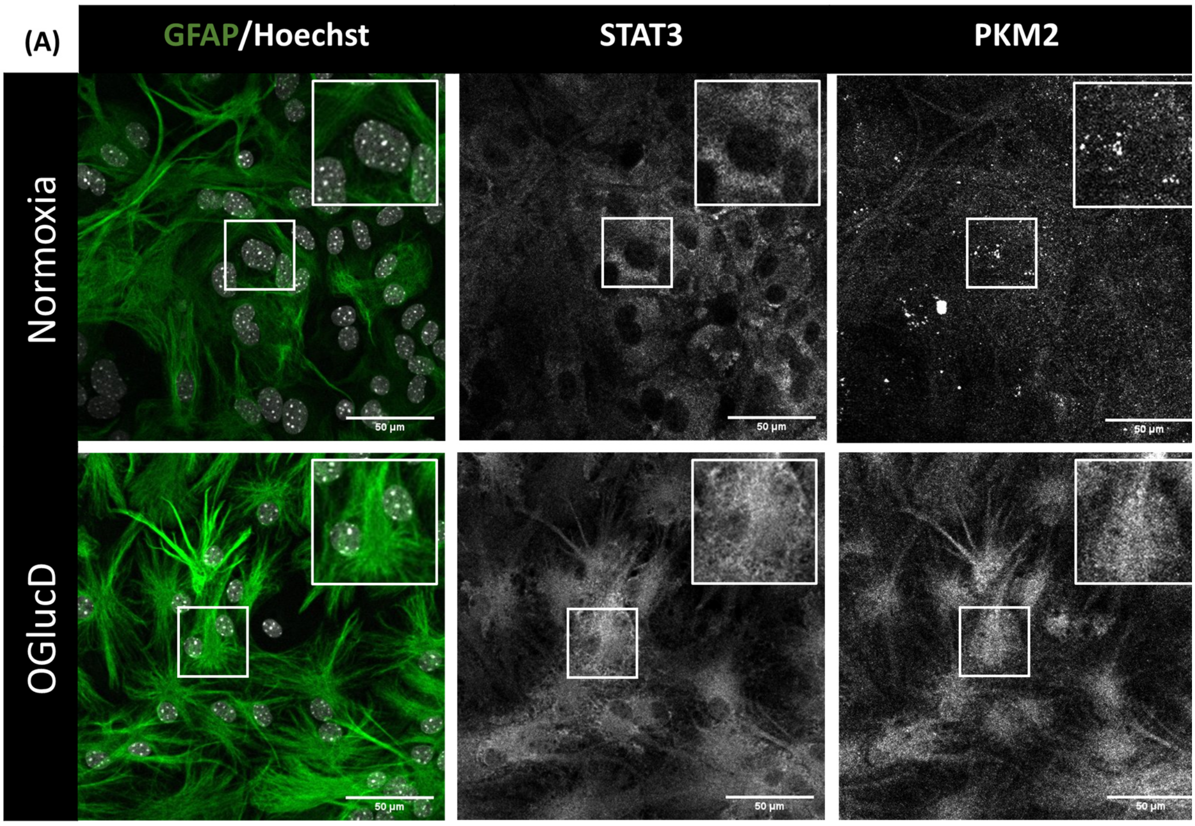

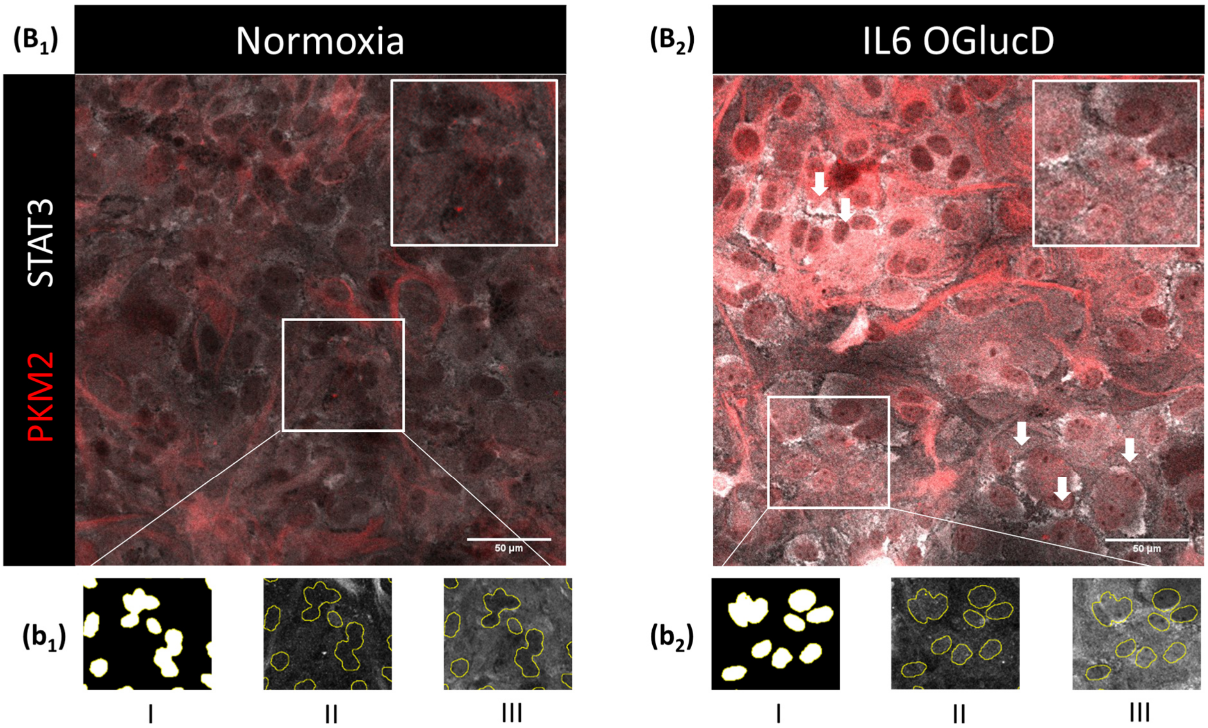

Figure 33: STAT3 and PKM2 reciprocal activation in I/R astrocytes

(A) Representative astrocyte immunostainings with GFAP (green) and Hoechst (grey, left), STAT3 (grey, middle) and PKM (grey, right) in normoxic (top) and OGlucD (bottom) conditions. Cropped white boxes represent similar ROIs in GFAP (left), STAT3 (middle) and PKM2 (right) immunostainings in normoxic and OGlucD astrocytes. **(B1 and 2)** colocalization of the STAT3 (grey) and PKM (red) in normoxic (B1) vs IL6-OGlucD (B2) astrocytes. Cropped white boxes represent similar ROIs in Hoechst (bI), STAT3 (bII) and PKM2 channels (bIII) in both normoxic vehicles and IL6-OGlucD astrocytes. White arrows show the membrane localization of the STAT3. Scale bar 50 µm.

4.6.2 STAT3 signaling activates PKM2 and HIF signaling in I/R astrocytes

PKM2 immunostaining in astrocytes (Figure 34, A and B) revealed that PKM2 nuclear translocation was increased significantly in the vehicle and IL6-OGlucD astrocytes (OGlucD:40±5%, IL6-OGlucD: 44±10%). In contrast, the nuclear translocation was reduced in Stattic-treated OGlucD astrocytes compared to the vehicle-OGlucD by 32±5%.

On the other hand, dual-luciferase reporter gene assay for hypoxic response element (HRE) (Figure 34, C and D) suggested that the HIF transcription activity was significantly increased after hypoxia (113±12%) and intensified after the IL6 treatment (144±18%). However, Stattic-treatment reduces HRE activity slightly in OGlucD astrocytes (11±16%).

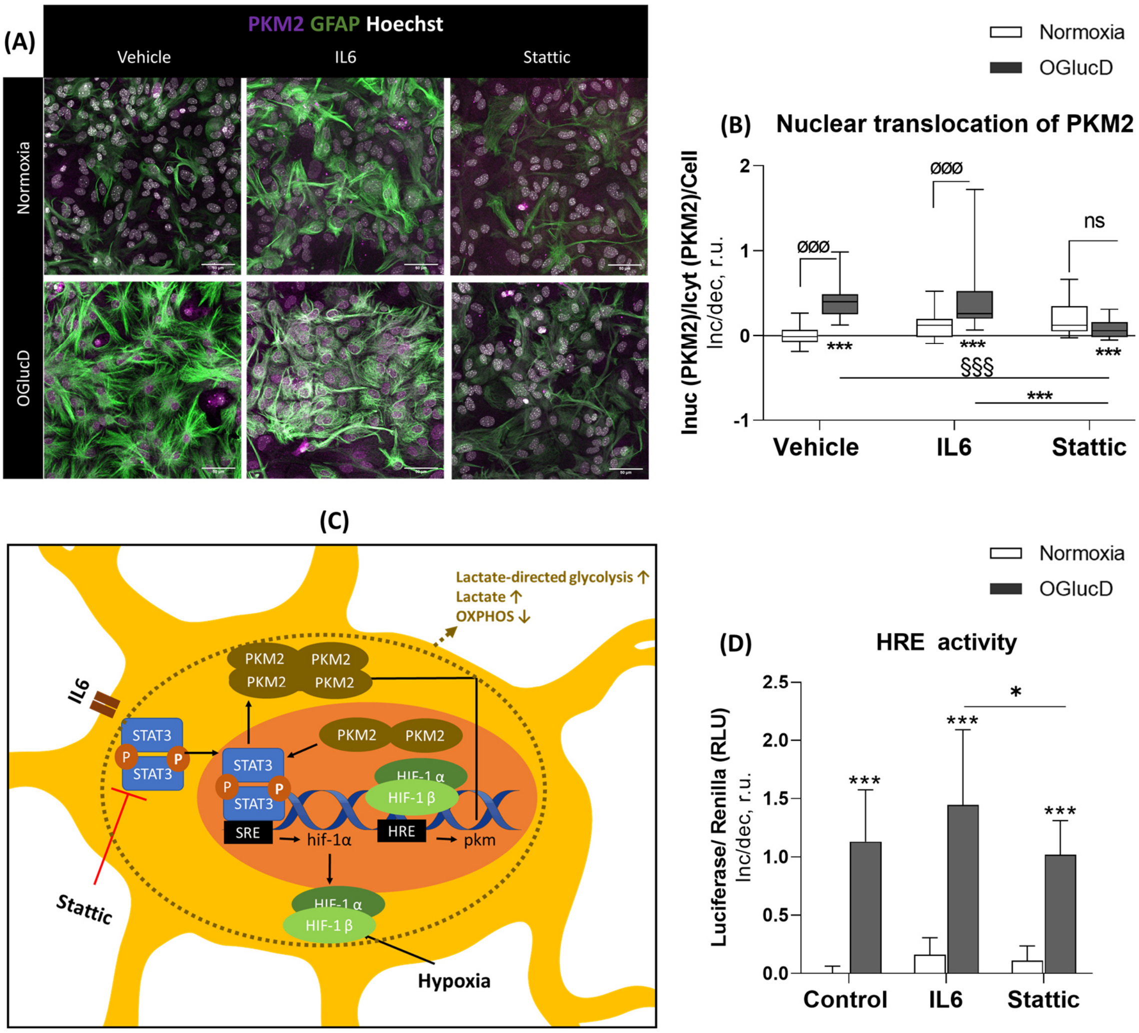

Figure 34: STAT3 signaling activates PKM2 and HIF in I/R astrocytes

(A) Representative immunostaining of astrocytes for PKM2 (purple), GFAP (green) and Hoechst (grey) in normoxic (top row), OGlucD (bottom row) in the vehicle (left column), IL6-treated (middle column), and Stattic-treated (right column). Scale bar 50 µm. (**B)** PKM2 nuclear translocation. (**C)** Schematic view of STAT3-PKM2-HIF crosstalk in astrocytes. STAT3 signaling induces hif-1α transcription. In turn, after ischemia, HIF-1α forms a complex with HIF-1β, undergoes nuclear translocation and regulates downstream genes such as hypoxic response elements (HRE) and PKM2 expression. STAT3 signaling causes nuclear translocation of PKM2 dimers, which facilitates the activation of nuclear STAT3. STAT3, PKM and HIF crosstalk promote lactate-directed glycolysis, decreasing OXPHOS. (**D)** HRE-luciferase activity. HIF transcription activity is verified by HRE-dependent firefly luciferase expression normalized to renilla luciferase (relative light unit, RLU). Normalized difference (r.u.) with the normoxic vehicle (control) mean is shown as box plots (IQR, min-max). Significant changes with the control are noted as *, effects of hypoxia and treatments are shown with § and ø, correspondingly. *, §, ø p≤0.05/**, §§, øø p≤0.005/***, §§§, øøø p≤0.0005, as indicated by 2-way ANOVA and Tukey tests, PKM2 nuclear translocation-n=3, HIF-luciferase assay-n=4. ns, no significant difference with the control.

4.7 The impact of astrocytic signaling on glycogen mobilization

Astrocytes undergo glycogenesis to store the excess glucose in glycogen form. In response to various metabolic demands, astrocytes consume glycogen through glycogenolysis. Following experiments focus on the impact of STAT3 signaling on glycogen mobilization and the impact of glycogenolysis on astrocytic mitochondrial and reducing properties as well as synaptogenesis in co-cultured neurons. In this respect, in addition to induction/inhibition of astrocytic STAT3, glycogenolysis was inhibited in astrocytes using 10 µM glycogen phosphorylase (GP) inhibitor (Table 16). GP is necessary for releasing glucose-1-P from the glycogen branches in an energy-independent process (Whelan 2007; BiochenDen 2020).

4.7.1 OGlucD promotes while IL6 inhibits glycogen mobilization

Immunostainings and quantification of glycogen bodies in treated astrocytes (Figure 35, A and B) suggest that I) Glycogen bodies were significantly reduced in the vehicle and Stattic-treated OGlucD astrocytes compared to their respective normoxic group (OGlucD: 38±5%, Stattic-OGlucD: 50±5%). II) Normoxic IL6-treated astrocytes contained more glycogen bodies (15±7%) than vehicle and Stattic-treated astrocytes. III) Glycogen degradation was insignificant in IL6-treated OGlucD compared to vehicle-OGlucD and normoxic IL6 treated astroctyes. Nevertheless, IL6-OGlucD astrocytes contained significantly more glycogen bodies than vehicle-OGlucD astrocytes (22±7%). IV) GP inhibition reduced glycogen degradation in OGlucD astrocytes by 45±7% and Stattic-OGlucD astrocytes by 61±9%, denoting a successful inhibition of glycogenolysis. On the contrary, glycogen bodies did not alter after GP inhibition in IL6 treated astrocytes significantly.

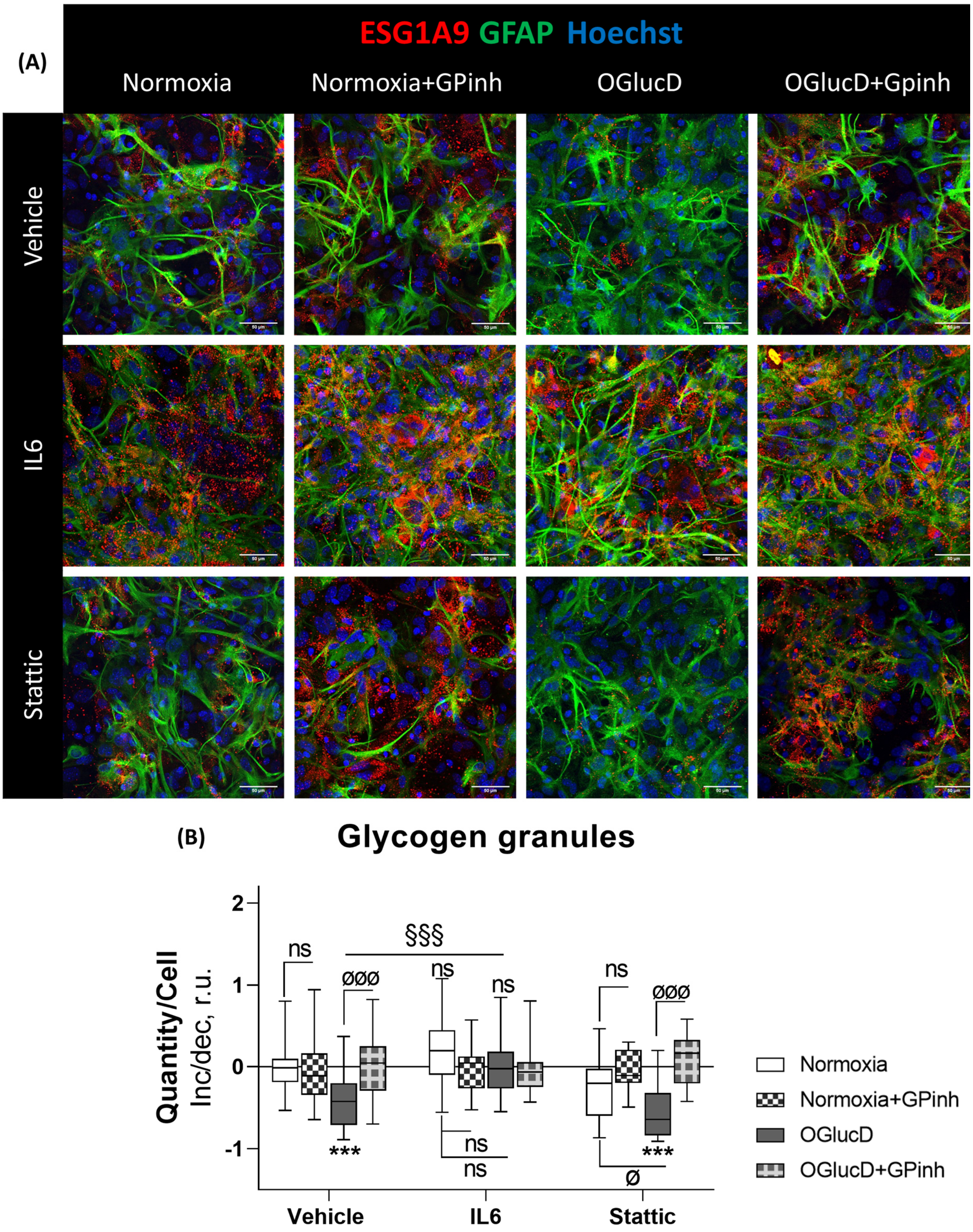

Figure 35: Glycogen mobilization in I/R astrocytes is inhibited by IL6

(A) Representative astrocyte immunostainings with ESG1A9 (red), GFAP (green) and Hoechst (blue) in the vehicle (top row), IL6-treated (middle row), and stattic-treated (bottom-row) in normoxia (first left column), glycogen phosphorylase inhibited (GPinh) normoxia (2nd left column), oxygen-glucose deprived (OGlucD, 3rd column) GPinh OGlucD astrocytes (right, 4th column). Scale bar 50 µm. (**B**) Astrocytic glycogen granules are normalized to nuclei (Hoechst staining). Normalized difference (r.u.) with the normoxic vehicle (control) mean is shown as box plots (IQR, min-max). Significant changes with the control are noted as *, effects of hypoxia and treatments are shown with § and ø, correspondingly. *, §, ø $p \leq 0.05$/**, §§, øø $p \leq 0.005$/***, §§§, øøø $p \leq 0.0005$, as indicated by 2-way ANOVA and Tukey tests, n=9. ns, no significant difference with the control.

4.7.2 GP inhibition abolishes OXPHOS in Stattic-inhibited I/R astrocytes

OXPHOS was reduced significantly in GP-inhibited (GPinh) Stattic-OGlucD astrocytes in both basal (62±12%) and ATP-linked (93±18%) levels (Figure 36, F and G). However, GP inhibition reduced vehicle-OGlucD astrocytes' respiration insignificantly, while it did not affect the OXPHOS in IL6-OGlucD astrocytes. Spare respiratory capacity was not triggered by GP inhibition (Figure 36, H).

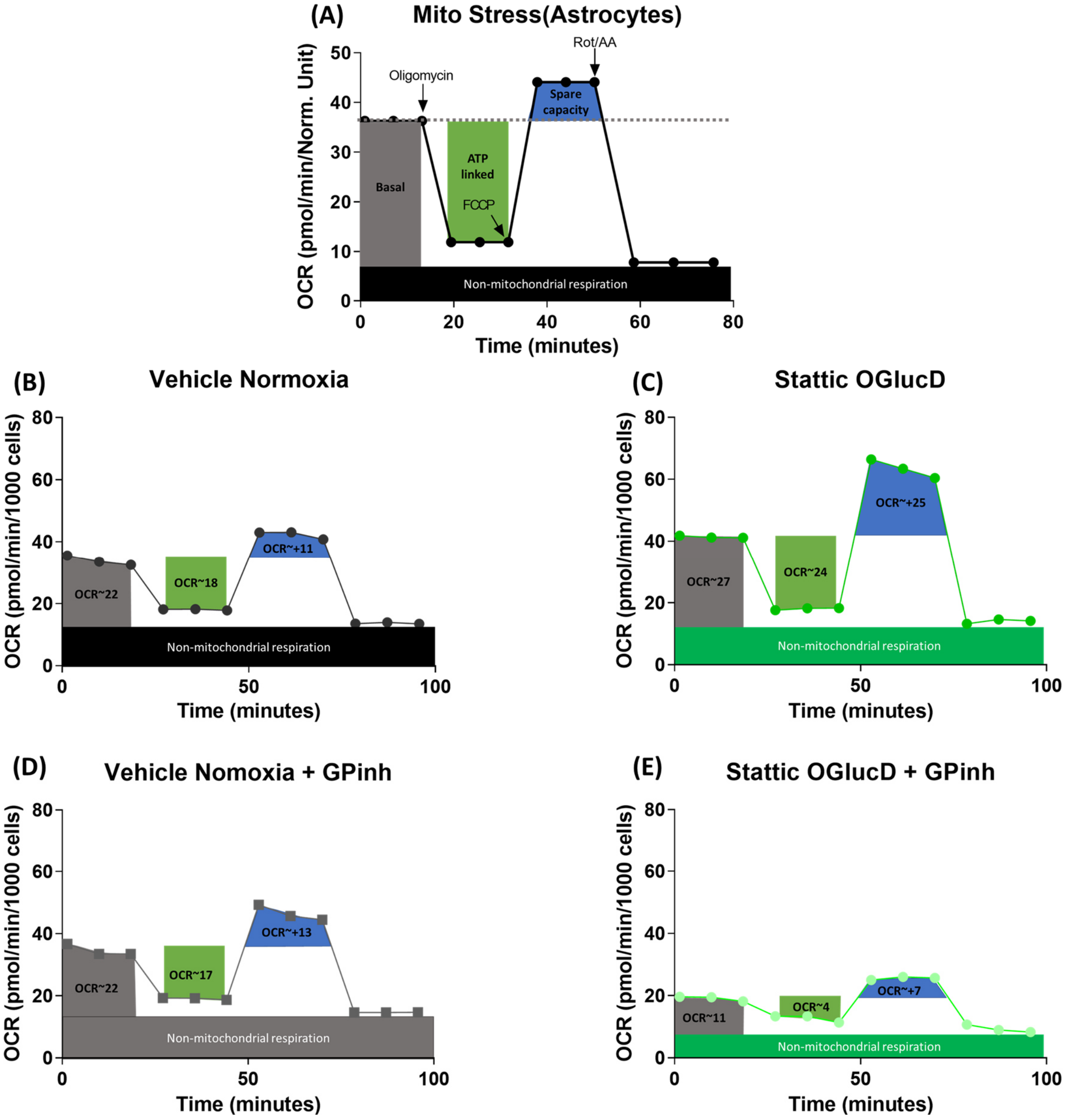

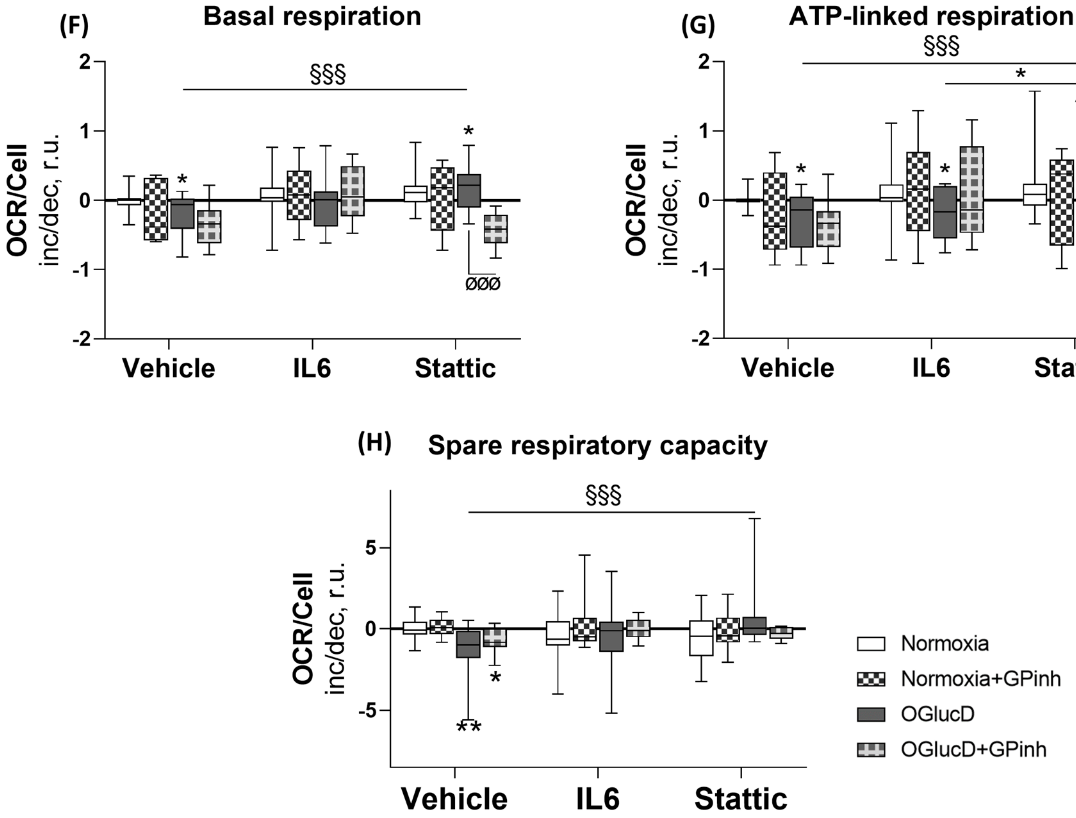

Figure 36: GP inhibition abolishes the OXPHOS in Stattic-OGlucD astrocytes

(A) Explanatory Seahorse mito stress assay (MSA) indicating basal OCR (grey column), ATP-linked OCR (green columns), spare respiratory (blue columns) and non-mitochondrial respiration (black boxes) in the **(B, black)** vehicle normoxic, **(C, green)** Stattic-OGlucD, **(D, grey)** vehicle normoxic incubated with 10 µM glycogen phosphorylase inhibitor **(GPinh)** and **(E, light green)** Stattic-OGlucD incubated with GP inhibitor**. (F)** Basal respiration **(G),** ATP-linked respiration and **(H)** spare respiratory capacity. All obtained values were normalized to the cell number (Hoechst staining) and normalized difference (r.u.) with the normoxic vehicle (control) mean is shown as box plots (IQR, min-max). Significant changes with the control are noted as *, effects of hypoxia and treatments are shown with §. *, § $p \leq 0.05$/**, §§ $p \leq 0.005$/***, §§§ $p \leq 0.0005$, as indicated by 3-way ANOVA and Tukey tests, n=8. ns, no significant difference with the control.

4.7.3 GP inhibition decreases astrocytic reducing capacity

Reducing tetrazolium (MTT) to purple formazan is a practical approach to measure the cellular reducing capacity in eukaryotic cells (Muraina, Suleiman, and Eloff 2009). MTT is reduced in both extramitochondrial compartments and mitochondrial ETC (Berridge and Tan 1993), involving several enzymes and reductants, namely, NADH, NADPH, and Succinate (Berridge and Tan 1993). This experiment focused on the capacity of astrocytes to reduce MTT after STAT3 induction/inhibition, I/R and GP inhibition.

Based on obtained data, the astrocytic reducing potential was decreased in I/R astrocytes regardless of STAT3-PKM2-HIF signaling (Vehicle-OGlucD 20±3%, IL6-OGlucD: 24±6% and Stattic-OGlucD: 17±5%).

Gp inhibition decreased astrocytic reducing ability in the vehicle and Stattic normoxic treated astrocytes by 20±3% and 13±6% as well as the vehicle and Stattic-OGlucD astrocytes (42±4% and 20±4%, respectively).

IL6 decreased astrocytic reducing potential by 7±2% in normoxic astrocytes, while the additional GPinh did not alter the response. Astrocytic ability to reduce MTT remained low in IL6-OGlucD astrocytes and Gp inhibition worsened the effect insignificantly.

No distinct difference was observed between vehicle and Stattic-treated normoxic astrocytes (Figure 37, B).

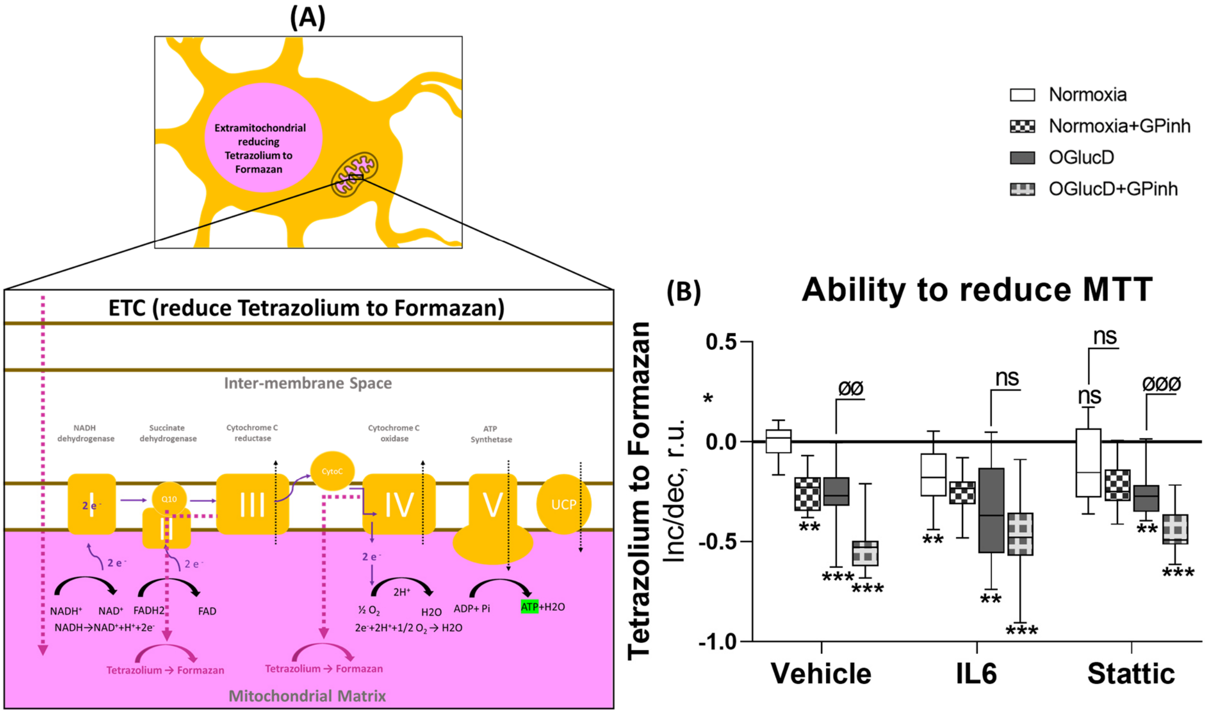

Figure 37: GP inhibition decreases the astrocytic ability to reduce MTT

(A) schematic view of cellular ability to reduce tetrazolium to formazan. Reducing process occurs in extramitochondrial compartments (top) and mitochondrial ETC. Within mitochondria, tetrazolium is reduced by electron transfer from cytochrome C to complex IV and to a lesser extent in succinate dehydrogenase (complex II) (Berridge and Tan 1993). **(B)** Whole-cell MTT colorimetric assay. Normalized difference (r.u.) with the normoxic vehicle (control) mean is shown as box plots (IQR, min-max). Significant changes with the control are noted as *, effects of hypoxia and treatments are shown with ø. *, ø $p \leq 0.05$/**, øø $p \leq 0.005$/***, øøø $p \leq 0.0005$, as indicated by 3-way ANOVA and Tukey tests, n=14. ns, no significant difference with the control.

4.7.4 GP-inhibited astrocytes fail to support synaptogenesis in co-cultured neurons

This study addressed synaptic density in neurons co-cultured with GP-inhibited STAT3-induced/inhibited I/R astrocytes (Table 16). Data from VGLUT1 and PSD 95 colocalized area (Figure 38) suggested that synaptic density is decreased in neurons co-cultured with with OGlucD astrocytes regardless of STAT3-PKM2-HIF signaling (vehicle-OGlucD: 28±3%, IL6-OGlucD: 22±6% and Stattic-OGlucD: 84±13%). In addition, the synaptic density of neurons co-cultured with GP inhibited normoxic Stattic-treated astrocytes was decreased dramatically by 55±9% compared with their non-Gp inhibited counterparts. These data show that astrocytic glycogen mobilization was crucial for synapse formation in co-cultured neurons.

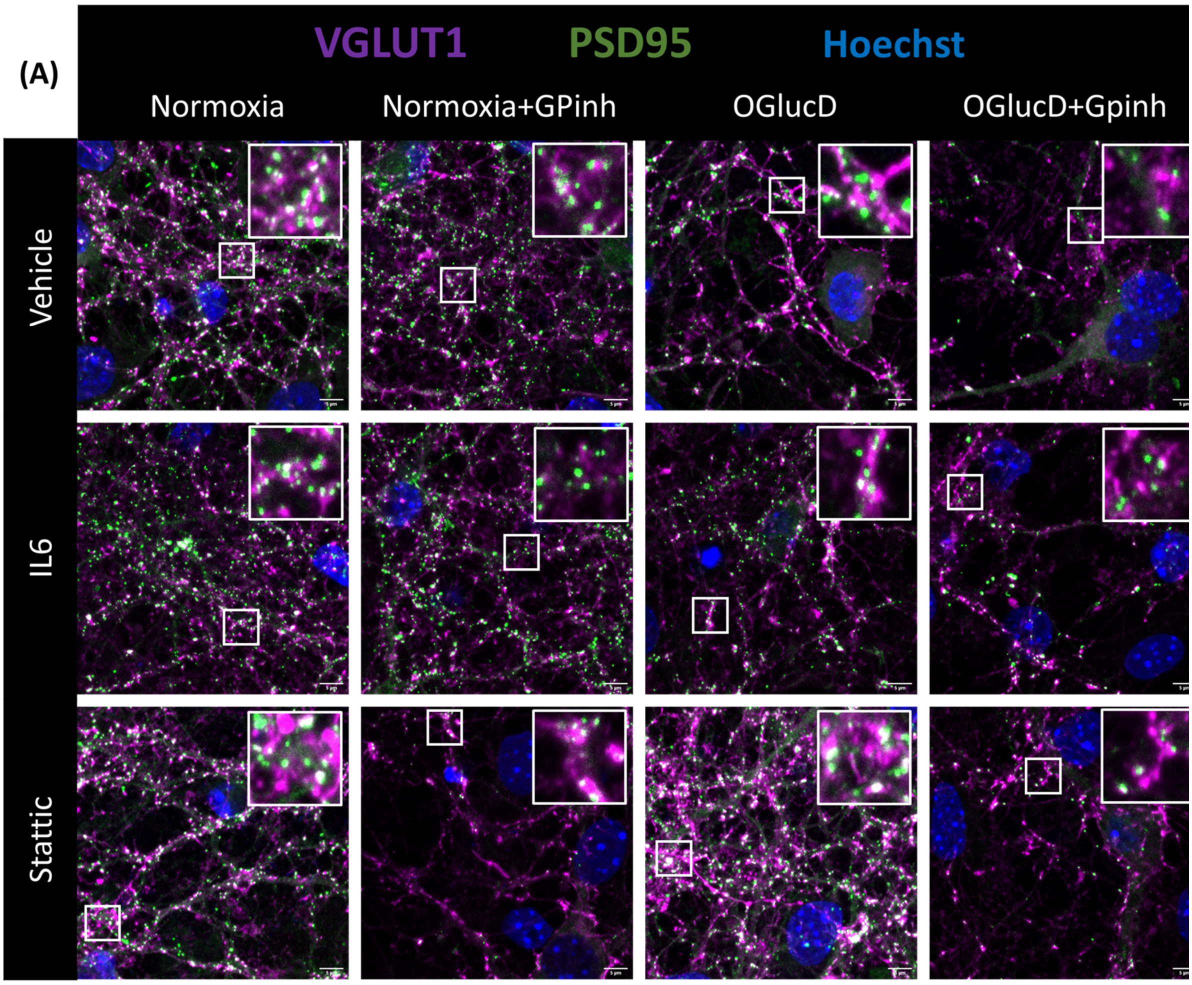

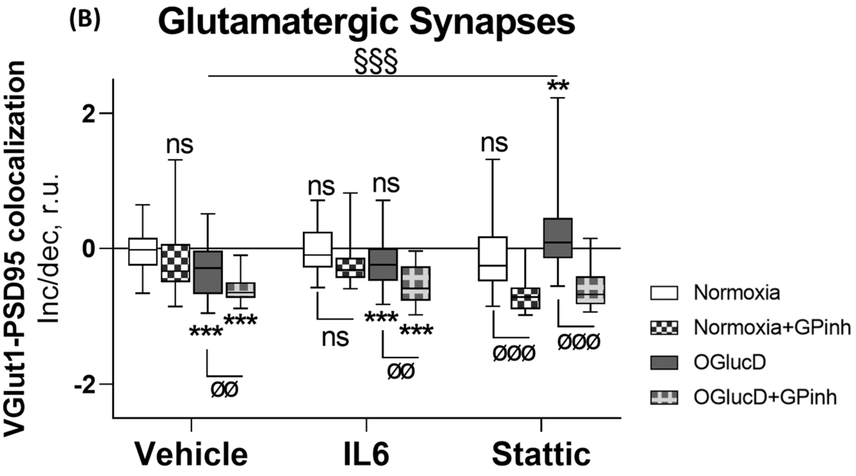

Figure 38: GP inhibited astrocytes fail to support neuronal synaptogenesis

(A) Representative neuron immunostainings of VGLUT1 (purple), PSD95 (green) and Hoechst (blue) co-cultured with vehicle (top row) IL6-treated (middle row) and stattic-treated (bottom-row) normoxic (left first column), Glycogen phosphorylase inhibited (GPinh) normoxic (2nd column), oxygen-glucose deprived (OGlucD, 3rd column) GPinh OGlucD astrocytes (right, 4th column). Cropped white boxes represent random zoomed areas. Scale bar 5 µm. **B)** Colocalization of pre-post synaptic markers (VGLU1-PSD95). Normalized difference (r.u.) with the normoxic vehicle (control) mean is shown as box plots (IQR, min-max). Significant changes with the control are noted as *, effects of hypoxia and treatments are shown with § and ø, correspondingly. *, §, ø p≤0.05/**, §§, øø p≤0.005/***, §§§, øøø p≤0.0005, as indicated by 3-way ANOVA and Tukey tests, n=10. ns, no significant difference with the control.

4.8 STAT3 regulates the metabolism of starved astrocytes

Our previous observation in this study indicated a discrepancy in STAT3 signaling and metabolic response in OGlnD and OGlucD astrocytes. Since hypoxia is a constant factor in both conditions, we postulated that this divergence is due to the different metabolic paths for glucose or glutamine in astrocytes. Therefore, astrocytes' STAT3 signaling, and metabolic properties were investigated in glucose or glutamine deprived (GlucD and GlnD) astrocytes.

4.8.1 GlucD astrocytes activate STAT3 signaling

STAT3 nuclear translocation and transcription activity (SRE/SIE- dual luciferase activity) was evaluated as described in section 4.2. STAT3 nuclear translocation (Figure 39, A and B) was increased in GlnD and GlucD by 21±1% and 19±1%, respectively. However, SIE-luciferase activity was only upregulated in GlucD astrocytes by 143±28% (Figure 39, C). GFAP immunoblots indicate a slight increase in astrocytic reactivity in GlucD astrocytes by 13±21% (Figure 39, D and E).

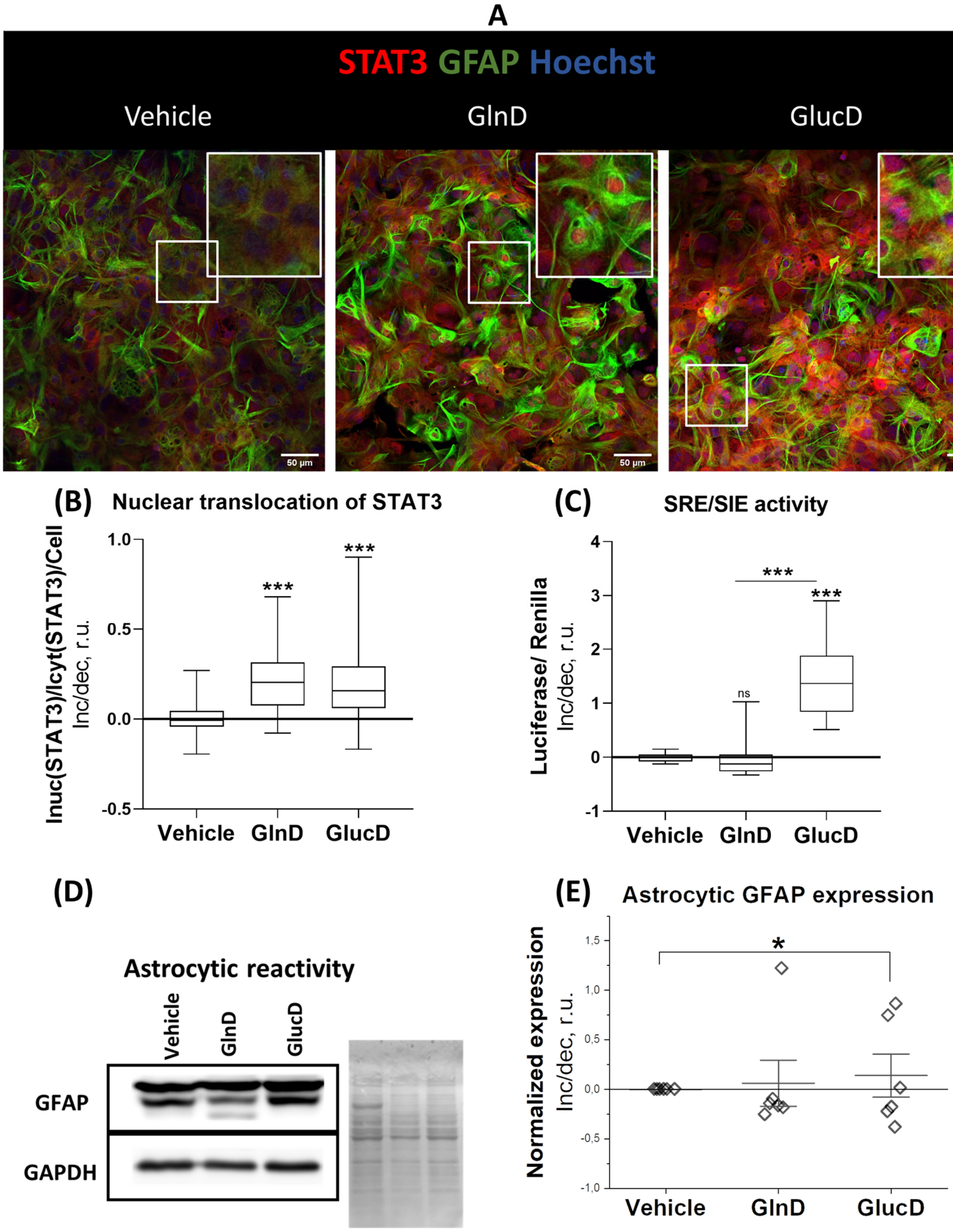

Figure 39: STAT3 signaling in GlucD reactive astrocytes

(A) Representative astrocyte immunostainings with STAT3 (red), GFAP (green) and Hoechst (blue) in the vehicle (left), glutamine-deprived (GlnD, middle) and glucose-deprived (GlucD, right) conditions. Cropped white boxes represent random zoomed areas. Scale bar 50 µm. **(B)** STAT3 nuclear translocation. **(C)** SRE/SIE luciferase activity. **(D)** Astrocytic reactivity. Representative immunoblots for GFAP (above), GAPDH (middle) and the total protein input (Ponceau, bottom) **E)** GFAP protein intensity normalized to total protein input. Normalized difference (r.u.) with the normoxic vehicle (control) mean is shown as box plots (IQR, min-max). Significant changes with the control are noted as *. * $p \leq 0.05$/** $p \leq 0.005$/*** $p \leq 0.0005$, as indicated by one-way ANOVA and Tukey tests, STAT3 nuclear translocation-n=9, SRE/SIE-luciferase assay-n=3, GFAP-blots-n=3. ns, no significant difference with the control.

4.8.2 STAT3/PKM2 nuclear colocalization in nutrient-depleted astrocytes

Immunostainings showed that both STAT3 and PKM2 colocalized in nuclei of GlnD and GlucD astrocytes (Figure 40, A) and a significant increase in the PKM2 nuclear translocation was observable in both GlnD (59±9%) and GlucD (52±7%) astrocytes (Figure 40, B).

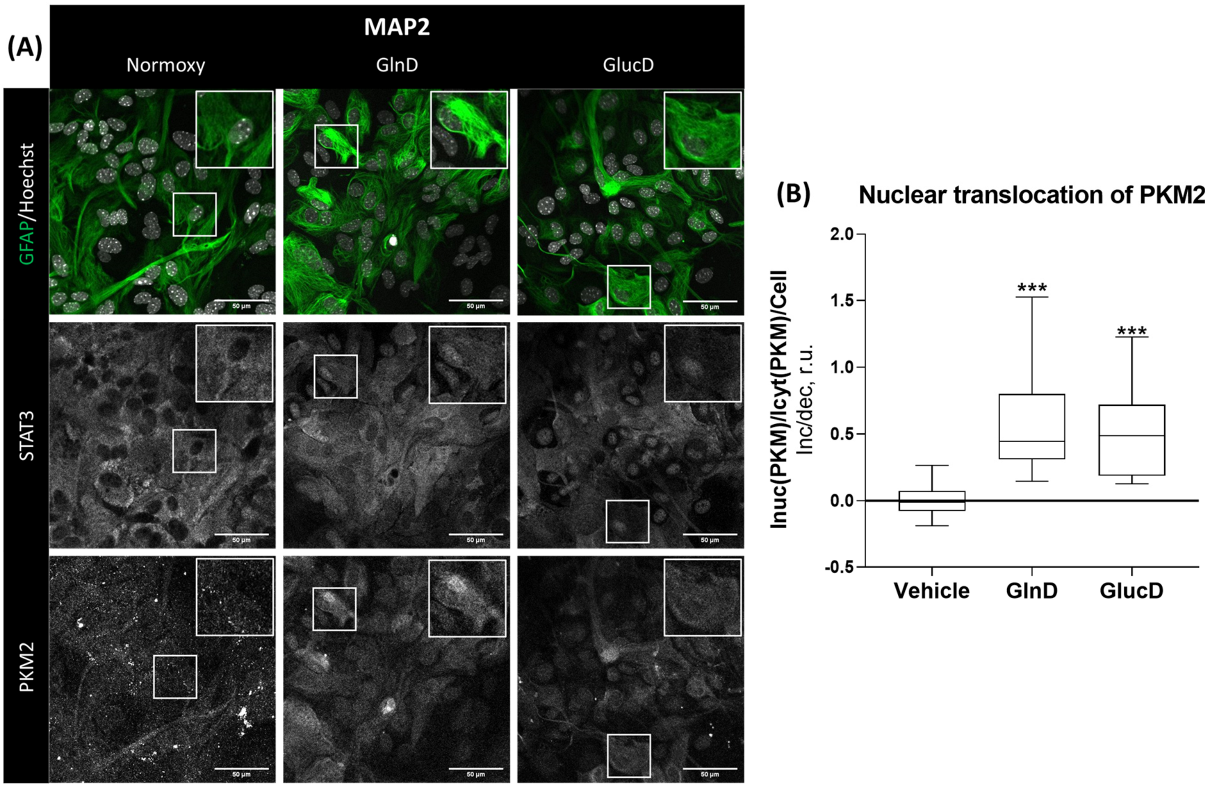

Figure 40: Nuclear colocalization of STAT3/PKM2 in GlnD and GlucD astrocytes

(A) Representative astrocyte immunostainings with GFAP (green) and Hoechst (top), STAT3 (middle) and PKM2 (bottom) in the vehicle (left), glutamine-deprived (GlnD, middle) and glucose-deprived (GlucD, bottom) astrocytes. Cropped white boxes represent similar ROIs in each immunostaining. Scale bar 50 µm. **(B)** PKM2 nuclear translocation**.** Normalized difference (r.u.) with the normoxic vehicle (control) mean is shown as box plots (IQR, min-max). Significant changes with the control are noted as *. * $p \leq 0.05$/** $p \leq 0.005$/*** $p \leq 0.0005$, as indicated by one-way ANOVA and Tukey tests, STAT3 nuclear translocation-n=3. ns, no significant difference with the control.

4.8.3 GlnD and GlucD astrocytes follow different glycolytic paths

Seahorse GRA data revealed that only GlnD astrocytes increase lactate-directed glycolysis significantly (12±5%) and released L-lactate to the conditioned medium equally as the vehicle group (Figure 41, D and E). On the other hand, according to the Seahorse GRA data, lactate-directed glycolysis was not changed in GlucD astrocytes, while L-lactate concentration was reduced in the conditioned medium of GlucD astrocytes significantly (compared to vehicle: 23±4%, compared to GlnD: 27±6%). Nevertheless, conditioned medium of GlucD astrocytes contained significant amount of lactate in comparison to astrocyte's culture medium (110±10%, mean±s.e.m.) (Figure 41D and F).

Mitochondria-directed glycolysis was increased in GlnD astrocytes by 11±4% and in GlucD astrocytes by 36±4%, with a significant increase in GlucD astrocytes (25±6%) (Figure 41, F).

Non-glycolytic (post-2-DG) acidification was also increased by 39±7% in GlucD astrocytes, while it was reduced by 25±6% in GlnD astrocytes (Figure 32, G).

This study indicated that GlnD astrocytes increased glycolysis to generate lactate and support mitochondrial respiration equally (Lactate-directed glycolysis: 12±5%, mitochondria-directed glycolysis: 11±4%). Therefore, GlnD astrocytes demonstrated neither glycolytic nor oxidative profile as the mitoOCR/glycoPER suggested (decline:17±12%, p-value: 0.18, Figure 41K).

In contrast, the prevalent glycolytic path in GlucD astrocytes was mitochondria-directed glycolysis with a 36±4% increase (P-value: 0.0000006) compared to the vehicle and a 25±6% increase in compared to GlnD astrocytes. Furthermore, higher mitochondria-directed glycolysis facilitated higher OXPHOS in GlucD than GlnD astrocytes as mitoOCR/glycoPER suggested (14±14%, mean±s.e.m.) (Figure 41, K).

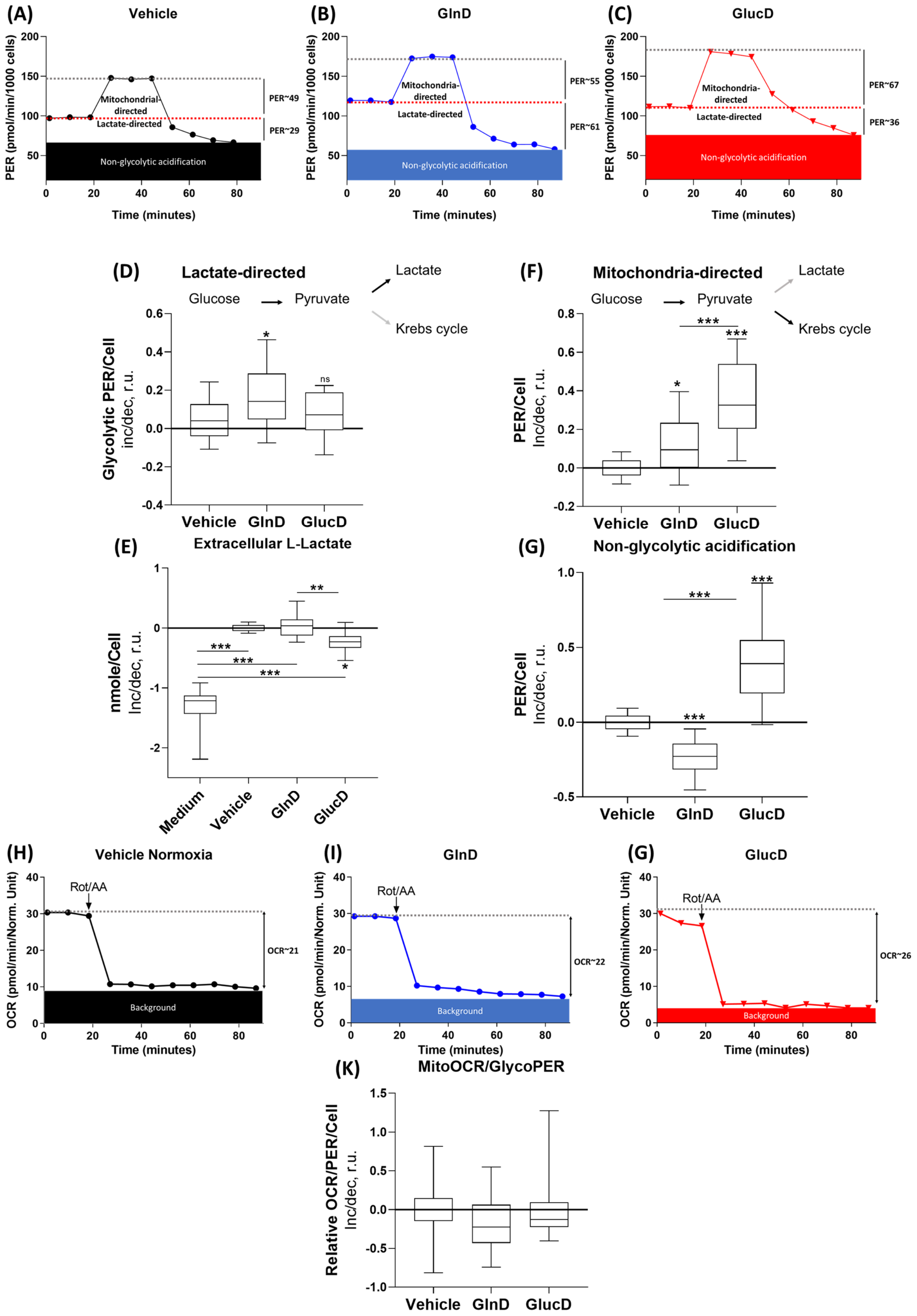

Figure 41: GlnD and GlucD astrocytes follow different glycolytic paths

(**A, B and C)** Representative Seahorse glycolytic rate assay (GRA) comprising lactate-directed glycolysis, mitochondria-directed glycolysis, and non-glycolytic acidification in vehicle (black), GlnD (blue), GlucD (red) astrocytes. **(D)** Lactate-directed glycolysis (glycoPER) **(E)** L-lactate in astrocytic CM measured via ELISA. **(F)** Mitochondria-directed glycolysis measured using GRA. **(G)** Non-glycolytic (Post-2-DG) acidification measured using GRA. (**H, I and J)** Representative simultaneous OCR for Vehicle (Black), GlnD (blue) and GlucD (red) astrocytes. **(K)** Ratio of mitochondrial OCR (MitoOCR) to the lactate-directed glycolysis (mitoOCR/glycoPER). All obtained values are normalized to the cell number (Hoechst staining). Normalized difference (r.u.) with the normoxic vehicle (control) mean is shown as box plots (IQR, min-max). Significant changes with the control are noted as *. * p≤0.05/** p≤0.005/*** p≤0.0005, as indicated by one-way ANOVA and Tukey tests, n=7. ns, no significant difference with the control.

4.8.4 Mitochondrial OXPHOS is increased in GlucD astrocytes

Seahorse MSA revealed that GlucD astrocytes had significantly higher basal and ATP-linked respiration compared to vehicle (basal: 35±9%, ATP-linked: 42±9%) and GlnD astrocytes (Basal: 28±11%, ATP-linked: 39±10%) (Figure 42, E and F). Spare respiratory capacity, which indicates the cellular potential to regain the mitochondrial membrane polarity to reduce oxygen at ETC complex IV was decreased in both GlnD and GlucD astrocytes by 164±67% and 211±67% respectively (Figure 42, G). This effect can be linked to glycogen voidance by the end of MSA (See section 4.8.7).

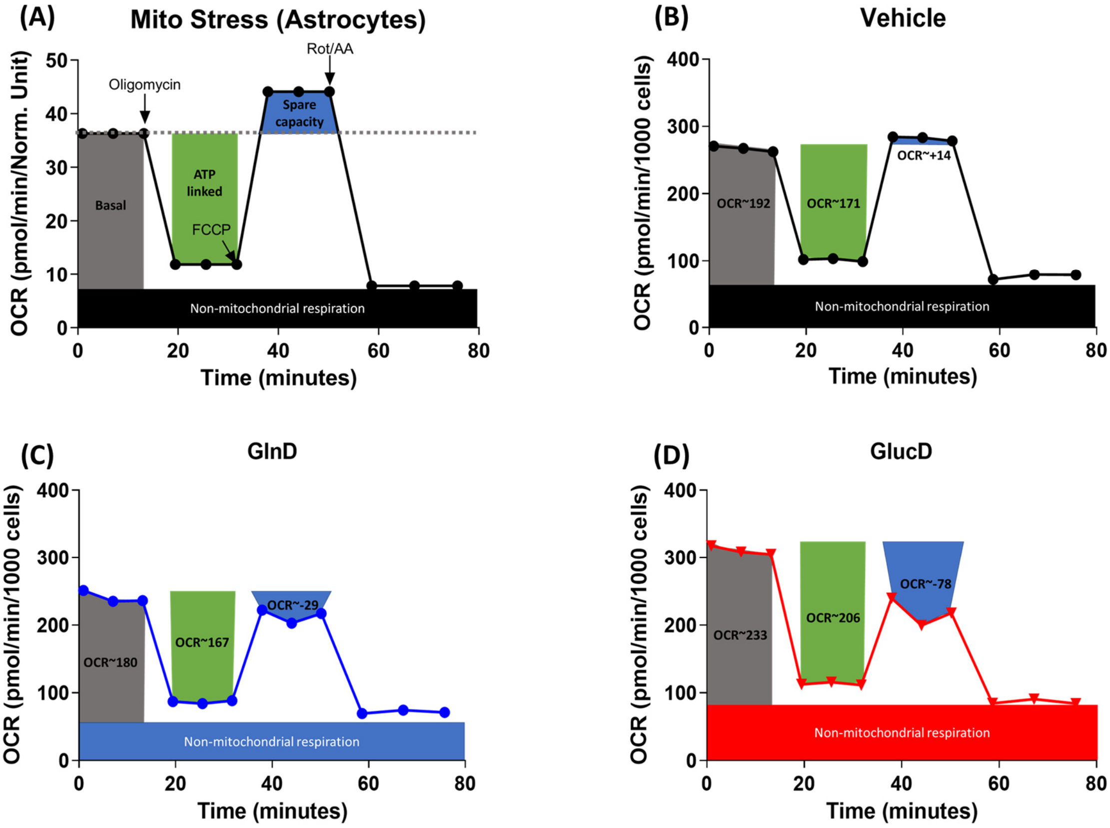

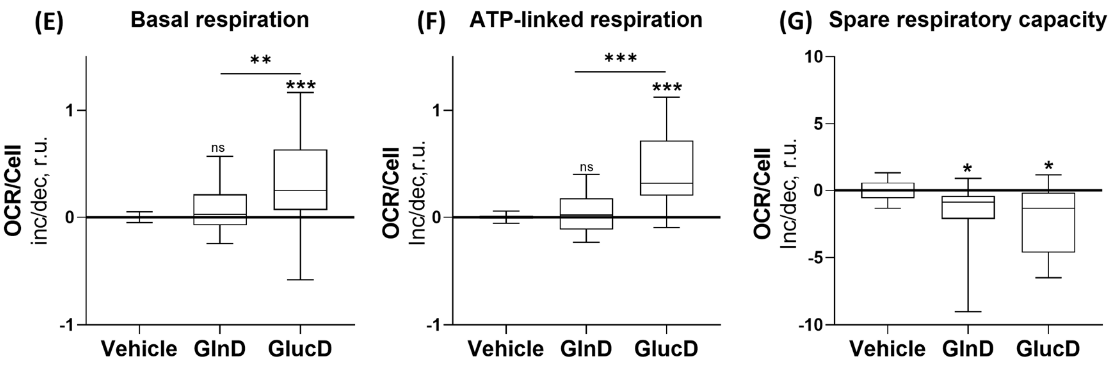

Figure 42: Mitochondrial OXPHOS is increased in GlucD astrocytes

(A) Explanatory Seahorse mito stress assay (MSA) indicating basal OCR (grey column), ATP-linked OCR (green columns), Spare respiratory (blue columns) and non-mitochondrial respiration (black boxes) in the **(B, black)** vehicle, **(C, blue)** GlnD and **(D, red)** GlucD astrocytes. **(E)** Basal respiration, **(F)** ATP-linked respiration and **(F)** spare respiratory capacity. Normalized difference (r.u.) with the normoxic vehicle (control) mean is shown as box plots (IQR, min-max). Significant changes with the control are noted as *. * $p \leq 0.05$/** $p \leq 0.005$/*** $p \leq 0.0005$, as indicated by one-way ANOVA and Tukey tests, n=5. ns, no significant difference with the control.

4.8.5 MMP is not affected by nutrient deprivation

MMP remained unchanged in GlnD and GlucD astrocytes (Figure 43, A and B), Nevertheless, GlucD astrocytes' mitochondria appeared fragmented in TMRM staining (Figure 43, C).

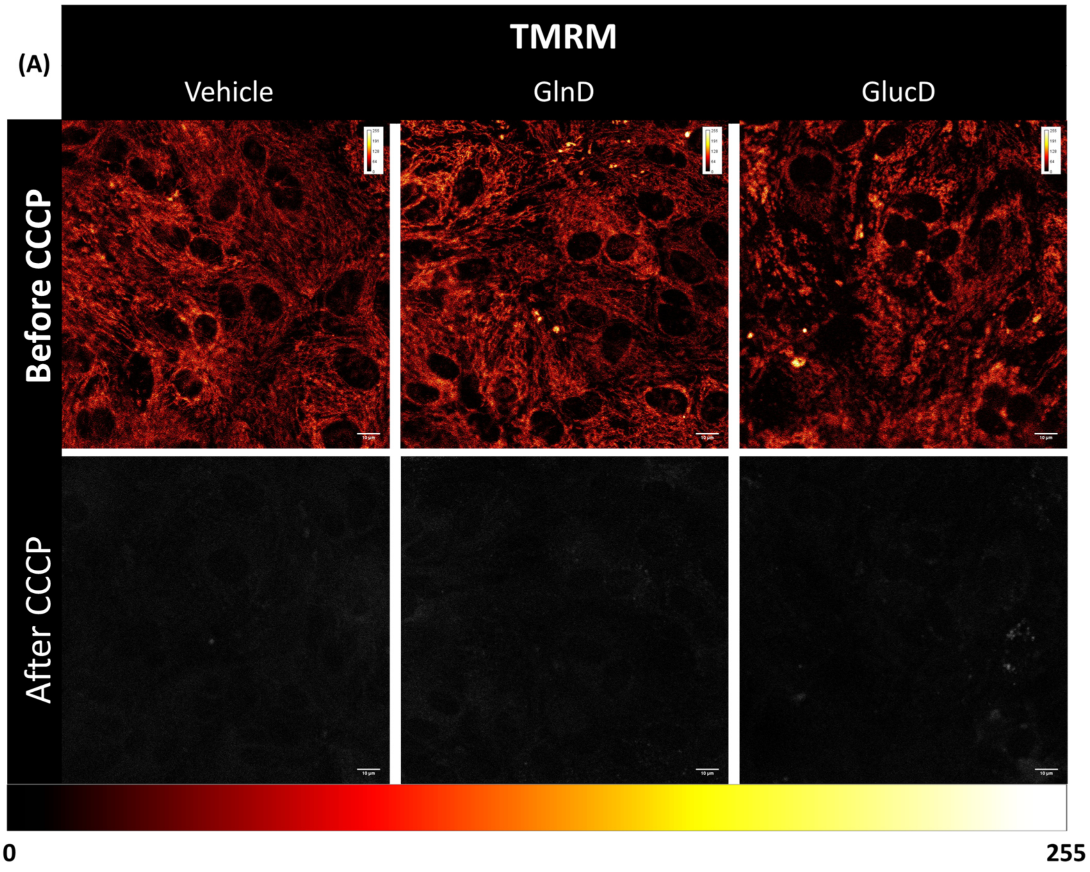

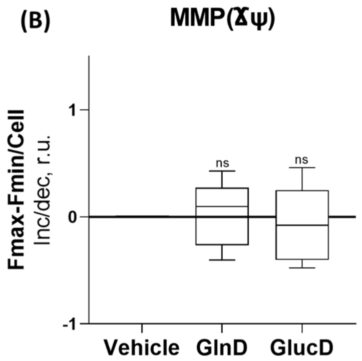

Figure 43: Unchanged MMP in GlnD/GlucD astrocytes

(A) Representative astrocytic TMRM staining in the vehicle (left), GlnD (middle) and GlucD astrocytes (right) before injection of the 5 µM uncoupler CCCP (top) and after (bottom). **(B)** Astrocytic MMP (Ɣψ). Ɣψ is calculated by subtracting the minimum TMRM fluorescent intensity after CCCP injection (Fmin) from maximum intensity prior to CCCP injection (Fmax), TMRM fluorescent intensity is normalized to the cell number in each field of view. Normalized difference (r.u.) with the normoxic vehicle (control) mean is shown as box plots (IQR, min-max). Significant changes with the control are noted as *. * p≤0.05/** p≤0.005/*** p≤0.0005, as indicated by one-way ANOVA and Tukey tests, n=6. ns, no significant difference with the control.

4.8.6 Higher Mito SOX in GlnD/GlucD and lower reducing capacity in GlucD astrocytes

Based on the normalized fluorescent intensity of the Mito SOX, mitochondrial superoxide was increased significantly in both GlnD and GlucD astrocytes by 311±48% and 140±23% respectively, while the effect was significantly higher in GlnD astrocytes (166±52%) (Figure 44, A and B). On the other hand, astrocytic ability to reduce MTT was dramatically decreased in GlucD astrocytes (79±2%) while it was not affected in GlnD astrocytes (Figure 44, C).

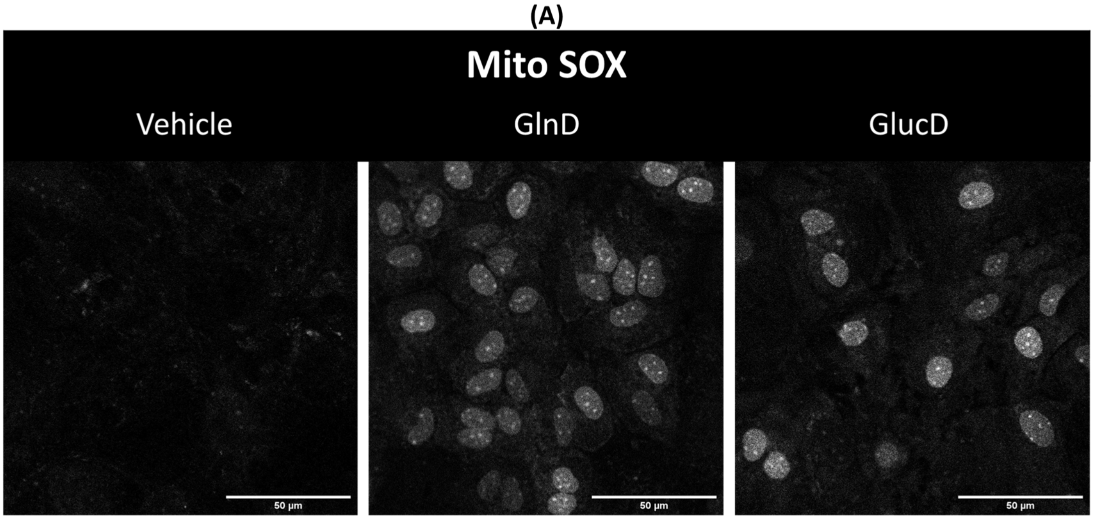

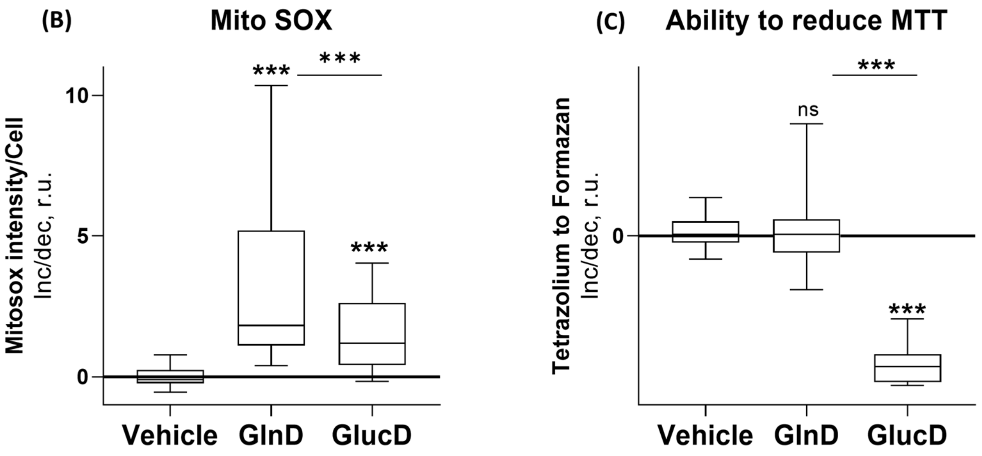

Figure 44: Higher Mito SOX in nutrient-deprived and lower reducing capacity in GlucD astrocytes

(A) Representative images of Mito SOX (grey) in the vehicle (left), GlnD (middle) and GlucD (right) astrocytes. Scale bars: 50 µm**. (B)** Astrocytic Mito SOX normalized to the cell number (Hoechst). **(C)** whole-cell MTT. Normalized difference (r.u.) with the normoxic vehicle (control) mean is shown as box plots (IQR, min-max). Significant changes with the control are noted as *. * p≤0.05/** p≤0.005/*** p≤0.0005, as indicated by one-way ANOVA and Tukey tests, n=5. ns, no significant difference with the control.

4.8.7 Both GlnD and GlucD astrocytes undergo glycogenolysis

Glycogen bodies quantification revealed that both GlnD and GlucD astrocytes had significantly fewer glycogen granules compared to the vehicle (GlnD: 47±5%, GlucD: 86±4%) with significantly fewer granules in GlucD astrocytes compared to GlnD astrocytes (38±5%) (Figure 45, A and B).

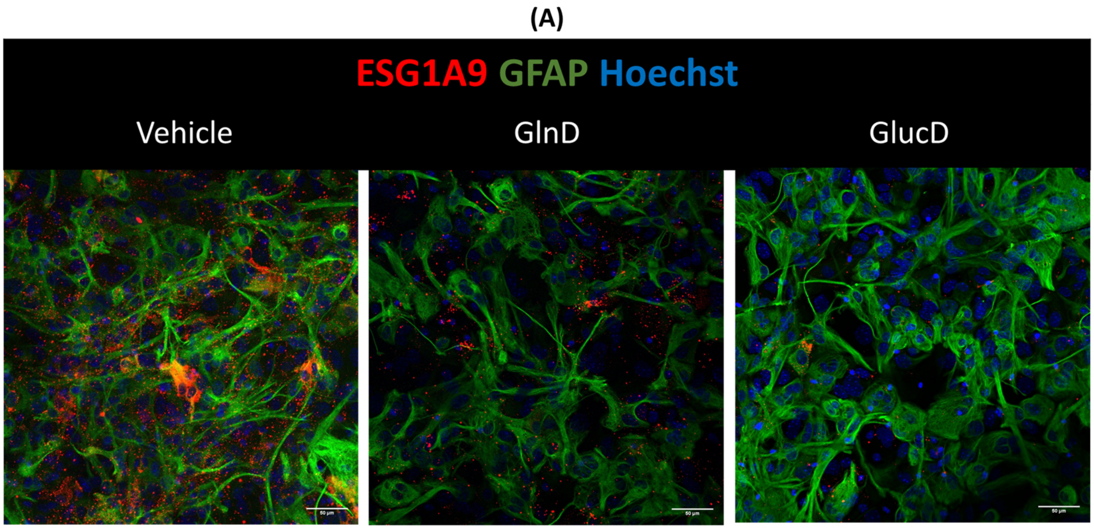

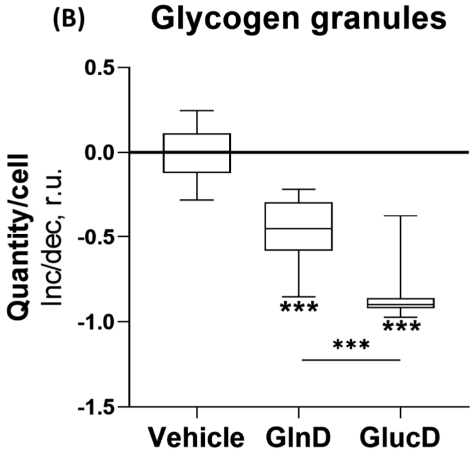

Figure 45: Decreased glycogen granules in GlnD/GlucD-deprived astrocytes

A) Representative astrocytes immunostaining with ESG1A9 (red), GFAP (green) and Hoechst (blue) in vehicle (left) GlnD (middle) and GlucD (right). Scale bar 50 µm. **B)** Glycogen granules are normalized to the nuclei number (Hoechst) in each field of view. Normalized difference (r.u.) with the normoxic vehicle (control) mean is shown as box plots (IQR, min-max). Significant changes with the control are noted as *. * p≤0.05/** p≤0.005/*** p≤0.0005, as indicated by one-way ANOVA and Tukey test, n=4. ns, no significant difference with the control.

4.8.8 GlnD astrocytes fail to support neuronal OXPHOS

MSA in neurons co-cultured with GlnD/GlucD astrocytes suggests a significantly lower mitochondrial respiration in Basal (16±5%) and ATP-linked (21±6%) respiration and spare respiratory capacity (60±14%) (Figure 46, E, F, G). On the contrary, mitochondrial respiration was not affected in neurons co-cultured with the GlucD astrocytes (Figure 46).

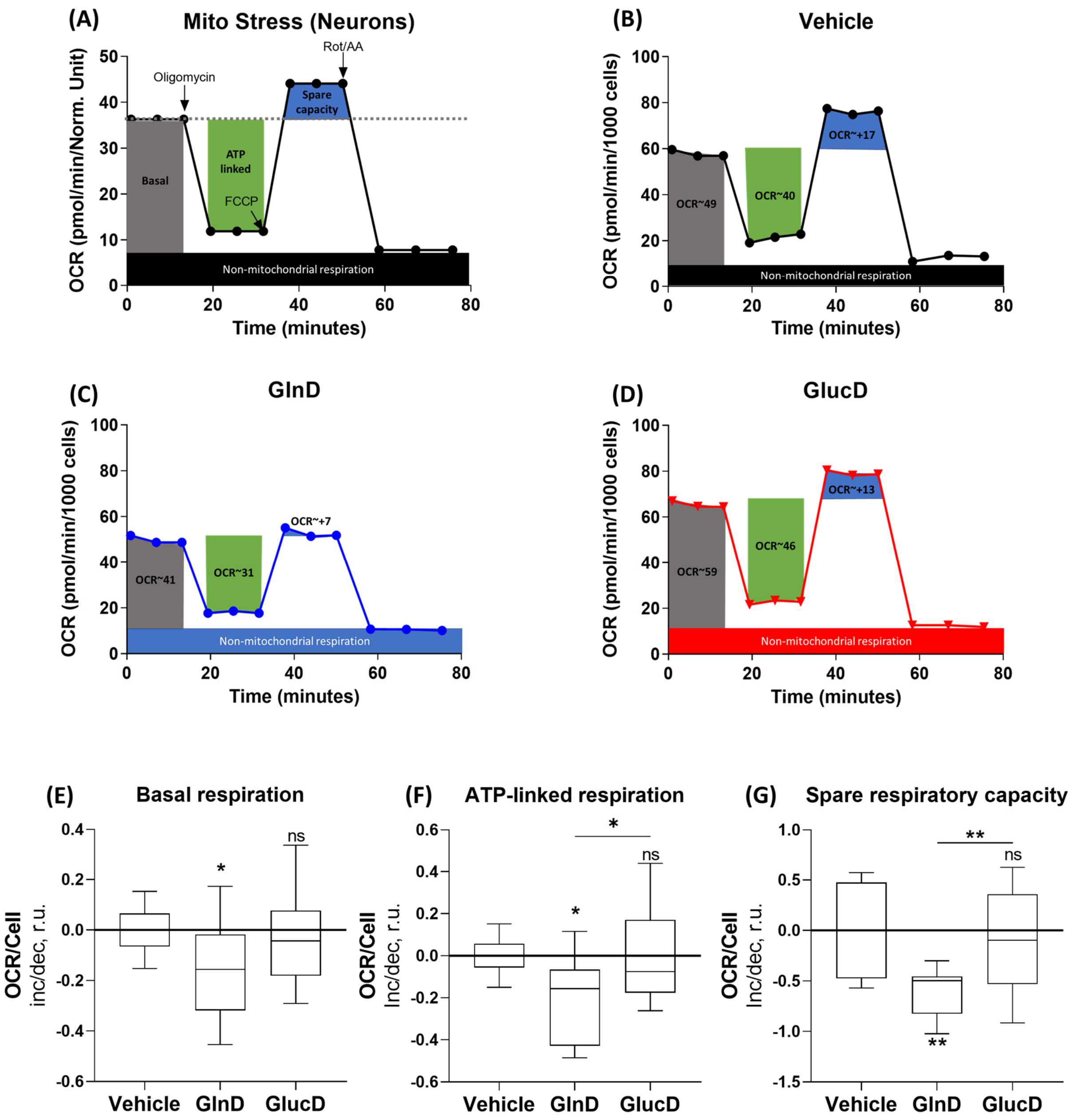

Figure 46: GlnD astrocytes fail to support neuronal OXPHOS

(A) Explanatory Seahorse mito stress assay (MSA) indicating basal OCR (grey column), ATP-linked OCR (green columns), spare respiratory (blue columns) and non-mitochondrial respiration (black boxes) in neurons co-cultured with the **(B, black)** vehicle, **(C, blue)** GlnD and **(D, red)** GlucD. **(E)** Basal respiration, **(F)** ATP-linked respiration and **(G)** spare respiratory capacity. All obtained values were normalized to the cell number (Hoechst staining) and normalized difference (r.u.) with the normoxic vehicle (control) mean is shown as box plots (IQR, min-max). Significant changes with the control are noted as *. * p≤0.05/** p≤0.005/*** p≤0.0005, as indicated by one-way ANOVA and Tukey tests, n=5. ns, no significant difference with the control.

4.8.9 GlnD astrocytes fail to support the neuronal synaptogenesis

Synaptic and neurite density in neurons co-cultured with GlnD and GlucD showed no difference in neurite density (Figure 47, C and D). However, significantly fewer synapses were observable in neurons co-cultured with GlnD astrocytes compared to the vehicle (21±6%) and GlucD astrocytes (32±10%). In contrast, neurons co-cultured with GlucD astrocytes increased synaptic density insignificantly (10±9%, p-value: 0.2) (Figure 47, C and D)

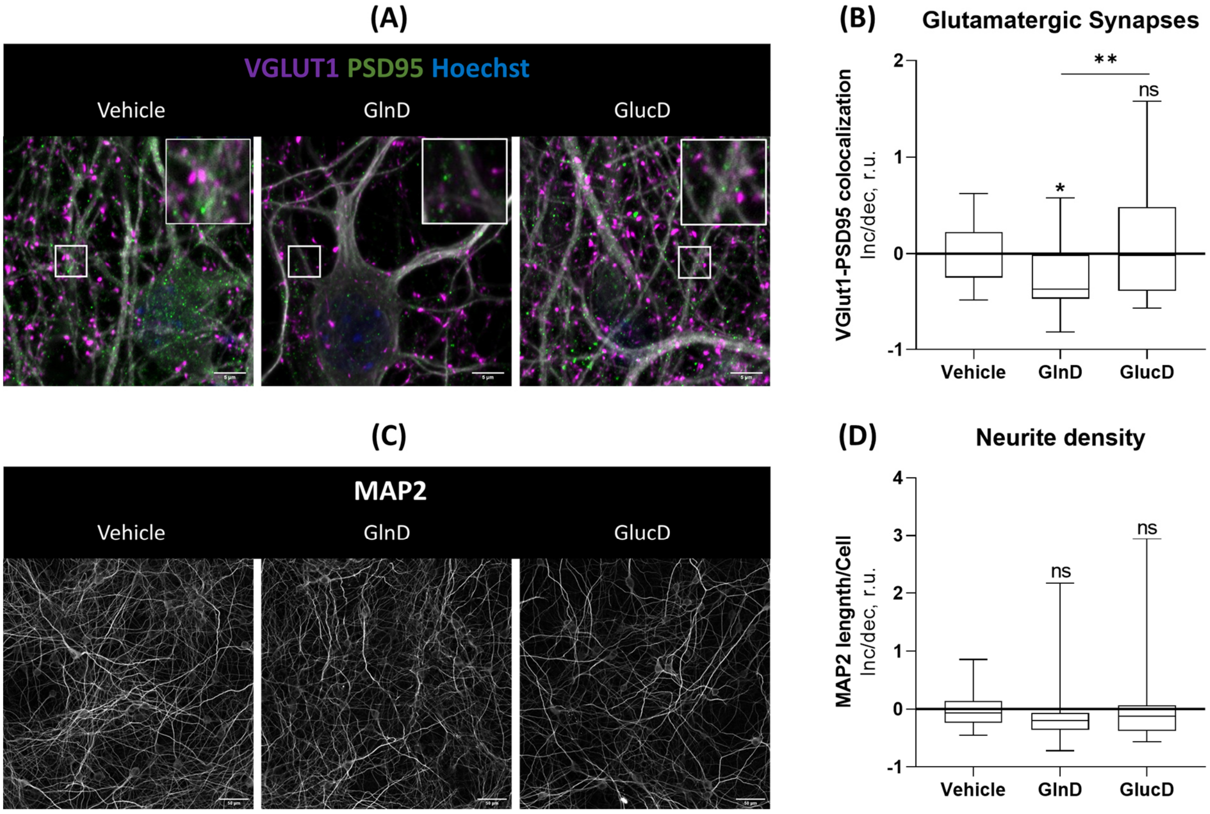

Figure 47: GlnD astrocytes fail to support neuronal synaptogenesis

A) Representative immunostainings of neurons with VGLUT1 (purple), PSD95 (green), MAP2 (grey) and Hoechst (blue), co-cultured with vehicle (left), GlnD (middle) and GlucD (right) astrocytes. The cropped white boxes represent random zoomed areas. Scale bar 5 µm. **B)** Colocalization of pre-post synaptic markers (VGLU1-PSD95). **C)** Representative immunostainings of neurons with MAP2 (grey) co-cultured with vehicle (left), GlnD (middle) and GlucD(right) astrocytes. Scale bars: 50 µm. **D)** Neurite density. followed by Tukey tests. Normalized difference (r.u.) with the normoxic vehicle (control) mean is shown as box plots (IQR, min-max). Significant changes with the control are noted as *. * p≤0.05/** p≤0.005/*** p≤0.0005, as indicated by one-way ANOVA and Tukey tests, n=5. ns, no significant difference with the control.

5 Discussion

The intention to rescue the ischemic brain is a paramount aim of medical and neurological treatments, which has encouraged scientists to develop tissue/cell-targeted therapies. Furthermore, emerging studies indicate a growing interest in targeting the post-ischemic brain with bioenergetic interventions such as mitochondrial transplantation (Norat et al. ; Zhang, Ma, et al. 2019) or direct ATP delivery (Puisieux et al. 1994). Nevertheless, our understanding of cell type-specific metabolism in the post-ischemic brain is limited to old observatory studies. Thus, characterizing metabolic features of cells in the post-ischemic brain paves the path for future therapeutic strategies.

It has been previously shown that a subpopulation of reactive astrocytes surrounding the infarct area displays nuclear STAT3 (Justicia, Gabriel, and Planas 2000; Choi et al. 2003; Cheng et al. 2018).Considering the pivotal role of canonical STAT3 signaling in cellular metabolic reprogramming (Demaria and Poli 2012), we postulated that nuclear STAT3 drives a similar metabolic switch in post-stroke astrocytes. STAT3 triggers PKM2 and HIF activation to promote a glycolytic profile in several cell types (Demaria and Poli 2012; Gao et al. 2012; Poli and Camporeale 2015; Wei et al. 2020).Whether STAT3 utilizes similar mechanisms to regulate the metabolism of post-stroke astrocytes and to which extent it affects neuronal health was addressed in the present study. Using an indirect astrocyte-neuron culture, we investigated the impact of STAT3-PKM2-HIF signaling on metabolic reprogramming in an ischemia/reperfusion (I/R) injury model comprised of cultured astrocytes and co-cultured neurons.

5.1 STAT3-PKM2-HIF activation promotes lactate-directed glycolysis in ischemic astrocytes

This study shows that a feedforward loop between STAT3, PKM2 and HIF promotes lactate-generating glycolysis in the vehicle and IL6-treated I/R astrocytes. In contrast, inhibition of STAT3 signaling by Stattic reduced STAT3-PKM2-HIF crosstalk and promoted mitochondrial respiration in I/R astrocytes.

The cellular glycolytic path determines the extent of the mitochondrial involvement in generating ATP. Higher lactate-directed glycolysis restricts mitochondrial pyruvate consumption (Demaria and Poli 2012) and minimizes ATP synthesis to glycolysis.

Astrocytes naturally have a preference towards glycolysis (Turner and Adamson 2011), a feature, which is highlighted in I/R astrocytes by activating STAT3-HIF-PKM2 feedforward loop. This way, I/R astrocytes bypass OXPHOS to protect the cell against oxidative stress (Zhou et al. 2020). This phenomenon is also confirmed by our observations as seen sections 3.3.8.2 and 3.3.9. Nevertheless, I/R-induced lactate-directed glycolysis increases the risk of ATP depletion and cellular incapability to perform ATP-dependent tasks such as ion exchange, glutamate clearance, scavenging and antioxidant defense (Anderson et al. 2005; Candelario-Jalil 2009; Dirnagl, Iadecola, and Moskowitz 1999).

On the other hand, the STAT3-PKM2-HIF crosstalk promotes intra and extracellular lactic acid acidosis in I/R astrocytes (as seen in glycolysis analysis, section 3.3.8.1), which might be cytotoxic to both astrocytes and their co-cultured neurons (Goldman et al. 1989). Our findings associate post-ischemic nuclear STAT3 in reactive astrocytes with upregulation of hypoxic-induced interstitial lactate. Welsh et al. were among the first groups that linked the deleterious impacts of hyperglycemia to lactate acidosis post-stroke. The authors appointed lactate as a major interfering factor in the reconstitution of cerebral ATP in cats' post-stroke (Welsh et al. 1980). Rehncrona, Rosen, and Siesjo et al. further elaborated on the energy state in post-ischemic tissue and the impact on neurophysiological parameters in starved versus hyperglycemic rats. Intriguingly, hypoglycemic rats exhibited a considerable increase in ATP level, followed by significant restoration of spontaneous electrical activity in the cortex and somatosensory-evoked responses. On the contrary, glucose administration to nutrient-depleted animals prior to incomplete ischemia increased tissue lactate and hampered cortical energy recovery (Rehncrona, Rosen, and Siesjo 1981). Kraig, Pulsinelli, and Plum et al. also observed that higher blood glucose peaked the tissue lactate and dismantled astroglia's ion exchange, contributing to infarct development in cardiac arrest-induced permanent brain ischemia (Kraig, Pulsinelli, and Plum 1985). Furthermore, Kraig and Chesler et al. showed that hyperglycemia induces astrocytic lactate acidosis and causes astrocytic degeneration. The authors believed that astrocytic-created interstitial acidosis is the first step toward infarction since it reduces the cell membrane's ability to exchange ions (Kraig and Chesler 1990).

However, it was not clear whether it is lactic acid per se, or any proton imbalance can foster the necrosis chain and infarction. Schneider et al. could prove that the source of hypoxia-derived interstitial acidification is lactate/H$^+$ co-transportation but no other proton exchange mechanisms (Schneider et al. 1993). Furthermore, Goldman et al. demonstrated that cell death occurs extensively in rat primary neurons and astrocytes subjected to lactic acid rather than hydrochloric acid (HCL). The authors associated the lactate cytotoxicity with the ability of lactic acid to induce cytoplasmic acidification in neurons and glia (Goldman et al. 1989).

Upregulation of lactate-generating glycolysis in reactive astrocytes has also been observed in other diseases; for instance, Wei et al. studied the STAT3-PKM2 reciprocal activation in astrocytes of the chronic inflammatory pain model. The authors discovered that STAT3-PKM2 signaling induces the Warburg effect, increasing interstitial lactate and pain. They also disclosed that Platelet-rich plasma (PRP) mitigates the pain by restricting STAT3-PKM2-induced lactate-directed glycolysis.

Further studies from Valeria Poli’s team reveals that many tumor cells express canonical STAT3 signaling consecutively due to long-term exposure to chronic inflammation. Consecutive canonical STAT3 signaling mediates lactate-directed glycolysis to resist apoptosis, promote survival and support migration by facilitating epithelial-mesenchymal transition (Camporeale et al. 2014; Demaria and Poli 2012; Poli and Camporeale 2015). A similar response pattern is seen in highly invasive reactive astrocytes of astrocytoma and glioblastoma (Rahaman et al. 2002; Sarmiento Soto et al. 2020). Interestingly, Sun et al. demonstrated that transferring normal human astrocytic mitochondria to glioma cells returns aerobic metabolism and makes glioma cells vulnerable to radiotherapy (Sun et al. 2019), indicating the importance of a glycolytic profile to escape cancer therapies.

Apart from cancer, several acute and chronic neurodegenerative diseases display nuclear STAT3, like traumatic brain injury (Xia et al. 2002), spinal cord injury (SPI)(Herrmann et al. 2008), and stroke. All cases share similar features such as activation of canonical STAT3, proliferation, and migration in reactive astrocytes.

Responsive metabolic switching is not restricted to astrocytes or cancer cells. In fact, a similar metabolic pattern has been observed in lymphocytes, such as memory CD8$^+$ T cells upon antigen encounter (Balmer et al. 2016; Sukumar et al. 2013). Gaining a glycolytic profile, T cells acquire their effector properties, while inhibiting glycolysis promotes formation of memory T cells (Sukumar et al. 2013; Menk et al. 2018).

In addition, pro-inflammatory (M1) macrophages exhibit a glycolytic profile, while anti-inflammatory (M2) macrophages are more dependent on OXPHOS (Viola et al. 2019). Based on our observation and previous studies, it is interesting to note that a metabolic reprogramming towards a glycolytic profile has been seen in cells with pro-inflammatory profiles, indicating a specific metabolic signature in these cells.

5.2 STAT3 determines the downstream metabolic path of glycogen-derived glucose in I/R astrocytes

Glucose concentration in a normoglycemic systemic circulation is tightly regulated between 4 to 7.2 mM to ensure glucose delivery to the brain. This system is extremely fine-tuned via pancreas-liver endocrine checks and balances, which supply the brain with glycogen-derived glucose through systemic circulation (Rich, Harris, and Brown 2019). Nevertheless, the mammalian central nervous system (CNS) and almost exclusively astrocytes contain their own glycogen deposits (Magistretti and Pellerin 1997). Although glycogen was shown in the astrocytes many decades ago, its functional role has not been fully understood. Rich, Harris, and Brown et al. reviewed the latest understanding of astrocytic glycogen and downstream metabolic path in both brain white and grey matter (Rich, Harris, and Brown 2019). They linked the glycogen neuroprotectivity in both optic nerve (Brown, Tekkok, and Ransom 2003) and highly active hippocampal neurons to the glycogen downstream lactate release (Rich, Harris, and Brown 2019). There is also culminative evidence that astrocytic glycogen facilitates memory consolidation by providing energy in lactate form (Suzuki et al. 2011; O'Dowd et al. 1994) or directly synthesizing glutamine through TCA-anaplerotic reactions (Hertz et al. 2003; Hertz, Peng, and Dienel 2007). All studies above acknowledged astrocytic glycogen as a transient and not permanent energy substrate, which is restricted to several astrocytic-neuronal metabolic compartments and acts in response to the temporary environmental clue in the brain.

This study also reveals that STAT3-PKM2-HIF signaling directs glycogen-derived glucose to lactate-generating glycolysis in I/R astrocytes (sections 3.3.8.1 and 3.3.8.2). In contrast, inhibition of STAT3 signaling by Stattic in I/R astrocytes shifts glycogen-derived glucose to mitochondrial metabolism (sections 3.3.8.1 and 3.3.8.2). Besides, diminished OXPHOS after inhibition of glycogenolysis in Stattic-OGlucD astrocytes confirms glycogen’s pivotal role in supplying OXPHOS after suppressing canonical STAT3 signaling. This observation supports previous arguments regarding lactate as one of the main products of glycogen-derived glucose. Nevertheless, based on our observations, glycogen-derived glucose per se is not the determining factor for lactate-generating glycolysis but the STAT3-PKM2 and HIF signaling.

Kajihara et al. were first to demonstrate glycogen aggregates in peri-infarct astrocytes and associated that with oxygen shortage in the peri-infarct tissue. The authors argued that the peri-infarct tissue is sufficiently provided with glucose but not oxygen; thus, non-metabolized glucose is stored as glycogen in peri-infarct astrocytes (Kajihara et al. 2001). More recent studies associated the post-stroke glycogen aggregation with the disability of astrocytes in performing glycogenolysis (Cai et al. 2020).

Nevertheless, our results obtained in cultured I/R astrocytes puts previous observation by Kajihara et al. on debate, and supports more recent conclusion by Cai et al. Our data show persistent glycogenolysis in I/R astrocytes despite 24 h of re-supplement 5 mM glucose (as seen in section 4.7), denoting that lack of oxygen urges astrocytes into irreversible glycogenolysis. Similar observations were made by Brown, Tekkok, and Ransom et al. in astrocytes surrounding the optic nerve under aglycaemia and induced high activity (Brown, Tekkok, and Ransom 2003).

Moreover, based on our findings, IL6 treatment inhibits glycogen mobilization in both normoxic and I/R astrocytes (section 4.7.1). Besides, GP inhibition neither affected the number of glycogen aggregates (section 4.7.1) nor OXPHOS (section 4.7.2) in IL6-treated astrocytes, indicating the ineffective glycogenolysis in these cells. Whether IL6 induces glycogenesis as it does in skeletal muscles (Jiang et al. 2013) or inhibits glycogenolysis remained unclear in this study. However, the inaccessibility of glycogen-derived glucose exacerbated cellular reducing capacities (as seen in section 4.7.3), increasing ROS in IL6-treated normoxic and I/R astrocytes (section 4.4.3). Our observations complete the puzzle in (Cai et al. 2020) study, indicating that post-stroke glycogen aggregation is likely due to the reduced glycogenolysis in astrocytes exposed to pro-inflammatory cytokines such as IL6.

Guo et al. show that STAT3-activated astrocytes mobilize glycogen to synthesize NADPH via PPP (Guo et al. 2021). Our findings elaborate this observation, showing that both STAT3-activated OGlucD and STAT3-inhibited OGlucD (Stattic-OGlucD) astrocytes mobilize glycogen; however, the former provides glucose for lactate-directed glycolysis while the latter supplies mitochondrial OXPHOS. In addition, ROS is increased (section 4.4.3), and cellular reducing capacity is decreased (section 4.7.4) in both STAT3-activated OGlucD astrocytes and STAT3-inhibited Stattic-OGlucD astrocytes. These data challenge Guo et al. arguments about the protective role of STAT3 against oxidative stress in astrocytes. Nevertheless, based on our data, glycogenolysis inhibition downregulates the reducing capacity in both STAT3 activated and inhibited conditions, which supports Guo et al. observation regarding the glycogen's crucial role in supporting the cellular scavenging system.

Guo et al. further argued that glycogen mobilization occurs only in the neuroprotective (A2) subtype of astrocytes (Guo et al. 2021), which is not in line with our observations. Based on our findings, neuronal mitochondrial function, and synapses (section 5.5) are boosted in Stattic-OGlucD and not in OGlucD, even though in both conditions, astrocytes undergo glycogenolysis. Therefore, we concluded that astrocytes do not acquire neuroprotectivity because of glycogen mobilization. In fact, astrocytes increase neuroprotective properties when glycogen-derived glucose supplies mitochondrial respiration.

5.3 Mitochondrial ROS generation is independent of STAT3 signaling

This study reveals that mitochondrial ROS is increased in I/R astrocytes regardless of STAT3 induction or inhibition. However, this effect is insignificantly less pronounced in Stattic-treated astrocytes.

Chen et al. 2018 appoint ROS as an inevitable byproduct of hypoxia/reperfusion and link the ROS's detrimental effects to the efficacy of the cellular scavenging system. They also dissect the ambiguous role of HIF in inducing or suppressing ROS after hypoxia. The authors argued that HIF reduces ROS by suppressing mitochondrial OXPHOS or increases it by increasing NADPH oxidase (NOX) expression (Brennan et al. 2009; Chen et al. 2018). Nevertheless, we could observe both downregulation of mitochondrial respiration (section 4.4.1) and increase in mitochondrial ROS in HIF-activated conditions (section 3.3.10). That suggests HIF strategy in minimizing oxidative stress by dampening mitochondria is failed due to deterioration in the astrocytic scavenging system.

Based on our findings, both STAT3-driven and inhibited I/R astrocytes consume their resources to either generate lactate (vehicle, IL6-treated I/R astrocytes) or enhance mitochondrial respiration (Stattic-treated I/R astrocytes). Neither showed better antioxidant and reducing properties (Mito SOX and MTT data), indicating that I/R astrocytes prioritize energy-producing metabolism over the biosynthesis of reductants such as NADPH. This metabolic response has also been observed in hypoxic glioblastoma (Kathagen et al. 2013), while Guo et al. confirmed a decreased NADPH synthesis in post-ischemic astrocytes (Guo et al. 2021).

Another point in this study is that Stattic-OGlucD astrocytes demonstrate an unexpectedly low ROS, despite a significant increase in OXPHOS. Interestingly, pharmacological inhibition and genetic knockdown of STAT3 signaling have been shown to block ROS production in the human brain's vascular smooth muscles and vascular endothelial cells (Mehla et al. 2021). Based on previous findings, we speculate that STAT3 inhibition in astrocytes might improve astrocytic antioxidant defense, probably through delivering sufficient ATP to enzymatic antioxidant defense (as seen in section 4.4.1).

This study also shows that glycogen-derived glucose supports astrocytic reducing capacity in both normoxic and I/R astrocytes (MTT data). Therefore, a lack of glycogen mobilization in IL6-OGlucD astrocytes can contribute to reductant depletion and an increase in ROS (MTT and Mito SOX data). Guo et al. also addressed the incapability of a subpopulation of astrocytes in mobilizing glycogen, which eventually reduced NADPH synthesis and increased ROS in post-ischemic astrocytes.

5.4 Ambivalent metabolism in STAT3-activated starved astrocytes

Despite a significant STAT3 nuclear translocation in both GlnD and GlucD astrocytes, only GlucD astrocytes increased STAT3 transcription activity. Based on this observation, we speculate that STAT3 is either inactivated by PIAS TF in GlnD astrocytes (Chung, Liao, et al. 1997; Dabir, Kluge, and Dowlati 2009) or nuclear STAT3 in GlnD astrocytes activates other namely kappaB-dependent genes (Yang et al. 2007).

In addition, both nutrient-depleted conditions significantly induced PKM2 translocation, which slightly promotes lactate-generating glycolysis while maintaining mitochondrial respiration at the control level in GlnD astrocytes. In contrast, Unlike I/R and GlnD astrocytes, STAT3/PKM2 activation boosts mitochondrial respiration in GlucD astrocytes. Furthermore, a significantly declined extracellular L-lactate was followed by unchanged lactate-directed glycolysis (Seahorse GRA, section 4.8.3) in GlucD astrocytes. Taken together, we postulate that GlucD-induced extracellular acidification, which was attributed to lactate-directed glycolysis previously in this study, is actually non-glycolytic cytoplasmic acidification. This observation was confirmed by the upregulation of post-2-DG acidification in GlucD astrocytes (as seen in section 4.8.3).

Interestingly, GlucD astrocytes exhibit signs of mitochondrial damage including fast turnover, fragmentation, and increased non-glycolytic acidification, which indicate mitophagy (Quintana et al. 2019; Lagadic-Gossmann, Huc, and Lecureur 2004). Therefore, we assume that by undergoing mitophagy, GlucD astrocytes attempt to rescue mitochondrial DNA (Parone et al. 2008) and systematically eradicate damaged mitochondria (Twig et al. 2008). Nevertheless, although mitophagy does not reduce mitochondrial ATP synthesis, whether elevated mitochondrial fission jeopardizes astrocytic survival is unknown (Quintana et al. 2019; Ong et al. 2010).

This study also shows significant glycogenolysis in both nutrient-depleted with a significant increase in GlucD astrocytes. Furthermore, 24 h nutrient depletion eventually weakened spare respiratory capacity, predicting an upcoming senescence process (as shown in glycogen quantifications and Seahorse MSA in nutrient-deprived astrocytes).

On the other hand, mitochondrial ROS was increased in GlnD and, to a lesser extent, GlucD astrocytes. ROS increase in GlucD astrocytes is a direct response to lower cellular reducing capacity (MTT) and presumably diminished PPP-derived NADPH (Kathagen et al. 2013; Takahashi 2011). However, no difference in GlnD reducing capacity highlights glutamine's crucial role in non-enzymatic antioxidant defense as the main substrate to GSH *de novo* synthesis (Aoyama, Watabe, and Nakaki 2008). Furthermore, due to our indirect co-culture model, astrocytes did not attain neuronal glutamate to recycle it into glutamine. On the other hand, a lack of glutamine supply force astrocytes to either increase glucose uptake or undergo glycogenolysis (as seen in section 4.8.7) to synthesize glutamine through anaplerotic reactions (Hertz et al. 2003; Rose et al. 2020). In both cases, limited glucose in the culture medium to supply glycolysis, mitochondrial respiration, and cellular reducing purposes decreases the chances of TCA-glutamine synthesis. Consequently, a lack of astrocytic glutamine as a gliotransmitter affects co-cultured neurons negatively (Bak, Schousboe, and Waagepetersen 2006; Andersen et al. 2021).

5.5 Due to STAT3-induced metabolism, I/R astrocytes fail to support neuronal OXPHOS and synaptogenesis

STAT3-PKM2-HIF driven metabolism in I/R astrocytes declines the astrocytic support for neuronal OXPHOS and synaptogenesis. On the contrary, glycogen mobilization enabled Stattic-treated I/R astrocytes consume glycogen-derived glucose to support OXPHOS and synaptogenesis of co-cultured neurons. Negative regulation of the neuronal activity by STAT3-activated reactive astrocytes has been shown previously in vivo. STAT3 ablation in reactive astrocytes following MCAO (Rakers et al. 2019) or Alzheimer's disease (AD) (Mehla et al. 2021; Reichenbach et al. 2019) is shown to improve neurological scores and cognitive functions.

At first, we hypothesized that decreased OXPHOS and synapse density in neurons co-cultured with STAT3-HIF-PKM2 activated astrocytes is due to possible cytotoxicity of lactic acid acidosis (Goldman et al. 1989; Kraig, Pulsinelli, and Plum 1985; Kraig and Chesler 1990; Welsh et al. 1980; Hillered, Siesjo, and Arfors 1984). Although it has been shown in vitro that lactate acidity is toxic for neurons and astrocytes (Goldman et al. 1989), the impact of the in vivo lactate administration on neural cells is unclear (Wolahan et al. 2018). In the present study, supplementing sodium lactate to neuronal cultures did not alter the synapse density, denoting the inability of cultured neurons to metabolize lactate for synapse formation. This data underlines the necessity of astrocytic ascorbate in neuronal lactate uptake. Further studies show that astrocytic ascorbate release is decreased after oxidative stress (Daskalopoulos et al. 2002). Therefore, presumably, in the present study, neurons co-cultured with I/R astrocytes do not take up lactate due to lesser astrocytic ascorbate support (Rice 2000; Castro et al. 2009). In addition, lactate supplementation to neurons did not decrease the synapse density in our neuronal cultures either, which puts the previous observations regarding the cytotoxicity of lactate acidosis under debate.

This study further reveals that synapse formation is boosted in neurons co-cultured with astrocytes compared to those grown without astrocytes. Besides, lactate supplementation (section 4.5.4) does not substitute the astrocytic support suggesting that astrocytes support neurons beyond lactate shuttling. On the other hand, neuronal mitochondria and synapses flourished in conditions, in which astrocytes exhibited the highest mitochondrial turnover, such as Stattic-OGlucD. That indicates that neuronal mitochondrial and synaptic prosperities rely on an astrocytic mitochondrial-derived signal, which is abolished after activation of STAT3-PKM2-HIF in I/R astrocytes (as seen in astrocytic MSA and synapse density data, sections 4.7.3 and 4.7.4). Astrocytes support neurons by releasing astrocytic ATP (Coco et al. 2003; Harada, Kamiya, and Tsuboi 2015) or viable mitochondria (Falchi et al. 2013; Hayakawa et al. 2016). In fact, administrating mitochondria has improved neurological deficits after MCAO (Norat et al. ; Zhang, Ma, et al. 2019).

Inhibition of glycogenolysis in astrocytes negatively affects neuronal OXPHOS and synapse density which delineates the neuro-supportive role of astrocytic glycogen. Our observations support Guo et al. 2021 regarding glycogen mobilization in neuroprotective subtypes of astrocytes. The authors show that glycogen mobilization in these astrocytes empowers the PPP and NADPH synthesis, resulting in less ROS production. In this study, glycogenolysis inhibition decreased astrocytic reducing capacity in all experimental groups, confirming the Guo et al. 2021 observations.

Based on our observation, neurons co-cultured with astrocytes with a high level of ROS (I/R, IL6-I/R, GlnD) demonstrated fewer functional synapses. Other studies showed that astrocytic ROS diminishes neuronal metabolism and synapse formation, which is an energy-demanding process (Vicente-Gutierrez et al. 2019; Li, Xiong, et al. 2020).

5.6 Significance of astrocytic glutamine for neuronal OXPHOS and synaptogenesis

Consecutive STAT3 activation in GlucD astrocytes and downstream metabolism maintained mitochondrial and synaptic properties of co-cultured neurons at the vehicle-treated level.

On the other hand, OXPHOS and synaptic density are diminished in neurons co-cultured with GlnD astrocytes. The most prominent feature in GlnD astrocytes is the higher mitochondrial ROS. Studies show that mitochondrial ROS can be transferred from astrocytes to neurons and modulate neuronal metabolism (Vicente-Gutierrez et al. 2019; Li, Xiong, et al. 2020). Altered neuronal metabolism consequently impairs synapse formation as an energy-demanding process (Li, Xiong, et al. 2020). Furthermore, interrupted glutamine supplementation to astrocytes affects their gliotransmitters release, hampering synapse formation. In vivo studies indicated that L-glutamine administration in the mouse MCAO model rescued neurons from apoptosis by increasing heat-shock protein 70 in astrocytes (Luo et al. 2019).

Based on the observations above, we conclude that GlucD astrocytes supported neuronal mitochondria and synapses due to their access to glutamine. Furthermore, higher mitochondrial respiration in GlucD astrocytes supported the neuronal respiration probably through ATP or mitochondria release (Falchi et al. 2013; Hayakawa et al. 2016), providing enough energy for synapse formation.

5.7 Methodological strengths and limitations

In this study, we utilized a well-established indirect co-culture of mouse primary astrocytes and neurons, which is often used to model astrocytic-neuronal interactions in many neurodegenerative diseases, namely ischemic stroke. This model provided a powerful tool to study the impact of ischemic STAT3-manipulated astrocytes unilaterally on neuronal mitochondrial functioning, synapse formation, and morphology which has been an open question for over two decades. Besides, this model enabled us to study astrocytic-neuronal metabolic characteristics individually, while combining their cultures indirectly, which is not possible in mixed astrocytic-neuronal cultures. However, this model restricts the cell-cell interaction between astrocytes and neurons and limits the astrocytic response to signals from neurons such as glutamate reuptake and recycling.

Mouse primary cultures were selected intentionally since we planned to perform follow-up in vivo positron emission tomography (PET) studies on glycogen metabolism in mouse MCAO/inflammation models. Furthermore, primary cultures have more physiological properties compared to immortalized or cancer cell lines. Nevertheless, obtaining pure and consistent cultures was challenging. To minimize the other cell type's contaminations, we performed several shaking steps following AraC treatments in astrocytic cultures, while the same individual performed the isolation procedure throughout the entire project. However, using mature human primary astrocytes and neurons would have been desirable.

The maturity of the cultures can still be a matter of debate. It has been shown that diploid cells age faster in vitro (Rubin 1997; Shall 1996). Nonetheless, in this study, astrocytes and neurons were incubated for 21 DIV and 14 DIV, respectively, for further maturation. In addition, our astrocyte cultures were positive for aldehyde dehydrogenase 1 L1 (ALDH1L1) as a marker for astrocytic maturity and negative for nestin and vimentin as a marker for stem and progenitor cells. Besides, our neuronal culture's age was optimal to study the alteration in glutamatergic synapses and mitochondrial function.

This study was based on a 2D culture model, which can be criticized for less physiological relevance. However, addressing the real-time metabolic alteration of cells in a 3D form using Seahorse XF analysis is technically challenging. 3D-specific culture matrices such as Matrigel disturb the formation of Seahorse XF-required transient microchamber and reduce the efficacy of inhibitors' penetration in cells. Furthermore, brain organoids represent the neonatal brain rather than the mature model for adult stroke. Besides, the neural cell composition varies between different brain organoids and should be characterized by every single experiment. That adds another layer of complexity to the normalization procedure of metabolic factors. Although our model provides insight into the astrocytic metabolic fingerprint upon the STAT3-induced reactivity, it can also be criticized for neglecting the other environmental metabolic cues from activated microglia, hypoxic neurons, and immune cells which exist in the post-ischemic brain. Therefore, an in sillico algorithm, which reconstructs metabolic pathways from existing databases, would be beneficial to understand possible metabolic interactions on a cell-type specific level after stroke.

Despite legitimate criticism of the specificity of IL6 in activating solemn canonical STAT3 pathway, this study favors IL6 treatment of astrocytes over genetic manipulation of STAT3 expression. The reason for that is that this treatment model is more translational to stroke pathophysiology since the IL6 level is upregulated in the acute phase of stroke (Waje-Andreassen et al. 2005). Furthermore, genetic manipulation of STAT3 may disturb the expression of non-canonical STAT3s. This study did not address non-canonical STAT3s in I/R astrocytes; however, accumulating evidence indicates a contrasting metabolic role between canonical and non-canonical, particularly mitochondrial STAT3 (Camporeale et al. 2014; Yang and Rincon 2016; Xu et al. 2016). To our knowledge, an approach that targets canonical or non-canonical

STAT3 specifically has not been demonstrated until now. Nevertheless, such study models can be beneficial for understanding the underlying metabolic pathways induced by STAT3 signaling or STAT3 non-canonical forms.

To further address the canonical STAT3 pathway, we used Stattic, which is known to “selectively inhibit the function of the STAT3 SH2 domain regardless of the STAT3 activation state in vitro” (Schust et al. 2006). Therefore, theoretically, Stattic cannot inhibit the activity of p (S727) STAT3, which is in the transactivation domain (TAD) of STAT3 C-terminus (Tolomeo and Cascio 2021). Comparing nuclear versus cytoplasmic STAT3 in our experimental group confirmed the efficacy of Stattic in hampering nuclear translocation, which was accompanied by less STAT3 transcription activity. However, more cytoplasmic localization of total STAT3 in Stattic-treated astrocytes does not solely represent cytoplasmic p (S727) STAT3s or clarify their subcellular localization. Our extensive attempts in immunostaining astrocytes with p (S727) and p (Y705) STAT3 with various antibodies remained inconclusive. Our colleagues saw similar technical hindrances in the NeuroScienceLab/peripheral nervous system team (Personal conversation of Mina Borbor with Dr. Markus Leo). Therefore, currently, together with Dr. Ulf Brockmeier, we focus on establishing an invitro model based on (Letra-Vilela et al. 2020) study to target the post-translational modification of STAT3 through introducing point mutations in p (S727) and p (Y705) residues of STAT3 in cultured astrocytes.

Another point that should be considered in inhibiting STAT3 signaling is the efficacy and specificity of the inhibitor in vivo and in vitro. Our attempts to inhibit the STAT3 canonical signaling using AG490, a selective inhibitor of the JAK2-STAT3 signaling pathway, were ineffective in astrocyte cultures. However, in vivo administration of AG490 has shown to alleviate the stoke outcome (Wang et al. 2021).

This study accentuates the role of astrocytes in supporting neuronal mitochondrial function and synapse formation. Nevertheless, we could not decipher the communication mechanism between astrocytic and neuronal mitochondria. Whether the astrocytes release more ATP or nourish neurons with mitochondrial fragments or metabolic substrates remained an open question in this study. Further secretum analysis could have provided a better insight into astrocytic-neuronal metabolic interaction. However, this study could not address that due to the limited number of primary astrocytes and neurons and astrocytic CM volume, challenging technical support for secretum analysis, and time scarcity.

5.8 Clinical relevance and future perspectives

This study proves that the STAT3-PKM2-HIF signaling cycle drives lactate-generating glycolysis in ischemic astrocytes, suppressing astrocytic mitochondrial respiration. As a result of this metabolic switch, astrocytes suspend supporting neurons metabolically and transfer the stress signal through ROS to neurons. Neurons, in turn, reduce their mitochondrial OXPHOS and synapse formation. This study further highlights the crucial neuroprotection provided by astrocytic glycogen storage and mobilization. Similar observations have not been demonstrated before. Therefore, our findings encourage proof-of-concept studies evaluating the reproducibility of these observations *in vivo*. For instance, recent advances in multimodal imaging techniques such as combined PET and magnetic resonance imaging (MRI) integrate the functional PET-derived metabolic readouts with structural input provided by MRI. Furthermore, today's versatility of radiopharmaceuticals from [^{18}F] Fluorodeoxyglucose, ^{13}C magnetic resonance spectroscopy , and several glycogen-tracing markers (Witney et al. 2014; Allott et al. 2020) allows basic researchers to draw a complete metabolic map in animals with CKO STAT3 in their reactive astrocytes (Herrmann et al. 2008; Rakers et al. 2019; Sarafian et al. 2010). In addition, a comparative functional study between mitochondria isolated from the brains of healthy WT, healthy KO, and their stroke model can be the first step towards a better understanding of STAT3-mediated mitochondrial metabolism post-stroke.

Besides, Our findings highlight the translational potential of direct administration of food and drug administration (FDA)-approved metabolic substrates such as L-glutamine (Luo et al. 2019), L-lactate (Wolahan et al. 2018), and ascorbic acid (Chang et al. 2020) to improve post-stroke neurological deficits.

This study nominates astrocytic glycogen as a therapeutic target and opens a new chapter in hormone and diet-targeted therapies. Previous in vivo studies revealed that the aging brain contains fewer glycogen deposits (Oe et al. 2016), and interestingly stroke occurs more in the elderly (Alamowitch et al. 2001). Other studies reveal that aging causes insulin resistance in CNS (Hallschmid and Schultes 2009; Marmentini et al. 2021), which not only results in cognitive decline in elderly patients (Feinkohl et al.

2014) but also might diminish glycogenesis in the aging brain. In addition, aging reduces the activity of glycogen synthetase (GS) and phosphorylase (GP) (Khandelwal, Enno, and Narayanan 1984) as well as insulin activity in the liver (Marmentini et al. 2021). Whether a similar course of events applies to the aging brain is remained to be investigated. Intriguingly, recent studies associated the post-stroke glycogen aggregations with the incapability of astrocytes to undergo glycogenolysis, which could be rescued by administering insulin during the reperfusion (Cai et al. 2020). Fortunately, intranasal administration of insulin, insulin analogs (Benedict et al. 2007) and insulin sensitizers (Watson et al. 2005) has been established in several neurodegenerative diseases. Similar approaches open a promising perspective for preventive hormone therapy to encourage glucose uptake, increase astrocytic glycogenesis and improve astrocytic glycogenolysis in aging CNS.

Apart from hormone-based therapies, diet and exercise have been shown to be effective in glycogen loading in young rodent brains (Soya et al. 2018; Meguid et al. 1993). Therefore, dietary studies should focus on improving brain biosynthesis, namely glycogenesis in aged brains. This way, prescribing a targeted diet for the elderly might minimize the deleterious outcome of possible stroke in a preventive approach. The first step, a retrospective study comparing the stroke frequency between different food cultures, might pave the path for further nutrition-directed studies. As a matter of fact, diet targeting has shown its efficacy in several neurological disorders. For instance, a ketogenic diet has a proven record in minimizing seizures in pharmacoresistant epileptic patients (D'Andrea Meira et al. 2019). Interestingly, (Valdebenito et al. 2016) showed that the ketogenic diet drives a mitochondrial metabolism in astrocytes, hampering lactate-directed glycolysis and modifying neuronal metabolism and excitability. In stroke, the hypoglycemic diet is neuroprotective due to the lower lactic acid generation (Welsh et al. 1980; Hillered, Siesjo, and Arfors 1984; Kraig, Pulsinelli, and Plum 1985; Kraig and Chesler 1990). To aid future diet-targeted therapies, extensive metabolomics research should be conducted in the healthy and stroke brain to provide a post-stroke cell type-specific energy map. This way, a preventive diet behavior can benefit patients at risk, and a post-stroke-targeted nutrition intake can be introduced to stroke patients to improve long-term neurobehavioral recovery.

Another important outcome of this study is the role of STAT3-HIF-PKM2 crosstalk in dampening astrocytic mitochondrial function, which in turn declines neuronal respiration and synapse formation. On the other hand, we demonstrated that STAT3-HIF-PKM2 interplay is essential for inducing reactive astrogliosis, a substantial process to minimize the injury in the stroke acute phase. However, consecutive activation of this pathway in stroke sub-acute and chronic phase weakens the astrocytic mitochondrial support and hinders synaptogenesis and neurobehavioral recovery. In this case, our pathway inhibition findings can provide translational benefits to improve stroke patients' cognitive development in subacute and chronic phases. Nevertheless, further basic studies should concentrate on the optimization of inhibition of the STAT3-HIF-PKM2 pathway in terms of specificity and side effects of inhibitors in animal models.

In recent years, astrocytic-neuronal mitochondrial communication has gained significant attention in several neurodegenerative diseases (Joshi et al. 2019; Hayakawa et al. 2016; Falchi et al. 2013). In addition, accumulating studies acknowledged the effectiveness of mitochondrial transplantation in metabolic and degenerative diseases. For instance, it has been shown that intra-arterial transplantation of exogenous mitochondrial releases the stroke burden in MCAO mice (Norat et al. ; Zhang, Ma, et al. 2019). Upon administration, viable autologous mitochondria are incorporated into neural cells, delivering the ATP to the peri-infarct region, mitigating reactive astrogliosis, and attenuating oxidative stress. Emani et al. 2017 were the first to successfully perform mitochondrial autotransplantation on a pediatric patient with myocardial infarction (Emani et al. 2017), which confirms the efficacy and feasibility of this approach for future translational aspects in stroke. Nevertheless, how the recipient cells take up the transplanted mitochondria and how the grafted mitochondria deliver the energy and underlying mechanisms have remained for basic researchers to study.

Another technical challenge is harvesting mitochondria from the tissue of the same individual. To overcome this shortcoming, basic researchers should propose a solution for propagating mitochondria in vitro and on a mass scale. Accumulating evidence suggests that mesenchymal stromal cells (MSCs) can actively donate mitochondria to promote tissue repair (Li et al. 2019). Furthermore, until now, 416 clinical trials exert MSCs in treating multiple diseases (Galderisi, Peluso, and Di Bernardo 2022), therefore both industrial and academic sectors developed efficient tools and reagents to propagate MSCs efficiently and sufficiently either for harvesting exosomes or other therapeutic applications. Therefore, MSCs can be potential candidates for mass propagation of mitochondria in vitro. Furthermore, our study proved that manipulating metabolic key regulators such as STAT3 in vitro can boost mitochondrial activity. Therefore, future studies should focus on boosting the mitochondrial functional properties in MSCs to enhance the efficiency of the outcome in recipient tissue.

As a final point, it is known that mitochondria are evolutionary originated from a symbiosis between intra-cellular parasitic alphaproteobacteria (Munoz-Gomez et al. 2017; Thrash et al. 2011) and eukaryotic cells. Considering alphaproteobacteria' accessibility and multiplication rate, it is worth investigating the possibility of generating functional mitochondria from these archaebacteria for therapeutic purposes.

6 Conclusion

Based the data obtained in this study, we conclude that STAT3 is a critical regulator of astrocytic metabolism post ischemia and is a promising target for stroke therapy. More specifically:

I) Ischemic astrocytes undergo STAT3-PKM2-HIF cascade activation via a feed-forward loop that can be downregulated using a STAT3 inhibitor Stattic.

II) The STAT3-PKM2-HIF pathway promotes astrocytic reactivity and glycogenolysis. Thereby, lactate-directed glycolysis in I/R astrocytes is increased and mitochondrial respiration is reduced. Inhibition of STAT3 makes mitochondrial metabolism reliant on the glycogen-derived glucose and blocking glycogenolysis severely impairs mitochondrial function in STAT3-inhibited I/R astrocytes.

III) IL6-induced glycogen aggregation in astrocytes but has no significant impact on mitochondrial respiration or lactate-directed glycolysis in I/R astrocytes. However, IL6 treatment downregulates antioxidant defense and reducing capacity in astrocytes.

IV) Astrocytic glycogenolysis is pivotal for maintaining cellular reducing capacity and neuron-supporting functions in both I/R and healthy astrocytes.

V) Reactive astrocytes after I/R injury exhibit increased glycolytic activity and fail to support neuronal mitochondria and synaptogenesis. Inhibition of STAT3 in I/R astrocytes increased mitochondrial respiration and synapse formation in co-cultures.

VI) In normoxic glucose-deprived astrocytes, STAT3 activation triggers glycogenolysis to support mitochondrial respiration. Thereby, astrocytes deprived of glucose maintain neuronal respiration and synaptogenesis.

VII) In normoxic glutamine-deprived astrocytes, the canonical STAT3 signaling pathway is not activated. Despite unchanged glycolytic and mitochondrial properties, glutamine-deprived astrocytes fail to support respiration and synaptogenesis in their co-cultured neurons. This response can be due to glutamine-deprived astrocytes' high level of ROS and interrupted glutamine supplementation to neurons.

7 Supplementary

7.1 Permissions

7.1.1 Permission 1

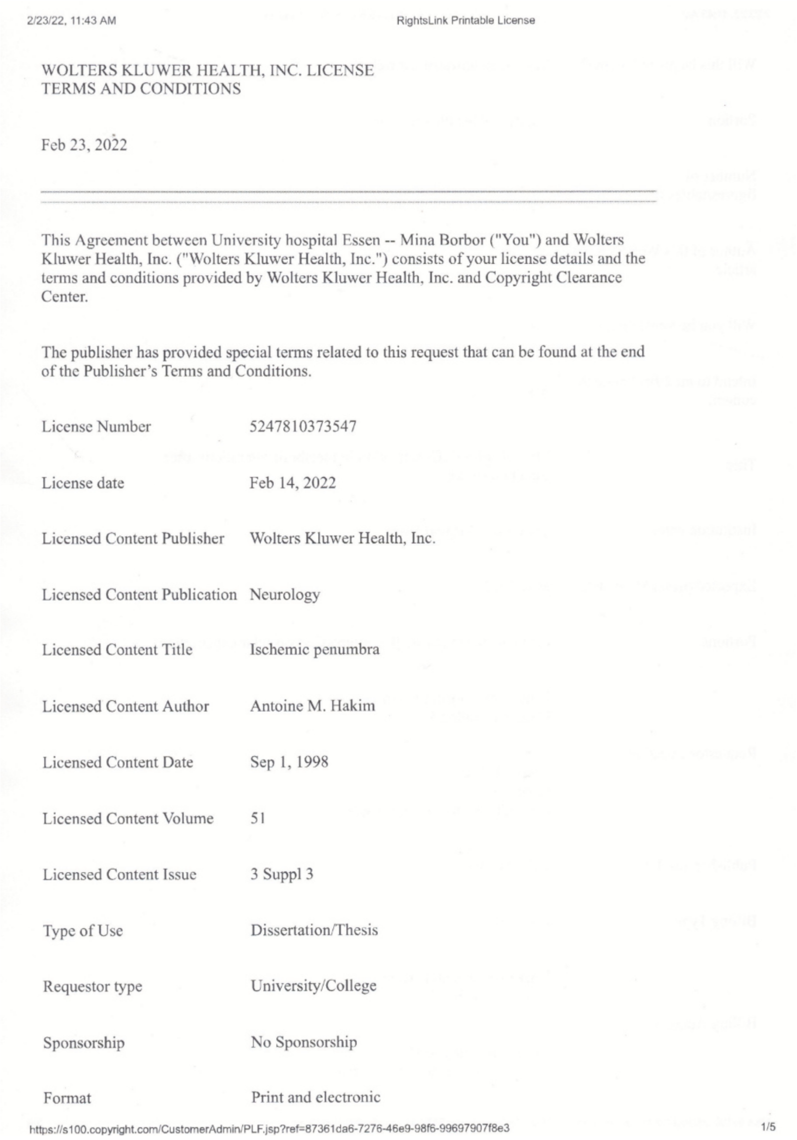

2/23/22, 11:43 AM RightsLink Printable License

WOLTERS KLUWER HEALTH, INC. LICENSE
TERMS AND CONDITIONS

Feb 23, 2022

This Agreement between University hospital Essen -- Mina Borbor ("You") and Wolters Kluwer Health, Inc. ("Wolters Kluwer Health, Inc.") consists of your license details and the terms and conditions provided by Wolters Kluwer Health, Inc. and Copyright Clearance Center.

The publisher has provided special terms related to this request that can be found at the end of the Publisher's Terms and Conditions.

License Number	5247810373547
License date	Feb 14, 2022
Licensed Content Publisher	Wolters Kluwer Health, Inc.
Licensed Content Publication	Neurology
Licensed Content Title	Ischemic penumbra
Licensed Content Author	Antoine M. Hakim
Licensed Content Date	Sep 1, 1998
Licensed Content Volume	51
Licensed Content Issue	3 Suppl 3
Type of Use	Dissertation/Thesis
Requestor type	University/College
Sponsorship	No Sponsorship
Format	Print and electronic

https://s100.copyright.com/CustomerAdmin/PLF.jsp?ref=87361da6-7276-46e9-98f6-99697907f8e3 1/5

Will this be posted online?	Yes, on an unrestricted website
Portion	Figures/tables/illustrations
Number of figures/tables/illustrations	1
Author of this Wolters Kluwer article	No
Will you be translating?	No
Intend to modify/change the content	No
Title	The role of STAT3 activation in metabolic alterations after ischemic stroke
Institution name	University hospital Essen
Expected presentation date	May 2022
Portions	cerebral events during the progressive vascular constriction
Requestor Location	University hospital Essen Hufelandstraße 55 Essen, 45122 Germany Attn: University hospital Essen
Publisher Tax ID	EU826013006
Billing Type	Invoice
Billing Address	University hospital Essen Hufelandstraße 55 Essen, Germany 45122 Attn: University hospital Essen

7.1.2 Permission 2

2/8/22, 8:34 AM https://marketplace.copyright.com/rs-ui-web/mp/license/d474e325-e656-451e-a7e5-d4689aff0282/de03e4da-581a-45a5-a24c-9b3...

CCC Marketplace™

This is a License Agreement between Mina Borbor ("User") and Copyright Clearance Center, Inc. ("CCC") on behalf of the Rightsholder identified in the order details below. The license consists of the order details, the CCC Terms and Conditions below, and any Rightsholder Terms and Conditions which are included below.

All payments must be made in full to CCC in accordance with the CCC Terms and Conditions below.

Order Date	08-Feb-2022	**Type of Use**	Republish in a thesis/dissertation
Order License ID	1186599-1	**Publisher**	ANNUAL REVIEWS
ISSN	1545-4126	**Portion**	Image/photo/illustration

LICENSED CONTENT

Publication Title	Annual review of neuroscience	**Rightsholder**	Annual Reviews, Inc.
Date	01/01/1978	**Publication Type**	e-Journal
Language	English	**URL**	http://arjournals.annualreviews.org/loi/neuro
Country	United States of America		

REQUEST DETAILS

Portion Type	Image/photo/illustration	**Distribution**	Worldwide
Number of images / photos / illustrations	1	**Translation**	Original language of publication
Format (select all that apply)	Print, Electronic	**Copies for the disabled?**	No
		Minor editing privileges?	No
Who will republish the content?	Academic institution	**Incidental promotional use?**	No
Duration of Use	Life of current edition	**Currency**	EUR
Lifetime Unit Quantity	Up to 499		
Rights Requested	Main product		

NEW WORK DETAILS

Title	Mrs.	**Institution name**	University Hospital Essen
Instructor name	Mina Borbor	**Expected presentation date**	2022-05-31

ADDITIONAL DETAILS

Order reference number	N/A	**The requesting person / organization to appear on the license**	Mina Borbor

REUSE CONTENT DETAILS

https://marketplace.copyright.com/rs-ui-web/mp/license/d474e325-e656-451e-a7e5-d4689aff0282/de03e4da-581a-45a5-a24c-9b3446227755 1/4

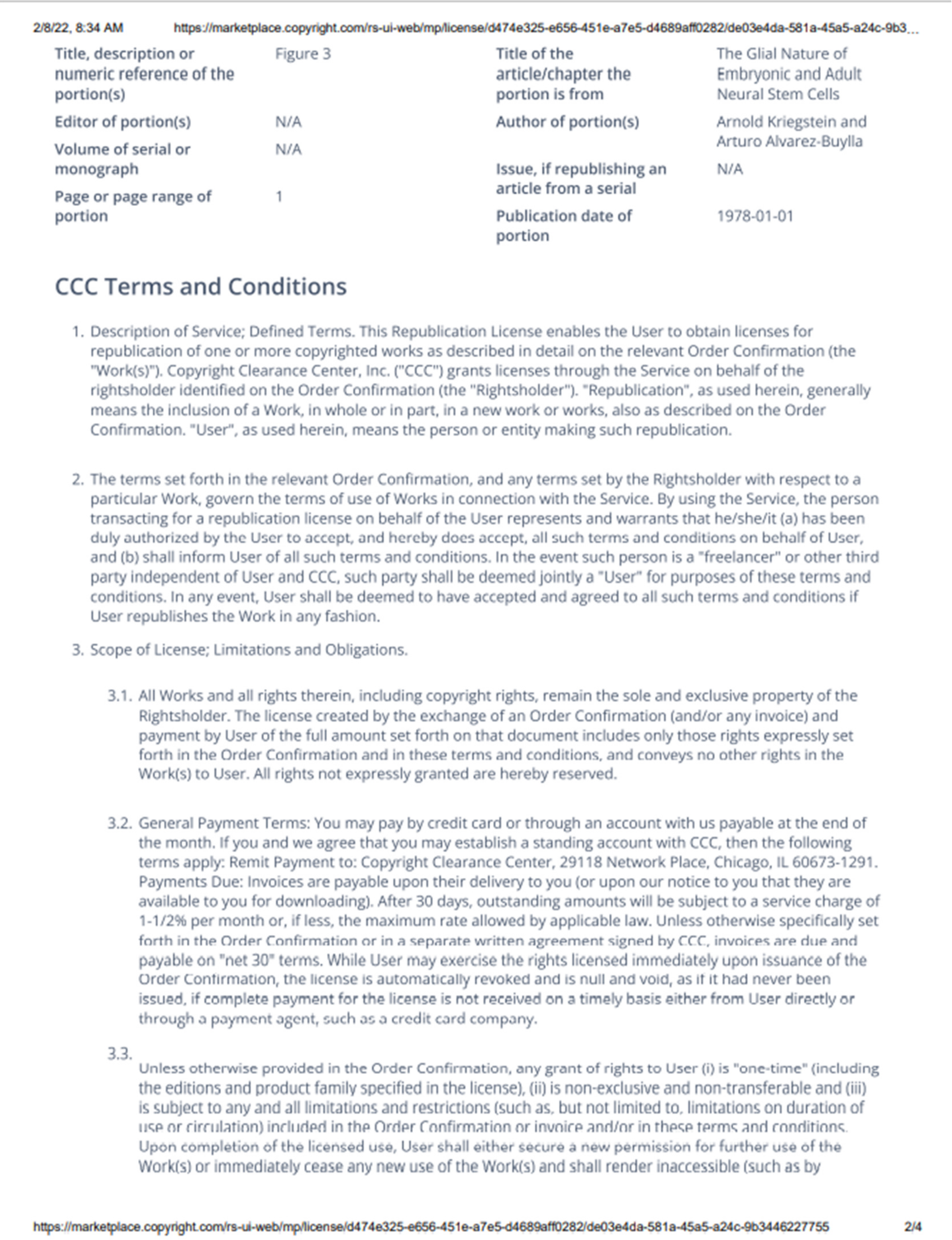

Title, description or numeric reference of the portion(s)	Figure 3	**Title of the article/chapter the portion is from**	The Glial Nature of Embryonic and Adult Neural Stem Cells
Editor of portion(s)	N/A	**Author of portion(s)**	Arnold Kriegstein and Arturo Alvarez-Buylla
Volume of serial or monograph	N/A	**Issue, if republishing an article from a serial**	N/A
Page or page range of portion	1	**Publication date of portion**	1978-01-01

CCC Terms and Conditions

1. Description of Service; Defined Terms. This Republication License enables the User to obtain licenses for republication of one or more copyrighted works as described in detail on the relevant Order Confirmation (the "Work(s)"). Copyright Clearance Center, Inc. ("CCC") grants licenses through the Service on behalf of the rightsholder identified on the Order Confirmation (the "Rightsholder"). "Republication", as used herein, generally means the inclusion of a Work, in whole or in part, in a new work or works, also as described on the Order Confirmation. "User", as used herein, means the person or entity making such republication.

2. The terms set forth in the relevant Order Confirmation, and any terms set by the Rightsholder with respect to a particular Work, govern the terms of use of Works in connection with the Service. By using the Service, the person transacting for a republication license on behalf of the User represents and warrants that he/she/it (a) has been duly authorized by the User to accept, and hereby does accept, all such terms and conditions on behalf of User, and (b) shall inform User of all such terms and conditions. In the event such person is a "freelancer" or other third party independent of User and CCC, such party shall be deemed jointly a "User" for purposes of these terms and conditions. In any event, User shall be deemed to have accepted and agreed to all such terms and conditions if User republishes the Work in any fashion.

3. Scope of License; Limitations and Obligations.

   3.1. All Works and all rights therein, including copyright rights, remain the sole and exclusive property of the Rightsholder. The license created by the exchange of an Order Confirmation (and/or any invoice) and payment by User of the full amount set forth on that document includes only those rights expressly set forth in the Order Confirmation and in these terms and conditions, and conveys no other rights in the Work(s) to User. All rights not expressly granted are hereby reserved.

   3.2. General Payment Terms: You may pay by credit card or through an account with us payable at the end of the month. If you and we agree that you may establish a standing account with CCC, then the following terms apply: Remit Payment to: Copyright Clearance Center, 29118 Network Place, Chicago, IL 60673-1291. Payments Due: Invoices are payable upon their delivery to you (or upon our notice to you that they are available to you for downloading). After 30 days, outstanding amounts will be subject to a service charge of 1-1/2% per month or, if less, the maximum rate allowed by applicable law. Unless otherwise specifically set forth in the Order Confirmation or in a separate written agreement signed by CCC, invoices are due and payable on "net 30" terms. While User may exercise the rights licensed immediately upon issuance of the Order Confirmation, the license is automatically revoked and is null and void, as if it had never been issued, if complete payment for the license is not received on a timely basis either from User directly or through a payment agent, such as a credit card company.

   3.3. Unless otherwise provided in the Order Confirmation, any grant of rights to User (i) is "one-time" (including the editions and product family specified in the license), (ii) is non-exclusive and non-transferable and (iii) is subject to any and all limitations and restrictions (such as, but not limited to, limitations on duration of use or circulation) included in the Order Confirmation or invoice and/or in these terms and conditions. Upon completion of the licensed use, User shall either secure a new permission for further use of the Work(s) or immediately cease any new use of the Work(s) and shall render inaccessible (such as by

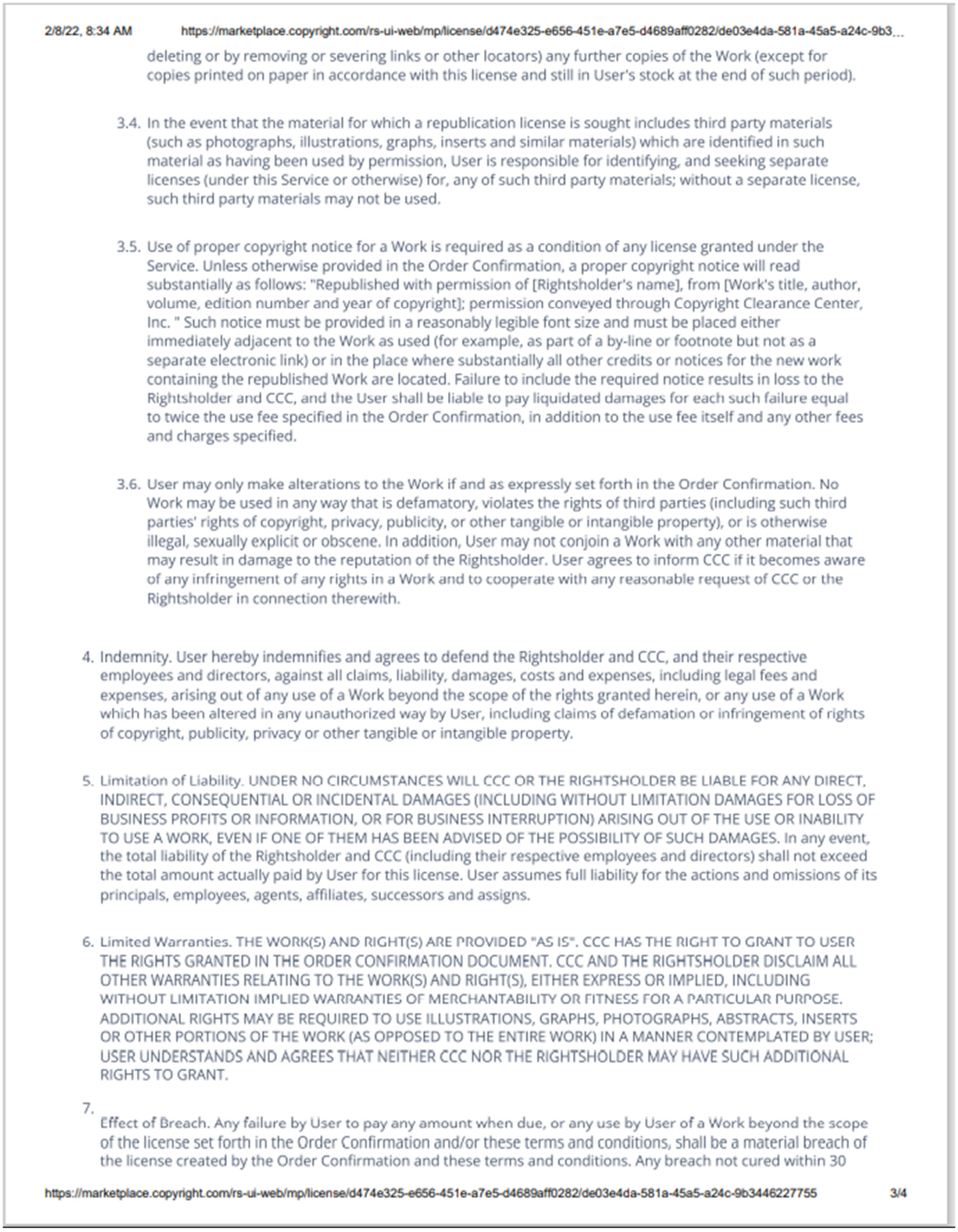

deleting or by removing or severing links or other locators) any further copies of the Work (except for copies printed on paper in accordance with this license and still in User's stock at the end of such period).

3.4. In the event that the material for which a republication license is sought includes third party materials (such as photographs, illustrations, graphs, inserts and similar materials) which are identified in such material as having been used by permission, User is responsible for identifying, and seeking separate licenses (under this Service or otherwise) for, any of such third party materials; without a separate license, such third party materials may not be used.

3.5. Use of proper copyright notice for a Work is required as a condition of any license granted under the Service. Unless otherwise provided in the Order Confirmation, a proper copyright notice will read substantially as follows: "Republished with permission of [Rightsholder's name], from [Work's title, author, volume, edition number and year of copyright]; permission conveyed through Copyright Clearance Center, Inc. " Such notice must be provided in a reasonably legible font size and must be placed either immediately adjacent to the Work as used (for example, as part of a by-line or footnote but not as a separate electronic link) or in the place where substantially all other credits or notices for the new work containing the republished Work are located. Failure to include the required notice results in loss to the Rightsholder and CCC, and the User shall be liable to pay liquidated damages for each such failure equal to twice the use fee specified in the Order Confirmation, in addition to the use fee itself and any other fees and charges specified.

3.6. User may only make alterations to the Work if and as expressly set forth in the Order Confirmation. No Work may be used in any way that is defamatory, violates the rights of third parties (including such third parties' rights of copyright, privacy, publicity, or other tangible or intangible property), or is otherwise illegal, sexually explicit or obscene. In addition, User may not conjoin a Work with any other material that may result in damage to the reputation of the Rightsholder. User agrees to inform CCC if it becomes aware of any infringement of any rights in a Work and to cooperate with any reasonable request of CCC or the Rightsholder in connection therewith.

4. Indemnity. User hereby indemnifies and agrees to defend the Rightsholder and CCC, and their respective employees and directors, against all claims, liability, damages, costs and expenses, including legal fees and expenses, arising out of any use of a Work beyond the scope of the rights granted herein, or any use of a Work which has been altered in any unauthorized way by User, including claims of defamation or infringement of rights of copyright, publicity, privacy or other tangible or intangible property.

5. Limitation of Liability. UNDER NO CIRCUMSTANCES WILL CCC OR THE RIGHTSHOLDER BE LIABLE FOR ANY DIRECT, INDIRECT, CONSEQUENTIAL OR INCIDENTAL DAMAGES (INCLUDING WITHOUT LIMITATION DAMAGES FOR LOSS OF BUSINESS PROFITS OR INFORMATION, OR FOR BUSINESS INTERRUPTION) ARISING OUT OF THE USE OR INABILITY TO USE A WORK, EVEN IF ONE OF THEM HAS BEEN ADVISED OF THE POSSIBILITY OF SUCH DAMAGES. In any event, the total liability of the Rightsholder and CCC (including their respective employees and directors) shall not exceed the total amount actually paid by User for this license. User assumes full liability for the actions and omissions of its principals, employees, agents, affiliates, successors and assigns.

6. Limited Warranties. THE WORK(S) AND RIGHT(S) ARE PROVIDED "AS IS". CCC HAS THE RIGHT TO GRANT TO USER THE RIGHTS GRANTED IN THE ORDER CONFIRMATION DOCUMENT. CCC AND THE RIGHTSHOLDER DISCLAIM ALL OTHER WARRANTIES RELATING TO THE WORK(S) AND RIGHT(S), EITHER EXPRESS OR IMPLIED, INCLUDING WITHOUT LIMITATION IMPLIED WARRANTIES OF MERCHANTABILITY OR FITNESS FOR A PARTICULAR PURPOSE. ADDITIONAL RIGHTS MAY BE REQUIRED TO USE ILLUSTRATIONS, GRAPHS, PHOTOGRAPHS, ABSTRACTS, INSERTS OR OTHER PORTIONS OF THE WORK (AS OPPOSED TO THE ENTIRE WORK) IN A MANNER CONTEMPLATED BY USER; USER UNDERSTANDS AND AGREES THAT NEITHER CCC NOR THE RIGHTSHOLDER MAY HAVE SUCH ADDITIONAL RIGHTS TO GRANT.

7. Effect of Breach. Any failure by User to pay any amount when due, or any use by User of a Work beyond the scope of the license set forth in the Order Confirmation and/or these terms and conditions, shall be a material breach of the license created by the Order Confirmation and these terms and conditions. Any breach not cured within 30

7.1.3 Permission 4

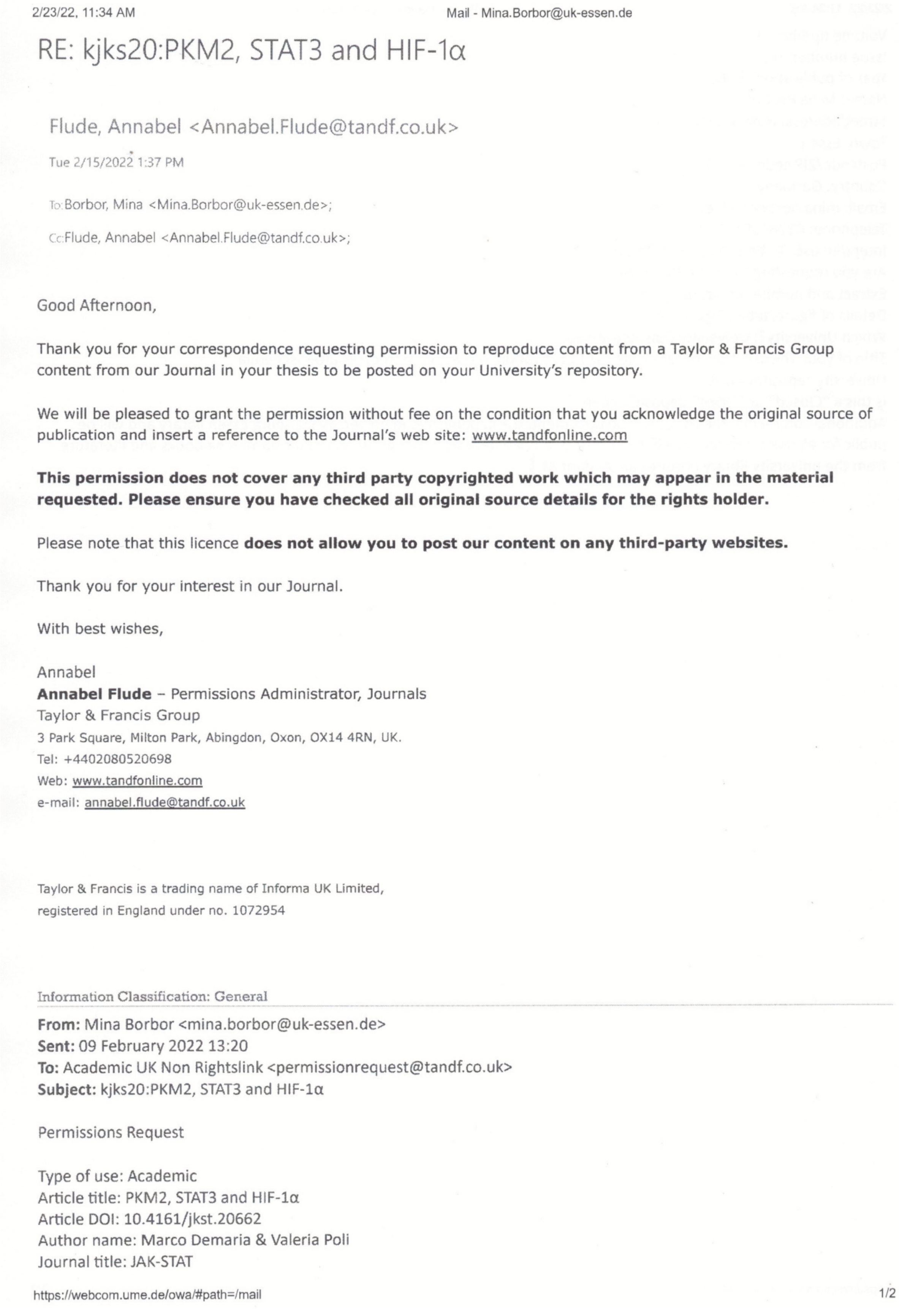

2/23/22, 11:34 AM Mail - Mina.Borbor@uk-essen.de

RE: kjks20:PKM2, STAT3 and HIF-1α

Flude, Annabel <Annabel.Flude@tandf.co.uk>

Tue 2/15/2022 1:37 PM

To: Borbor, Mina <Mina.Borbor@uk-essen.de>;

Cc: Flude, Annabel <Annabel.Flude@tandf.co.uk>;

Good Afternoon,

Thank you for your correspondence requesting permission to reproduce content from a Taylor & Francis Group content from our Journal in your thesis to be posted on your University's repository.

We will be pleased to grant the permission without fee on the condition that you acknowledge the original source of publication and insert a reference to the Journal's web site: www.tandfonline.com

This permission does not cover any third party copyrighted work which may appear in the material requested. Please ensure you have checked all original source details for the rights holder.

Please note that this licence **does not allow you to post our content on any third-party websites.**

Thank you for your interest in our Journal.

With best wishes,

Annabel
Annabel Flude – Permissions Administrator, Journals
Taylor & Francis Group
3 Park Square, Milton Park, Abingdon, Oxon, OX14 4RN, UK.
Tel: +4402080520698
Web: www.tandfonline.com
e-mail: annabel.flude@tandf.co.uk

Taylor & Francis is a trading name of Informa UK Limited,
registered in England under no. 1072954

Information Classification: General

From: Mina Borbor <mina.borbor@uk-essen.de>
Sent: 09 February 2022 13:20
To: Academic UK Non Rightslink <permissionrequest@tandf.co.uk>
Subject: kjks20:PKM2, STAT3 and HIF-1α

Permissions Request

Type of use: Academic
Article title: PKM2, STAT3 and HIF-1α
Article DOI: 10.4161/jkst.20662
Author name: Marco Demaria & Valeria Poli
Journal title: JAK-STAT

https://webcom.ume.de/owa/#path=/mail 1/2

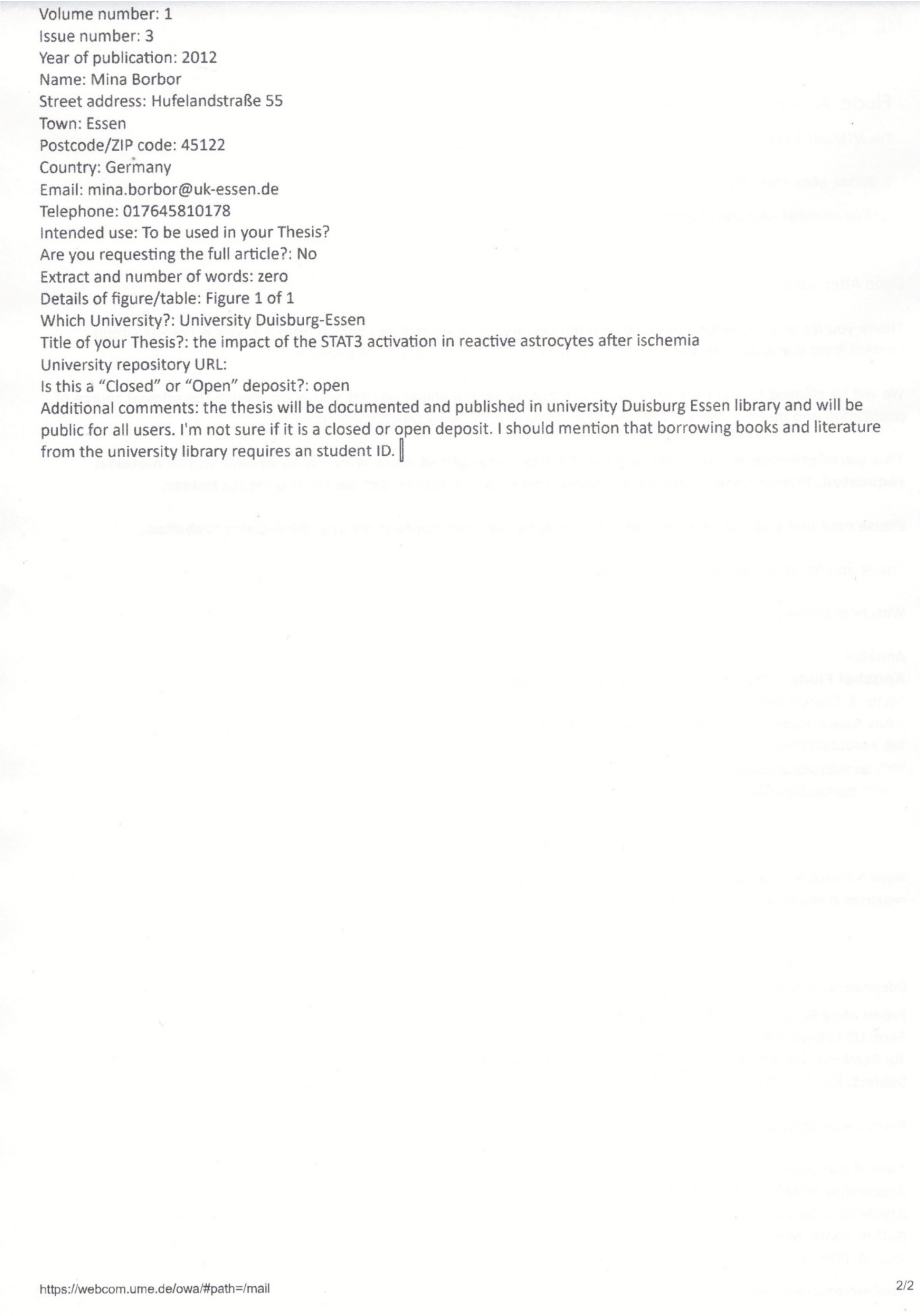

Volume number: 1
Issue number: 3
Year of publication: 2012
Name: Mina Borbor
Street address: Hufelandstraße 55
Town: Essen
Postcode/ZIP code: 45122
Country: Germany
Email: mina.borbor@uk-essen.de
Telephone: 017645810178
Intended use: To be used in your Thesis?
Are you requesting the full article?: No
Extract and number of words: zero
Details of figure/table: Figure 1 of 1
Which University?: University Duisburg-Essen
Title of your Thesis?: the impact of the STAT3 activation in reactive astrocytes after ischemia
University repository URL:
Is this a “Closed” or “Open” deposit?: open
Additional comments: the thesis will be documented and published in university Duisburg Essen library and will be public for all users. I'm not sure if it is a closed or open deposit. I should mention that borrowing books and literature from the university library requires an student ID.

7.1.4 Permission 5

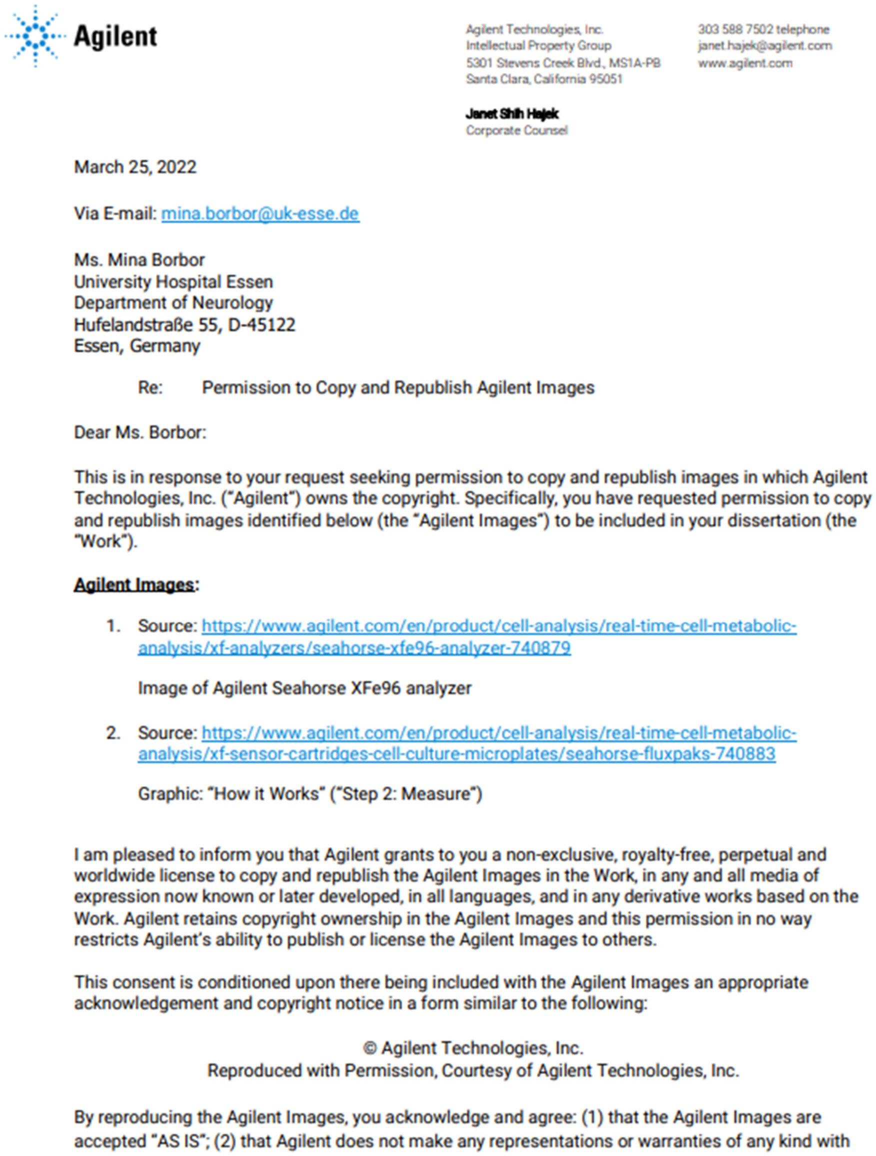

Agilent

Agilent Technologies, Inc.
Intellectual Property Group
5301 Stevens Creek Blvd., MS1A-PB
Santa Clara, California 95051

303 588 7502 telephone
janet.hajek@agilent.com
www.agilent.com

Janet Shih Hajek
Corporate Counsel

March 25, 2022

Via E-mail: mina.borbor@uk-esse.de

Ms. Mina Borbor
University Hospital Essen
Department of Neurology
Hufelandstraße 55, D-45122
Essen, Germany

Re: Permission to Copy and Republish Agilent Images

Dear Ms. Borbor:

This is in response to your request seeking permission to copy and republish images in which Agilent Technologies, Inc. ("Agilent") owns the copyright. Specifically, you have requested permission to copy and republish images identified below (the "Agilent Images") to be included in your dissertation (the "Work").

Agilent Images:

1. Source: https://www.agilent.com/en/product/cell-analysis/real-time-cell-metabolic-analysis/xf-analyzers/seahorse-xfe96-analyzer-740879

   Image of Agilent Seahorse XFe96 analyzer

2. Source: https://www.agilent.com/en/product/cell-analysis/real-time-cell-metabolic-analysis/xf-sensor-cartridges-cell-culture-microplates/seahorse-fluxpaks-740883

   Graphic: "How it Works" ("Step 2: Measure")

I am pleased to inform you that Agilent grants to you a non-exclusive, royalty-free, perpetual and worldwide license to copy and republish the Agilent Images in the Work, in any and all media of expression now known or later developed, in all languages, and in any derivative works based on the Work. Agilent retains copyright ownership in the Agilent Images and this permission in no way restricts Agilent's ability to publish or license the Agilent Images to others.

This consent is conditioned upon there being included with the Agilent Images an appropriate acknowledgement and copyright notice in a form similar to the following:

© Agilent Technologies, Inc.
Reproduced with Permission, Courtesy of Agilent Technologies, Inc.

By reproducing the Agilent Images, you acknowledge and agree: (1) that the Agilent Images are accepted "AS IS"; (2) that Agilent does not make any representations or warranties of any kind with

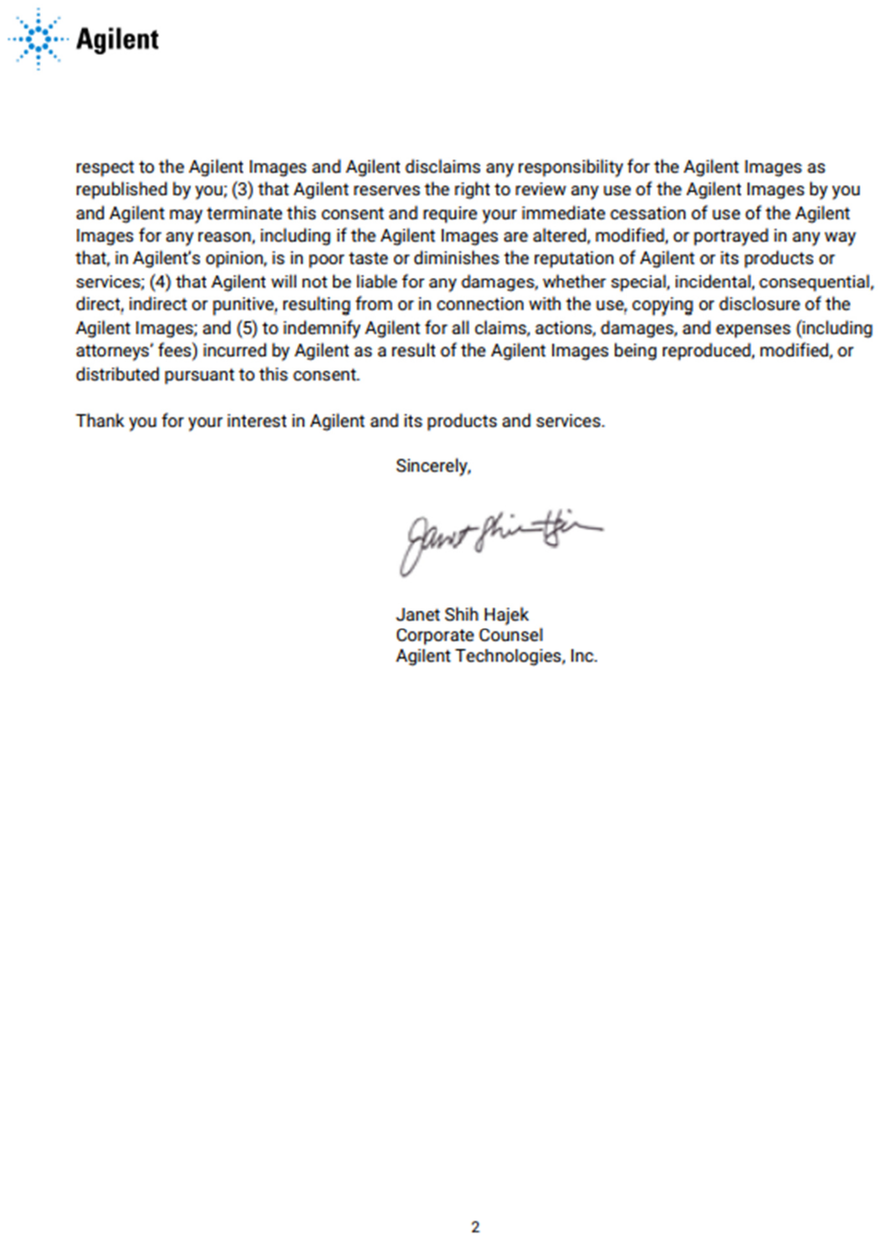

Agilent

respect to the Agilent Images and Agilent disclaims any responsibility for the Agilent Images as republished by you; (3) that Agilent reserves the right to review any use of the Agilent Images by you and Agilent may terminate this consent and require your immediate cessation of use of the Agilent Images for any reason, including if the Agilent Images are altered, modified, or portrayed in any way that, in Agilent's opinion, is in poor taste or diminishes the reputation of Agilent or its products or services; (4) that Agilent will not be liable for any damages, whether special, incidental, consequential, direct, indirect or punitive, resulting from or in connection with the use, copying or disclosure of the Agilent Images; and (5) to indemnify Agilent for all claims, actions, damages, and expenses (including attorneys' fees) incurred by Agilent as a result of the Agilent Images being reproduced, modified, or distributed pursuant to this consent.

Thank you for your interest in Agilent and its products and services.

Sincerely,

Janet Shih Hajek
Corporate Counsel
Agilent Technologies, Inc.

7.1.5 Permission 6

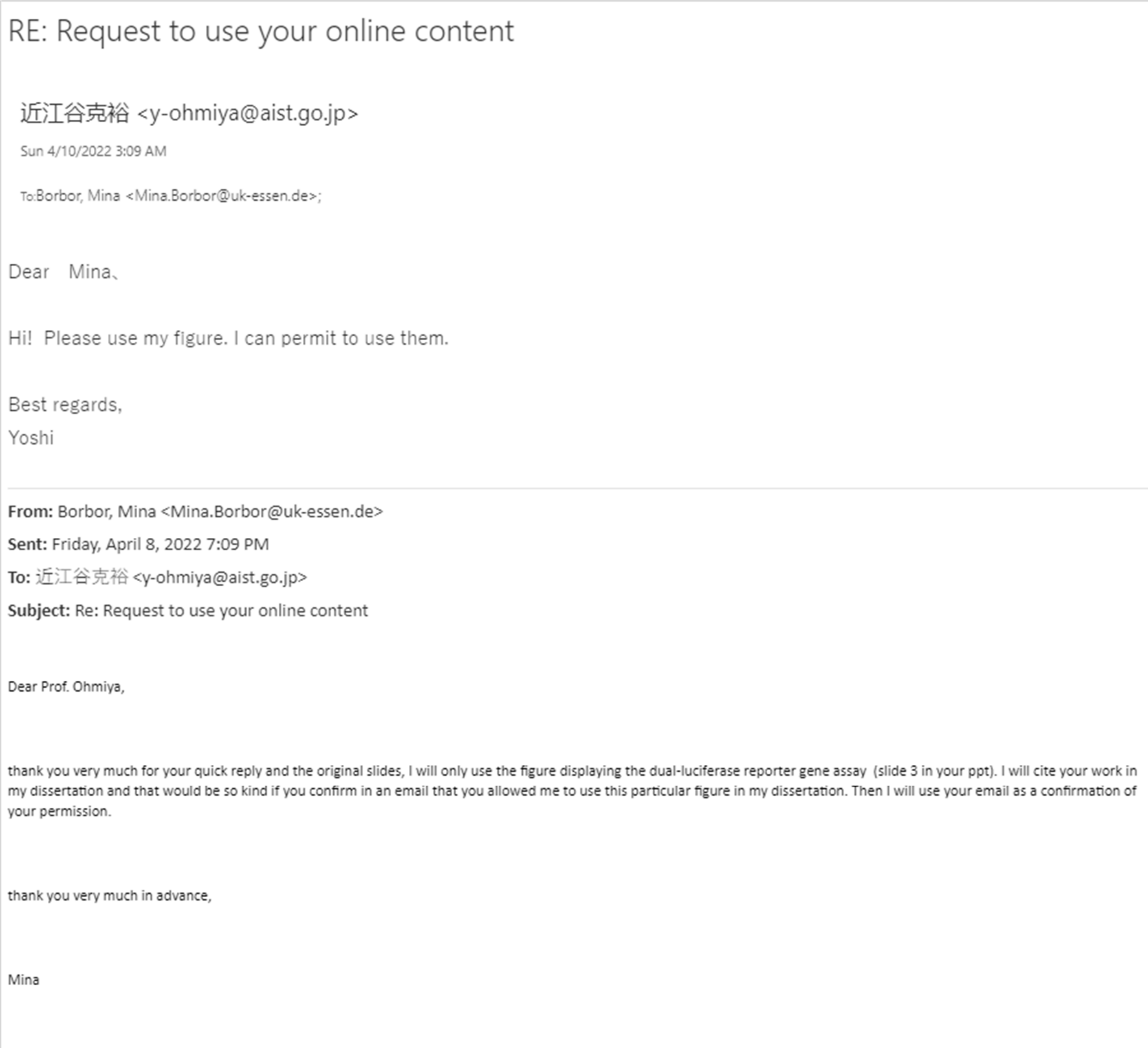

RE: Request to use your online content

近江谷克裕 <y-ohmiya@aist.go.jp>

Sun 4/10/2022 3:09 AM

To:Borbor, Mina <Mina.Borbor@uk-essen.de>;

Dear　Mina、

Hi! Please use my figure. I can permit to use them.

Best regards,
Yoshi

From: Borbor, Mina <Mina.Borbor@uk-essen.de>
Sent: Friday, April 8, 2022 7:09 PM
To: 近江谷克裕 <y-ohmiya@aist.go.jp>
Subject: Re: Request to use your online content

Dear Prof. Ohmiya,

thank you very much for your quick reply and the original slides, I will only use the figure displaying the dual-luciferase reporter gene assay (slide 3 in your ppt). I will cite your work in my dissertation and that would be so kind if you confirm in an email that you allowed me to use this particular figure in my dissertation. Then I will use your email as a confirmation of your permission.

thank you very much in advance,

Mina

7.2 Macros and scripts

7.2.1 Nuclear translocation

```
run("Multiply...", "value=5");
run("Subtract Background...", "rolling=50");
if (getTitle()==DAPI) {
run("Kuwahara Filter","sampling=9");
run("Gaussian Blur...", "sigma=2");
run("Maximum...","radius=4");
run("Auto Threshold", "method=Otsu white");
run("Fill Holes");
wait(1000);


selectWindow(DAPI);
run("Create Selection");
run("Enlarge...", "enlarge=-2 pixel");
selectWindow(NFKB);
rename(Title +" whole");
run("Multiply...", "value=3");
run("Gamma...", "value=1.40");
run("Measure");
run("Restore Selection");

rename(Title +" inside");
run("Measure");
run("Make Inverse");
rename(Title +" outside");
run("Measure");
close("*");
```

7.2.2 Glycogen bodies

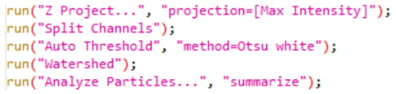

```
run("Z Project...", "projection=[Max Intensity]");
run("Split Channels");
run("Auto Threshold", "method=Otsu white");
run("Watershed");
run("Analyze Particles...", "summarize");
```

7.2.3 Nuclei count

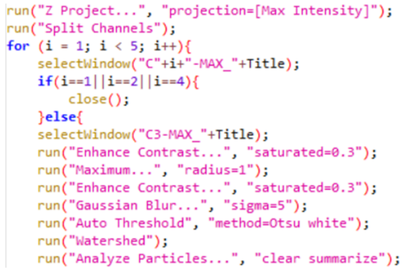

```
run("Z Project...", "projection=[Max Intensity]");
run("Split Channels");
for (i = 1; i < 5; i++){
    selectWindow("C"+i+"-MAX_"+Title);
    if(i==1||i==2||i==4){
        close();
    }else{
    selectWindow("C3-MAX_"+Title);
    run("Enhance Contrast...", "saturated=0.3");
    run("Maximum...", "radius=1");
    run("Enhance Contrast...", "saturated=0.3");
    run("Gaussian Blur...", "sigma=5");
    run("Auto Threshold", "method=Otsu white");
    run("Watershed");
    run("Analyze Particles...", "clear summarize");
```

7.2.4 Neurite density

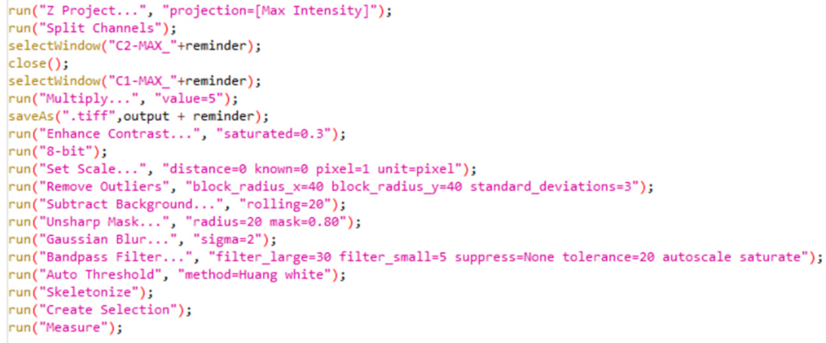

```
run("Z Project...", "projection=[Max Intensity]");
run("Split Channels");
selectWindow("C2-MAX_"+reminder);
close();
selectWindow("C1-MAX_"+reminder);
run("Multiply...", "value=5");
saveAs(".tiff",output + reminder);
run("Enhance Contrast...", "saturated=0.3");
run("8-bit");
run("Set Scale...", "distance=0 known=0 pixel=1 unit=pixel");
run("Remove Outliers", "block_radius_x=40 block_radius_y=40 standard_deviations=3");
run("Subtract Background...", "rolling=20");
run("Unsharp Mask...", "radius=20 mask=0.80");
run("Gaussian Blur...", "sigma=2");
run("Bandpass Filter...", "filter_large=30 filter_small=5 suppress=None tolerance=20 autoscale saturate");
run("Auto Threshold", "method=Huang white");
run("Skeletonize");
run("Create Selection");
run("Measure");
```

7.2.5 Preparation for synapse counter

```
run("Z Project...", "projection=[Max Intensity]");
run("8-bit");
run("Split Channels");
for (i = 1; i <= channels; i++) {
    selectWindow("C"+i+"-MAX_"+Title);
    rename("C"+i);
    test= "C"+i;
    if(postsynapse==test){
    run("Enhance Contrast...", "saturated=0.3");
}
}
run("Merge Channels...", "c1="+nuclei+" c2="+postsynapse+" c3="+presynapse+" keep");
run("Enhance Contrast...", "saturated=0.3");
saveAs(output+"merge"+Title+".tif");
rename(Title);
myImageID = getImageID();
makeRectangle(150, 150, 940, 940);
waitForUser("Hello please move the rectangle into an appropriate position");
selectImage(myImageID);
if (selectionType() != 0){
exit("Sorry, no rectangle");
}else{
run("Duplicate...", "title="+Title);
close("\\Others");
saveAs(output+Title+".tif");
}
close("*");
```

7.3 Supplementary data

7.3.1 IL6 after 3 h

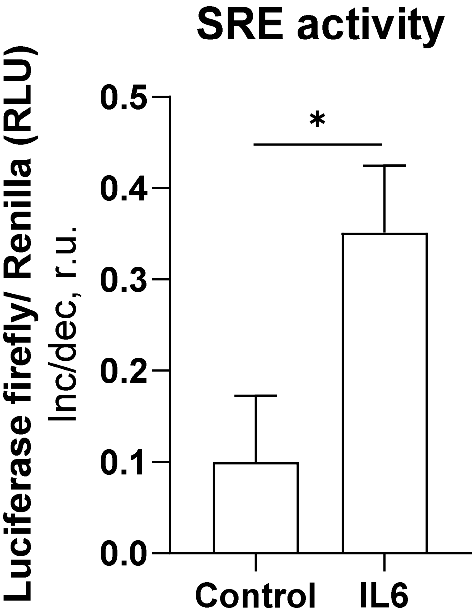

Figure 48: IL6 increases SRE activity after 3 h

SRE/SIE luciferase activity. Normalized difference (r.u.) with the vehicle (control) mean is shown as bar graph (Mean±SD). Significant changes with the control are noted as * $p \leq 0.05$/** $p \leq 0.005$/*** $p \leq 0.0005$, as indicated by two-tailed student t-tests, n=3..

8 Acknowledgements

This work is dedicated to all the little Iranian girls who dare to dream of becoming scientists, and to the scientists with big hearts who helped make that dream a reality for one of those girls.

First and foremost, I want to express my heartfelt gratitude to my soulmate, Till Neuhaus, who stood by me with unwavering support and love through every step of this journey. I also want to thank my Iranian family, including my Dadashi, Aji Jooni, and Muli, as well as my maman joon and baba joon, for their strength and unwavering love, even when we were far apart.

I am forever grateful to my late grandmother, Zia maman, who remains an inspiring figure in my life.

Special thanks go to my German family, including Jürgen Golan and all the Neuhaus family, especially Mattis the knight, Kaami the little prince, Yam, and Pati, as well as my friends Hanieh and Claas, who brought love and happiness into my life.

I am indebted to Prof. Dirk Hermann for believing in me and making this project possible. I would also like to acknowledge my colleagues in the NeuroScienceLab, particularly Dr. Egor Dzyubenko and Dr. Ulf Brockmeier, for their brilliant technical supervision and the long discussions we had to overcome the project's milestones. My special thanks go to Mattias Pillath-Eilers and Marius Doeckel for being fantastic team members, Dr. Ayan Mohamud Yusuf and Britta Kaltwasser for their technical and emotional support, and Dr. Chen Wang for being my adorable bestie.

I would like to express my greatest appreciation to my colleagues in the CardioScienceLabs, particularly Andrea Odersky.

Finally, I want to acknowledge the BIOME graduate school, particularly the ischemia-reperfusion core, for training us to be professional, fair, and happy scientists.

Through your support, love, and dedication, you have made an incredible impact on my life and helped me achieve my dreams. I hope that our work inspires the next generation of young scientists and change-makers to push boundaries and make a positive impact in the world. Together, we can make a difference and shape a brighter future for all.

9 Declarations

In accordance with § 6 (para. 2, clause g) of the Regulations Governing the Doctoral Proceedings of the Faculty of Biology for awarding the doctoral degree Dr. rer. nat., I hereby declare that I represent the field to which the topic "STAT3-induced metabolic reprogramming in post-ischemic astrocytes and the further impact on neuronal respiration and synaptogenesis" is assigned in research and teaching and that I support the application of Mina Borbor.

Essen,
date

	Name of the scientific supervisor/member of the University of Duisburg-Essen	Signature of the supervisor/member of the University of Duisburg Essen

Declaration:

In accordance with § 7 (para. 2, clause d and f) of the Regulations Governing the Doctoral Proceedings of the Faculty of Biology for awarding the doctoral degree Dr. rer. nat., I hereby declare that I have written the herewith submitted dissertation independently using only the materials listed, and have cited all sources taken over verbatim or in content as such.

Essen,
date

Signature of the doctoral candidate

Declaration:

In accordance with § 7 (para. 2, clause e and g) of the Regulations Governing the Doctoral Proceedings of the Faculty of Biology for awarding the doctoral degree Dr. rer. nat., I hereby declare that I have undertaken no previous attempts to attain a doctoral degree, that the current work has not been rejected by any other faculty, and that I am submitting the dissertation only in this procedure.

Essen,
date

Signature of the doctoral candidate

10 References

Alamowitch, S., M. Eliasziw, A. Algra, H. Meldrum, H. J. Barnett, and Group North American Symptomatic Carotid Endarterectomy Trial. 2001. 'Risk, causes, and prevention of ischaemic stroke in elderly patients with symptomatic internal-carotid-artery stenosis', *Lancet*, 357: 1154-60.

Allott, Louis, Diana Brickute, Cen Chen, Marta Braga, Chris Barnes, Ning Wang, and Eric O. Aboagye. 2020. 'Development of a fluorine-18 radiolabelled fluorescent chalcone: evaluated for detecting glycogen', *EJNMMI Radiopharmacy and Chemistry*, 5: 17.

Andersen, J. V., S. K. Christensen, E. W. Westi, M. Diaz-delCastillo, H. Tanila, A. Schousboe, B. I. Aldana, and H. S. Waagepetersen. 2021. 'Deficient astrocyte metabolism impairs glutamine synthesis and neurotransmitter homeostasis in a mouse model of Alzheimer's disease', *Neurobiol Dis*, 148: 105198.

Anderson, T. R., C. R. Jarvis, A. J. Biedermann, C. Molnar, and R. D. Andrew. 2005. 'Blocking the anoxic depolarization protects without functional compromise following simulated stroke in cortical brain slices', *J Neurophysiol*, 93: 963-79.

Aoyama, K., M. Watabe, and T. Nakaki. 2008. 'Regulation of neuronal glutathione synthesis', *J Pharmacol Sci*, 108: 227-38.

Bak, L. K., A. Schousboe, and H. S. Waagepetersen. 2006. 'The glutamate/GABA-glutamine cycle: aspects of transport, neurotransmitter homeostasis and ammonia transfer', *J Neurochem*, 98: 641-53.

Balmer, M. L., E. H. Ma, G. R. Bantug, J. Grahlert, S. Pfister, T. Glatter, A. Jauch, S. Dimeloe, E. Slack, P. Dehio, M. A. Krzyzaniak, C. G. King, A. V. Burgener, M. Fischer, L. Develioglu, R. Belle, M. Recher, W. V. Bonilla, A. J. Macpherson, S. Hapfelmeier, R. G. Jones, and C. Hess. 2016. 'Memory CD8(+) T Cells Require Increased Concentrations of Acetate Induced by Stress for Optimal Function', *Immunity*, 44: 1312-24.

Becerra-Calixto, A., and G. P. Cardona-Gomez. 2017. 'The Role of Astrocytes in Neuroprotection after Brain Stroke: Potential in Cell Therapy', *Front Mol Neurosci*, 10: 88.

Benarroch, E. E. 2010. 'Glycogen metabolism: metabolic coupling between astrocytes and neurons', *Neurology*, 74: 919-23.

Benedict, Christian, Manfred Hallschmid, Katrin Schmitz, Bernd Schultes, Frank Ratter, Horst L. Fehm, Jan Born, and Werner Kern. 2007. 'Intranasal Insulin Improves Memory in Humans: Superiority of Insulin Aspart', *Neuropsychopharmacology*, 32: 239-43.

Berridge, M. V., and A. S. Tan. 1993. 'Characterization of the cellular reduction of 3-(4,5-dimethylthiazol-2-yl)-2,5-diphenyltetrazolium bromide (MTT): subcellular localization, substrate dependence, and involvement of mitochondrial electron transport in MTT reduction', *Arch Biochem Biophys*, 303: 474-82.

BiochenDen. 2020. 'Glycogenesis: How to Synthesize Glycogen?', BiochenDen, Accessed 2020. https://biochemden.com/carbohydrate-metabolism-glycogenesis/.

Bonni, A., Y. Sun, M. Nadal-Vicens, A. Bhatt, D. A. Frank, I. Rozovsky, N. Stahl, G. D. Yancopoulos, and M. E. Greenberg. 1997. 'Regulation of gliogenesis in the central nervous system by the JAK-STAT signaling pathway', *Science*, 278: 477-83.

Brennan, A. M., S. W. Suh, S. J. Won, P. Narasimhan, T. M. Kauppinen, H. Lee, Y. Edling, P. H. Chan, and R. A. Swanson. 2009. 'NADPH oxidase is the primary source of superoxide induced by NMDA receptor activation', *Nat Neurosci*, 12: 857-63.

Brown, A. M., S. B. Tekkok, and B. R. Ransom. 2003. 'Glycogen regulation and functional role in mouse white matter', *J Physiol*, 549: 501-12.

Bush, T. G., N. Puvanachandra, C. H. Horner, A. Polito, T. Ostenfeld, C. N. Svendsen, L. Mucke, M. H. Johnson, and M. V. Sofroniew. 1999. 'Leukocyte infiltration, neuronal degeneration, and neurite outgrowth after ablation of scar-forming, reactive astrocytes in adult transgenic mice', *Neuron*, 23: 297-308.

Cai, Y., H. Guo, Z. Fan, X. Zhang, D. Wu, W. Tang, T. Gu, S. Wang, A. Yin, L. Tao, X. Ji, H. Dong, Y. Li, and L. Xiong. 2020. 'Glycogenolysis Is Crucial for Astrocytic Glycogen Accumulation and Brain Damage after Reperfusion in Ischemic Stroke', *iScience*, 23: 101136.

Camporeale, A., M. Demaria, E. Monteleone, C. Giorgi, M. R. Wieckowski, P. Pinton, and V. Poli. 2014. 'STAT3 Activities and Energy Metabolism: Dangerous Liaisons', *Cancers (Basel)*, 6: 1579-96.

Candelario-Jalil, E. 2009. 'Injury and repair mechanisms in ischemic stroke: considerations for the development of novel neurotherapeutics', *Curr Opin Investig Drugs*, 10: 644-54.

Castro, M. A., C. Angulo, S. Brauchi, F. Nualart, and Concha, II. 2008. 'Ascorbic acid participates in a general mechanism for concerted glucose transport inhibition and lactate transport stimulation', *Pflugers Arch*, 457: 519-28.

Castro, M. A., F. A. Beltran, S. Brauchi, and Concha, II. 2009. 'A metabolic switch in brain: glucose and lactate metabolism modulation by ascorbic acid', *J Neurochem*, 110: 423-40.

Castro, M. A., M. Pozo, C. Cortes, L. Garcia Mde, Concha, II, and F. Nualart. 2007. 'Intracellular ascorbic acid inhibits transport of glucose by neurons, but not by astrocytes', *J Neurochem*, 102: 773-82.

Ceyzeriat, K., L. Abjean, M. A. Carrillo-de Sauvage, L. Ben Haim, and C. Escartin. 2016. 'The complex STATes of astrocyte reactivity: How are they controlled by the JAK-STAT3 pathway?', *Neuroscience*, 330: 205-18.

Chang, C. Y., J. Y. Chen, M. H. Wu, and M. L. Hu. 2020. 'Therapeutic treatment with vitamin C reduces focal cerebral ischemia-induced brain infarction in rats by attenuating disruptions of blood brain barrier and cerebral neuronal apoptosis', *Free Radic Biol Med*, 155: 29-36.

Chen, R., U. H. Lai, L. Zhu, A. Singh, M. Ahmed, and N. R. Forsyth. 2018. 'Reactive Oxygen Species Formation in the Brain at Different Oxygen Levels: The Role of Hypoxia Inducible Factors', *Front Cell Dev Biol*, 6: 132.

Chen, Y., and R. A. Swanson. 2003. 'Astrocytes and brain injury', *J Cereb Blood Flow Metab*, 23: 137-49.

Cheng, X., H. Zhao, F. Yan, Z. Tao, R. Wang, Z. Han, G. Li, Y. Luo, and X. Ji. 2018. 'Limb remote ischemic post-conditioning mitigates brain recovery in a mouse model of ischemic stroke by regulating reactive astrocytic plasticity', *Brain Res*, 1686: 94-100.

Choi, J. S., S. Y. Kim, J. H. Cha, Y. S. Choi, K. W. Sung, S. T. Oh, O. N. Kim, J. W. Chung, M. H. Chun, S. B. Lee, and M. Y. Lee. 2003. 'Upregulation of gp130 and STAT3 activation in the rat hippocampus following transient forebrain ischemia', *Glia*, 41: 237-46.

Chung, C. D., J. Liao, B. Liu, X. Rao, P. Jay, P. Berta, and K. Shuai. 1997. 'Specific inhibition of Stat3 signal transduction by PIAS3', *Science*, 278: 1803-5.

Chung, J., E. Uchida, T. C. Grammer, and J. Blenis. 1997. 'STAT3 serine phosphorylation by ERK-dependent and -independent pathways negatively modulates its tyrosine phosphorylation', *Mol Cell Biol*, 17: 6508-16.

Clark, W. M., G. W. Albers, K. P. Madden, and S. Hamilton. 2000. 'The rtPA (alteplase) 0- to 6-hour acute stroke trial, part A (A0276g) : results of a double-blind, placebo-controlled, multicenter study. Thromblytic therapy in acute ischemic stroke study investigators', *Stroke*, 31: 811-6.

Coco, S., F. Calegari, E. Pravettoni, D. Pozzi, E. Taverna, P. Rosa, M. Matteoli, and C. Verderio. 2003. 'Storage and release of ATP from astrocytes in culture', *J Biol Chem*, 278: 1354-62.

Costa, S., T. Planchenault, C. Charriere-Bertrand, Y. Mouchel, C. Fages, S. Juliano, T. Lefrancois, G. Barlovatz-Meimon, and M. Tardy. 2002. 'Astroglial permissivity for neuritic outgrowth in neuron-astrocyte cocultures depends on regulation of laminin bioavailability', *Glia*, 37: 105-13.

D'Andrea Meira, I., T. T. Romao, H. J. Pires do Prado, L. T. Kruger, M. E. P. Pires, and P. O. da Conceicao. 2019. 'Ketogenic Diet and Epilepsy: What We Know So Far', *Front Neurosci*, 13: 5.

Dabir, S., A. Kluge, and A. Dowlati. 2009. 'The association and nuclear translocation of the PIAS3-STAT3 complex is ligand and time dependent', *Mol Cancer Res*, 7: 1854-60.

Daskalopoulos, R., J. Korcok, L. Tao, and J. X. Wilson. 2002. 'Accumulation of intracellular ascorbate from dehydroascorbic acid by astrocytes is decreased after oxidative stress and restored by propofol', *Glia*, 39: 124-32.

Demaria, M., and V. Poli. 2012. 'PKM2, STAT3 and HIF-1alpha: The Warburg's vicious circle', *JAKSTAT*, 1: 194-6.

Dirnagl, Ulrich, Costantino Iadecola, and Michael A. Moskowitz. 1999. 'Pathobiology of ischaemic stroke: an integrated view', *Trends in Neurosciences*, 22: 391-97.

Dzyubenko, E., A. Rozenberg, D. M. Hermann, and A. Faissner. 2016. 'Colocalization of synapse marker proteins evaluated by STED-microscopy reveals patterns of neuronal synapse distribution in vitro', *J Neurosci Methods*, 273: 149-59.

Emani, S. M., B. L. Piekarski, D. Harrild, P. J. Del Nido, and J. D. McCully. 2017. 'Autologous mitochondrial transplantation for dysfunction after ischemia-reperfusion injury', *J Thorac Cardiovasc Surg*, 154: 286-89.

Falchi, A. M., V. Sogos, F. Saba, M. Piras, T. Congiu, and M. Piludu. 2013. 'Astrocytes shed large membrane vesicles that contain mitochondria, lipid droplets and ATP', *Histochem Cell Biol*, 139: 221-31.

Feinkohl, I., P. P. Aung, M. Keller, C. M. Robertson, J. R. Morling, S. McLachlan, I. J. Deary, B. M. Frier, M. W. Strachan, J. F. Price, and Investigators Edinburgh Type 2 Diabetes Study. 2014. 'Severe hypoglycemia and cognitive decline in older people with type 2 diabetes: the Edinburgh type 2 diabetes study', *Diabetes Care*, 37: 507-15.

Galderisi, U., G. Peluso, and G. Di Bernardo. 2022. 'Clinical Trials Based on Mesenchymal Stromal Cells are Exponentially Increasing: Where are We in Recent Years?', *Stem Cell Rev Rep*, 18: 23-36.

Gandhi, G. K., N. F. Cruz, K. K. Ball, and G. A. Dienel. 2009. 'Astrocytes are poised for lactate trafficking and release from activated brain and for supply of glucose to neurons', *J Neurochem*, 111: 522-36.

Gao, X., H. Wang, J. J. Yang, X. Liu, and Z. R. Liu. 2012. 'Pyruvate kinase M2 regulates gene transcription by acting as a protein kinase', *Mol Cell*, 45: 598-609.

Ge, H., Y. Wen, G. Yang, and A. L. Betz. 2000. 'Increased expression of intercellular adhesion molecule-1 in mouse focal cerebral ischemia model', *Chin Med J (Engl)*, 113: 75-9.

Goldman, S. A., W. A. Pulsinelli, W. Y. Clarke, R. P. Kraig, and F. Plum. 1989. 'The effects of extracellular acidosis on neurons and glia in vitro', *J Cereb Blood Flow Metab*, 9: 471-7.

Gottschling, C., E. Dzyubenko, M. Geissler, and A. Faissner. 2016. 'The Indirect Neuron-astrocyte Coculture Assay: An In Vitro Set-up for the Detailed Investigation of Neuron-glia Interactions', *J Vis Exp*.

Gruetter, R. 2003. 'Glycogen: the forgotten cerebral energy store', *J Neurosci Res*, 74: 179-83.

Guo, H., Z. Fan, S. Wang, L. Ma, J. Wang, D. Yu, Z. Zhang, L. Wu, Z. Peng, W. Liu, W. Hou, and Y. Cai. 2021. 'Astrocytic A1/A2 paradigm participates in glycogen mobilization mediated neuroprotection on reperfusion injury after ischemic stroke', *J Neuroinflammation*, 18: 230.

Hacke, W., M. Kaste, E. Bluhmki, M. Brozman, A. Davalos, D. Guidetti, V. Larrue, K. R. Lees, Z. Medeghri, T. Machnig, D. Schneider, R. von Kummer, N. Wahlgren, D. Toni, and Ecass Investigators. 2008. 'Thrombolysis with alteplase 3 to 4.5 hours after acute ischemic stroke', *N Engl J Med*, 359: 1317-29.

Hakim, A. M. 1998. 'Ischemic penumbra: the therapeutic window', *Neurology*, 51: S44-6.

Hallschmid, M., and B. Schultes. 2009. 'Central nervous insulin resistance: a promising target in the treatment of metabolic and cognitive disorders?', *Diabetologia*, 52: 2264-69.

Harada, K., T. Kamiya, and T. Tsuboi. 2015. 'Gliotransmitter Release from Astrocytes: Functional, Developmental, and Pathological Implications in the Brain', *Front Neurosci*, 9: 499.

Hata, R., K. Maeda, D. Hermann, G. Mies, and K. A. Hossmann. 2000. 'Dynamics of regional brain metabolism and gene expression after middle cerebral artery occlusion in mice', *J Cereb Blood Flow Metab*, 20: 306-15.

Hayakawa, K., E. Esposito, X. Wang, Y. Terasaki, Y. Liu, C. Xing, X. Ji, and E. H. Lo. 2016. 'Transfer of mitochondria from astrocytes to neurons after stroke', *Nature*, 535: 551-5.

Heinrich, P. C., I. Behrmann, S. Haan, H. M. Hermanns, G. Muller-Newen, and F. Schaper. 2003. 'Principles of interleukin (IL)-6-type cytokine signalling and its regulation', *Biochem J*, 374: 1-20.

Heiss, W. D., L. W. Kracht, A. Thiel, M. Grond, and G. Pawlik. 2001. 'Penumbral probability thresholds of cortical flumazenil binding and blood flow predicting tissue outcome in patients with cerebral ischaemia', *Brain*, 124: 20-9.

Henneberger, C., T. Papouin, S. H. Oliet, and D. A. Rusakov. 2010. 'Long-term potentiation depends on release of D-serine from astrocytes', *Nature*, 463: 232-6.

Herrmann, J. E., T. Imura, B. Song, J. Qi, Y. Ao, T. K. Nguyen, R. A. Korsak, K. Takeda, S. Akira, and M. V. Sofroniew. 2008. 'STAT3 is a critical regulator of astrogliosis and scar formation after spinal cord injury', *J Neurosci*, 28: 7231-43.

Hertz, L., B. S. O'Dowd, K. T. Ng, and M. E. Gibbs. 2003. 'Reciprocal changes in forebrain contents of glycogen and of glutamate/glutamine during early memory consolidation in the day-old chick', *Brain Res*, 994: 226-33.

Hertz, L., L. Peng, and G. A. Dienel. 2007. 'Energy metabolism in astrocytes: high rate of oxidative metabolism and spatiotemporal dependence on glycolysis/glycogenolysis', *J Cereb Blood Flow Metab*, 27: 219-49.

Hillered, L., B. K. Siesjo, and K. E. Arfors. 1984. 'Mitochondrial response to transient forebrain ischemia and recirculation in the rat', *J Cereb Blood Flow Metab*, 4: 438-46.

Huang, L., S. Li, Q. Dai, A. Zhang, Q. Yu, W. Du, P. Zhao, Y. Mo, K. Xu, S. Chen, and J. Wang. 2020. 'Astrocytic Yes-associated protein attenuates cerebral ischemia-induced brain injury by regulating signal transducer and activator of transcription 3 signaling', *Exp Neurol*, 333: 113431.

Hui, C., P. Tadi, and L. Patti. 2022. 'Ischemic Stroke.' in, *StatPearls* (Treasure Island (FL)).

Joshi, A. U., P. S. Minhas, S. A. Liddelow, B. Haileselassie, K. I. Andreasson, G. W. Dorn, 2nd, and D. Mochly-Rosen. 2019. 'Fragmented mitochondria released from microglia trigger A1 astrocytic response and propagate inflammatory neurodegeneration', *Nat Neurosci*, 22: 1635-48.

Judge, A., and M. S. Dodd. 2020. 'Metabolism', *Essays Biochem*, 64: 607-47.

Jung, J. E., G. S. Kim, and P. H. Chan. 2011. 'Neuroprotection by interleukin-6 is mediated by signal transducer and activator of transcription 3 and antioxidative signaling in ischemic stroke', *Stroke*, 42: 3574-9.

Jung, J. E., G. S. Kim, P. Narasimhan, Y. S. Song, and P. H. Chan. 2009. 'Regulation of Mn-superoxide dismutase activity and neuroprotection by STAT3 in mice after cerebral ischemia', *J Neurosci*, 29: 7003-14.

Justicia, C., C. Gabriel, and A. M. Planas. 2000. 'Activation of the JAK/STAT pathway following transient focal cerebral ischemia: signaling through Jak1 and Stat3 in astrocytes', *Glia*, 30: 253-70.

Kajihara, H., E. Tsutsumi, A. Kinoshita, J. Nakano, K. Takagi, and S. Takeo. 2001. 'Activated astrocytes with glycogen accumulation in ischemic penumbra during the early stage of brain infarction: immunohistochemical and electron microscopic studies', *Brain Res*, 909: 92-101.

Kathagen, A., A. Schulte, G. Balcke, H. S. Phillips, T. Martens, J. Matschke, H. S. Gunther, R. Soriano, Z. Modrusan, T. Sandmann, C. Kuhl, A. Tissier, M. Holz, L. A. Krawinkel, M. Glatzel, M. Westphal, and K. Lamszus. 2013. 'Hypoxia and oxygenation induce a metabolic switch between pentose phosphate pathway and glycolysis in glioma stem-like cells', *Acta Neuropathol*, 126: 763-80.

Khandelwal, R. L., T. L. Enno, and N. Narayanan. 1984. 'Effects of age on glycogen synthase and phosphorylase activities in rat liver', *Mech Ageing Dev*, 28: 13-22.

Kim, J. Y., J. Park, J. Y. Chang, S. H. Kim, and J. E. Lee. 2016. 'Inflammation after Ischemic Stroke: The Role of Leukocytes and Glial Cells', *Exp Neurobiol*, 25: 241-51.

Kindy, M. S., A. N. Bhat, and N. R. Bhat. 1992. 'Transient ischemia stimulates glial fibrillary acid protein and vimentin gene expression in the gerbil neocortex, striatum and hippocampus', *Brain Res Mol Brain Res*, 13: 199-206.

Kraig, R. P., and M. Chesler. 1990. 'Astrocytic acidosis in hyperglycemic and complete ischemia', *J Cereb Blood Flow Metab*, 10: 104-14.

Kraig, R. P., W. A. Pulsinelli, and F. Plum. 1985. 'Hydrogen ion buffering during complete brain ischemia', *Brain Res*, 342: 281-90.

Kristian, T., and B. K. Siesjo. 1998. 'Calcium in ischemic cell death', *Stroke*, 29: 705-18.

Krueger, M., B. Mages, C. Hobusch, and D. Michalski. 2019. 'Endothelial edema precedes blood-brain barrier breakdown in early time points after experimental focal cerebral ischemia', *Acta Neuropathol Commun*, 7: 17.

L, L., W. X, and Y. Z. 2016. 'Ischemia-reperfusion Injury in the Brain: Mechanisms and Potential Therapeutic Strategies', *Biochem Pharmacol (Los Angel)*, 5.

Lagadic-Gossmann, D., L. Huc, and V. Lecureur. 2004. 'Alterations of intracellular pH homeostasis in apoptosis: origins and roles', *Cell Death Differ*, 11: 953-61.

Lallukka, T., J. Ervasti, E. Lundstrom, E. Mittendorfer-Rutz, E. Friberg, M. Virtanen, and K. Alexanderson. 2018. 'Trends in Diagnosis-Specific Work Disability Before and After Stroke: A Longitudinal Population-Based Study in Sweden', *J Am Heart Assoc*, 7.

Lane, D. J., and A. Lawen. 2013. 'The glutamate aspartate transporter (GLAST) mediates L-glutamate-stimulated ascorbate-release via swelling-activated anion channels in cultured neonatal rodent astrocytes', *Cell Biochem Biophys*, 65: 107-19.

Le Foll, C., and B. E. Levin. 2016. 'Fatty acid-induced astrocyte ketone production and the control of food intake', *Am J Physiol Regul Integr Comp Physiol*, 310: R1186-92.

LeComte, Matthew D., Issei S. Shimada, Casey Sherwin, and Jeffrey L. Spees. 2015. 'Notch1–STAT3–ETB_R signaling axis controls reactive astrocyte proliferation after brain injury', *Proceedings of the National Academy of Sciences*, 112: 8726-31.

Letra-Vilela, R., B. Cardoso, C. Silva-Almeida, A. Maia Rocha, F. Murtinheira, J. Branco-Santos, C. Rodriguez, V. Martin, M. Santa-Marta, and F. Herrera. 2020. 'Can asymmetric post-translational modifications regulate the behavior of STAT3 homodimers?', *FASEB Bioadv*, 2: 116-25.

Li, C., M. K. H. Cheung, S. Han, Z. Zhang, L. Chen, J. Chen, H. Zeng, and J. Qiu. 2019. 'Mesenchymal stem cells and their mitochondrial transfer: a double-edged sword', *Biosci Rep*, 39.

Li, L., A. Lundkvist, D. Andersson, U. Wilhelmsson, N. Nagai, A. C. Pardo, C. Nodin, A. Stahlberg, K. Aprico, K. Larsson, T. Yabe, L. Moons, A. Fotheringham, I. Davies, P. Carmeliet, J. P. Schwartz, M. Pekna, M. Kubista, F. Blomstrand, N. Maragakis, M. Nilsson, and M. Pekny. 2008. 'Protective role of reactive astrocytes in brain ischemia', *J Cereb Blood Flow Metab*, 28: 468-81.

Li, S., G. J. Xiong, N. Huang, and Z. H. Sheng. 2020. 'The cross-talk of energy sensing and mitochondrial anchoring sustains synaptic efficacy by maintaining presynaptic metabolism', *Nat Metab*, 2: 1077-95.

Li, Y., J. Sun, R. Wu, J. Bai, Y. Hou, Y. Zeng, Y. Zhang, X. Wang, Z. Wang, and X. Meng. 2020. 'Mitochondrial MPTP: A Novel Target of Ethnomedicine for Stroke Treatment by Apoptosis Inhibition', *Front Pharmacol*, 11: 352.

Liang, Q., C. Ma, Y. Zhao, G. Gao, and J. Ma. 2013. 'Inhibition of STAT3 reduces astrocytoma cell invasion and constitutive activation of STAT3 predicts poor prognosis in human astrocytoma', *PLoS One*, 8: e84723.

Liddelow, S. A., and B. A. Barres. 2017. 'Reactive Astrocytes: Production, Function, and Therapeutic Potential', *Immunity*, 46: 957-67.

Liddelow, S. A., K. A. Guttenplan, L. E. Clarke, F. C. Bennett, C. J. Bohlen, L. Schirmer, M. L. Bennett, A. E. Munch, W. S. Chung, T. C. Peterson, D. K. Wilton, A. Frouin, B. A. Napier, N. Panicker, M. Kumar, M. S. Buckwalter, D. H. Rowitch, V. L. Dawson, T. M. Dawson, B. Stevens, and B. A. Barres. 2017. 'Neurotoxic reactive astrocytes are induced by activated microglia', *Nature*, 541: 481-87.

Liebeskind, D. S., E. Juttler, Y. Shapovalov, A. Yegin, J. Landen, and E. C. Jauch. 2019. 'Cerebral Edema Associated With Large Hemispheric Infarction', *Stroke*, 50: 2619-25.

Liesz, Arthur, Alexander Dalpke, Eva Mracsko, Stefan Roth, Wei Zhou, Huan Yang, Shin-Young Na, Mustafa Akhisaroglu, Thomas Fleming, Tatjana Eigenbrod, Peter P. Nawroth, Kevin J. Tracey, and Roland Veltkamp. 2015. 'DAMP Signaling is a Key Pathway Inducing Immune Modulation after Brain Injury', *The Journal of Neuroscience*, 35: 583-98.

Liu, S., S. R. Levine, and H. R. Winn. 2010. 'Targeting ischemic penumbra: part I - from pathophysiology to therapeutic strategy', *J Exp Stroke Transl Med*, 3: 47-55.

Liu, X., X. Zhang, J. Zhang, N. Kang, N. Zhang, H. Wang, J. Xue, J. Yu, Y. Yang, H. Cui, L. Cui, L. Wang, and X. Wang. 2014. 'Diosmin protects against cerebral ischemia/reperfusion injury through activating JAK2/STAT3 signal pathway in mice', *Neuroscience*, 268: 318-27.

Lo, E. H. 2008. 'A new penumbra: transitioning from injury into repair after stroke', *Nat Med*, 14: 497-500.

Lopez-Fabuel, I., J. Le Douce, A. Logan, A. M. James, G. Bonvento, M. P. Murphy, A. Almeida, and J. P. Bolanos. 2016. 'Complex I assembly into supercomplexes determines differential mitochondrial ROS production in neurons and astrocytes', *Proc Natl Acad Sci U S A*, 113: 13063-68.

Ludikhuize, M. C., M. Meerlo, B. M. T. Burgering, and M. J. Rodriguez Colman. 2021. 'Protocol to profile the bioenergetics of organoids using Seahorse', *STAR Protoc*, 2: 100386.

lukemiller.org. 2010. 'Analyzing gels and western blots with ImageJ', lukemiller.org. https://lukemiller.org/index.php/2010/11/analyzing-gels-and-western-blots-with-image-j/.

Luo, L. L., Y. F. Li, H. M. Shan, L. P. Wang, F. Yuan, Y. Y. Ma, W. L. Li, T. T. He, Y. Y. Wang, M. J. Qu, H. B. Liang, Z. J. Zhang, G. Y. Yang, Y. H. Tang, and Y. T. Wang. 2019. 'L-glutamine protects mouse brain from ischemic injury via up-regulating heat shock protein 70', *CNS Neurosci Ther*, 25: 1030-41.

Lyngso, D., L. Simonsen, and J. Bulow. 2002. 'Metabolic effects of interleukin-6 in human splanchnic and adipose tissue', *J Physiol*, 543: 379-86.

Magistretti, P. J., and L. Pellerin. 1997. 'Regulation by neurotransmitters of glial energy metabolism', *Adv Exp Med Biol*, 429: 137-43.

Marmentini, C., G. M. Soares, G. A. Bronczek, S. Piovan, C. E. Mareze-Costa, E. M. Carneiro, A. C. Boschero, and M. A. Kurauti. 2021. 'Aging Reduces Insulin Clearance in Mice', *Front Endocrinol (Lausanne)*, 12: 679492.

McCarthy, K. D., and J. de Vellis. 1980. 'Preparation of separate astroglial and oligodendroglial cell cultures from rat cerebral tissue', *J Cell Biol*, 85: 890-902.

McKenna, M. C., U. Sonnewald, X. Huang, J. Stevenson, and H. R. Zielke. 1996. 'Exogenous glutamate concentration regulates the metabolic fate of glutamate in astrocytes', *J Neurochem*, 66: 386-93.

McKeon, RJ, RC Schreiber, JS Rudge, and J Silver. 1991. 'Reduction of neurite outgrowth in a model of glial scarring following CNS injury is correlated with the expression of inhibitory molecules on reactive astrocytes', *The Journal of Neuroscience*, 11: 3398-411.

Meguid, M. M., J. L. Beverly, Z. J. Yang, J. R. Gleason, R. A. Meguid, and M. X. Yue. 1993. 'Parenteral nutrition, brain glycogen, and food intake', *Am J Physiol*, 265: R1387-91.

Mehla, Jogender, Itender Singh, Deepti Diwan, James W. Nelson, Molly Lawrence, Eunjae Lee, Adam Q. Bauer, David M. Holtzman, and Gregory J. Zipfel. 2021. 'STAT3 inhibitor mitigates cerebral amyloid angiopathy and parenchymal amyloid plaques while improving cognitive functions and brain networks', *Acta Neuropathologica Communications*, 9: 193.

Menk, A. V., N. E. Scharping, R. S. Moreci, X. Zeng, C. Guy, S. Salvatore, H. Bae, J. Xie, H. A. Young, S. G. Wendell, and G. M. Delgoffe. 2018. 'Early TCR Signaling Induces Rapid Aerobic Glycolysis Enabling Distinct Acute T Cell Effector Functions', *Cell Rep*, 22: 1509-21.

Munoz-Gomez, S. A., J. G. Wideman, A. J. Roger, and C. H. Slamovits. 2017. 'The Origin of Mitochondrial Cristae from Alphaproteobacteria', *Mol Biol Evol*, 34: 943-56.

Muraina, I. A., M. M. Suleiman, and J. N. Eloff. 2009. 'Can MTT be used to quantify the antioxidant activity of plant extracts?', *Phytomedicine*, 16: 665-8.

Musuka, T. D., S. B. Wilton, M. Traboulsi, and M. D. Hill. 2015. 'Diagnosis and management of acute ischemic stroke: speed is critical', *CMAJ*, 187: 887-93.

Nakamura-Tsuruta, S., M. Yasuda, T. Nakamura, E. Shinoda, T. Furuyashiki, R. Kakutani, H. Takata, Y. Kato, and H. Ashida. 2012. 'Comparative analysis of carbohydrate-binding specificities of two anti-glycogen monoclonal antibodies using ELISA and surface plasmon resonance', *Carbohydr Res*, 350: 49-54.

Nedergaard, M. 1988. 'Mechanisms of brain damage in focal cerebral ischemia', *Acta Neurol Scand*, 77: 81-101.

Nedergaard, M., B. Ransom, and S. A. Goldman. 2003. 'New roles for astrocytes: redefining the functional architecture of the brain', *Trends Neurosci*, 26: 523-30.

Nogueira, R. G., A. P. Jadhav, D. C. Haussen, A. Bonafe, R. F. Budzik, P. Bhuva, D. R. Yavagal, M. Ribo, C. Cognard, R. A. Hanel, C. A. Sila, A. E. Hassan, M. Millan, E. I.

Levy, P. Mitchell, M. Chen, J. D. English, Q. A. Shah, F. L. Silver, V. M. Pereira, B. P. Mehta, B. W. Baxter, M. G. Abraham, P. Cardona, E. Veznedaroglu, F. R. Hellinger, L. Feng, J. F. Kirmani, D. K. Lopes, B. T. Jankowitz, M. R. Frankel, V. Costalat, N. A. Vora, A. J. Yoo, A. M. Malik, A. J. Furlan, M. Rubiera, A. Aghaebrahim, J. M. Olivot, W. G. Tekle, R. Shields, T. Graves, R. J. Lewis, W. S. Smith, D. S. Liebeskind, J. L. Saver, T. G. Jovin, and Dawn Trial Investigators. 2018. 'Thrombectomy 6 to 24 Hours after Stroke with a Mismatch between Deficit and Infarct', *N Engl J Med*, 378: 11-21.

Norat, Pedro, Jennifer D Sokolowski, Catherine M Gorick, Sauson Soldozy, Youngrok Chae, Kaan Yagmurlu, Khadijeh A Sharifi, Melanie Walker, Michael R Levitt, and Alexander L Klibanov. 'Intra-Arterial Transplantation of Mitochondria after Ischemic Stroke Reduces Cerebral Infarction', *Available at SSRN 3535869*.

O'Dowd, B. S., M. E. Gibbs, K. T. Ng, E. Hertz, and L. Hertz. 1994. 'Astrocytic glycogenolysis energizes memory processes in neonate chicks', *Brain Res Dev Brain Res*, 78: 137-41.

Oe, Y., O. Baba, H. Ashida, K. C. Nakamura, and H. Hirase. 2016. 'Glycogen distribution in the microwave-fixed mouse brain reveals heterogeneous astrocytic patterns', *Glia*, 64: 1532-45.

Ohmiya, Yoshihiro. 2014. "APPLICATIONS OF BIOLUMINESCENCE (Cell Based Assays and Imaging)." In. Biomedical Research Institute, National Institute of Advanced Industrial Science and Technology (AIST): Biomedical Research Institute, National Institute of Advanced Industrial Science and Technology (AIST).

Okada, S., M. Nakamura, H. Katoh, T. Miyao, T. Shimazaki, K. Ishii, J. Yamane, A. Yoshimura, Y. Iwamoto, Y. Toyama, and H. Okano. 2006. 'Conditional ablation of Stat3 or Socs3 discloses a dual role for reactive astrocytes after spinal cord injury', *Nat Med*, 12: 829-34.

Oliet, S. H., and J. P. Mothet. 2006. 'Molecular determinants of D-serine-mediated gliotransmission: from release to function', *Glia*, 54: 726-37.

Ong, S. B., S. Subrayan, S. Y. Lim, D. M. Yellon, S. M. Davidson, and D. J. Hausenloy. 2010. 'Inhibiting mitochondrial fission protects the heart against ischemia/reperfusion injury', *Circulation*, 121: 2012-22.

Parone, P. A., S. Da Cruz, D. Tondera, Y. Mattenberger, D. I. James, P. Maechler, F. Barja, and J. C. Martinou. 2008. 'Preventing mitochondrial fission impairs mitochondrial function and leads to loss of mitochondrial DNA', *PLoS One*, 3: e3257.

Payen, Valéry L., Luca X. Zampieri, Paolo E. Porporato, and Pierre Sonveaux. 2019. 'Pro- and antitumor effects of mitochondrial reactive oxygen species', *Cancer and Metastasis Reviews*, 38: 189-203.

Pekny, M., and M. Nilsson. 2005. 'Astrocyte activation and reactive gliosis', *Glia*, 50: 427-34.

Poli, V., and A. Camporeale. 2015. 'STAT3-Mediated Metabolic Reprograming in Cellular Transformation and Implications for Drug Resistance', *Front Oncol*, 5: 121.

Prebil, M., J. Jensen, R. Zorec, and M. Kreft. 2011. 'Astrocytes and energy metabolism', *Arch Physiol Biochem*, 117: 64-9.

Priego, N., L. Zhu, C. Monteiro, M. Mulders, D. Wasilewski, W. Bindeman, L. Doglio, L. Martinez, E. Martinez-Saez, Y. Cajal S. Ramon, D. Megias, E. Hernandez-Encinas, C. Blanco-Aparicio, L. Martinez, E. Zarzuela, J. Munoz, C. Fustero-Torre, E. Pineiro-Yanez, A. Hernandez-Lain, L. Bertero, V. Poli, M. Sanchez-Martinez, J. A. Menendez, R. Soffietti, J. Bosch-Barrera, and M. Valiente. 2018. 'STAT3 labels a subpopulation of reactive astrocytes required for brain metastasis', *Nat Med*, 24: 1024-35.

Puisieux, F., E. Fattal, M. Lahiani, J. Auger, P. Jouannet, P. Couvreur, and J. Delattre. 1994. 'Liposomes, an interesting tool to deliver a bioenergetic substrate (ATP). in vitro and in vivo studies', *J Drug Target*, 2: 443-8.

Quintana, D. D., J. A. Garcia, S. N. Sarkar, S. Jun, E. B. Engler-Chiurazzi, A. E. Russell, J. Z. Cavendish, and J. W. Simpkins. 2019. 'Hypoxia-reoxygenation of primary astrocytes results in a redistribution of mitochondrial size and mitophagy', *Mitochondrion*, 47: 244-55.

Rahaman, S. O., P. C. Harbor, O. Chernova, G. H. Barnett, M. A. Vogelbaum, and S. J. Haque. 2002. 'Inhibition of constitutively active Stat3 suppresses proliferation and induces apoptosis in glioblastoma multiforme cells', *Oncogene*, 21: 8404-13.

Rakers, C., M. Schleif, N. Blank, H. Matuskova, T. Ulas, K. Handler, S. V. Torres, T. Schumacher, K. Tai, J. L. Schultze, W. S. Jackson, and G. C. Petzold. 2019. 'Stroke target identification guided by astrocyte transcriptome analysis', *Glia*, 67: 619-33.

Ranjan, A., D. Theodore, R. P. Haran, and M. J. Chandy. 1993. 'Ascorbic acid and focal cerebral ischaemia in a primate model', *Acta Neurochir (Wien)*, 123: 87-91.

Rathore, S. S., A. R. Hinn, L. S. Cooper, H. A. Tyroler, and W. D. Rosamond. 2002. 'Characterization of incident stroke signs and symptoms: findings from the atherosclerosis risk in communities study', *Stroke*, 33: 2718-21.

Rehncrona, S., I. Rosen, and B. K. Siesjo. 1981. 'Brain lactic acidosis and ischemic cell damage: 1. Biochemistry and neurophysiology', *J Cereb Blood Flow Metab*, 1: 297-311.

Reichenbach, N., A. Delekate, M. Plescher, F. Schmitt, S. Krauss, N. Blank, A. Halle, and G. C. Petzold. 2019. 'Inhibition of Stat3-mediated astrogliosis ameliorates pathology in an Alzheimer's disease model', *EMBO Mol Med*, 11.

Reichert, Susan A., Jeong Sook Kim-Han, and Laura L. Dugan. 2001. 'The Mitochondrial Permeability Transition Pore and Nitric Oxide Synthase Mediate Early Mitochondrial Depolarization in Astrocytes during Oxygen–Glucose Deprivation', *The Journal of Neuroscience*, 21: 6608-16.

Rice, M. E. 2000. 'Ascorbate regulation and its neuroprotective role in the brain', *Trends Neurosci*, 23: 209-16.

Rich, L. R., W. Harris, and A. M. Brown. 2019. 'The Role of Brain Glycogen in Supporting Physiological Function', *Front Neurosci*, 13: 1176.

Rose, J., C. Brian, A. Pappa, M. I. Panayiotidis, and R. Franco. 2020. 'Mitochondrial Metabolism in Astrocytes Regulates Brain Bioenergetics, Neurotransmission and Redox Balance', *Front Neurosci*, 14: 536682.

Rubin, H. 1997. 'Cell aging in vivo and in vitro', *Mech Ageing Dev*, 98: 1-35.

Sarafian, T. A., C. Montes, T. Imura, J. Qi, G. Coppola, D. H. Geschwind, and M. V. Sofroniew. 2010. 'Disruption of astrocyte STAT3 signaling decreases mitochondrial function and increases oxidative stress in vitro', *PLoS One*, 5: e9532.

Sarmiento Soto, M., J. R. Larkin, C. Martin, A. A. Khrapitchev, M. Maczka, V. Economopoulos, H. Scott, C. Escartin, G. Bonvento, S. Serres, and N. R. Sibson. 2020. 'STAT3-Mediated Astrocyte Reactivity Associated with Brain Metastasis Contributes to Neurovascular Dysfunction', *Cancer Res*, 80: 5642-55.

Satriotomo, I., K. K. Bowen, and R. Vemuganti. 2006. 'JAK2 and STAT3 activation contributes to neuronal damage following transient focal cerebral ischemia', *J Neurochem*, 98: 1353-68.

Schneider, U., R. C. Poole, A. P. Halestrap, and P. Grafe. 1993. 'Lactate-proton co-transport and its contribution to interstitial acidification during hypoxia in isolated rat spinal roots', *Neuroscience*, 53: 1153-62.

Schousboe, Arne, Lasse Bak, and Helle Waagepetersen. 2013. 'Astrocytic Control of Biosynthesis and Turnover of the Neurotransmitters Glutamate and GABA', *Frontiers in Endocrinology*, 4.

Schust, J., B. Sperl, A. Hollis, T. U. Mayer, and T. Berg. 2006. 'Stattic: a small-molecule inhibitor of STAT3 activation and dimerization', *Chem Biol*, 13: 1235-42.

Shall, Sydney. 1996. 'Ageing of Cells in Vitro.' in Suresh I. S. Rattan and Olivier Toussaint (eds.), *Molecular Gerontology: Research Status and Strategies* (Springer US: Boston, MA).

Sims, N. R., and W. A. Pulsinelli. 1987. 'Altered mitochondrial respiration in selectively vulnerable brain subregions following transient forebrain ischemia in the rat', *J Neurochem*, 49: 1367-74.

Sirko, S., G. Behrendt, P. A. Johansson, P. Tripathi, M. Costa, S. Bek, C. Heinrich, S. Tiedt, D. Colak, M. Dichgans, I. R. Fischer, N. Plesnila, M. Staufenbiel, C. Haass, M. Snapyan, A. Saghatelyan, L. H. Tsai, A. Fischer, K. Grobe, L. Dimou, and M. Gotz. 2013. 'Reactive glia in the injured brain acquire stem cell properties in response to sonic hedgehog. [corrected]', *Cell Stem Cell*, 12: 426-39.

Smith-Thomas, L. C., J. Fok-Seang, J. Stevens, J. S. Du, E. Muir, A. Faissner, H. M. Geller, J. H. Rogers, and J. W. Fawcett. 1994. 'An inhibitor of neurite outgrowth produced by astrocytes', *J Cell Sci*, 107 (Pt 6): 1687-95.

Smith, G. M., R. H. Miller, and J. Silver. 1986. 'Changing role of forebrain astrocytes during development, regenerative failure, and induced regeneration upon transplantation', *J Comp Neurol*, 251: 23-43.

Sofroniew, M. V. 2000. 'Astrocyte failure as a cause of CNS dysfunction', *Mol Psychiatry*, 5: 230-2.

———. 2009. 'Molecular dissection of reactive astrogliosis and glial scar formation', *Trends Neurosci*, 32: 638-47.

Soya, Mariko, Takashi Matsui, Takeru Shima, Subrina Jesmin, Naomi Omi, and Hideaki Soya. 2018. 'Hyper-hippocampal glycogen induced by glycogen loading with exhaustive exercise', *Scientific Reports*, 8: 1285.

Sukumar, M., J. Liu, Y. Ji, M. Subramanian, J. G. Crompton, Z. Yu, R. Roychoudhuri, D. C. Palmer, P. Muranski, E. D. Karoly, R. P. Mohney, C. A. Klebanoff, A. Lal, T. Finkel, N. P. Restifo, and L. Gattinoni. 2013. 'Inhibiting glycolytic metabolism enhances CD8+ T cell memory and antitumor function', *J Clin Invest*, 123: 4479-88.

Sun, C., X. Liu, B. Wang, Z. Wang, Y. Liu, C. Di, J. Si, H. Li, Q. Wu, D. Xu, J. Li, G. Li, Y. Wang, F. Wang, and H. Zhang. 2019. 'Endocytosis-mediated mitochondrial transplantation: Transferring normal human astrocytic mitochondria into glioma cells rescues aerobic respiration and enhances radiosensitivity', *Theranostics*, 9: 3595-607.

Supplie, L. M., T. Duking, G. Campbell, F. Diaz, C. T. Moraes, M. Gotz, B. Hamprecht, S. Boretius, D. Mahad, and K. A. Nave. 2017. 'Respiration-Deficient Astrocytes Survive As Glycolytic Cells In Vivo', *J Neurosci*, 37: 4231-42.

Suzuki, A., S. A. Stern, O. Bozdagi, G. W. Huntley, R. H. Walker, P. J. Magistretti, and C. M. Alberini. 2011. 'Astrocyte-neuron lactate transport is required for long-term memory formation', *Cell*, 144: 810-23.

Suzuki, S., K. Tanaka, S. Nogawa, T. Dembo, A. Kosakai, and Y. Fukuuchi. 2001. 'Phosphorylation of signal transducer and activator of transcription-3 (Stat3) after focal cerebral ischemia in rats', *Exp Neurol*, 170: 63-71.

Takahashi, S. 2011. '[Astroglial protective mechanisms against ROS under brain ischemia]', *Rinsho Shinkeigaku*, 51: 1032-5.

———. 2021. 'Neuroprotective Function of High Glycolytic Activity in Astrocytes: Common Roles in Stroke and Neurodegenerative Diseases', *Int J Mol Sci*, 22.

Tanaka, E., S. Yamamoto, Y. Kudo, S. Mihara, and H. Higashi. 1997. 'Mechanisms underlying the rapid depolarization produced by deprivation of oxygen and glucose in rat hippocampal CA1 neurons in vitro', *J Neurophysiol*, 78: 891-902.

Thrash, J. C., A. Boyd, M. J. Huggett, J. Grote, P. Carini, R. J. Yoder, B. Robbertse, J. W. Spatafora, M. S. Rappe, and S. J. Giovannoni. 2011. 'Phylogenomic evidence for a common ancestor of mitochondria and the SAR11 clade', *Sci Rep*, 1: 13.

Toft, A. D., A. Falahati, and A. Steensberg. 2011. 'Source and kinetics of interleukin-6 in humans during exercise demonstrated by a minimally invasive model', *Eur J Appl Physiol*, 111: 1351-9.

Tolomeo, M., and A. Cascio. 2021. 'The Multifaced Role of STAT3 in Cancer and Its Implication for Anticancer Therapy', *Int J Mol Sci*, 22.

Turner, D. A., and D. C. Adamson. 2011. 'Neuronal-astrocyte metabolic interactions: understanding the transition into abnormal astrocytoma metabolism', *J Neuropathol Exp Neurol*, 70: 167-76.

Twig, G., A. Elorza, A. J. Molina, H. Mohamed, J. D. Wikstrom, G. Walzer, L. Stiles, S. E. Haigh, S. Katz, G. Las, J. Alroy, M. Wu, B. F. Py, J. Yuan, J. T. Deeney, B. E. Corkey, and O. S. Shirihai. 2008. 'Fission and selective fusion govern mitochondrial segregation and elimination by autophagy', *EMBO J*, 27: 433-46.

Unnithan, A. K. A., and P. Mehta. 2022. 'Hemorrhagic Stroke.' in, *StatPearls* (Treasure Island (FL)).

Valdebenito, R., I. Ruminot, P. Garrido-Gerter, I. Fernandez-Moncada, L. Forero-Quintero, K. Alegria, H. M. Becker, J. W. Deitmer, and L. F. Barros. 2016. 'Targeting of astrocytic glucose metabolism by beta-hydroxybutyrate', *J Cereb Blood Flow Metab*, 36: 1813-22.

Vicente-Gutierrez, C., N. Bonora, V. Bobo-Jimenez, D. Jimenez-Blasco, I. Lopez-Fabuel, E. Fernandez, C. Josephine, G. Bonvento, J. A. Enriquez, A. Almeida, and J. P. Bolanos. 2019. 'Astrocytic mitochondrial ROS modulate brain metabolism and mouse behaviour', *Nat Metab*, 1: 201-11.

Viola, A., F. Munari, R. Sanchez-Rodriguez, T. Scolaro, and A. Castegna. 2019. 'The Metabolic Signature of Macrophage Responses', *Front Immunol*, 10: 1462.

Virani, S. S., A. Alonso, H. J. Aparicio, E. J. Benjamin, M. S. Bittencourt, C. W. Callaway, A. P. Carson, A. M. Chamberlain, S. Cheng, F. N. Delling, M. S. V. Elkind, K. R. Evenson, J. F. Ferguson, D. K. Gupta, S. S. Khan, B. M. Kissela, K. L. Knutson, C. D. Lee, T. T. Lewis, J. Liu, M. S. Loop, P. L. Lutsey, J. Ma, J. Mackey, S. S. Martin, D. B. Matchar, M. E. Mussolino, S. D. Navaneethan, A. M. Perak, G. A. Roth, Z. Samad, G. M. Satou, E. B. Schroeder, S. H. Shah, C. M. Shay, A. Stokes, L. B. VanWagner, N. Y. Wang, C. W. Tsao, Epidemiology American Heart Association Council on, Committee Prevention Statistics, and Subcommittee Stroke Statistics. 2021. 'Heart Disease and Stroke Statistics-2021 Update: A Report From the American Heart Association', *Circulation*, 143: e254-e743.

Waje-Andreassen, U., J. Krakenes, E. Ulvestad, L. Thomassen, K. M. Myhr, J. Aarseth, and C. A. Vedeler. 2005. 'IL-6: an early marker for outcome in acute ischemic stroke', *Acta Neurol Scand*, 111: 360-5.

Wang, Y. Y., S. Y. Lin, C. Y. Chang, C. C. Wu, W. Y. Chen, S. L. Liao, Y. F. Chen, W. Y. Wang, and C. J. Chen. 2021. 'Jak2 Inhibitor AG490 Improved Poststroke Central and Peripheral Inflammation and Metabolic Abnormalities in a Rat Model of Ischemic Stroke', *Antioxidants (Basel)*, 10.

Wanner, I. B., M. A. Anderson, B. Song, J. Levine, A. Fernandez, Z. Gray-Thompson, Y. Ao, and M. V. Sofroniew. 2013. 'Glial scar borders are formed by newly proliferated, elongated astrocytes that interact to corral inflammatory and fibrotic cells via STAT3-dependent mechanisms after spinal cord injury', *J Neurosci*, 33: 12870-86.

Warner, D. S., S. Takaoka, B. Wu, P. S. Ludwig, R. D. Pearlstein, A. D. Brinkhous, and F. Dexter. 1996. 'Electroencephalographic burst suppression is not required to elicit maximal neuroprotection from pentobarbital in a rat model of focal cerebral ischemia', *Anesthesiology*, 84: 1475-84.

Watson, G. S., B. A. Cholerton, M. A. Reger, L. D. Baker, S. R. Plymate, S. Asthana, M. A. Fishel, J. J. Kulstad, P. S. Green, D. G. Cook, S. E. Kahn, M. L. Keeling, and S. Craft. 2005. 'Preserved cognition in patients with early Alzheimer disease and amnestic mild cognitive impairment during treatment with rosiglitazone: a preliminary study', *Am J Geriatr Psychiatry*, 13: 950-8.

Weber, B., and L. F. Barros. 2015. 'The Astrocyte: Powerhouse and Recycling Center', *Cold Spring Harb Perspect Biol*, 7.

Wei, X., X. H. Jin, X. W. Meng, J. Hua, F. H. Ji, L. N. Wang, and J. P. Yang. 2020. 'Platelet-rich plasma improves chronic inflammatory pain by inhibiting PKM2-mediated aerobic glycolysis in astrocytes', *Ann Transl Med*, 8: 1456.

Welsh, F. A., M. D. Ginsberg, W. Rieder, and W. W. Budd. 1980. 'Deleterious effect of glucose pretreatment on recovery from diffuse cerebral ischemia in the cat. II. Regional metabolite levels', *Stroke*, 11: 355-63.

Wen, Z., Z. Zhong, and J. E. Darnell, Jr. 1995. 'Maximal activation of transcription by Stat1 and Stat3 requires both tyrosine and serine phosphorylation', *Cell*, 82: 241-50.

Whelan, W. J. 2007. 'Why the linkage of glycogen to glycogenin was so difficult to determine', *Biochem Mol Biol Educ*, 35: 313-5.

Witney, T. H., L. Carroll, I. S. Alam, A. Chandrashekran, Q. D. Nguyen, R. Sala, R. Harris, R. J. DeBerardinis, R. Agarwal, and E. O. Aboagye. 2014. 'A novel radiotracer to image glycogen metabolism in tumors by positron emission tomography', *Cancer Res*, 74: 1319-28.

Wolahan, S. M., H. C. Mao, C. Real, P. M. Vespa, and T. C. Glenn. 2018. 'Lactate supplementation in severe traumatic brain injured adults by primed constant infusion of sodium L-lactate', *J Neurosci Res*, 96: 688-95.

WSO. 2022. "Global Stroke Fact Sheet." In. https://www.world-stroke.org/assets/downloads/WSO_Global_Stroke_Fact_Sheet.pdf: World Stroke Organization.

Wu, Q. J., and M. Tymianski. 2018. 'Targeting NMDA receptors in stroke: new hope in neuroprotection', *Mol Brain*, 11: 15.

Xia, X. G., H. D. Hofmann, T. Deller, and M. Kirsch. 2002. 'Induction of STAT3 signaling in activated astrocytes and sprouting septal neurons following entorhinal cortex lesion in adult rats', *Mol Cell Neurosci*, 21: 379-92.

Xu, Y. S., J. J. Liang, Y. Wang, X. J. Zhao, L. Xu, Y. Y. Xu, Q. C. Zou, J. M. Zhang, C. E. Tu, Y. G. Cui, W. H. Sun, C. Huang, J. H. Yang, and Y. E. Chin. 2016. 'STAT3 Undergoes Acetylation-dependent Mitochondrial Translocation to Regulate Pyruvate Metabolism', *Sci Rep*, 6: 39517.

Yamashita, Toru, and Koji Abe. 2012. 'Potential treatment strategies for enhancing neuroplasticity and regeneration after ischemic stroke', *Future Neurology*, 7: 279-85.

Yang, J., X. Liao, M. K. Agarwal, L. Barnes, P. E. Auron, and G. R. Stark. 2007. 'Unphosphorylated STAT3 accumulates in response to IL-6 and activates transcription by binding to NFkappaB', *Genes Dev*, 21: 1396-408.

Yang, J., and G. R. Stark. 2008. 'Roles of unphosphorylated STATs in signaling', *Cell Res*, 18: 443-51.

Yang, R., and M. Rincon. 2016. 'Mitochondrial Stat3, the Need for Design Thinking', *Int J Biol Sci*, 12: 532-44.

Yeo, S., S. Bandyopadhyay, A. Messing, and M. Brenner. 2013. 'Transgenic analysis of GFAP promoter elements', *Glia*, 61: 1488-99.

Yi, J. H., and A. S. Hazell. 2006. 'Excitotoxic mechanisms and the role of astrocytic glutamate transporters in traumatic brain injury', *Neurochem Int*, 48: 394-403.

Zamanian, J. L., L. Xu, L. C. Foo, N. Nouri, L. Zhou, R. G. Giffard, and B. A. Barres. 2012. 'Genomic analysis of reactive astrogliosis', *J Neurosci*, 32: 6391-410.

Zhang, Z., X. Deng, Y. Liu, Y. Liu, L. Sun, and F. Chen. 2019. 'PKM2, function and expression and regulation', *Cell Biosci*, 9: 52.

Zhang, Z., Z. Ma, C. Yan, K. Pu, M. Wu, J. Bai, Y. Li, and Q. Wang. 2019. 'Muscle-derived autologous mitochondrial transplantation: A novel strategy for treating cerebral ischemic injury', *Behav Brain Res*, 356: 322-31.

Zhou, Qionglin, Mingzhu Tang, Lu He, and Shuiping Chen. 2020. 'PKM2: a crucial neuroprotective target against oxidative stress', *Acta Biochimica et Biophysica Sinica*, 52: 1432-34.